# Coherence and relaxation of an optically-driven bosonic quantum gas : experiments with ultracold ytterbium atoms

Manel Bosch Aguilera

## To cite this version:

Manel Bosch Aguilera. Coherence and relaxation of an optically-driven bosonic quantum gas : experiments with ultracold ytterbium atoms. Quantum Physics [quant-ph]. Sorbonne Université, 2019. English. NNT : 2019SORUS174 . tel-02932168

**HAL Id: tel-02932168**
**https://theses.hal.science/tel-02932168v1**

Submitted on 7 Sep 2020

LABORATOIRE KASTLER BROSSEL COLLÈGE DE FRANCE

# THÈSE DE DOCTORAT DE SORBONNE UNIVERSITÉ

préparée par

**MANEL BOSCH AGUILERA**

---

# COHERENCE AND RELAXATION OF AN OPTICALLY-DRIVEN BOSONIC QUANTUM GAS

## EXPERIMENTS WITH ULTRACOLD YTTERBIUM ATOMS

---

À soutenir le 26 septembre 2019 devant le jury composé de :

| | |
|---|---|
| M. Herwig OTT | Rapporteur |
| Mme. Leticia TARRUELL | Rapporteuse |
| M. David CLÉMENT | Examinateur |
| M. Jean-Noël FUCHS | Examinateur |
| M. Jérôme BEUGNON | Membre invité |
| M. Fabrice GERBIER | Directeur de thèse |

# ABSTRACT

In this thesis I report on a series of experimental studies performed with ultracold ytterbium gases driven in different optical transitions. Ytterbium belongs to the family of the so-called alkaline-earth-like atoms, which feature a rich electronic structure, with an optical clock transition free of spontaneous emission and a narrow intercombination transition, making them very appealing for metrological and quantum simulation proposals.

By performing spectroscopy on the clock transition, I prove on a first set of experiments in deep optical lattices our ability to drive this transition coherently for long times. This coherent control is then used for different studies. First, as tool to measure the scattering lengths of the states involved in the clock transition. Then, to prepare a small open quantum system, where dissipation arises in the form of two-body losses. By enabling the coupling adiabatically, we observe a strong suppression of these losses, which is interpreted as a signature of the quantum Zeno effect. I ultimately use the coherent driving to study the relaxation dynamics of a dissipative bulk Bose-Einstein condensate.

Finally, I elaborate an investigation on a strongly-interacting open system. Dissipation is artificially induced in the form of spontaneous emission using the intercombination transition. Here, I study in which manner spontaneous emission destroys the spatial coherence of a superfluid in an optical lattice. These experiments reveal that the presence of strong interactions partially protects a residual amount of coherence and makes decoherence develop in a non-trivial manner, unveiling the emergence of a subdiffusive relaxation channel.

# RÉSUMÉ

Dans ce travail de thèse, je présente une série d'études expérimentales réalisées avec des gaz d'ytterbium ultrafroids excités sur différentes transitions optiques. L'ytterbium appartient à la famille des atomes dits alcalino-terreux. Ces atomes possèdent une structure électronique riche, avec une transition d'horloge exempte d'émission spontanée et une transition étroite d'intercombinaison, ce qui les rend très intéressants pour la métrologie et la simulation quantique.

Avec des expériences de spectroscopie sur la transition d'horloge dans des réseaux optiques profonds, je montre notre capacité à exciter cette transition de manière cohérente pendant de longues périodes. Ce contrôle est ensuite utilisé dans un premier temps en tant qu'outil pour mesurer les longueurs de diffusion des états impliqués dans la transition d'horloge et, ensuite, pour préparer un petit système quantique ouvert où la dissipation prend la forme de pertes à deux corps. En branchant ce couplage adiabatiquement, nous observons une forte suppression de ces pertes, ce qui est interprété comme une signature de l'effet Zénon quantique. J'utilise finalement ce transfert cohérent pour étudier la dynamique de relaxation d'un condensat de Bose-Einstein.

Enfin, je développe une étude sur un système ouvert avec des interactions fortes. Ici, on induit artificiellement de la dissipation sous la forme d'émission spontanée en utilisant la transition d'intercombinaison, et j'étudie comment la cohérence spatiale d'un superfluide dans un réseau optique est détruite. Ces expériences révèlent que la présence d'interactions fortes protège partiellement une cohérence résiduelle et entraîne un développement non-triviale de la décohérence, révélant ainsi l'émergence d'un canal de relaxation subdiffusif.

# Contents

# Glossary

In this manuscript, I use the following acronyms:

**1BZ** First Brillouin zone,

**AOM** Acousto-optic modulator,

**BEC** Bose-Einstein condensate,

**CDT** Crossed dipole trap,

**EP** Exceptional point,

**GP(E)** Gross-Pitaevskii (equation),

**EOM** Electro-optic modulator,

**MOT** Magneto-optical trap,

**OBE** Optical Bloch equations

**PDH** Pound-Drever-Hall,

**TOF** Time-of-flight,

**ULE** Ultra-low expansion.

# Introduction

## Quantum simulation

It is quite common in physics to encounter situations where it is not feasible to address a problem without resorting to important assumptions and simplifications. A relevant tool, useful through all subdomains of physics, is the mean-field approximation. Here, a system of many interacting particles is reduced to the physics of a single particle evolving in a self-consistent potential, accounting for the average effect of the rest of particles. Sometimes, such an idealized description allows one to make useful (in some cases, even accurate) predictions about the physical system of interest. However, in other cases, the correlations neglected in the mean-field description are an essential component and this idealization fails to describe the physics at hand.

Condensed matter physics offers many examples of both situations. On the one hand, many materials are well described by band theory and the Landau quasiparticle description. On the other hand, ensembles of strongly interacting electrons under extreme external conditions, such as low temperatures or strong magnetic fields, have led to a plethora of rich phenomena, like high-temperature superconductivity (Bednorz et al. 1986) or the fractional quantum Hall effect (Tsui et al. 1982), where a complete theoretical description is still lacking. Here, even the proposed minimal models of interacting electrons (Basov et al. 2005; Stern 2008), such as the celebrated Hubbard models or generalizations of it, are not analytically solvable beyond the one dimensional case. Besides, quasi-exact numerical solutions are limited to very small number of particles, and other numerical approaches are difficult to apply due to the large number of degrees of freedom involved.

Here comes into play the idea put forward by Richard Feynman of building *«a quantum machine that could imitate any quantum system...»*[1] (Feynman 1982), i.e. a quantum simulator: A model system, controlled by experimentalists, to mimic the model Hamiltonian of interest. Here, instead of looking for the spectrum of such Hamiltonian, the experiment itself gives direct access, by measurement, to the observables themselves. There are many experimental platforms today where implementations of this idea are pursued, including systems of trapped ions, superconducting cavity quantum electrodynamics, photonic systems and, last but not least, quantum gases of ultracold atoms in optical lattices (Georgescu et al. 2014).

---

[1] *«...including the physical world.»* (Feynman 1982).

### Ultracold quantum gases

Ultracold quantum gases constitute on their own a well-established field of physics nowadays. The invention of the laser in the 1960s led to vertiginous advances in atomic physics and, in turn, to a better understanding of the interaction between light with matter, allowing full control of the internal and external degrees of freedom of atoms. This gave birth (Hänsch et al. 1975) to the development of laser cooling in the 1980s (Phillips 1998; Cohen-Tannoudji 1998; Chu 1998). This cooling mechanism and other techniques, such as evaporative cooling (Hess 1986; Davis et al. 1995), were key in the production of the first Bose-Einstein condensates (Anderson et al. 1995; Bradley et al. 1995) and, shortly after, the first degenerate Fermi gases (DeMarco et al. 1999).

Since then, a tremendous amount of work has been invested towards the comprehension of these new states of matter (Dalfovo et al. 1999; Leggett 2001; Giorgini et al. 2008). Among others, these researches brought to light the wave nature of ultracold matter, with experiments displaying interferences and underscoring the presence of long-range order in Bose-Einstein condensates (Andrews et al. 1997; Bloch et al. 2000).

Despite being very dilute entities, these systems are interacting and feature superfluid behavior (Raman et al. 1999; Matthews et al. 1999; Sidorenkov et al. 2013). Besides, thanks to mechanisms such as Feshbach resonances, quantum gases can be brought to the strongly interacting regime (Bloch et al. 2008), showing for instance the universality of Fermi gases at unitarity (Nascimbène et al. 2010; Cao et al. 2011; Ku et al. 2012). The emergent use of gases with long-ranged dipolar interactions (Ferrier-Barbut et al. 2016; Tanzi et al. 2019; Böttcher et al. 2019) and the careful tailoring of short-ranged interactions (Cabrera et al. 2018; Semeghini et al. 2018) has allowed experimentalists in the past few years to bring these dilute systems towards new states of matter, some of them featuring supersolidity, a phase predicted long ago, where superfluidity coexists with a tendency to form spatially orderred structures, breaking translational symmetry (Leggett 1970; Nozières 2004; Boninsegni et al. 2012).

Alternatively, the strongly interacting regime can be reached by confining particles into standing waves of light, the so-called optical lattices. This was first shown in the seminal experiment of Greiner et al. (2002), where the transition from a superfluid to a strongly correlated Mott insulator was witnessed. Atoms in optical lattices are described by Hubbard-type Hamiltonians (Jaksch et al. 1998; Tarruell et al. 2018) and mimic the physics of electrons in a crystal, establishing a direct analogy with condensed matter systems with strong correlations. In quantum gases, however, the dynamics take place at much lower energy scales thanks to their diluteness. In addition, these systems are much pure and tuneable, allowing for probing techniques which are beyond reach in real solid state systems.

Thanks to all these properties, quantum gases have become one of the main pillars of quantum simulation (Cirac et al. 2012; Lewenstein et al. 2012).

### Alkaline-earth-like atoms as quantum simulators

Most of the physics concerning quantum gases was first studied with alkali atoms, but slowly, other atomic species were brought to quantum degeneracy, as is the case of two-electron atoms (Takasu et al. 2003). One of the main interest of alkaline-earth atoms, including Sr, Ca, Mg and Yb (which is a lanthanide but has the same low-lying electronic structure as alkaline-earth atoms) lies in their electronic structure, featuring an optical clock transition. This has made them very attractive in the realm of frequency standards (Ludlow et al. 2015) and metrological applications (Katori 2011). Nowadays, the most accurate clocks drive these atoms in optical lattices, and can beat the accuracy of standard fountain clocks by orders of magnitude, with performances well below the $10^{-17}$ level, rising the question of a new definition of the second (Riehle 2015; McGrew et al. 2019). In addition to the existence of an optical clock transition, other characteristics of their atomic structure make these atoms interesting for light-matter interaction studies (Bromley et al. 2016) and these species have also been proposed for the quantum simulation of a great variety of systems (Cazalilla et al. 2009; Gorshkov et al. 2010; Daley 2011; Daley et al. 2011; Olmos et al. 2013; Cazalilla et al. 2014).

A particular application, which motivated the choice of ytterbium in our experiment, is the potential these atoms have for the simulation of artificial magnetism in optical lattices (Jaksch et al. 2003; Gerbier et al. 2010), thanks to the existence of two long-lived states. The interplay of interactions, magnetism and the discrete nature of an optical lattice gives rise to a rich phase diagram, where strongly correlated states such as (the bosonic version of) the paradigmatic Laughlin state, appearing widely in the theory of the fractional quantum Hall effect, emerge (Sørensen et al. 2005; Umucalılar et al. 2010). Experiments with alkaline-earth-like atoms have already exploited the clock transition in this direction, mostly in one-dimensional fermionic systems where the long-lived excited state plays the role of a synthetic dimension (Livi et al. 2016; Kolkowitz et al. 2017; Bromley et al. 2018)[2]. So far, mainly the modification of the single-particle band structure has been studied, but one hopes to access the rich physics of interacting systems in external gauge potentials.

### Open quantum systems

No system is truly isolated. Instead, entities are usually coupled to an environment, eventually affecting its dynamics. In many cases, the environment is too large to keep a detailed track of its evolution and one ends up disregarding the information being transferred to it through the coupling. This leads to a phenomenon known as *decoherence* (Zurek 2007). Here, the interferences between different components of a system become suppressed[3], destroying quantum superpositions.

Quantum gases samples are produced in clean systems, extremely well separated from the environment, and the many everyday forms of decoherence are strongly inhibited in these systems or, at least, play a minor role in the timescale of experiments[4]. This makes of such systems a good experimental platform to study decoherence, by artificially inducing it. In the past years, this problem has been tackled both in the

---

[2] In parallel, a large number of experiments have also explored these physics with alkali atoms both in weakly interacting bulk systems (Schweikhard et al. 2004; Lin et al. 2009) and optical lattices, where spin-orbit coupling and artificial magnetism at the single-particle level has been observed [see e.g. Dalibard et al. (2011); Goldman et al. (2014) or Aidelsburger (2018) for a review of these topics] .

[3] In more precise terms, the coherences of the reduced density matrix of the system $\rho_{ij}$ at two different times, $t > t_0$, obey $\rho_{ij}(t) < \rho_{ij}(t_0)$.

[4] Still, dissipative mechanisms inherent to atomic physics, such as processes leading to atom losses or heating mechanisms, might be present and destroy the coherence of quantum gases.

theoretical and experimental sides, studying how dissipation mechanisms, mostly in the form of spontaneous emission or atom losses, impact the evolution of a system.

These studies have already revealed many fascinating, and even counter-intuitive, phenomena such as the observation of the quantum Zeno effect (Syassen et al. 2008; Barontini et al. 2013; Zhu et al. 2014), where strong enough losses would be acting as a continuous measurement (Breuer et al. 2007; García-Ripoll et al. 2009) and in Patil et al. (2015), where the act of continously measuring a system inhibited coherent tunneling.

Other experiments studying dissipation have observed bistability regions in the phase diagram of a driven-dissipative superfluid (Labouvie et al. 2016), where losses were locally induced at a given site of an optical lattice. Here, superfluid and normal currents coexist at intermediate loss strengths, with the emergence of the one or the other depending on the initial conditions. Also, the effect of dissipation in many-body localisation has been studied in Lüschen et al. (2017).

However, there is still much to understand on the role played by interactions in dissipative processes. In particular, whether these interactions will hasten or slow down the decay towards steady, fully decohered states.

## This thesis

The two main topics covered throughout this manuscript are the coherent control of the degrees of freedom of a quantum gas, and the dissipation mechanisms competing against this coherent driving. The interplay between driving, dissipation and also the possibility to study it in the presence of weak and strong interactions, have led us to witness and study a variety of rich and interesting phenomena, such as the observation of quantum Zeno dynamics and subdiffusive processes.

This manuscript contains a series of studies that are organized from the investigation of *simple* few body isolated systems, to open many-body quantum systems. We first start by characterizing one of our main probing tools: a clock laser. We do this in small isolated systems, where the external dynamics of the particles are frozen in deep optical lattices. In these measurements, we show the capability of driving the internal dynamics of these simpler systems for long times. This allows us then to study and characterize more elaborated organizations, with two or many interacting particles, where the relaxation dynamics occur in much shorter timescales. We have used the clock transition to measure the scattering properties of the states involved in it and to probe the dissipative dynamics of atom pairs and a weakly interacting Bose-Einstein condensate. Finally, using a broader transition, we have induced dissipation in the form of spontaneous emission in a strongly interacting system, and analyzed its dynamics towards its steady-state.

More in detail, the discussion and exposition of the results obtained during this thesis have been arranged as follows:

- **Part I** describes the main theory elements and the experimental framework of this thesis. First of all, in **chapter 1** we recall the basic concepts of Bose-Einstein condensation and those of single and interacting particles in optical lattices. Then, in **chapter 2** we present our experimental setup: Here, we detail the production and probing techniques of Bose-Einstein condensates and their subsequent loading in optical lattices.

- **Part II** is devoted to the physics of one- and two-particle systems driven on the clock transition.

  First, in **chapter 3** we present the laser systems and the techniques used to drive the clock transition and image atoms in the metastable state. Then, we review the key notions of atom-light interactions in an optical lattice. Finally, we show a set of measurements corresponding to different kind of spectroscopic techniques performed on single particles loaded in deep optical lattices. The analysis of these experiments allows us then to estimate the coherence time of our coupling laser.

  In **chapter 4** we deal with interacting bosonic pairs isolated in deep latices. First, we use the clock transition to probe this system and infer the scattering properties of the clock states. Then, we investigate the role dissipation has when coherently driving these atomic pairs. We observe in the weak-coupling regime a strong suppression of the losses. This inhibition can be understood from a non-Hermitian description of the system, which allows us to link our observations to the quantum Zeno effect.

- **Part III** focuses on the study of dissipative many-body systems.

  In **chapter 5** we study the relaxation mechanisms of a weakly interacting Bose-Einstein condensate driven on the clock transition. Here, we identify three possible relaxation mechanisms: Doppler broadening, elastic interactions and inelastic two-body losses. We develop then a series of heuristic models to determine the strength of each mechanism and we also compare our measurements to coupled two-component dissipative Gross Pitaevskii equations, which account well for the observed dynamics.

  In **chapter 6** we study the loss of phase coherence in a gas of strongly interacting bosons in optical lattices submitted to spontaneous emission. Here, we observe that interactions compete with the dissipation and slow down the loss of coherence. This competition drives the system into a non-equilibrium state displaying anomalous momentum diffusion, a behavior well captured by a theoretical model also addressed in this chapter.

- A series of **supplementary materials**, comprised in **appendices A-F**, offer finally some complementary or more developed discussions of certain aspects addressed in the main text.

# Part I

# Experimental and theoretical aspects of ultracold bosons

# CHAPTER 1

# Theoretical background on bosonic quantum gases

In this first chapter I aim at presenting the essential concepts underlying the theoretical description of interacting ultracold bosons confined in the two different kinds of potentials used in this thesis: a harmonic trap and a periodic potential.

These configurations allow one to study the physics in two different regimes, one in which inter-particle correlations are negligible (harmonic trap) and another in which they become essential (periodic potential). Atoms confined in a harmonic trap belong to the so-called weakly interacting or dilute regime. One of the main characteristics of this regime is the simplicity of its description: atoms form a Bose-Einstein condensate (BEC) and it is possible to use a single macroscopic wave function to describe the ensemble, thus neglecting correlations between particles. However, by loading atoms in an optical lattice, bosons become tightly confined in the minima of the periodic potential. Then, if one is able to load one or more particles at each site, the role of interactions becomes essential and it is possible to drive the system to the strongly interacting regime. Here, a transition from a BEC to a phase of matter with strong correlations among particles, called a Mott insulator, takes place.

The first part of this chapter concerns the dynamics of a BEC. I start by recalling the definition of BEC both for an ideal and an interacting system, with a rapid discussion on the concepts of long-range order and order parameter. After this, by assuming a very simple form for the interaction between atoms, the *contact interaction*, I present the Gross-Pitaevskii equation (GPE), which describes the physics of $N$ weakly interacting bosons at temperature $T = 0$. I conclude this section by discussing the spectrum of the elementary excitations.

In the second part I focus on the physics of atoms trapped in a periodic potential. After briefly discussing the non-interacting case, which allows to set the necessary conditions to work in what is known as the tight-binding framework, I present the Bose-Hubbard Hamiltonian and describe its phase diagram within the Gutzwiller approximation. I finish the chapter with a discussion on the adiabaticity criteria that need to be satisfied in order to transfer adiabatically a weakly interacting BEC created in a harmonic trap into a periodic potential, thereby preparing the ground state of the Bose-Hubbard Hamiltonian.

## 1.1 Bose-Einstein Condensation

Here, we present the main theoretical tools to describe the physics concerning Bose-Einstein condensates of dilute quantum gases. The concepts exposed in the following sections are developed in more details in the following references: Dalfovo et al. (1999); Leggett (2001); Pitaevskii et al. (2003); Leggett (2006) and Pethick et al. (2008).

### 1.1.1 Bose-Einstein condensation in an ideal system

We start by recalling the basic ideas linked to the concept of Bose-Einstein condensation in an ideal system, namely the saturation of the excited states in thermal equilibrium (Pethick et al. 2008). In particular, for an ensemble of $N$ non-interacting bosons described by a Hamiltonian $\hat{H} = \sum_j \hat{h}_j$, the mean number of particles $N_\alpha$ in a given eigenstate $|\phi_\alpha\rangle$ of $\hat{h}_j$ with energy $\varepsilon_\alpha$ and at a temperature $T$ is given by the Bose-Einstein distribution (Pathria et al. 2011):

$$N_\alpha = \frac{1}{\exp[(\varepsilon_\alpha - \mu)/(k_\mathrm{B}T)] - 1}, \tag{1.1}$$

with $\mu < \min(\varepsilon_\alpha)$ the chemical potential of the system and $N = \sum_\alpha N_\alpha$. This constraint on the chemical potential sets the maximum number of particles that can be accommodated in the excited states:

$$N' < N'_\mathrm{max}(T) = \sum_{\alpha \neq 0} \frac{1}{\exp[(\varepsilon_\alpha - \varepsilon_0)/(k_\mathrm{B}T)] - 1}. \tag{1.2}$$

At high temperatures we have $N_\alpha \ll 1$ and $\mu \ll \epsilon_0$, where we have labeled the lowest-energy eigenstate of $\hat{h}_j$ as $\varepsilon_0$. However, as temperature decreases and $\mu$ approaches $\varepsilon_0$, a situation in which $N > N'_\mathrm{max}(T)$ can be reached. When this happens the remaininig $N_0 = N - N'_\mathrm{max}(T)$ bosons occupy necessarily the lowest-energy state $|\phi_0\rangle$ and we then talk of Bose-Einstein condensation. At $T = 0$, all the bosons occupy $|\phi_0\rangle$, and the state of the system is given by:

$$|\Phi\rangle = \frac{(\hat{a}_0^\dagger)^{\otimes N}}{\sqrt{N!}} |\mathrm{vac}\rangle, \tag{1.3}$$

where $\hat{a}_0^\dagger$ creates a particle in state $|\phi_0\rangle$.

### 1.1.2 Bose-Einstein condensation in an interacting system

When interactions between particles are included, the previous definition of BEC is not appropriate anymore. The most commonly accepted definition of what is a BEC was given by Penrose and Onsager (Penrose et al. 1956), and relies on the appearance of a macroscopic eigenvalue of the one-body density matrix.

#### The Penrose-Onsager criterion

In their argument, Penrose and Onsager (Penrose et al. 1956) start by considering a many-body system of $N$ interacting bosons described by a density matrix $\hat{\rho}$. Then, they focus on the 1-body density matrix or first-order correlation function $G_1(\boldsymbol{r}, \boldsymbol{r}') = \langle \hat{\Psi}^\dagger(\boldsymbol{r}) \hat{\Psi}(\boldsymbol{r}') \rangle$. Here $\hat{\Psi}(\boldsymbol{r})$ is the field operator annihilating a boson at a point $\boldsymbol{r}$. The density of the system is found by setting $\boldsymbol{r} = \boldsymbol{r}'$, i.e. $n(\boldsymbol{r}) = \langle \hat{\Psi}^\dagger(\boldsymbol{r})\hat{\Psi}(\boldsymbol{r})\rangle$. The eigenvalues decomposition of $G_1$ is:

$$G_1(\boldsymbol{r}, \boldsymbol{r}') = \sum_i \rho_i \phi_i^*(\boldsymbol{r})\phi_i(\boldsymbol{r}'), \tag{1.4}$$

with the normalization condition $\sum_i \rho_i = N$. Penrose and Onsager argue that the system exhibits Bose-Einstein condensation if one of the eigenvalues is of the order of the total number of particles $N$, all the others being of order 1. From now on, we label this state as $\phi_0$, which is called the *wave function of the condensate*. In the thermodynamic limit, the occupation of this state remains finite while $\rho_{i\neq 0}/N \to 0$.

### Long-range order and order parameter

Let us now split $G_1$ as follows:

$$G_1(\boldsymbol{r}, \boldsymbol{r}') = N_0 \phi_0^*(\boldsymbol{r})\phi_0(\boldsymbol{r}') + \sum_{i\neq 0} \rho_i \phi_i^*(\boldsymbol{r})\phi_i(\boldsymbol{r}'). \tag{1.5}$$

If we now take the limit $|\boldsymbol{r} - \boldsymbol{r}'| \to \infty$, the different $\phi_{i\neq 0}$ corresponding to $\rho_i \ll N$ will scramble, and the terms in the sum end up canceling themselves[5]. Then, one has:

$$\lim_{|\boldsymbol{r}-\boldsymbol{r}'|\to\infty} G_1(\boldsymbol{r}, \boldsymbol{r}') = N_0 \phi_0^*(\boldsymbol{r})\phi_0(\boldsymbol{r}'). \tag{1.7}$$

The $G_1$ function characterizes *phase coherence* (Naraschewski et al. 1999), and then, what the expression above states is that if a BEC is present, the system exhibits off-diagonal long range order, or long-range phase coherence, which is also used as a definition of a BEC (Pitaevskii et al. 2003). In the case of a non-homogeneous system, the limit $|\boldsymbol{r} - \boldsymbol{r}'| \to \infty$ has to be replaced by the effective size $L$ of the system defined by the trapping potential.

From equation (1.7), one can define an *order parameter*:

$$\Phi_0(\boldsymbol{r}) = \sqrt{N_0}\phi_0(\boldsymbol{r}), \tag{1.8}$$

normalized so that $\int |\Phi(\boldsymbol{r})|^2 \, \mathrm{d}^3 r = N_0$. The condensed fraction is then given by $f_\mathrm{c} = N_0/N$.

## 1.1.3 Interacting dilute gases: Gross-Pitaevskii equation and elementary excitations

### Interactions in a dilute system

In a dilute gas, interactions between atoms are mainly due to two-body elastic collisions described through a potential $U_\mathrm{int}$. In the description of the collision between two

---

[5] This can be easily seen if one takes a uniform system with $\phi_{\boldsymbol{k}_i}(\boldsymbol{r}) = \exp(-\mathrm{i}\boldsymbol{k}_i \cdot \boldsymbol{r})/\sqrt{V}$. Since the system is uniform, we can put $\boldsymbol{u} = \boldsymbol{r} - \boldsymbol{r}'$ and we have:

$$G_1(\boldsymbol{u}) = \frac{N_0}{V} + \frac{1}{V}\sum_{i\neq 0} \rho_i \mathrm{e}^{\mathrm{i}\boldsymbol{k}_i\cdot\boldsymbol{u}}. \tag{1.6}$$

The sum consists of many terms oscillating each at a different frequency and therefore, the contribution of the non-condensed part will vanish as $\boldsymbol{u} \to \infty$ leading to $G_1(u \to \infty) = N_0/V \neq 0$.

atoms (Messiah 1999), the center of mass motion of the system decouples from the relative motion, the latter being characterized by the *scattering amplitude* $f(\boldsymbol{k}, \boldsymbol{k}')$, with $\boldsymbol{k}$ and $\boldsymbol{k}'$ the incident and outgoing momentum, respectively. For low energies, $s$-wave scattering is dominant. Then, the scattering amplitude $f$ becomes isotropic in momentum space and becomes independent of energy:

$$\lim_{k\to 0} f(k) = -a. \tag{1.9}$$

Here $a$ is the so-called *scattering length*. The exact details of the potential $U_{\mathrm{int}}$ are no longer important and one typically uses an effective potential to describe interactions between atoms. The most common choice is to employ Fermi's contact potential (Pethick et al. 2008):

$$U_{\mathrm{int}}(\boldsymbol{r} - \boldsymbol{r}') = g\delta(\boldsymbol{r} - \boldsymbol{r}'), \tag{1.10}$$

with $g$ the coupling constant, related to the scattering length as $g = 4\pi\hbar^2 a/M$, with $M$ the mass of the particle (Pethick et al. 2008).

### Time-independent Gross-Pitaevskii equation

The Hamiltonian of $N$ trapped bosons of mass $M$ interacting through a two-body contact potential is given by:

$$\hat{H} = \sum_{j=1}^{N} \left( \frac{\hat{\boldsymbol{p}}_j^2}{2M} + V_{\mathrm{trap}}(\hat{\boldsymbol{r}}_i) \right) + \frac{g}{2} \sum_{i\neq j} \delta(\hat{\boldsymbol{r}}_i - \hat{\boldsymbol{r}}_j). \tag{1.11}$$

In order to find the eigenfunctions $\Psi(\boldsymbol{r}_1, \ldots, \boldsymbol{r}_N)$ of this Hamiltonian, the most common method is to assume that, if the system is dilute and interactions are weak enough (we will give a criterion for this later), the many-body wave function retains the same structure as an ideal gas and can be written as in equation (1.3) with $\hat{a}_0$ defined as:

$$\hat{a}_0 = \int \phi_0(\boldsymbol{r}) \hat{\Psi}(\boldsymbol{r}) \, \mathrm{d}^3 r, \tag{1.12}$$

where $\phi_0$ is the wave function of the BEC. This is a *mean-field* or *Hartree* ansatz and all spatial correlations between particles that might have been introduced by the presence of the interactions are neglected. The wave function $\phi_0$ can be found in the grand canonical formalism by minimizing the free-energy functional $F[\phi_0(\boldsymbol{r})] = \langle \Psi | \hat{H} - \mu \hat{N} | \Psi \rangle$, with $\mu$ the chemical potential. This leads to the *time-independent Gross-Pitaevskii equation*:

$$\mu \Phi_0(\boldsymbol{r}) = -\frac{\hbar^2}{2M} \boldsymbol{\nabla}^2 \Phi_0(\boldsymbol{r}) + V_{\mathrm{trap}}(\boldsymbol{r}) \Phi_0(\boldsymbol{r}) + g n(\boldsymbol{r}) \Phi_0(\boldsymbol{r}), \tag{1.13}$$

with $\Phi_0 = \sqrt{N}\phi_0$ the stationary order parameter and $n(\boldsymbol{r}) = |\Phi_0(\boldsymbol{r})|^2$ the density.

### Thomas-Fermi approximation in a harmonic trap

In the case of repulsive scattering lengths ($g > 0$), interactions tend to smoothen the density profile. In this situation, for large $N$ the kinetic energy term $\boldsymbol{\nabla}^2\Phi_0$, also known as *quantum pressure* term becomes negligible and equation (1.13) leads to:

$$\mu = V_{\mathrm{trap}}(\boldsymbol{r}) + g n(\boldsymbol{r}), \tag{1.14}$$

which is known as the *Thomas-Fermi approximation* (Dalfovo et al. 1999). In this case, the shape of the BEC is mainly determined by the trapping potential:

$$n(\boldsymbol{r}) = |\Phi_0(\boldsymbol{r})|^2 = \Theta\left(\frac{\mu - V_{\text{trap}}(\boldsymbol{r})}{g}\right), \tag{1.15}$$

with $\Theta(x) = x\theta(x)$ and $\theta(x)$ the Heaviside step function.

In many experimental situations, the BEC is obtained in a harmonic trap. The density of the cloud can then be written as:

$$n(\boldsymbol{r}) = n_0\Theta\left(1 - \frac{x^2}{R_x^2} - \frac{y^2}{R_y^2} - \frac{z^2}{R_z^2}\right), \tag{1.16}$$

which manifests the *inverted parabola* profile. In this expression $n_0$ is the peak density and $R_j = [2\mu/(m\omega_j^2)]^{1/2}$ is called the Thomas-Fermi radius in the $j$-direction, after which the density is exactly zero. The chemical potential then reads:

$$\mu = \frac{\hbar\bar{\omega}}{2}\left(\frac{15aN}{a_{\text{ho}}}\right)^{2/5}, \tag{1.17}$$

with $\bar{\omega} = (\omega_x\omega_y\omega_z)^{1/3}$ the geometric mean of the trapping frequencies, $N$ the total atom number and $a_{\text{ho}} = [\hbar/(m\bar{\omega})]^{1/2}$ the associated harmonic oscillator length. The peak density is in this case $n_0 = 15N/(8\pi R_xR_yR_z)$.

An interesting property of BECs trapped in harmonic potentials is their evolution under time-dependent trapping frequencies $\omega_j(t)$. It has been shown that the density of the BEC evolves keeping the form given by equation (1.16) with its radii dilated as $R_j(t) = \lambda_j(t)R_j$, with $\lambda_j(t)$ the dilation coefficient and $R_j$ the Thomas-Fermi radii at $t = 0$. The scaling factors satisfy the equations (Castin et al. 1996):

$$\ddot{\lambda}_j(t) = \frac{\omega_j^2(0)}{\lambda_j(t)\lambda_1(t)\lambda_2(t)\lambda_3(t)} - \omega_j^2(t)\lambda_j(t). \tag{1.18}$$

In particular, this means that the shape of the BEC after time of flight (TOF), i.e., when the traps are suddenly switched off [in other words, with $\omega_j(0) = \omega_j$ and $\omega_j(t > 0) = 0$] still reflects the *in situ* density distribution.

### Gas and interaction strength parameters

The GP description previously introduced relies on the diluteness of the gas (i.e., no correlations among particles and binary collisions). Moreover, within this framework, the Thomas-Fermi approximation requires that interactions be strong enough to neglect the quantum pressure term $\boldsymbol{\nabla}^2\Phi$. These two conditions can be stated in a more precise way by introducing the so-called *gas parameter* $\gamma$ and the interaction strength $\chi$.

For this, we can consider $N$ particles confined in a 3D volume. In the non-interacting case, each boson is completely delocalized in order to minimize its kinetic energy. All of them can then be described by the same single particle wave function [see equation (1.3)] and all the wave functions overlap. As interactions start increasing, particles start repelling each other and the size of each particle's wave function $R$ shrinks.

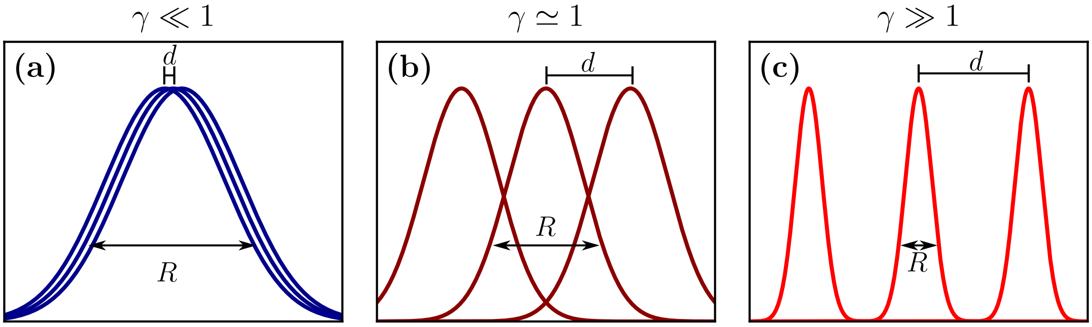

**Figure 1.1** – **(a):** Weakly interacting regime. Here, interactions play a minor role and particles minimize their kinetic energy by delocalizing and occupying the whole volume. The system can still be described by a single wave function in this case. **(b)** and **(c):** As interactions increase, it becomes more favorable to localize the particles in order to minimize the interaction energy due to the overlap of the wave functions.

This translates into the creation of short-range correlations on the order of the inter-particle distance $d$ [see figure 1.1(a)]. As interactions increase, the repulsion becomes more important and the short-range correlations can become on the order $d \simeq R$ [see figures 1.1(b)-(c)]. Therefore, the effect of interactions is to localize the particles, leading to a correlated state. The kinetic energy $\simeq p^2/(2M)$ required to create these correlations [i.e. to create a state such as the one shown in figure 1.1(c)] is then given by $\varepsilon_{\text{kin}} \propto \hbar^2/(2Md^2) = \hbar^2 n^{2/3}/(2M)$ with $n = d^{-3}$. In turn, the interaction energy of having all wave functions overlapped [such as 1.1(a)] is given by $\varepsilon_{\text{int}} \propto gn$. The ratio of the energies between these two limit cases allows us to define a diluteness criterion through the gas parameter:

$$\gamma = na^3, \tag{1.19}$$

which quantifies the ratio $\varepsilon_{\text{int}}/\varepsilon_{\text{kin}} \propto \gamma^{1/3}$. The weakly interacting regime is then characterized by $\gamma \ll 1$, or $\mu \ll \hbar^2 n^{2/3}/(2M)$. This is satisfied for dilute Bose gases with typical densities $n \simeq 10^{14}\,\text{at/cm}^3$ and scattering lengths on the order of several Bohr radius [e.g. for $^{174}$Yb the scattering length is $a = 105\,a_0 \simeq 5.5\,\text{nm}$ (Kitagawa et al. 2008)].

In the dilute regime, the criterion that needs to be satisfied in order to perform the Thomas-Fermi approximation can be stated by comparing the ratio between the mean-field kinetic and trapping energies $\langle -\hbar^2\boldsymbol{\nabla}^2/(2M) + V_{\text{trap}}\rangle$ on the one hand, and interaction energy $\langle gn\rangle$ on the other hand. In a harmonic trap, the parameter characterizing this ratio is the so-called interaction strength parameter[6] (Dalfovo et al. 1999):

$$\chi = \frac{Na}{a_{\text{ho}}}, \tag{1.20}$$

which can be made $\chi \gg 1$ while still satisfying $\gamma \ll 1$. In other words, the energy hierarchies are: $\hbar\bar{\omega} \ll \mu \ll \hbar^2 n^{2/3}/(2M)$.

---

[6] This can also be seen by writing the GPE in equation (1.13) in a dimensionless form:

$$\tilde{\mu}\varphi = \left[-\frac{1}{2}\tilde{\boldsymbol{\nabla}}^2 + \frac{1}{2}\tilde{r}^2 + 4\pi\chi|\varphi|^2\right]\varphi,$$

where the parameter $\chi$ determines the strength of the nonlinear term due to the interactions with respect to the trapping and kinetic energy contributions (Dalfovo et al. 1999).

### Broken symmetry approach

The bosonic field operator can be expanded as:

$$\hat{\Psi}(\boldsymbol{r}) = \hat{\Psi}_0(\boldsymbol{r}) + \delta\hat{\Psi}(\boldsymbol{r}) = \phi_0(\boldsymbol{r})\hat{a}_0 + \sum_{i\neq 0}\phi_i(\boldsymbol{r})\hat{a}_i. \tag{1.21}$$

We now make the so-called *Bogoliubov approximation*, which can be performed in the weakly interacting or dilute regime when a condensate is present, i.e. when $N_0 \simeq N$. This approximation consists in remarking that, for large $N_0$, the states with $N_0$ and $N_0 \pm 1$ atoms are approximately equivalent in what concerns the dynamics of the BEC. Then, one replaces the operators $\hat{a}_0^\dagger$ and $\hat{a}_0$ with a *c*-number $a_0 = a_0^* = \sqrt{N_0}$. With this, the field operator can be written in terms of the order parameter as:

$$\hat{\Psi}(\boldsymbol{r}) = \Phi_0(\boldsymbol{r}) + \delta\hat{\Psi}(\boldsymbol{r}). \tag{1.22}$$

In a dilute ultracold Bose gas (i.e., with $\gamma \ll 1$) the excited states can be neglected to a first approximation and one usually sets $\delta\hat{\Psi}(\boldsymbol{r}) = 0$, which corresponds to the GP theory introduced earlier (Dalfovo et al. 1999). Under this approximation, the field operator coincides exactly with the order parameter $\hat{\Psi}(\boldsymbol{r}) = \Phi_0(\boldsymbol{r})$. In particular, this implies that $\langle\hat{\Psi}\rangle = \Phi_0$, which is known in the literature as *spontaneously broken gauge symmetry* (Anderson 1997). This amounts to consider that the condensate is in a coherent state:

$$|\Phi_0\rangle \simeq |\alpha\rangle = \mathrm{e}^{-|\alpha^2|/2}\sum_N \frac{\alpha^N}{\sqrt{N!}}|N\rangle, \tag{1.23}$$

with $\alpha = \sqrt{N_0}$. This approximation poses the conceptual problem that the number of particles is no longer conserved (Leggett 2006). Actually the fluctuatons are of order $\sqrt{N_0}$ around the mean value $N_0$ (which does not mean that the atom number fluctuates in experiments, but rather that one needs to work in the grand canonical ensemble to compute thermodynamic quantities, as if the system was in contact with a particle reservoir). This description is commonly used in the literature and as we will see in section 1.2.3, it proves particularly useful for a BEC in a periodic potential.

### Time-dependent Gross-Pitaveskii equation

The broken symmetry approach allows us to derive the time-evolution of the order parameter in a simple way. We first write the many-body Hamiltonian in equation (1.11) in second quantization:

$$\hat{H} = \int \hat{\Psi}^\dagger(\boldsymbol{r})\left[-\frac{\hbar^2\boldsymbol{\nabla^2}}{2M} + V_{\mathrm{trap}}(\boldsymbol{r})\right]\hat{\Psi}(\boldsymbol{r})\,\mathrm{d}^3r + \frac{g}{2}\int \hat{\Psi}^\dagger(\boldsymbol{r})\hat{\Psi}^\dagger(\boldsymbol{r})\hat{\Psi}(\boldsymbol{r})\hat{\Psi}(\boldsymbol{r})\,\mathrm{d}^3r. \tag{1.24}$$

Then, the evolution of the system, can be derived by computing the equation of motion of the field operator in the Heisenberg picture, which reduces to an equation for the evolution of the order parameter in the absence of quantum fluctuations by putting $\langle\hat{\Psi}(\boldsymbol{r},t)\rangle = \Phi_0(\boldsymbol{r},t)$:

$$\mathrm{i}\hbar\frac{\partial\Phi_0(\boldsymbol{r},t)}{\partial t} = -\frac{\hbar^2}{2M}\boldsymbol{\nabla}^2\Phi_0(\boldsymbol{r},t) + V_{\mathrm{trap}}(\boldsymbol{r})\Phi_0(\boldsymbol{r},t) + g|\Phi_0(\boldsymbol{r},t)|^2\Phi_0(\boldsymbol{r},t). \tag{1.25}$$

This is the so-called *time-dependent Gross-Pitaevskii equation* (Dalfovo et al. 1999; Leggett 2001; Pitaevskii et al. 2003). We then see that the evolution of stationary states $\Phi_0(\boldsymbol{r})$ obeying equation (1.13) is given by the chemical potential $\mu$:

$$\Phi(\boldsymbol{r},t) = \Phi_0(\boldsymbol{r})\,\mathrm{e}^{-\mathrm{i}\mu t/\hbar}. \tag{1.26}$$

### Elementary excitations

We end the section on BECs by discussing the spectrum of the elementary excitations for weak perturbations. For this, one usually takes the stationary form of the order parameter and adds a small perturbation $\delta\Phi_0$ (Pitaevskii et al. 2003):

$$\Phi(\boldsymbol{r},t) = [\Phi_0(\boldsymbol{r}) + \delta\Phi_0(\boldsymbol{r},t)]\mathrm{e}^{-\mathrm{i}\mu t/\hbar}, \tag{1.27}$$

where $\delta\Phi_0(\boldsymbol{r},t)$ consists of oscillations around the equilibrium value of the form:

$$\delta\Phi_0(\boldsymbol{r},t) = \sum_i \left[u_i(\boldsymbol{r})\mathrm{e}^{-\mathrm{i}\omega_i t} + v_i^*(\boldsymbol{r})\mathrm{e}^{\mathrm{i}\omega_i t}\right]. \tag{1.28}$$

Then, the weakest excitations are obtained by linearising the GPE using equation (1.27). An analytical solution can be found for a homogeneous BEC of density $n$ and chemical potential $\mu = gn$. By considering in this situation a perturbation of momentum $\boldsymbol{p} = \hbar\boldsymbol{q}$ and putting $u_{\boldsymbol{q}}(\boldsymbol{r}) = u_{\boldsymbol{q}}\exp(\mathrm{i}\boldsymbol{q}\cdot\boldsymbol{r})$ and $v_{\boldsymbol{q}}(\boldsymbol{r}) = v_{\boldsymbol{q}}\exp(\mathrm{i}\boldsymbol{q}\cdot\boldsymbol{r})$, one obtains the famous *Bogoliubov dispersion law* for the elementary excitations of the system:

$$\epsilon(\boldsymbol{q}) = \hbar\omega(\boldsymbol{q}) = \sqrt{\frac{\hbar^2\boldsymbol{q}^2}{2M}\left(\frac{\hbar^2\boldsymbol{q}^2}{2M} + 2gn\right)} \tag{1.29}$$

At low momenta the dispersion relation has a *phonon-like* branch of energy $\epsilon_{\mathrm{ph}}(q) \simeq \hbar q c_{\mathrm{s}}$, with $c_{\mathrm{s}} = \sqrt{gn/M}$ the speed of sound in the BEC. In this situation, the collective oscillations consist of many atoms with momenta $\boldsymbol{q}$ and $-\boldsymbol{q}$. At high momenta, the dispersion law approaches the dispersion relation $\epsilon_{\mathrm{fp}}(\boldsymbol{q}) = \hbar^2\boldsymbol{q}^2/(2M) + gn$ of a free-particle with a mean field term shift $gn$ (Pitaevskii et al. 2003). The transition between these two regimes occurs at momenta such that $\hbar q/M \simeq c_{\mathrm{s}}$ (Pitaevskii et al. 2003).

In the case of a trapped BEC of size $L$ and for excitations such that $1/q \ll L$, one can use a local form of the Bogoliubov dispersion relation $\epsilon(\boldsymbol{q}) \to \epsilon(\boldsymbol{q},\boldsymbol{r})$ with $n \to n(\boldsymbol{r})$ (Stenger et al. 1999; Stamper-Kurn et al. 1999; Zambelli et al. 2000). In a trap, the low-energy excitations correspond to collective modes involving the whole BEC. In the case of an isotropic harmonic trap of frequency $\omega_0$, the finite size of the system, given by the Thomas-Fermi radii $R_{\mathrm{TF}} \propto 1/\omega_0$, quantizes the possible momenta $q \propto 2\pi/R_{\mathrm{TF}} \propto \omega_0$ and the possible low-energy excitations $\epsilon_{\mathrm{ph}}(q) \simeq \hbar q c_{\mathrm{s}}$ are then proportional to the trapping frequency $\omega_0$ (Jin et al. 1996). As an example, these excitations correspond to center of mass oscillations at $\omega = \omega_0$ or breathing oscillations with a compression frequency $\omega = \sqrt{5}\,\omega_0$ (Pitaevskii et al. 2003) or $\omega \simeq 2\,\omega_\perp$ in the case of an elongated trap with $\omega_\perp \gg \omega_z$ (Chevy et al. 2002). Both the center of mass oscillations and the breathing mode are commonly used in experiments to calibrate the trapping frequencies [see section 2.1.4].

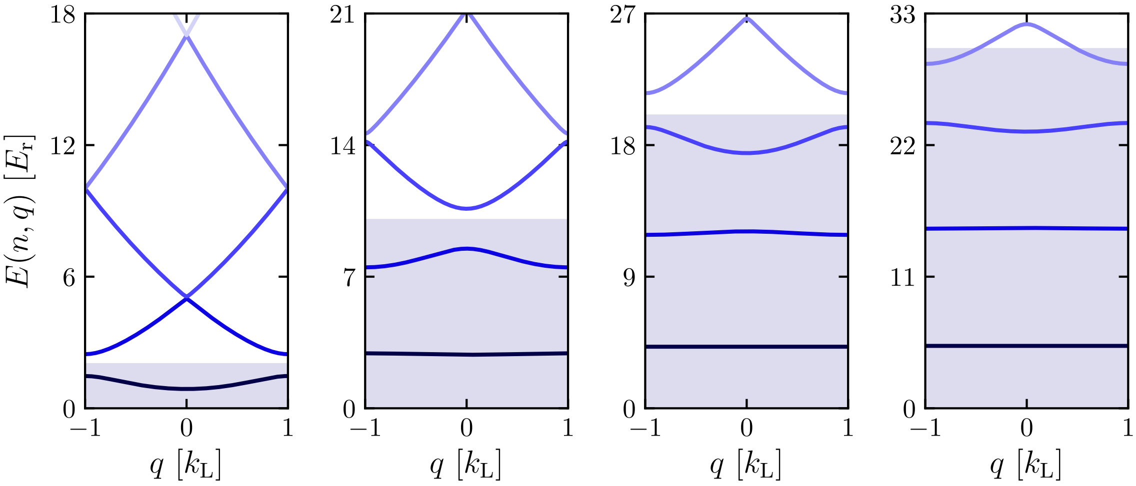

**Figure 1.2** – Lowest energy bands $E(n,q)$ in the 1BZ for lattice depths $V_0 = 2\,E_\mathrm{r}, 10\,E_\mathrm{r}, 20\,E_\mathrm{r}$ and $30\,E_\mathrm{r}$. The blue shaded region represents the region of bands whose energy is smaller than $V_0$. As the lattice depth is increased, the bands become flatter and the bandgap is larger [see figure 1.4(b)].

## 1.2 Quantum gases in optical lattices

By loading atoms in an optical lattice, the strongly interacting regime (where the system can no longer be described by a macroscopic wave function) can be reached. This is due to the fact that the ratio $E_\mathrm{int}/E_\mathrm{kin}$ is determined on the one hand by the tunneling amplitude a particle has for hoping from one site to another, $J$, and the on-site interaction energy $U$ on the other hand[7]. This ratio $U/J$ increases drastically with the lattice depth, mostly because the tunneling is suppressed in an exponential manner, and a situation in which $E_\mathrm{int}/E_\mathrm{kin} = U/J \gg 1$ can be attained even if the gas remains dilute with $n \propto d^{-1/3}$, where $d$ is the lattice spacing, on the order of $0.1-1\,\mu\mathrm{m}$ in typical experiments (Zwerger 2003).

### 1.2.1 Single particle considerations: tight-binding Hamiltonian

In this section, we will quickly review the main ideas concerning the motion of a single particle in a periodic potential of the form (Ashcroft et al. 1976):

$$V(\boldsymbol{r}) = -V_0 \cos^2(k_\mathrm{L} z). \tag{1.30}$$

In the previous expression, $V_0$ is the depth of the potential at the position of its minima, usually called the *lattice depth*, $z$ is the space coordinate and $k_\mathrm{L} = 2\pi/\lambda_\mathrm{L}$.

#### Band structure in a 1D periodic potential

The evolution of the particle in a periodic potential is governed by the Hamiltonian $\hat{H} = -\hbar^2\partial_z^2/(2m) - V_0\cos^2(k_\mathrm{L}z)$, which sets the following natural units: distances will

---

[7] An effective mass for a particle in an optical lattice can be computed through the band structre dispersion relation (Ashcroft et al. 1976). This effective mass turns out to be $M^* \propto 1/J$. Thus, the effective kinetic energy of the particle becomes $E_\mathrm{kin} \simeq \hbar^2/(2M^*d^2) \propto J$. The interaction energy $gn$ is determined by the width of the wave function $\sigma$ in the lattice site, and we have $E_\mathrm{int} \propto g/\sigma^3 = U$.

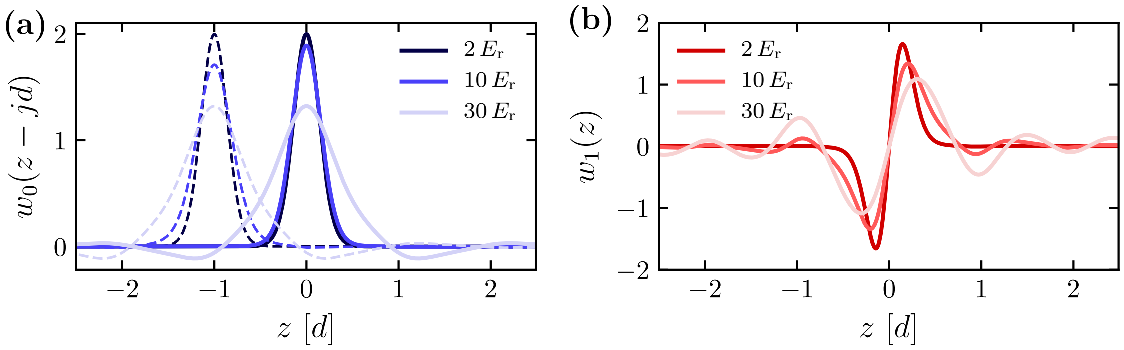

**Figure 1.3** – Wannier functions for **(a)** the fundamental band $w_0(z)$ and **(b)** the first band $w_1(z)$ for different lattice depths. The dashed curves in **(a)** correspond to the Wannier function displaced of one lattice site $w_0(z - d)$.

be given in units of the lattice spacing $d = \lambda_\mathrm{L}/2$, the natural momentum is $\hbar k_\mathrm{L}$ and the natural measure of energy is the recoil energy $E_\mathrm{r} = \hbar^2 k_\mathrm{L}^2/(2M)$, with $M$ the mass of the particle.

The translational invariance of the Hamiltonian allows us to use Bloch's theorem to diagonalise it. The eigenstates can then be written as *Bloch waves* (Ashcroft et al. 1976):

$$\phi_{n,q}(z) = \mathrm{e}^{\mathrm{i}qz} u_{n,q}(z), \tag{1.31}$$

with $u_{n,q}(z + d) = u_{n,q}(z)$ the *Bloch functions*. These wave functions are characterized by the *quasimomentum* $q$ and an integer $n$ called the *band index*. Because of the periodicity of $\hat{H}$, changing the quasimomentum by a multiple of the reciprocal-lattice vector $Q_m = 2mk_\mathrm{L}$, with $m \in \mathbb{Z}$, leaves the Bloch wave unchanged. This restricts the dynamics to the so-called *first Brillouin zone* (1BZ), with $q \in (-k_\mathrm{L}, k_\mathrm{L}]$. The spectrum of $\hat{H}$ can be numerically calculated and leads to the *Bloch energy bands* $E(n, q)$, with allowed regions labelled by the band index $n$ separated by the band-gaps. We show the lowest energy bands at different lattice depths in figure 1.2. In this basis, the Hamiltonian is diagonal and, in second quantisation, reads:

$$\hat{H} = \sum_n \int_{-k_\mathrm{L}}^{k_\mathrm{L}} E(n, q)\, \hat{b}_{n,q}^\dagger \hat{b}_{n,q}\, \mathrm{d}q, \tag{1.32}$$

where $\hat{b}_{n,q}$ destroys a particle in the Bloch wave $\phi_{n,q}(z)$.

### Wannier functions

Bloch waves are delocalised over the whole lattice. However, as one starts increasing the lattice depth, the particle gets more and more localized and an alternative description becomes useful, specially when interactions are be present. For this, we first define the *Wannier wave functions* (Wannier 1937):

$$w_n(z - z_j) = \sqrt{\frac{d}{2\pi}} \int_{-k_\mathrm{L}}^{k_\mathrm{L}} \phi_{n,q}(z)\, \mathrm{e}^{-\mathrm{i}qz_j}\, \mathrm{d}q, \tag{1.33}$$

where $z_j = jd$ is a point located at the $j$th minimum of the potential. These new states are not eigenstates of the periodic Hamiltonian but they offer an intuitive description

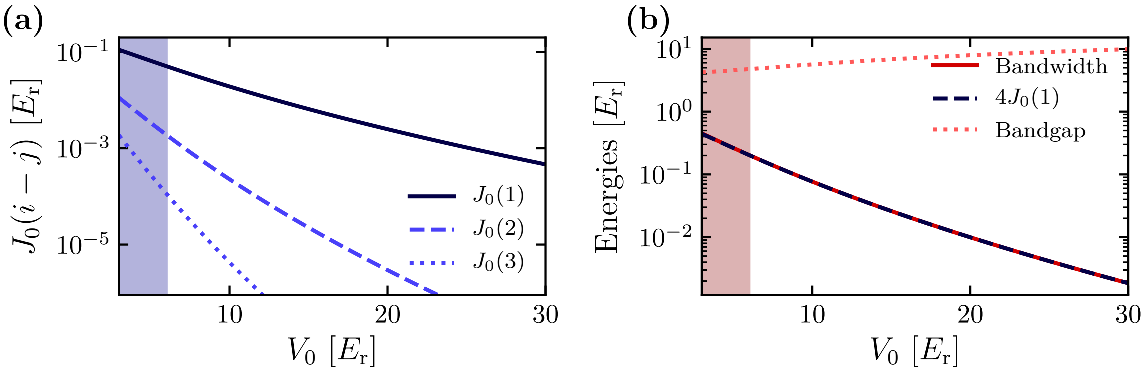

**Figure 1.4** – Comparison of tunneling energies. **(a):** Tunneling energies to first (solid), second (dashed) and third (dotted) nearest neighbor as a function of the lattice depth. **(b):** Bandgap (dotted line) and bandwith (solid line) in the tight binding regime. The bandwith is compared to the 1D prediction $4J_0(1)$ (dashed line).

in the limit of large lattice depths. To see this, we can write the Hamiltonian from equation (1.32) in the Wannier basis:

$$\hat{H} = -\sum_{\substack{n\\ i,j}} J_n(z_i - z_j)\, \hat{a}^\dagger_{n,i}\hat{a}_{n,j}, \tag{1.34}$$

where $\hat{a}_{n,i}$ destroys a particle in the Wannier state $w_n(z - z_i)$. In this picture, the Hamiltonian describes the hoping through quantum tunneling between sites $i$ and $j$ of a particle in the band $n$. The strengths of these processes are given by the matrix elements $J_n(i - j)$, which can be related to the Fourier transform of the dispersion relation:

$$\begin{aligned} J_n(i-j) &= \int w_n^*(z - z_j)\left[\frac{\hbar^2}{2M}\frac{\partial^2}{\partial z^2} - V(z)\right] w_n(z - z_i)\,\mathrm{d}z \qquad (1.35)\\ &= -\frac{d}{2\pi}\int_{-k_\mathrm{L}}^{k_\mathrm{L}} E(n,q)\,\mathrm{e}^{-\mathrm{i}q(z_i - z_j)}\,\mathrm{d}q. \qquad (1.36)\end{aligned}$$

### Tight-binding approximation

We now perform some approximations. First we note that as the lattice depth is increased, the Wannier wave functions become more and more localized[8] (see figure 1.3) and the strength of the tunneling parameter decreases exponentially. For lattice depths $V_0 \geq 6\,E_\mathrm{r}$, tunneling to second or higher neighbors is strongly suppressed [figure 1.4(a)][9]. Then, from now on we will just consider nearest-neighbor tunneling. The second important approximation, valid at high lattice depths, is to restrain the dynamics of the particle to the fundamental band $n = 0$. The single-band approximation is

---

[8] For a one-dimensional symmetric potential, a proper choice of the phases of the Bloch waves allows us to define the Wannier wave functions so that for each band they are (i) real, (ii) with a defined symmetry with respect to the origin and (iii) exponentially decaying with the distance. This is achieved by imposing $\phi_{n,q}(z=0) \in \mathbb{R}^+$ for $n$ even and $\partial_z\phi_{n,q}(z=0) \in \mathbb{R}^+$ for $n$ odd (Kohn 1959).

[9] As we will see in the following sections, at lattice depths $V_0 \geq 6\,E_\mathrm{r}$ the interaction energy (which dictates the dynamics in the fundamental band) is at least one order of magnitude smaller compared to the bandgap [see figure 1.9] and thus, cannot induce transition to higher bands

usually fulfilled in quantum gases experiments, where one starts with a gas that is cold enough to be loaded in the fundamental band of the lattice. Then, if the band-gap is higher than the inverse timescale of the intrinsic dynamics in the fundamental band, this is a valid approximation.

The single-band and nearest-neighbor hopping approximations allow us to define the *tight-binding hamiltonian*:

$$\hat{H}_{\mathrm{TB}} = -J \sum_{i} \hat{a}^{\dagger}_{i+1} \hat{a}_{i} + \mathrm{h.c.}, \tag{1.37}$$

with $J \equiv J_0(|i-j|=0)$ and $\hat{a}_i \equiv \hat{a}_{n=0,i}$.

By inverting equation (1.36), we see that, under this approximation, the dispersion relation takes the simple form $E(q) = -2J\cos(qd)$, and the bandwidth of the fundamental band is $\Delta E = 4J$ (Ashcroft et al. 1976).

The previous picture can be easily extended to 2D or 3D in the case of a square or cubic lattice, by superimposing two or three standing waves in orthogonal directions (Bloch et al. 2008). With a suitable choice of polarization and frequencies, beams corresponding to different standing waves should not interfere with one another [see discussion in section 2.2.1] and the total potential is obtained by the incoherent sum of each potential:

$$V(\boldsymbol{r}) = V_{0x}\cos^2(k_{\mathrm{L}}x) + V_{0y}\cos^2(k_{\mathrm{L}}y) + V_{0z}\cos^2(k_{\mathrm{L}}z). \tag{1.38}$$

The dispersion relation reads $\epsilon(q) = -zJ\cos(qd)$, with $z$ the number of nearest neighbors. The bandwidth of the fundamental band is then $2zJ$ (see figure 1.4(b)).

### External confinement

In usual experimental conditions [section 2.2.1], the periodic potential generated by the lattice is spatially modulated by a Gaussian profile (Bloch et al. 2008). Taking this into account, the full potential can be written as:

$$V(\boldsymbol{r}) = -V_0 \cos^2(k_{\mathrm{L}}z)\, \mathrm{e}^{-2\rho^2/w(z)^2}. \tag{1.39}$$

Here $z$ is the propagation direction and $\rho^2 = x^2 + y^2$. We have denoted by $w(z)$ the length scale above which the lattice modulation varies in a plane transverse to the propagation direction. In general, close to the absolute minimum of equation (1.39), $w$ changes slowly with $z$ and we can neglect the axial dependency, i.e., $w(z) \simeq w_0$. Typically, this length $w_0$ is large compared to the atomic cloud dimension, $R$, and the lattice spacing $d$. This allows us to treat the modulation as a perturbation of the periodic potential by expanding it: $\exp(-2\rho^2/w_0) \simeq 1 - 2\rho^2/w_0$.

The zeroth order of the perturbation is nothing but the periodic potential discussed so far. We now concentrate on the first order of the perturbation $\delta V_z = 2V_0\cos^2(k_{\mathrm{L}}z)\rho^2/w_0^2$. As several standing waves are involved, the main effect of this perturbation is to modify the transverse confinement of the lattices generated by the orthogonal beams (e.g. at first order, the effect of lattice in the $z$ direction is to create a *residual* confinement in the $x-y$ plane). By treating this contribution perturbatively, it is possible to write the potential in a separable form.

Within the tight-binding approximation, the perturbation modifies the Hamiltonian in equation (1.37) by adding a site-dependent energy shift. We can write it as:

$$\begin{aligned}\delta\hat{H}_z &= \frac{2V_{0z}}{w_0^2}\sum_i \langle w_{z_i}|\cos^2(k_\mathrm{L}z)|w_{z_i}\rangle\langle w_{\perp_i}|\rho^2|w_{\perp_i}\rangle\, \hat{a}_i^\dagger\hat{a}_i \\ &\simeq \frac{2V_{0z}}{w_0^2}\sum_i \left[1-k_\mathrm{L}^2\langle w_{z_0}|z^2|w_{z_0}\rangle\right]\langle w_{\perp_i}|\rho^2|w_{\perp_i}\rangle\, \hat{a}_i^\dagger\hat{a}_i, \qquad (1.40)\end{aligned}$$

where from the first to the second line we have developed the cosine around the potential absolute minimum at $z_i = 0$, valid in the tight-binding limit where the wave functions are strongly localized (figure 1.3). Denoting by $\sigma_i$ the rms-width of the Wannier function in the $i-$direction, the previous expression can be rewritten as:

$$\delta\hat{H}_z = \frac{2V_{0z}}{w_0^2}\sum_i \left[1-(k_\mathrm{L}\sigma_z)^2\right]\left[(\sigma_x^2+x_i^2)+(\sigma_y^2+y_i^2)\right]\hat{a}_i^\dagger\hat{a}_i. \qquad (1.41)$$

We note that $(k_\mathrm{L}\sigma_z)^2 \ll 1$, and therefore we neglect this term in the following. Then, up to a small offset $\sim \sigma^2$, the correction reads:

$$\delta\hat{H}_z = \sum_i \frac{1}{2}M\omega_{\mathrm{ext},z}^2(x_i^2+y_i^2)\,\hat{a}_i^\dagger\hat{a}_i, \qquad (1.42)$$

where we have defined the *external frequency* as $\omega_{\mathrm{ext},z} = [4V_{0z}/(Mw_0^2)]^{1/2}$. With this, the tight-banding Hamiltonian can be expressed as the sum of a periodic potential and a harmonic confinement. For a cubic lattice, it reads:

$$\hat{H}_\mathrm{TB} = -J\sum_{\langle \boldsymbol{i},\boldsymbol{j}\rangle}(\hat{a}_{\boldsymbol{i}}^\dagger\hat{a}_{\boldsymbol{j}}+\hat{a}_{\boldsymbol{j}}^\dagger\hat{a}_{\boldsymbol{i}}) + \sum_{\boldsymbol{i}}\frac{1}{2}M(\Omega_x^2x_{\boldsymbol{i}}^2+\Omega_y^2y_{\boldsymbol{i}}^2+\Omega_z^2z_{\boldsymbol{i}}^2)\,\hat{a}_{\boldsymbol{i}}^\dagger\hat{a}_{\boldsymbol{i}}, \qquad (1.43)$$

where $\langle\cdot\rangle$ denotes nearest-neighbor and where $\Omega_\alpha^2 = \omega_{\mathrm{ext},\beta}^2+\omega_{\mathrm{ext},\gamma}^2$, with $\alpha \perp (\beta,\gamma)$.

### 1.2.2 Interactions in an optical lattice: Bose-Hubbard Hamiltonian

We now turn to the description of an ensemble of identical bosons interacting in the fundamental band of a cubic lattice (Jaksch et al. 1998). We will consider that atoms interact via the short-range contact potential, characterized by the coupling parameter $g = 4\pi\hbar^2a/M$, with $a$ the $s$-wave scattering length.

The interaction Hamiltonian reads:

$$\hat{H}_\mathrm{int} = \frac{g}{2}\int \hat{\Psi}^\dagger(\boldsymbol{r})\hat{\Psi}^\dagger(\boldsymbol{r})\hat{\Psi}(\boldsymbol{r})\hat{\Psi}(\boldsymbol{r})\,\mathrm{d}^3r = \frac{1}{2}\sum_{\boldsymbol{ijkl}}U_{\boldsymbol{ijkl}}\hat{a}_{\boldsymbol{i}}^\dagger\hat{a}_{\boldsymbol{j}}^\dagger\hat{a}_{\boldsymbol{k}}\hat{a}_{\boldsymbol{l}}, \qquad (1.44)$$

with $\hat{\Psi}(\boldsymbol{r}) = \sum_{\boldsymbol{i}} w(\boldsymbol{r}-\boldsymbol{r}_i)\hat{a}_{\boldsymbol{i}}$. Now we place ourselves again within the tight-binding approximation, where the Wannier functions are strongly localized and therefore the overlap between wave functions at different sites is strongly suppressed. In this case, the matrix element is purely local ($\boldsymbol{i}=\boldsymbol{j}=\boldsymbol{k}=\boldsymbol{l}$) and we define the on-site interaction strength as:

$$U = g\int |w(\boldsymbol{r})|^4\,\mathrm{d}^3r. \qquad (1.45)$$

The combination of the single-particle and interaction Hamiltonians leads to the Bose-Hubbard Hamiltonian (Fisher et al. 1989; Jaksch et al. 1998):

$$\hat{H}_{\mathrm{BH}} = -J \sum_{\langle \boldsymbol{i},\boldsymbol{j} \rangle} (\hat{a}_{\boldsymbol{i}}^{\dagger} \hat{a}_{\boldsymbol{j}} + \hat{a}_{\boldsymbol{j}}^{\dagger} \hat{a}_{\boldsymbol{i}}) + \frac{U}{2} \sum_{\boldsymbol{i}} \hat{n}_{\boldsymbol{i}} (\hat{n}_{\boldsymbol{i}} - 1) + \sum_{\boldsymbol{i}} \epsilon_{\boldsymbol{i}} \hat{n}_{\boldsymbol{i}}, \tag{1.46}$$

where $\hat{n}_{\boldsymbol{i}} = \hat{a}_{\boldsymbol{i}}^{\dagger} \hat{a}_{\boldsymbol{i}}$ is the number operator, counting the number of particles at site $\boldsymbol{i}$ and $\epsilon_{\boldsymbol{i}}$ contains the energy shift due to the Gaussian envelope in equation (1.43). The ground state of this system results from the competition of two terms (Zwerger 2003):

1. The kinetic energy contribution, whose strength is given by $J$, which tends to minimize the kinetic energy by delocalizing atoms along the lattice through quantum tunneling.
2. The on-site energy contribution, of strength $U$, which will tend to minimize the interactions by localizing particles in the lattice sites.

We will discuss this in the next section[10].

### 1.2.3 Phase diagram of the homogeneous Bose-Hubbard Hamiltonian

#### Gutzwiller ansatz

The Bose-Hubbard Hamiltonian from equation (1.46) is not analytically solvable for finite $J/U$ (Fisher et al. 1989). In this section, we use a variational mean-field technique that uses a class of wave functions known as *Gutzwiller ansatz* (Rokhsar et al. 1991; Sheshadri et al. 1993). This method captures the essential physics of the dynamics governed by Bose-Hubbard Hamiltonian.

To simplify the notations, we will consider a 1D system with $L$ sites and $N$ bosons, and we first focus on the homogeneous situation with $\epsilon_{\boldsymbol{i}} = 0$. The basic idea of this approach is to use a many-body state $|\Phi_{\mathrm{G}}\rangle$ that factorizes as a product of on-site states $|\psi\rangle_j$:

$$|\Phi_{\mathrm{G}}\rangle = \bigotimes_{j=1}^{L} |\psi\rangle_j, \quad \text{with} \quad |\psi\rangle_j = \sum_{n=0}^{\infty} c(n) |n\rangle_j, \tag{1.48}$$

with $|n\rangle_j$ a Fock state with $n$ atoms at site $j$ and $\sum_n |c(n)|^2 = 1$. Because of translational invariance, each state $|\psi\rangle$ is the same at each lattice site $j$. This kind of ansatz is then a *mean-field* ansatz that neglects possible correlations among different sites.

---

[10] One can also write the following approximate forms for the tunneling and the 3D on-site interaction strengths (Zwerger 2003):

$$J \simeq \frac{4E_{\mathrm{r}}}{\sqrt{\pi}} \left( \frac{V_0}{E_{\mathrm{r}}} \right)^{3/4} \exp\left[ -2\sqrt{\frac{V_0}{E_{\mathrm{r}}}} \right], \qquad U \simeq E_{\mathrm{r}} \sqrt{\frac{8}{\pi}} k_{\mathrm{L}} a \left( \frac{V_0}{E_{\mathrm{r}}} \right)^{3/4} = \frac{g}{(\sqrt{2\pi} a_{\mathrm{ho}})^3}. \tag{1.47}$$

We thus see that the ratio $J/U \propto \exp(-2\sqrt{V_0/E_{\mathrm{r}}})$ can be scanned over several orders of magnitude by ramping up the optical lattice depth to several tens of recoil energies.

In the uniform case, the Gutwziller ansatz is exact in two cases (Zwerger 2003):

1. In the weakly interacting case, where $J/U \to \infty$. In this situation the system remains a BEC. The ground state is then just a product state in which all particles occupy the lowest Bloch state $|\boldsymbol{q} = \mathbf{0}\rangle$ and atoms are completely delocalized along the lattice. For $N$ particles and $L$ sites, the state reads:

   $$|\Phi\rangle_{\mathrm{SF}} \propto (\hat{b}^{\dagger}_{\boldsymbol{q}=\mathbf{0}})^{\otimes N} |\mathrm{vac}\rangle \propto \left( \sum_{j=1}^{L} \hat{a}^{\dagger}_j \right)^{\otimes N} |\mathrm{vac}\rangle. \tag{1.49}$$

   For large $N$ and $L$, the probability of having $n$ atoms in a given site is close to a Poissonian distribution and the state can be described as a product of coherent states in each site, i.e.:

   $$|\Phi\rangle_{\mathrm{SF}} \propto \bigotimes_{j=0}^{L} |\alpha\rangle_j, \quad \text{with} \quad |\alpha\rangle_j = \mathrm{e}^{-|\alpha_j|/2} \sum_{n=0}^{\infty} \frac{\alpha_j^n}{\sqrt{n!}} |n\rangle_j, \tag{1.50}$$

   which corresponds to the *discrete* version of the broken symmetry approximation introduced in section 1.1.3. The order parameter becomes in this case $|\langle \hat{a} \rangle|^2 = |\alpha|^2 = \bar{n}$ with $\bar{n}$ the mean occupation number of the site.

2. In the strongly interacting regime, with $J/U \to 0$. This is the so-called *atomic limit* and the lattice can be seen as an ensemble of wells of infinite depth. In this case, the atoms are completely localized at each site and the system is described by a product of Fock states. In the case of commensurate fillings (i.e. for $N/L = n_0 \in \mathbb{N}$) the state reads:

   $$|\Phi\rangle_{\mathrm{MI}} \propto \bigotimes_{j=1}^{L} |n_0\rangle_j. \tag{1.51}$$

The Gutwziller ansatz is able to describe the main aspects of the transition between these two regimes as the lattice depth increases and the ratio $J/U$ decreases. In particular, it accounts for the fact that the states in equations (1.50) and (1.51) are connected by a quantum phase transition, where the system goes from a superfluid state, where $|\psi\rangle_j$ is approximately a coherent state $|\alpha\rangle_j$, to a Mott insulating state with $|\psi\rangle_j$ a Fock state $|n_0\rangle_j$.

Let us now focus in the intermediate values of $J/U$. In the grand canonical point of view, the coefficients $c(n)$ are found by minimizing the free-energy functional $\langle \hat{F} \rangle = \langle \hat{H}_{\mathrm{BH}} - \mu \hat{N} \rangle$, with $\mu$ the chemical potential. The function to minimize at each site is then:

$$\frac{\langle \hat{F} \rangle}{L} = -zJ|\alpha|^2 + \frac{U}{2} \left( \langle \hat{n}^2 \rangle - \langle \hat{n} \rangle \right) - \mu \langle \hat{n} \rangle, \quad \text{with} \quad \sum_{n} |c(n)|^2 = 1, \tag{1.52}$$

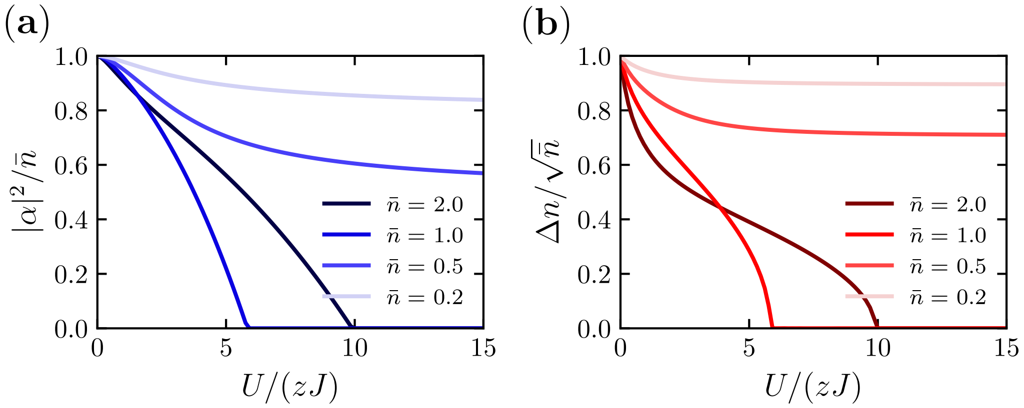

**Figure 1.5** – Gutzwiller analysis of the Bose-Hubbard Hamiltonian. **(a):** Variation of the order parameter $|\alpha|$ as a function of the ratio $U/(zJ)$ for different fixed $\bar{n}$. **(b):** Evolution of the density fluctuations $\Delta n$. The Gutzwiller ansatz predicts a transition from the superfluid to the Mott insulator phase at $U/(zJ) = 5.8$ for $\bar{n} = 1$ and at $U/(zJ) = 9.9$ for $\bar{n} = 2$, where both the order parameter and the density fluctuations vanish. The many-body state is then described by a product of Fock states at each lattice site.

and where $z = 2, 4, 6$ is the number of nearest-neighbors for a 1D, 2D or 3D system, respectively, and:

$$\alpha = \langle \psi | \hat{a} | \psi \rangle = \sum_{n=0}^{\infty} \sqrt{n+1} c^*(n) c(n+1), \tag{1.53}$$

$$\langle \hat{n} \rangle = \sum_{n=0}^{\infty} n |c(n)|^2 \tag{1.54}$$

are the expectation values of the matter wave field and the average density. Density fluctuations are then given by: $\Delta n^2 = \langle \hat{n}^2 \rangle - \langle \hat{n} \rangle^2 = \sum_n (n - \langle \hat{n} \rangle)^2 |c(n)|$. In the Gutzwiller approximation, the first order correlation function $g(i,j)$ becomes independent of the distance between sites and reads:

$$g(i,j) = \langle \hat{a}_i^\dagger \hat{a}_j \rangle = \left| \sum_{n=0}^{\infty} \sqrt{n+1} c^*(n) c(n+1) \right|^2, \tag{1.55}$$

which is just the order parameter $|\alpha|^2$. We then see that in the regime where $J/U \to \infty$, we have $g(i,j) = \langle \hat{a}_i^\dagger \hat{a}_j \rangle = \bar{n}$ and, therefore, phase coherence extends over the whole lattice, i.e., the system has off-diagonal long range order and there is a BEC according to the Penrose and Onsager argument (Penrose et al. 1956) (see section 1.1.2). However, in the atomic limit the order parameter vanishes and $g(i,j) = n_0 \delta_{ij}$, with $\delta_{ij}$ the Kronecker delta. Therefore, the condensate disappears and phase coherence is completely lost.

The condensed fraction is given by

$$f_c = \frac{1}{N} \langle \hat{b}_{\mathbf{q=0}}^\dagger \hat{b}_{\mathbf{q=0}} \rangle = \frac{1}{NL} \sum_{i,j} \langle \hat{a}_i^\dagger \hat{a}_j \rangle = \frac{|\alpha|^2}{\bar{n}}. \tag{1.56}$$

As the order parameter, the density fluctuations and $g(i,j)$, the condensed fraction also vanishes in the insulating phase. Therefore, the Gutzwiller ansatz predicts a transition

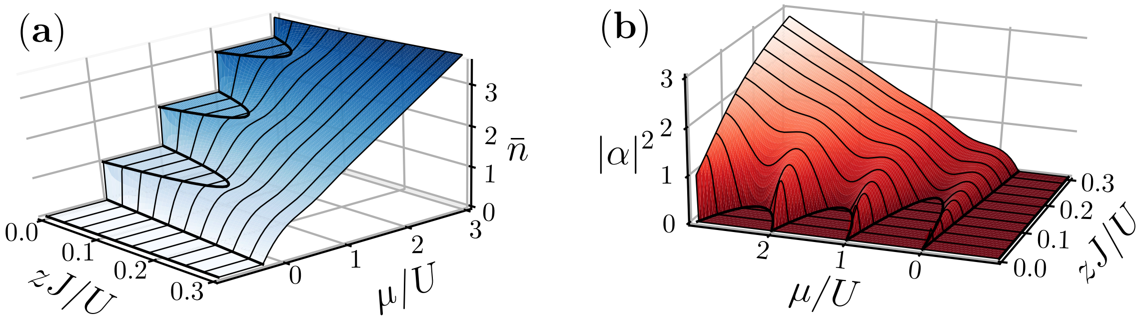

**Figure 1.6** – Phase diagram of the Bose-Hubbard Hamiltonian at $T = 0$ predicted by the Gutzwiller ansatz. **(a):** Variation of the mean atom number per site $\bar{n}$ as a function of the ratio $zJ/U$ and the chemical potential $\mu/U$. **(b):** Variation of the order parameter $|\alpha|$. The thick solid lines mark out the Mott insulator lobes, which occur at integer values of $\bar{n}$ **(a)** or the regions of vanishing order parameter **(b)**, and the rest of the diagram corresponds to the superfluid phase.

from the superfluid phase, with non-zero order parameter and density fluctuations, to the insulating phase[11] at values $U/(zJ) \simeq 5.8$ for $\bar{n} = 1$ and $U/(zJ) \simeq 9.9$ for $\bar{n} = 2$ (see figure 1.5 for the evolution of $|\alpha|^2$ and $\Delta n$ at fixed $\bar{n}$ for different ratios of $U/J$).

We show in figure 1.6(a) the phase diagram[12] $\bar{n}(\mu, zJ/U)$ of the Bose-Hubbard Hamiltonian in the homogeneous case. The variation of the order parameter, characterizing the phase transition at $T = 0$, is shown in figure 1.6(b).

From figure 1.6(a) we see that in the Mott insulator regime (i.e. for $zJ/U$ small enough) the atom number per site $\bar{n}$ is constant in an interval of variation $[\mu_-, \mu_+]/U$ [with $\mu_- = nU$ and $\mu_+ = (n+1)U$ for $J = 0$ and $\bar{n} = n$]. This is what characterizes the Mott insulator phase: on the one hand, the cost to create an excitation (i.e. to add particle at a site and a hole in another site) is $\propto U$ and, on the other hand, the phase is incompressible $\kappa \propto \partial\bar{n}/\partial\mu = 0$ in the interval $\mu \in [\mu_-, \mu_+]$.

The first experimental evidence of the transition between a superfluid and a Mott insulator was given in Greiner et al. (2002), and it consists in the reversible observation of the loss of long-range phase coherence through images in TOF as the lattice depth is increased. We will discuss this in details in section 2.2.3. The superfluid behavior of the gas in the lattice and its disappearence when reaching the Mott transition was shown in Mun et al. (2007) in relation with a previous theoretical study performed by Altman et al. (2005).

---

[11] Monte-Carlo simulations predict a slightly different depth (and in closer agreement with the experiments) for which this transition occurs. For a 2D lattice like the one described in chapter 2, the transition takes place at $U/J = 16.9$ for $\bar{n} = 1$ and at $U/J = 28.7$ for $\bar{n} = 2$, corresponding to $V_\perp = 9.1\,E_\mathrm{r}$ and $V_\perp = 10.9\,E_\mathrm{r}$, respectively (Capogrosso-Sansone et al. 2008).

[12] The solid lines in the figure represent the boundaries between the superfluid phase and the Mott insulator predicted by the Gutzwiller ansatz. They can be analytically calculated by truncating the Fock basis to only three states $c(n)$ and $c(n \pm 1)$. The boundaries correspond to:

$$\mu_\pm/U = \left(n_0 - \frac{1}{2}\right) - \frac{zJ}{2U} \pm \frac{1}{2}\sqrt{1 - 2\frac{zJ}{U}(2n_0+1) + \left(\frac{zJ}{U}\right)^2}.$$

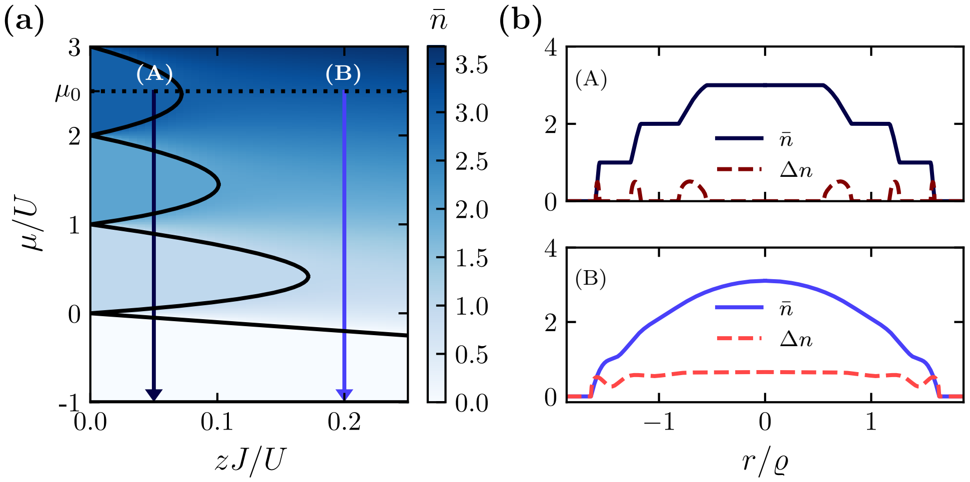

**Figure 1.7** – Shell structure of a trapped Mott insulator. **(a):** Phase diagram of the homogeneous Bose-Hubbard Hamiltonian. The horizontal dashed line corresponds to the global chemical potential $\mu_0$. The trapped density profile is obtained by performing a local density approximation $\mu_{\text{loc}} = \mu_0 - V$, and corresponds to scan, at fixed $zJ/U$, the homogeneous phase diagram from $\mu_0$ to $\mu_0 - V(R)$, with $R$ the in-trap size of the gas (solid arrows in the diagram). **(b):** Density profiles (solid lines) corresponding to $\mu_0 = 2.5U$. Path (A) corresponds to the Mott regime for $U/(zJ) = 0.05$ and path (B) to a superfluid where $U/(zJ) = 0.2$. The Mott insulator regions in the density profile are characterized by vanishing density fluctuations (dashed lines).

### 1.2.4 Local density approximation in an optical lattice

We now turn to the inhomogeneous case, in which the lattice potential is modulated by a harmonic trapping potential [$\epsilon_{\boldsymbol{i}} \neq 0$ in equation (1.46)] of frequency $\Omega$. If the residual confinement is smooth enough, the energy shift between two adjacent sites is very small and one can define cells consisting of several sites before a significant energy shift due to the confinement emerges. The change in the density within these cells is also small and it is possible to use a *local density approximation* to describe the trapped system where, for each cell, we define a local chemical potential:

$$\mu_{\text{loc}}(\boldsymbol{r}) = \mu_0 - V(\boldsymbol{r}). \tag{1.57}$$

Then, we can first compute the density for a homogeneous system $n_{\text{hom}}(\mu_0, zJ/U)$ and the density of the trapped gas, $n_{\text{inh}}(\boldsymbol{r}, \Omega, \mu, zJ/U) = n_{\text{hom}}[\mu_{\text{loc}}(\boldsymbol{r}), zJ/U]$ corresponds to scan the phase diagram at fixed $zJ/U$ from a value $\mu_{\text{loc}}(0) = \mu_0$ to a final value $\mu_{\text{loc}}(R) = \mu_0 - M\Omega^2 R^2/2$ with $r = R$ at the edge of the cloud.

In the atomic limit, a lobe with $\bar{n} = p$ atoms per site is reached when $\mu_{\text{loc}} = pU$. This allows us to define a characteristic radius $\varrho$:

$$\varrho = \sqrt{\frac{2U}{M\Omega^2}} \tag{1.58}$$

so that at distances $R_p = \varrho\sqrt{\mu_0/U - p}$ a lobe with $\bar{n} = p$ atoms per site would be reached in the case of $J = 0$.

Crossing the phase diagram leads to a shell structure (see figure 1.7) with incompressible Mott insulator phases with different occupancies separated by a superfluid layer

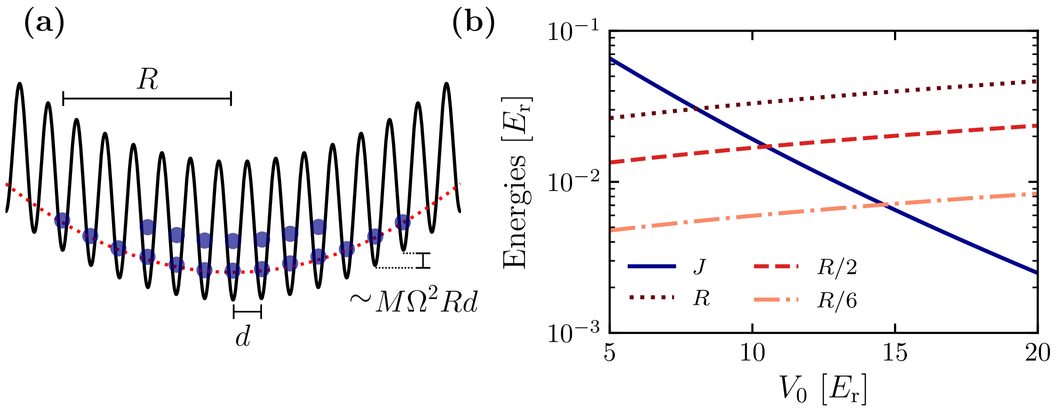

**Figure 1.8** – **(a)** Scheme of a Mott insulator to illustrate the suppression of tunneling at the edges of the lattice in the presence of harmonic confinement (see text). The vertical axis corresponds to the energy, which depends on the lattice site because of the residual harmonic confinement (red dotted line). **(b)** Neighboring sites energy shift due to the external confinement at different lattice sites: at the edge of the cloud (dotted line), at $R/2$ (dashed line) and at $R/6$ (semi-dashed line). The solid line corresponds to the tunneling energy. The calculation is performed for our typical experimental parameters, where $R \simeq 10\,\mu\mathrm{m}$ and $V_z = 27\,E_\mathrm{r}$ [see section 2.2.2].

(the so-called *wedding-cake structure*). Experimental evidence of the shell structure in the presence of an external confinement was seen through absorption imaging in Fölling et al. (2006), or by fluorescence in a quantum gas microscope in Sherson et al. (2010).

An important remark is that the site-dependent energy shift due to the Gaussian envelope of the trap can lead to an effective suppression of tunneling at large lattice depths. This suppression arrives earlier in the edges of the cloud. The energy shift [see figure 1.8(a)] between two adjacent sites reads $\Delta E = \epsilon(j+1) - \epsilon(j) = M\Omega^2(1+2j)d^2/2$. At the edges of the cloud this becomes approximately $\Delta E \simeq m\Omega^2 Rd$, with $R = jd$. If this shift becomes much larger than the tunneling energy, tunneling will be suppressed. When this happens, the local density approximation becomes no longer completely valid and, furthermore, an adiabatic loading (see next section) will no longer be practical, since the wells will be almost disconnected. In the most limiting case (i.e., in the edges of the cloud) to avoid this issue, one needs to keep

$$M\Omega^2 Rd \leq J. \tag{1.59}$$

We show the depths at which this happens in figure 1.8(b) in three different regions of the atomic cloud.

### 1.2.5 Adiabatic loading of an optical lattice

#### Adiabatic following

In this section we focus on the conditions that need to be satisfied in order to prepare a system which is as close as possible to the ground state of the Bose-Hubbard Hamiltonian. In a real experiment, the atomic ensemble is usually at a finite, although low, temperature. The loading needs to be performed in a finite amount of time during which atom losses can occur, which could also be an additional heating source. Taking all these effects into account to model the loading of the lattice is a complicated task, and some simplifications are needed. In particular, we will assume that the system is originally in the ground state and at $T = 0$, and that the lattice can be loaded arbitrarily slow without any atom loss.

The method usually employed in order to prepare a BEC in a harmonic trap, evaporative cooling, does not work well in a periodic potential[13]. Therefore, it is complicated to cool atoms directly in an optical lattice and an alternative procedure needs to be employed (Morsch et al. 2006).

The most common procedure to load an ultracold gas in the fundamental band of an optical lattice relies on the transfer of a BEC, previously prepared in a regular harmonic trap, into the lattice potential. Within the simplifications previously drawn, if the lattice potential is slowly ramped while the harmonic trap is simultaneously removed, the system remains ideally all time in the instantaneous ground state.

In this section, we examine the relevant energy scales so that the loading becomes as close as possible to the adiabatic limit[14]. In general, if a system is prepared in an eigenstate $|i\rangle$ of a time-dependent Hamiltonian $\hat{H}(t)$, the probability of remaining in this eigenstate during the evolution is close to 1 provided that, at all times [see Messiah (1999) or appendix E],

$$\hbar \left| \langle j| \frac{\partial \hat{H}}{\partial t} |i\rangle \right| \ll |E_i - E_j|^2, \tag{1.60}$$

for all states $i \neq j$, with $E_i$ and $E_j$ the instantaneous eigenenergies. In particular, this criterion shows explicitly that adiabaticity is violated whenever a level crossing occurs.

### Adiabaticity with respect to the band structure

At the single particle level, the adiabaticity criterion to satisfy is the following (Greiner 2003): During the loading, no transitions to excited bands should be induced. This criterion is known as *adiabaticity with respect to the band structure*. To extract the timescale required to avoid band transitions we consider the following argument: The initial BEC can be treated as a wavepacket localized in momentum space $|\boldsymbol{p} \simeq \boldsymbol{0}\rangle$. In the Bloch basis, it reads $|n, \boldsymbol{q}\rangle = |n = 0, \boldsymbol{q}_0\rangle$ with $\boldsymbol{q}_0 \simeq \boldsymbol{0}$. As we increase the lattice depth, quasimomentum remains unchanged (the periodicity of the lattice does not change) but the lattice band can change. The adiabaticity condition is then:

$$\hbar |\dot{V}_0| \ll |E(n, \boldsymbol{q} \simeq \boldsymbol{0}) - E(0, \boldsymbol{q} \simeq \boldsymbol{0})|^2, \tag{1.61}$$

which sets the maximal speed at which the lattice depth can change. For exemple, for a lattice at 760 nm and ytterbium atoms, this is satisfied for $|\dot{V}_0|/E_\mathrm{r} \ll 32\sqrt{2}E_\mathrm{r}/\hbar \simeq$

---

[13] In an optical lattice, the evaporation rate is strongly suppressed because of the band structure, which strongly reduces the density of states with energies close to the trap threshold (Blakie et al. 2004; Ho et al. 2009).

[14] The concept of adiabaticity in quantum mechanics is linked to the probability of following a single eigenstate $|i(t)\rangle$ without population transfer to any of the other states $|j(t)\rangle$. The entropy of the system is given by $S = \sum_k p_k \log(p_k)$, where $p_k$ is the population of each state. The entropy will be constant in time, $\dot{S} = 0$, provided $\dot{p}_j = 0$, which means that the process will be adiabatic in thermodynamical sense *if* the process is adiabatic in the quantum mechanical sense.

$6 \times 10^5\,\mathrm{s}^{-1}$. The characteristic times are on the order of the tens of µs and the adiabaticity criterion is fulfilled by performing ramps with a duration on the order of the ms, or larger.

### Adiabaticity in the presence of interactions

As soon as interactions are included in the picture, quasimomentum is no longer a good quantum number. In this case, the previous argument is just a necessary condition but not a sufficient one.

During the lattice ramp-up, we explore different regimes, each with its adiabaticity criteria:

1. While the lattice is still shallow ($V_0 \leq 5 - 6\,E_\mathrm{r}$), the Bose-Hubbard regime is not valid and one needs to avoid transitions to excited bands [see figure 1.9(a)].
2. Once the Bose-Hubbard regime is reached ($V_0 \geq 5 - 6\,E_\mathrm{r}$), the single-band and tight-binding approximations are valid and adiabaticity is set with respect to the many-body excitations that can appear in the system (see below).
3. Once the system is in the Mott-insulator regime, excitations have a large gap $\propto U$ and adiabaticity is more easilly fulfilled (Greiner 2003).
4. As previously discussed, once the depth is high enough so that $M\Omega^2 Rd \geq J$, tunneling is suppressed at the borders of the system and neither adiabaticity nor the local density approximation are valid anymore.

We will now detail the conditions to satisfy in the superfluid regime, once the Bose-Hubbard formalism applies. Let us then focus on a framework where the depth of the lattice is high enough so that we can work within the Bose-Hubbard approximation but where interactions are weak enough so that there is still a BEC. In this situation, the spatial density of the cloud can still be calculated using the Thomas-Fermi approximation (Pedri et al. 2001; Cataliotti et al. 2001) and the local chemical potential reads:

$$\mu_j = \epsilon_j + U\bar{n}_j, \tag{1.62}$$

with $\epsilon_j = m\Omega^2(jd)^2/2$ and $\bar{n}_j$ the occupation number of site $j$. As the lattice depth is raised both the interaction energy $U$ and the external frequencies $\Omega$ increase. Consequently, the instantaneous density changes too. For the system to be in the ground state at all times, the phases of the states in each lattice site need to evolve at the same rate during the ramp. This requires the local chemical potentials to be all equal. Otherwise, excitations will appear and this will lead to a heating of the sample. Therefore, even if tunneling does not affect much the equilibrium profile, atoms still need to redistribute fast enough to compensate via $\bar{n}_j$ for the changes in $U$ and $\Omega$ (Greiner 2003).

Adiabaticity depends thus on three energy scales: the interaction energy $U \propto V_0^{3/4}$, the external confinement $\Omega^2 \propto V_0$, both changing slowly with the lattice depth, and the tunneling $J \propto V_0^{3/4}\exp(-2V_0^{1/2})$, which drops exponentially with the lattice depth [see figure 1.9]. Then, to derive an adiabaticity criterion we first need to compute

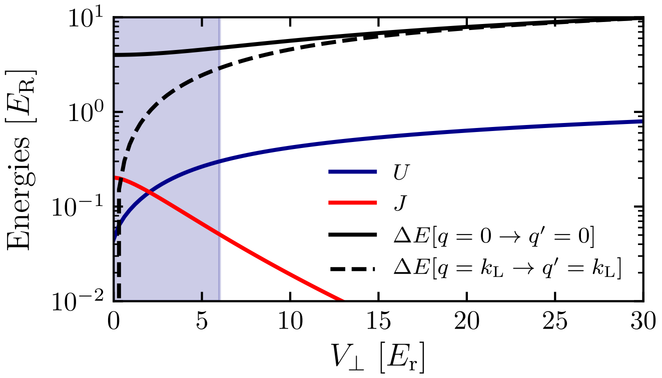

**Figure 1.9** – Different energy scales as a function of the lattice depth. $U$ represents the on-site interaction energy, $J$ is the tunneling amplitude, and $\Delta E$ corresponds to the bandgap in the center (solid line) or the edge (dashed line) of the 1BZ. The calculations are performed for $^{174}$Yb in the experimental conditions described in section 2.2.

the energy spectrum of the possible excitations of the system and then compare it to the rate of change of the parameters of the Bose-Hubbard Hamiltonian. Again, we perform some approximations to derive these criteria: In particular, we will first draw some arguments for an infinite system, and after that, we will specialize for the case of a uniform system but with a finite size. In order to compute the excitation spectrum, we will work within the Bogoliubov framework. However, one should keep in mind that, strictly speaking, the Bogoliubov approach is only valid for a small non-condensed fraction, i.e., far from the transition to the Mott insulator regime (see figure 1.5).

Let us then start by considering an infinite homogeneous system. A quantitative adiabaticity criterion has been derived in Kajtoch et al. (2018) in the regime of weak interactions, where the Bogoliubov theory applies, and we follow here their approach. We start by writing the time-dependent Bose-Hubbard Hamiltonian in the Wannier basis:

$$\hat{H}_\mathrm{BH}(t) = -J(t)\sum_{\langle \boldsymbol{i},\boldsymbol{j}\rangle} \hat{a}^\dagger_{\boldsymbol{i}}(t)\hat{a}_{\boldsymbol{j}}(t) + \frac{U(t)}{2}\sum_{\boldsymbol{i}} \hat{n}_{\boldsymbol{i}}(t)[\hat{n}_{\boldsymbol{i}}(t)-1]. \tag{1.63}$$

In order to compute the spectrum of the excitations, Kajtoch et al. (2018) write the Bose-Hubbard Hamiltonian in the Bloch basis and then work within the Bogoliubov framework. Within this approach, it is assumed that the $\boldsymbol{q}=\boldsymbol{0}$ mode alone is macroscopically populated. Then, to leading order in the non-condensed modes $\hat{b}_{\boldsymbol{q}\neq\boldsymbol{0}}$, the Hamiltonian becomes quadratic and can be diagonalised by a Bogoliubov transformation, introducing the quasiparticle operator $\hat{c}_{\boldsymbol{q}}$. In terms of the Bloch creation operators, this quasiparticle operator reads: $\hat{c}_{\boldsymbol{q}}(t) = u_{\boldsymbol{q}}(t)\hat{b}_{\boldsymbol{q}}(t) - v^*_{-\boldsymbol{q}}(t)\hat{b}^\dagger_{-\boldsymbol{q}}(t)$. With these transformations, equation (1.63) becomes:

$$\hat{H}_\mathrm{Bog}(t) = H_0(t) + \sum_{\boldsymbol{q}\neq\boldsymbol{0}} \hbar\omega(\boldsymbol{q},t)\left[\frac{1}{2} + \hat{c}^\dagger_{\boldsymbol{q}}(t)\hat{c}_{\boldsymbol{q}}(t)\right]. \tag{1.64}$$

Here $\hbar\omega(\boldsymbol{q},t)$ is the Bogoliubov dispersion relation given in (1.29) and, in the case of an optical lattice becomes:

$$\hbar\omega(\boldsymbol{q},t) = \sqrt{\Delta\epsilon(\boldsymbol{q},t)\left[\Delta\epsilon(\boldsymbol{q},t) + 2U(t)n\right]}, \tag{1.65}$$

where:

$$\Delta\epsilon(\boldsymbol{q},t) = zJ(t)[1-\cos(qd)], \tag{1.66}$$

is the single-particle dispersion relation in the tight-binding approximation (Ashcroft et al. 1976), with $z$ the number of nearest neighbors and $d = \lambda_\mathrm{L}/2$.

Let us now take the time derivative of equation (1.64):

$$\mathrm{i}\hbar\frac{\mathrm{d}}{\mathrm{d}t}\hat{H}_\mathrm{Bog} = \mathrm{i}\hbar\frac{\mathrm{d}}{\mathrm{d}t}H_0 + \mathrm{i}\hbar\sum_{\boldsymbol{q}\neq\boldsymbol{0}}\hbar\frac{\mathrm{d}\omega}{\mathrm{d}t}\left[\frac{1}{2}+\hat{c}^\dagger_{\boldsymbol{q}}\hat{c}_{\boldsymbol{q}}\right] + \mathrm{i}\hbar\sum_{\boldsymbol{q}\neq\boldsymbol{0}}\hbar\omega\left[\frac{\mathrm{d}\hat{c}^\dagger_{\boldsymbol{q}}}{\mathrm{d}t}\hat{c}_{\boldsymbol{q}}+\hat{c}^\dagger_{\boldsymbol{q}}\frac{\mathrm{d}\hat{c}_{\boldsymbol{q}}}{\mathrm{d}t}\right]. \tag{1.67}$$

The first two terms are diagonal in the quasiparticle basis and thus do not create any excitations. However, the last term involves the time derivative of the Bogoliubov operator and reads (Kajtoch et al. 2018):

$$\mathrm{i}\hbar\left[\frac{\mathrm{d}\hat{c}^\dagger_{\boldsymbol{q}}}{\mathrm{d}t}\hat{c}_{\boldsymbol{q}}+\hat{c}^\dagger_{\boldsymbol{q}}\frac{\mathrm{d}\hat{c}_{\boldsymbol{q}}}{\mathrm{d}t}\right] = -\mathrm{i}\hbar\Omega(\boldsymbol{q},t)[\hat{c}_{-\boldsymbol{q}}\hat{c}_{\boldsymbol{q}}+\hat{c}^\dagger_{\boldsymbol{q}}\hat{c}^\dagger_{-\boldsymbol{q}}]. \tag{1.68}$$

The term $\hbar\Omega(\boldsymbol{q},t)$ can be computed by using the coefficients of the Bogoliubov transformation and reduces to (Kajtoch et al. 2018):

$$\hbar\Omega(\boldsymbol{q},t) = \frac{\hbar}{2}\frac{\mathrm{d}}{\mathrm{d}t}\left[\log\left(\frac{\Delta\epsilon(\boldsymbol{q},t)}{\hbar\omega(\boldsymbol{q},t)}\right)\right]. \tag{1.69}$$

The products of operators in equation (1.68) connect the Bogoliubov ground state, i.e., the vacuum of quasiparticles $\hat{c}_{\boldsymbol{q}}|\mathrm{vac}\rangle = 0$, to an excited state with two quasiparticles of opposite momenta:

$$\langle 1:\boldsymbol{q}, 1:-\boldsymbol{q}|\hat{c}^\dagger_{\boldsymbol{q}}\hat{c}^\dagger_{-\boldsymbol{q}}|\mathrm{vac}\rangle = 1, \tag{1.70}$$

and therefore $\hbar\Omega(\boldsymbol{q},t)$ corresponds to the LHS of equation (1.60). The RHS is given by the energy difference between $|\mathrm{vac}\rangle$ and $|1:\boldsymbol{q},1:-\boldsymbol{q}\rangle$ which is $2\hbar\omega(\boldsymbol{q},t)$. The adiabaticity condition becomes then:

$$\alpha(\boldsymbol{q},t) = \frac{\hbar|\Omega(\boldsymbol{q},t)|}{2\hbar\omega(\boldsymbol{q},t)} \ll 1. \tag{1.71}$$

The criterion $\alpha(\boldsymbol{q},t) \ll 1$ becomes much more difficult to fulfill in the phonon-like regime of small quasimomenta. We show this in figure 1.10(a) where, for linear lattice ramps, we plot the maximum value of $\alpha$ for each value of $q$ for a ramp of 10 ms. This can also be understood by expanding the adiabaticity criterion in the limit of small $q$: Here, the single-particle dispersion relation is approximately quadratic $\Delta\epsilon(\boldsymbol{q},t) = zJ(t)q^2d^2/2$, and the Bogoliubov dispersion approximately linear:

$$\hbar\omega_\mathrm{ph}(\boldsymbol{q},t) \simeq \hbar c_\mathrm{s}(t)q \quad \text{with} \quad c_\mathrm{s}(t) = \frac{d}{\hbar}\sqrt{zJ(t)U(t)n}, \tag{1.72}$$

where $c_\mathrm{s}(t)$ is the speed of sound of the collective excitations in the lattice. Then, at low quasimomenta, the adiabaticity criterion becomes:

$$\alpha_\mathrm{ph}(\boldsymbol{q},t) = \frac{1}{8\omega_\mathrm{ph}(\boldsymbol{q},t)}\left|\frac{\dot{J}(t)}{J(t)} - \frac{\dot{U}(t)}{U(t)}\right| \ll 1, \tag{1.73}$$

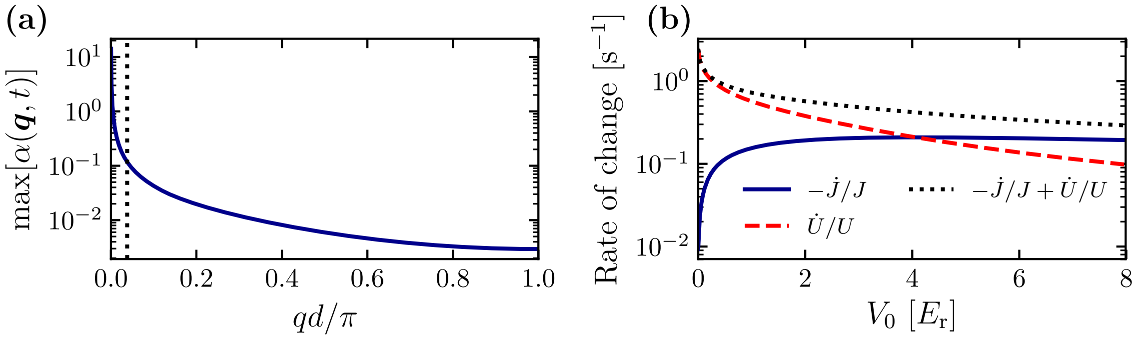

**Figure 1.10** – **(a):** Evolution of the adiabaticity parameter as a function of $q$ for a linear ramp from $V_0 = 0$ to $V_f = 8\,E_r$ in 10 ms. The solid blue line corresponds to equation (1.71) without the low-momenta approximation. The vertical dotted black line indicates the minimum momentum allowed by the finite size of the system, which in our experiment is $q_{\min}d = 2\pi d/L_{\mathrm{TF}} \simeq 0.12$ with $L_{\mathrm{TF}} = 20\,\mu\mathrm{m}$. **(b):** Rates of change of the energies in equation (1.73). We have used our experimental parameters for which the vertical lattice depth is fixed at $V_z = 27\,E_r$, and we focus on the adiabatic loading of the horizontal ones (see section 2.2.2 in chapter 2).

which diverges as $1/q$. This shows in particular that, in an infinite system, where $q$ can take a continuum of values, adiabaticity cannot be fulfilled.

As discussed in the previous sections, in experiments, an external confinement is present and this gives a finite size to the system. This size is given at small lattice depths by the Thomas-Fermi radius[15] $L_{\mathrm{TF}} = 2R_{\mathrm{TF}}$. If we consider a uniform system in a box of size $L_{\mathrm{TF}}$, then, the allowed momenta are quantized. With this, the lowest excitation has a quasimomentum $q_{\min} = 2\pi/L_{\mathrm{TF}}$ [black dotted line in 1.10(a)], and because of it, from now on we will quantify the adiabaticity criterion at this fixed $q = q_{\min}$ [see dotted line in figure 1.10(a)].

We now have all the ingredients to evaluate equation (1.73). To do this, we consider linear ramps $V_0(t) = V_f t/\tau_{\mathrm{ramp}}$ for a lattice ramped up to $8\,E_r$. The evolution of the terms $\dot{J}/J$ and $\dot{U}/U$ are shown in figure 1.10(b) as a function of the lattice depth. In figures 1.11(a) we show the behavior of $\alpha_{\mathrm{ph}}$ for two different ramp times. As expected, the slower the ramp the smaller the adiabatic parameter. In order to choose a duration for our experimental ramps, we look at the maximum value of $\alpha$ for each $\tau_{\mathrm{ramp}}$ once the lattice depth $V(t)$ is around $6\,E_r$. We plot these values as a function of the ramp time in figure 1.11(b). We then see that in order to avoid excitations by having the adiabatic parameter on the order of $\alpha \simeq 0.01$ we need ramps with a duration $\tau_{\mathrm{ramp}} \simeq 100$ ms.

This estimation is in good agreement with our actual experimental ramp times [see section 2.2.2]. As we go to deeper lattices, it will be tunneling the main limiting factor (Gericke et al. 2007) and the adiabaticity criteria will be roughly given by $|\dot{J}/J| \ll$

---

[15] The Thomas-Fermi radius is in principle time-dependent since it is related to the external frequencies as $1/\Omega(t)$. However, these time-dependence is weak because the trapping frequencies change slowly with the lattice depth $\propto V^{1/2}$. This change has even a smaller influence for the experimental situation described in chapter 2, where the cloud is tightly confined in the vertical direction during the stages in which the horizontal lattices are ramped up, and we simplify the discussion here by considering the size of the system constant in time.

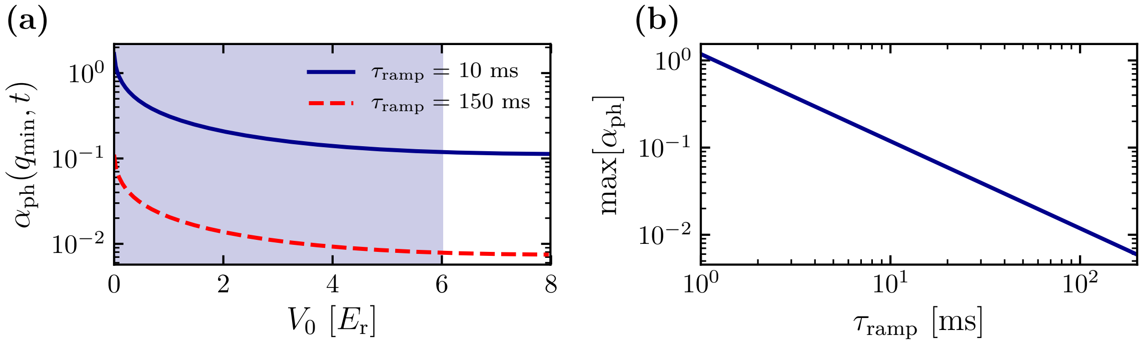

**Figure 1.11** – **(a):** Evolution of the adiabaticity parameter evaluated at $q = q_{\min}$ [equation (1.73)] for a linear ramp from $V_0 = 0$ to $V_{\mathrm{f}} = 8\,E_{\mathrm{r}}$ in 10 ms (solid blue line) and 150 ms (red dashed line). **(b):** Adiabaticity parameter for different ramp times. The maximum value is taken from the zone without shading in **(a)**, which corresponds to the regime in which the Bose-Hubard framework is not completely valid.

$\omega(q_{\min}) \propto \Omega_{\mathrm{trap}}$, which also leads to time scales on the order of tens of ms for the ramps. Moreover, as discussed in the previous sections, in a trapped system, a Mott insulator coexists with intermediate superfluid regions. In real experiments, in the edges of the system, these superfluid regions are prone to form a normal gas because of finite temperature effects and the residual confinement. All these effects will also end up limiting adiabaticity and have been ignored in the present discussion.

# CHAPTER 2

# Loading $^{174}$Yb ultracold gases in optical lattices

The production of Bose-Einstein condensates and their subsequent loading into an optical lattice have become nowadays standard experimental techniques (Metcalf et al. 1999; Ketterle et al. 1999; Bloch et al. 2008). Yet every atomic species has its own subtleties and so does each experiment. In this chapter, I will present an overview of the current status of our experimental setup and the techniques we employ.

This chapter consists of two parts. In the first one, I start by introducing the electronic structure, among some other properties, of ytterbium. I then give an overview of the experimental apparatus and expose the cooling steps that allow us to obtain a BEC. I conclude this first section by giving some details on our implementation of absorption imaging.

The second part is devoted to describing the loading of a BEC into a stack of independent 2D optical lattices. The success of this loading is confirmed by observing the signature of the quantum phase transition from a superfluid to a Mott insulator, namely the reversible disappearance of phase coherence. Finally I also show how atoms in an optical lattice can be used as a calibration tool for several useful experimental quantities such as on-site interactions and the magnification and resolution of an optical system.

## 2.1 Production and detection of an ytterbium Bose-Einstein condensate

Reaching quantum degeneracy exploits basically two techniques: Laser cooling (Metcalf et al. 1999) and evaporative cooling of trapped atoms (Ketterle et al. 1999). The first one relies on light-matter interactions to slow down and trap the atoms. The second one depends on two mechanisms: First, the removal of high-energy atoms out of the ensemble by lowering the depth of the trap; second, the thermalization of the sample at a lower temperature thanks to elastic collisions between atoms. For thermalization to be efficient, a high rate of collisions is necessary, and therefore a high density is desirable at the beginning of this second step. This sets the necessary performance of the laser cooling stage, which needs to be able to produce a cold and dense cloud, usually achieved by loading atoms into a magneto-optical trap (MOT). Furthermore, for magneto-optical trapping to work atoms need to be already slowed down. Consequently, the realization of a slow atomic beam is the mandatory first step in our experiments. The goal of this first section is to see how these essentials are met and to briefly describe each stage in our experimental context.

### 2.1.1 Ytterbium essentials

#### Atomic properties

Ytterbium is a lanthanide atom with atomic number $Z = 70$. It can be found in nature under the form of seven stable isotopes, five of which are bosons: $^{168}$Yb, $^{170}$Yb, $^{172}$Yb, $^{174}$Yb and $^{176}$Yb, with nuclear spin $I = 0$. The other two: $^{171}$Yb, with $I = 1/2$, and $^{173}$Yb, with $I = 5/2$, are fermions. All the results shown in this thesis have been obtained with the most abundant (32%) bosonic isotope: $^{174}$Yb.

Ytterbium is a so-called alkaline-earth-like atom. This nomenclature is used to designate all atoms such that: (i) Their internal shells are completely filled and (ii) their valence shell is an $s$-shell filled with two electrons; which is also the case for noble gases and group-II atoms.

The ground state configuration can be written as $[\mathrm{Xe}]4f^{14}6s^2$. Similarly to helium, the two electrons in the valence shell determine most of the atomic properties (Bethe et al. 1957). In particular, these two electrons can either pair to form a singlet (total spin $S = 0$) or a triplet state ($S = 1$). The electronic orbital ground state is symmetric (total orbital momentum $L = 0$), which imposes a singlet spin state for the ground state. We denote this state as $^1\mathrm{S}_0$ following the $^{2S+1}\mathrm{L}_J$ notation. Here, $\boldsymbol{J} = \boldsymbol{L}+\boldsymbol{S}$ is the total electronic angular momentum. Ytterbium has therefore no electronic magnetic moment in the ground state. A last detail concerning the bosonic isotopes is that their nuclear spin is $I = 0$. As a consequence, their ground state has no hyperfine structure at all ($\boldsymbol{F} = \boldsymbol{I} + \boldsymbol{J} = \boldsymbol{0}$). These properties mark a first important difference between alkalies and alkaline-earth-like atoms: the ground state is not sensitive to magnetic fields[16].

The first excited states are obtained by promoting one of the electrons to a $p$ shell: $[\mathrm{Xe}]4f^{14}6s6p$. These first excitations either lead to a singlet $^1\mathrm{P}_1$ or a triplet $^3\mathrm{P}_J$ state. We show the first energy levels together with the main transitions employed in this thesis in figure 2.1. From these, two are used for laser cooling: the $^1\mathrm{S}_0 \rightarrow {}^1\mathrm{P}_1$ transition, which we use for Zeeman slowing and also for absorption imaging and the $^1\mathrm{S}_0 \rightarrow {}^3\mathrm{P}_1$ transition, used for magneto-optical trapping. We then have ytterbium's *clock* transition $^1\mathrm{S}_0 \rightarrow {}^3\mathrm{P}_0$ and finally the $^3\mathrm{P}_0 \rightarrow {}^3\mathrm{D}_1$ transition, that we use to repump the atoms in the metastable state $^3\mathrm{P}_0$ back to the ground state. These two last transitions will be discussed in details in chapter 3.

---

[16] For fermionic ytterbium, having a hyperfine structure in the ground state ($I \neq 0$), the sensitivity to magnetic fields is given by the nuclear magnetic moment $\mu_\mathrm{I}$, which is orders magnitude smaller than the Bohr magneton $\mu_\mathrm{B}$. Therefore, techniques such as magnetic trapping or Stern-Gerlach separation are not realistic for the fermionic ground state either (Scazza 2015).

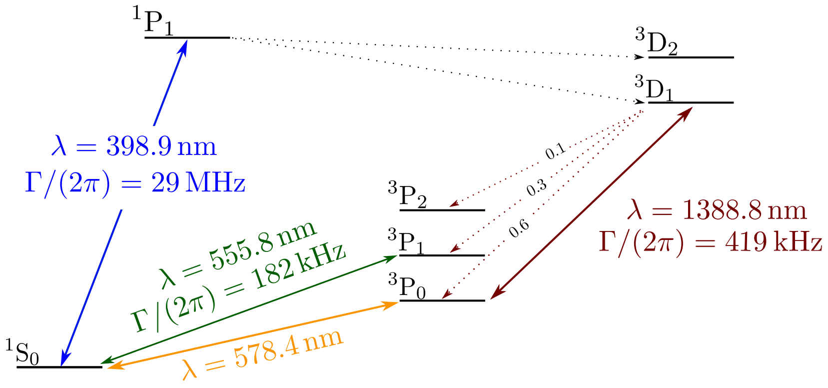

**Figure 2.1** – Scheme of the lowest energy levels of ytterbium. The solid colored lines indicate optical transitions we use in the experiment, together with the wavelength and the associated linewidth. Dotted lines indicate possible decay channels. The branching ratios concerning the possible decays from $^3\mathrm{D}_J$ to $^3\mathrm{P}_J$ are also indicated.

### Laser cooling with ytterbium: main considerations

We now discuss the properties of the transitions used for laser cooling. We first recall that the steady-state of the laser cooling process is reached once the cooling rate is equal to the heating rate induced by the momentum diffusion imparted by spontaneosuly emitted photons. The competition between these two mechanisms sets the lowest achievable temperature, the *Doppler temperature*, given by (Metcalf et al. 1999):

$$T_\mathrm{D} = \frac{\hbar\Gamma}{2k_\mathrm{B}}, \tag{2.1}$$

with $\Gamma$ the linewidth of the transition involved.

For ytterbium, the first excited states interesting for laser cooling correspond to the following transitions:

1. $^1\mathrm{S}_0 \rightarrow {}^1\mathrm{P}_1$ *blue* transition at $\lambda_\mathrm{b} = 398.9\,\mathrm{nm}$. It is a broad transition ($\Gamma_\mathrm{b} = 2\pi \times 29\,\mathrm{MHz}$). The saturation intensity is $I_\mathrm{sat} = 60\,\mathrm{mW/cm^2}$. This transition is not closed: atoms in $^1\mathrm{P}_1$ can leak into the $^3\mathrm{D}_J$ manifold (Honda et al. 1999). These decay afterwards to the $^1\mathrm{S}_0$ state via the $^3\mathrm{P}_J$ states.

2. $^1\mathrm{S}_0 \rightarrow {}^3\mathrm{P}_1$ *green* transition at $\lambda_\mathrm{g} = 555.8\,\mathrm{nm}$. It is a narrow transition ($\Gamma_\mathrm{g} = 2\pi \times 182\,\mathrm{kHz}$). The saturation intensity is $I_\mathrm{sat} = 0.14\,\mathrm{mW/cm^2}$. If we could ignore spin-orbit coupling, this transition would be electric-dipole forbidden with $\Delta S = 1$. However spin-orbit coupling is relatively large for ytterbium and the concerning selection rule within this framework, $\Delta J = 1$, is verified. The transition is therefore weakly allowed. Electric dipole transitions not conserving the spin are called *intercombination transitions*.

The limit temperature from equation (2.1) suggests using the narrow *green* transition for magneto-optical trapping, which leads to a low Doppler temperature $T_\mathrm{D} \simeq 4.4\,\mu\mathrm{K}$. However, this advantage comes at a price: the capture velocity (i.e. the limit velocity above which atoms will not be trapped) is small. An upper bound for this velocity can be obtained by assuming a constant force on the atom $F = \hbar k \Gamma$ (Metcalf et al. 1999). Then, the maximum velocity is determined by requiring that the atom be stopped within the volume defined by the size (i.e. the waist) $w_0$ of the MOT beams. This velocity is $v_\mathrm{c} \simeq \sqrt{2\hbar k \Gamma w_0 / M}$, with $M$ the mass of the atom and $k = 2\pi/\lambda$. For the *green* transition and $w_0 \simeq 1.5\,\mathrm{cm}$, this velocity is $v_\mathrm{c} \simeq 10\,\mathrm{m/s}$.

As previously announced, this small capture velocity requires that an earlier cooling mechanism be implemented. One option, carried out in some groups, is to load a first MOT using the *blue* transition. However, since the $^3\mathrm{P}_{0,2}$ shells are metastable (Barber 2007) the cooling cycle is stopped for atoms falling into these states . This results in important atom losses unless additional transitions are used to repump these atoms back to the ground state (Cho et al. 2012). Another possibility, which is the solution employed in our group, is to address the *blue* transition in a Zeeman slower only and load the MOT directly on the intercombination line.

### 2.1.2 Experimental apparatus

We now present an overview of our experimental setup, focusing mainly in the vacuum system and on the lasers used for slowing down the atoms. Much more details on these aspects can be found in the theses of the previous PhD students: Matthias Scholl (Scholl 2014) and Alexandre Dareau (Dareau 2015).

#### Vacuum system

We show in figure 2.2 a scheme consisting of the main parts of the experiment: the oven, the Zeeman slower and the MOT chamber [figure 2.2 (a)] and, finally, the science chamber[17] [figure 2.2(b)-(c)]. Each one of these parts is separated by a differential pumping stage. Vacuum in the oven part is achieved thanks to two 20 L/s ion pumps[18]. At working temperature, the pressure in this zone is on the order of $10^{-8}$ mbar. Then, after a first differential pumping stage another 20 L/s ion pump allows to reach a pressure of $10^{-9}$ mbar in the Zeeman tube. Pumping in the MOT chamber is achieved by means of a 40 L/s ion pump and a getter pump. With these, the pressure in the MOT chamber is below $10^{-10}$ mbar. Finally, a tube connects the MOT chamber to the science chamber, where we perform our experiments. In this chamber, we reach a vacuum on the order of $10^{-11}$ mbar thanks to a pump[19] combining a 2 L/s ion pump and a non-evaporative getter pump. We then see that both the MOT chamber and the science chamber are in the ultra-high vacuum regime, which reduces considerably collisions with the background gas, resulting in longer lifetimes for our atomic samples.

As a side note, from the schematics shown in figure 2.2(a), we see that the viewport through which the Zeeman beam passes is facing the oven and, therefore, the atomic beam. After some time, we realised that Yb was getting deposited in this viewport, and most part of the Zeeman beam was reflected and/or absorbed. We removed this coating (Yamaguchi 2008) by focusing 3 W of light at 532 nm to a waist of approximately 50 µm. The signature of desorption was the observation of a fast increase of our vacuum pressure by about two orders of magnitude, which then quickly went back to its steady

---

[17] Spherical octagon UHV vacuum chamber. Kimball

[18] Medium VacIon Plus Pumps. Agilent.

[19] NEXTorr D 200-5. SAES Getters

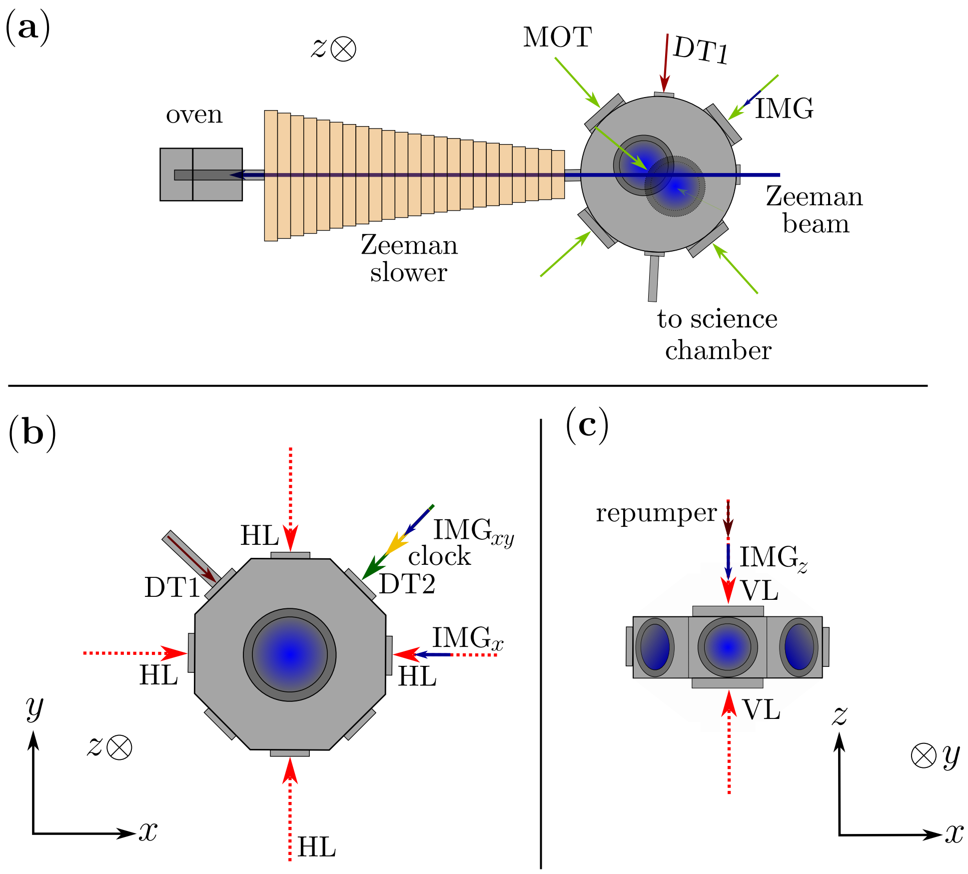

**Figure 2.2** – Experimental setup **(a): Top view of the oven, the Zeeman slower and the MOT chamber.** An oven filled with ytterbium is connected to a Zeeman slower, where atoms are slowed down thanks to the Zeeman beam. These atoms then arrive to the MOT chamber where they are further cooled thanks to the MOT beams and trapped by a quadrupole magnetic field. Atoms are then loaded in a first optical dipole trap (DT1) which is used to transport them to the science chamber. **(b): Top view of the science chamber**. Atoms arrive to the science chamber and DT1 is crossed with another dipole trap DT2 where evaporation is performed to obtain a BEC. The BEC is subsequently loaded in an optical lattice (HL: horizontal lattice beams and VL: vertical lattice beams). Atoms can then be probed on the clock transition thanks to the clock beam. **(c): Front view of the science chamber**. A repumper is available to transfer atoms in the metastable state back to the ground state. The different available imaging axis (IMG) are also shown.

value. We then scanned the whole surface thanks to a 2-axis piezoelectric actuator installed in a mirror mount. After removing the Yb from the viewport, the loading rate improved by a factor of about 10. We now repeat this procedure on a weekly basis in order to maintain constant optimal parameters for the MOT loading.

### Lasers for cooling

In this paragraph, we present the main details concerning the frequency generation and stabilization of the lasers we employ for cooling: a blue laser for the Zeeman slower imaging and a green laser for magneto-optical trapping.

1. Blue laser: Light at 399 nm is obtained by frequency doubling of infrared light at 798 nm delivered by a commercial diode laser[20]. The 1.5 W available are injected into a doubling cavity with a non-linear crystal[21] inside (Scholl 2014; Dareau 2015). With this, we obtain 330 mW of blue light. The cavity error signal is generated by modulating the laser current and the lock is performed thanks to a piezoelectric actuator mounted on one of the cavity mirrors. The frequency of this blue light is subsequently stabilized by correcting the laser current thanks to a modulation transfer spectroscopy scheme (Bouganne 2018) performed in a hollow cathode lamp with Yb inside.
2. Green laser: Light at 556 nm is also obtained by frequency doubling. In this case, the seed is a narrow-line distributed feedback fiber laser[22] at the near-infrared wavelength 1112 nm. This light is then amplified thanks to a fiber amplifier[23]. Subsequent frequency doubling in a cavity with a non-linear crystal[24] inside allows us to obtain around 1 W of green light. The cavity error signal is obtained by frequency modulation thanks to an EOM, and the lock is performed by acting on a piezoelectric actuator mounted on one of the cavity mirrors. Frequency stabilization is then performed by saturated absorption spectroscopy in a glass cell containing iodine (Dareau 2015), which allows us to stabilize the frequency by correcting the current of the seed laser.

## 2.1.3 Atomic beam and Zeeman slower

The first step in our experiments is the generation of an atomic beam. Our source consists of an oven filled with solid ytterbium that we heat to a working temperature of 450 °C. This produces a gas with enough vapor pressure and density. The atomic beam is subsequently obtained by transverse collimation thanks to a tube of length $L = 10\,\mathrm{mm}$ and diameter $d = 4\,\mathrm{mm}$. This generates a stream with a divergence angle $\theta \simeq d/(2L) = 11.5°$.

At this stage the beam enters the Zeeman slower. The average longitudinal velocity of the atoms is $v_0 \simeq 300\,\mathrm{m/s}$ and they need to be slowed down to $v_\mathrm{c} \simeq 10\,\mathrm{m/s}$, so that they can be trapped by the MOT. For this, we send a counterpropagating laser beam at $\lambda_\mathrm{b} = 398.9\,\mathrm{nm}$, resonant with the ${}^1\mathrm{S}_0 \rightarrow {}^1\mathrm{P}_1$ transition. The beam is collimated and has a power of 70 mW. As atoms travel through the Zeeman tube, they are slowed down and get out of resonance due to the Doppler effect. The principle of a Zeeman slower

---

[20] TA pro, Toptica.

[21] ppKTP (*periodically poled potassium titanyl phosphate*) crystal from Raicol crystals.

[22] Koheras Adjustik. NKT photonics

[23] Eylsa. Quantel laser.

[24] ppSLT (*periodically poled stoichiometric lithium tanalate*) crystal from Covesion.

is to use a longitudinal magnetic field gradient to compensate for this shift. Then, the atoms feel an approximately constant radiation pressure force (Dareau 2015).

### 2.1.4 Magneto-optical trap and crossed optical dipole trap

**MOT: basic principles and figures of merit**

After the Zeeman slower stage, the atomic beam reaches the MOT chamber. Atoms slow enough to be captured experience a force $\boldsymbol{F}(\boldsymbol{r}, \dot{\boldsymbol{r}}) = -\alpha\dot{\boldsymbol{r}} - \kappa\boldsymbol{r}$. The first term corresponds to a friction force due to the radiation pressure of three counter-propagating, circularly polarized, red-detuned beams resonant with the $^1\mathrm{S}_0 \to {}^3\mathrm{P}_1$ transition. This force is the responsible of slowing down the atoms. The second term is obtained by applying a quadrupole magnetic field. In doing so, a spatial dependence is added to the force. This promotes the absorption of those photons that push the atom towards the center of the trap, defined by the zero of the magnetic field (and thus the spring-like character of the force). The combined effect of these two forces produces a dense and cold cloud confined at the center of the trap (Metcalf et al. 1999). The details concerning our MOT functioning can be found in Scholl (2014).

As previously indicated, because of the narrow intercombination line, the capture velocity is small. Then, in order to address enough velocity classes and increase the loading rate, the transition needs to be artificially broadened: we do this by (i) power-broadening the transition and (ii) using red-detuned sidebands. Moreover, due to the small linewidth of the $^3\mathrm{P}_1$ state, one needs small magnetic field gradients on the order of $1\,\mathrm{G/m}$ (about one order of magnitude smaller compared to alkalis) to keep the atoms on resonance inside the volume defined by the MOT beams. These aspects make the MOT optimization somewhat sensitive.

We can model the loading of the MOT by the following equation $\dot{N}(t) = R - N/\tau$. The two parameters $R$ and $\tau$ design the rate of atoms coming from the Zeeman slower successfully loaded in the MOT (which we assume constant) and the lifetime of atoms, respectively. This lifetime is mainly determined by one-body collisions with the background gas. The atom number evolves then as:

$$N(t) = R\tau\left(1 - \mathrm{e}^{-t/\tau}\right). \tag{2.2}$$

We can apply this model to the data in figure 2.3(a), where we show the atom number for different loading times. By doing so, we extract a loading rate $R = 3.5 \times 10^7\,\mathrm{s}^{-1}$ and a lifetime $\tau = 50\,\mathrm{s}$. The maximum achievable atom number is then given by $N_\infty = R\tau = 1.75 \times 10^9$ atoms. In our typical working conditions, we load the MOT in $6\,\mathrm{s}$ ending up with an atom number of $2 \times 10^8$ atoms.

Another parameter interesting to extract is the cloud temperature, which can be inferred by recording several TOF expansion images. The temperature is estimated by fitting a Gaussian distribution to the data, by using the fact that the density distribution after TOF reflects the *in situ* momentum distribution. The width of the distribution is then related to the temperature of the ensemble and is given by (Ketterle et al. 1999):

$$\sigma_k(t) = \sigma_{0,k} + \frac{k_\mathrm{B}T}{m}t^2. \tag{2.3}$$

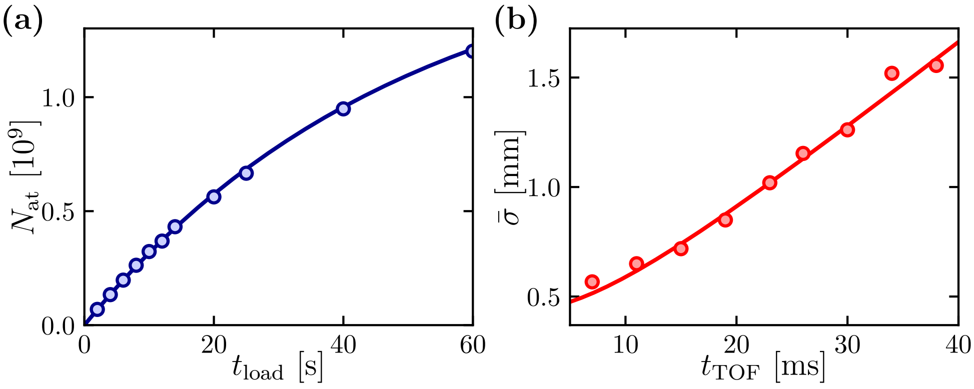

**Figure 2.3** – Loading and characterization of the MOT **(a)**: MOT loading curve: the number of atoms captured in the MOT is shown for different loading times. By fitting equation (2.2) to the data, we extract the loading rate: $R = 3.5 \times 10^7\,\mathrm{s}^{-1}$ and the lifetime $\tau = 50\,\mathrm{s}$. **(b):** Mean size $\bar{\sigma} = (\sigma_x + \sigma_y)/2$ of atoms released from a MOT for different TOFs. By using equation (2.3) we extract the temperature of the cloud: $T = 35\,\mu\mathrm{K}$.

This can then be used to determine the temperature of the sample by recording several images after TOF. We have used this method to extract the temperature of our atomic clouds. The data is shown in figure 2.3(b) and the corresponding fit with equation (2.3) leads to a temperature $T \simeq 35\,\mu\mathrm{K}$, several times higher than the Doppler temperature associated to $^3\mathrm{P}_1$. Cooling further is possible (Scholl 2014; Dareau 2015) but results in a subsequent smaller atom number loaded in the optical dipole trap, and the optimization is therefore performed to maximize the atom number.

### Optical dipole traps

Our dipole traps are generated by lasers. The spatial profile is very well described by a symmetric Gaussian beam of intensity:

$$I(\boldsymbol{r}) = \frac{2P}{\pi w^2(z)}\, \mathrm{e}^{-2\rho^2/w^2(z)}. \tag{2.4}$$

Here $z$ is the propagation axis and $\rho^2 = x^2 + y^2$, $P$ is the beam power and $w(z) = w_0[1 + (z/z_{\mathrm{R}})^2]^{1/2}$ is the $1/\mathrm{e}^2$ beam diameter, determined by the waist at the focus position, $w_0$, and the Rayleigh length $z_{\mathrm{R}} = \pi w_0^2/\lambda$.

The dipole potential felt by the atom reads (Grimm et al. 2000):

$$V(\boldsymbol{r}, \lambda) = -\frac{1}{2\epsilon_0 c}\mathrm{Re}[\alpha_j(\lambda)] I(\boldsymbol{r}), \tag{2.5}$$

where $\alpha_j(\lambda)$ is the atomic polarizability. This polarizability (and therefore the dipole potential) depends on the wavelength $\lambda$ of the light employed to generate the trap and on the atomic state $j$. Depending on the sign of $\alpha$, atoms will either be attracted towards the intensity maxima (*red* detuned trap) or repelled away from them (*blue* detuned trap).

In most situations, the atomic cloud size $\bar{\sigma}$ is small compared to the beam waist and

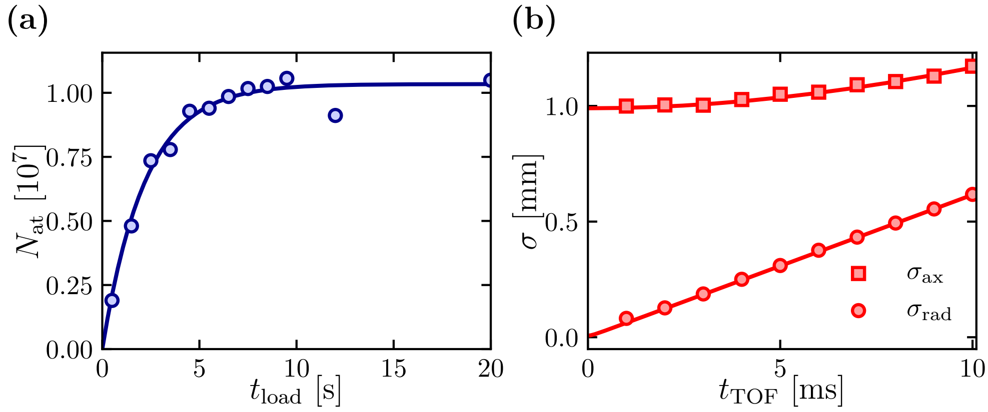

**Figure 2.4** – Loading and characterization of the infrared dipole trap **(a):** Atom number in the dipole trap for different MOT loading times. A fit to the data by equation (2.2) leads to $R = 4.7 \times 10^6\,\mathrm{s}^{-1}$ and $\tau = 2.2\,\mathrm{s}$. **(b):** Temperature measurement of atoms in the dipole trap: the data show the evolution of the axial and radial sizes of the cloud for different TOFs. This allows us to extract the temperature $T = 40\,\mu\mathrm{K}$ by fitting equation (2.8) to the data. We see that for the radial direction, the asymptotic regime is soon reached, and its evolution becomes independent of the initial size.

the Rayleigh length. This allows to rewrite equation (2.5) as:

$$V(\boldsymbol{r}) \simeq -V_0 + \frac{1}{2}M(\omega_{\rm rad}^2 r^2 + \omega_{\rm ax} z^2). \tag{2.6}$$

We call $V_0 = P\mathrm{Re}[\alpha(\lambda)]/(\pi\epsilon_0 c w_0^2)$ the trap depth. The axial and radial frequencies are given by:

$$\omega_{\rm ax} = \sqrt{\frac{8V_0}{k^2 M w_0^2}}, \qquad \omega_{\rm rad} = \sqrt{\frac{4V_0}{M w_0^2}}, \tag{2.7}$$

with $k = 2\pi/\lambda$. We can also generate traps consisting of several beams. In particular, for a crossed dipole trap (CDT) generated by two non-interfering orthogonal beams, the total depth is given by $V_0 = V_1 + V_2$ and the trapping frequencies in the axis defined by the beams are $\omega_j = (\omega_{j,1}^2 + \omega_{j,2}^2)^{1/2}$.

### Loading and characterization of an optical dipole trap

The last cooling step in the MOT consists in compressing the atomic cloud by increasing the magnetic field gradient and shifting its position to make it coincide with the focus of an optical dipole trap, which is already switched on. After this, the power of the MOT beams is decreased and its frequency is driven closer to resonance. Atoms start then being cooled in the dipole trap, which we load in 200 ms.

The dipole trap is generated by using a high-intensity infrared fiber laser[25] of power $P = 45\,\mathrm{W}$ and wavelength $\lambda = 1070\,\mathrm{nm}$. The polarizability at this wavelength is $\alpha_g(\lambda) \simeq 164\alpha_0$, with $\alpha_0 \simeq 1.65 \times 10^{-41}\,\mathrm{C^2m^2/J}$ the atomic unit of electric polarizability. We focus this beam at $w_0 \simeq 40\,\mu\mathrm{m}$. This creates a trap of depth $V_0/k_{\rm B} \simeq 660\,\mu\mathrm{K}$, much higher than the MOT temperature and therefore sufficient to trap the cloud.

---

[25] YLR-50-LP-AC-Y12.IPG Photonics.

We show in figure 2.4(a) a loading curve for this trap as a function of the MOT loading time. Before releasing the cloud and measuring the atom number after a TOF, a hold time inside the dipole trap of 1 s is performed. Using equation (2.2) to fit the data, we extract the following loading parameters: $R = 4.7 \times 10^6\,\mathrm{s}^{-1}$ and $\tau = 2.2\,\mathrm{s}$. After 4-5 s of loading, the dipole trap loading is saturated. Working in these conditions ensures that possible atom number fluctuations at the MOT stage are suppressed and do not propagate to the latter stages of the experiment. In our experiments we typically work with $t_{\mathrm{load}} = 6\,\mathrm{s}$, which provides an number $N \simeq 1.5 \times 10^7$ of atoms in the trap.

In order to extract the trapping frequencies defined in equation (2.7) we employ two different methods. The axial frequency is measured by inducing center of mass oscillations along the longitudinal axis of the trap. This is achieved by rapidly shifting the focus of the dipole trap. Atoms undergo a kick and start oscillating in the harmonic potential at the axial frequency $\omega_{\mathrm{ax}}$. In figure 2.5(a) we show the result of this measurement, where the position of the center of the cloud is monitored in time after the perturbation. The axial frequency is inferred by fitting a damped sinusoidal to the data, from which we obtain $\omega_{\mathrm{ax}} = 2\pi \times 8.5\,\mathrm{Hz}$. The observed damping might be due to the fact that during the oscillation, atoms start exploring regions of the trap where the harmonic oscillator approximation no longer holds.

Radial frequencies are in the kHz range. Measuring center of mass oscillations at these frequencies is experimentally challenging (indeed, because of the high trapping frequencies, the movement of the center of mass takes place in a small region, which is not easily resolved because of the finite image resolution) and another method is usually employed. This method, known as parametric heating (Savard et al. 1997), consists in modulating[26] the laser power so that $P(t) = P_0[1 + \eta(t)]$, with $\eta(t) = \eta_0 \cos(2\pi f_{\mathrm{mod}} t)$. From equation (2.6), this is equivalent to applying a perturbation $V_\eta(t) = m\omega_{\mathrm{rad}}\eta(t)r^2/2$. In a quantum picture, this perturbation induces transitions between levels of the harmonic oscillator $|n\rangle$ with a matrix element proportional to $\langle m|r^2|n\rangle$. The parity of Hermite polynomials imposes $m = n + 2k$ with $k \in \mathbb{Z}$. Energy conservation requires then $f_{\mathrm{mod}} = 2kf_{\mathrm{rad}}$. Once a resonance is reached, the energy of the atom increases exponentially with time, until at some point its kinetic energy is higher than the depth of the trap, and the atom is lost. Such a loss spectrum is shown in figure 2.5(b), where we record the remaining atom number at each modulation frequency. By fitting a sum of two inverted Gaussians we extract $\omega_{\mathrm{rad}} = 2\pi \times 1400\,\mathrm{Hz}$ . We see that another peak at $f_{\mathrm{mod}} = f_{\mathrm{rad}}$ appears. The nature of this peak could be explained by a modulation of laser pointing according to Savard et al. (1997). This spatial modulation could be due to thermal lensing induced by the power modulation . Both measurements are in agreement with the estimated waist, independently calculated by Gaussian beam propagation.

Once the trapping frequencies are known, it is possible to extract the temperature of the cloud using the same experimental procedure employed to determine the temperature of atoms in the MOT. For a thermal cloud, the sizes evolve during TOF as (Ketterle et al. 1999):

$$\sigma_k^2(t) = \sigma_{k,0}^2[1 + (\omega_k t)^2], \tag{2.8}$$

and become independent of the trapping frequencies $\sigma_k^2(t) \to 2k_{\mathrm{B}}Tt^2/m$ for long times

---

[26] Experimentally, we apply the modulation during 200 ms with an amplitude $\eta_0 = 10\%$.

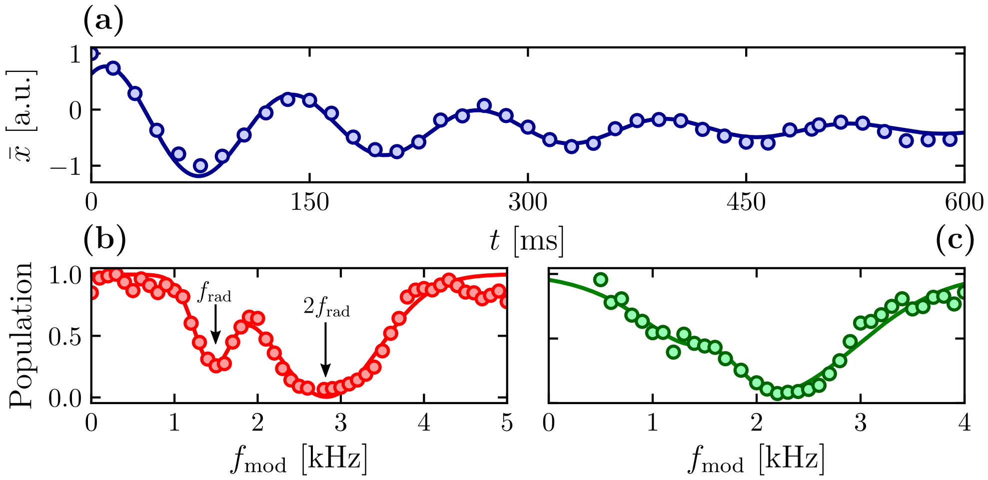

**Figure 2.5** – Calibration of the frequencies of the dipole traps. **(a):** Axial frequency of the infrared trap. By recording center of mass oscillations, we extract the frequency $\omega_{\mathrm{ax}} = 2\pi \times 8\,\mathrm{Hz}$. The data shows the center of mass position as a function of time after the perturbation described in the main text. The solid line is a damped sinusoidal fit to the data. **(b):** Radial frequency of the infrared trap by using the parametric heating technique. We show the atom number for different modulation frequencies. The solid line is a fit corresponding to the sum of two inverted Gaussians. This allows to extract (see text) the radial frequency $\omega_{\mathrm{rad}} = 2\pi \times 1.4\,\mathrm{kHz}$. **(c):** Radial frequency of the visible dipole trap. By the parametric heating technique we infer $\omega_{\mathrm{rad}} = 2\pi \times 1.1\,\mathrm{kHz}$.

$\omega_k t \gg 1$. In figure 2.4(b) we show the rms-size of the cloud after TOF in the radial and axial directions. The solid lines are fits to the data using equation (2.8), from which we extract a temperature $T = 40\,\mu\mathrm{K}$, well below the trap depth and in good agreement with the temperature of the MOT.

### Transport and transfer into a crossed optical dipole trap

The slackness of the optical trap in the axial direction prevents from keeping the necessary densities required for an efficient thermalization while evaporation takes place. To improve this, we employ another optical dipole trap. By intersecting both lasers at the position of each focus, we can obtain a tight confinement in all directions.

Before doing so, we first transport the atoms from the MOT to the science chamber. This chamber has a better vacuum level and higher optical access. Transport is performed by moving the focus of the infrared dipole trap. We do this by means of a corner cube mirror mounted on a translation stage[27] (Scholl 2014), which allows us to transport the atoms over a distance of 18 cm in 1.5 s, with an efficiency around 80% mostly limited by the evaporation of the hottest atoms.

Once atoms reach the science chamber, we intersect the cloud with another optical trap propagating at 90° in the horizontal plane. This second trap consists of a visible laser[28] at a wavelength $\lambda = 532\,\mathrm{nm}$, for which $\alpha_g(\lambda) \simeq 262.5\alpha_0$. We set its power to $P = 1\,\mathrm{W}$ and we focus it at $w_0 \simeq 16\,\mu\mathrm{m}$. This generates a trap of depth $V_0/k_{\mathrm{B}} \simeq 100\,\mu\mathrm{K}$.

---

[27] XMS160. Newport.

[28] Verdi V-6. Coherent.

The radial frequency of this dipole trap is also measured by the parametric heating technique previously described [see figure 2.5(c)].

### 2.1.5 Evaporative cooling and Bose-Einstein condensation

#### Experimental implementation

Experimentally, we perform evaporation by reducing the power of the dipole traps in 4 s. We first evaporate the infrared dipole trap until both traps are at the same depth. After this, an important fraction of the atoms gathers in the crossing region. Further evaporation is performed by lowering the depth of both dipole traps. Details on the ramps employed for evaporation can be found in Scholl (2014) and Dareau (2015).

The shot-to-shot reproducibility of the evaporation ramps is essential for position and atom number stability. This is achieved on the one hand by stabilizing the power of the lasers. The power of the visible dipole trap is controlled by means of an AOM, whose diffraction efficiency is controlled by a feedback loop. Control of the infrared laser power is performed by a dual control. First, the power is lowered down to 10% of its maximum value by changing the laser current itself. Below this point, lasing would stop and another method is needed to achieve the extinction levels on the order of 1% required for evaporation. We use for this a half-wave plate mounted in a motorized rotation stage[29] followed by a Glan-Taylor polarizer[30] with an achievable extinction level well below 1%. Combined with a feedback loop on the laser current, this step allows us to stabilize the power seen by the atoms (Scholl 2014).

On the other hand, stability also requires minimizing drifts and pointing fluctuations of the traps. We monitor the dipole trap positions by imaging each focus onto a position detector. This detector, together with a motorized mirror installed in each optical path is inside a feedback loop, which allows us to keep the crossing position stable[31]. In practice, the position stabilization is not continuous, and we activate this feedback a couple of times per day to correct possible drifts.

#### Characterization of the Bose-Einstein condensate

As evaporation is performed, the temperature of the gas decreases. Once this temperature is low enough, the critical phase space density is reached and we observe the phase transition from a thermal gas to a BEC (see 2.6). We see a bimodal distribution appear, which is a clear experimental signature of Bose-Einstein condensation. By analyzing these profiles, one can extract parameters such as the condensed fraction or the temperature of the thermal part (Ketterle et al. 1999). For temperatures below 100 nK the thermal fraction is too small to be detected. In our setup, the total experimental sequence to produce a BEC lasts 12 s. After this, we obtain pure BECs ($f_c$>80%) of $8 \times 10^4$ atoms with a relative atom number fluctuation below 5%.

In the Thomas-Fermi approximation (see section 1.1.3) the density of the BEC in the CDT is given by equation (1.16). The ground state scattering length of $^{174}$Yb has

---

[29] DRTM-40. OWIS

[30] GL15-C26. Thorlabs.

[31] Aligna 4D. TEM Messtechnik.

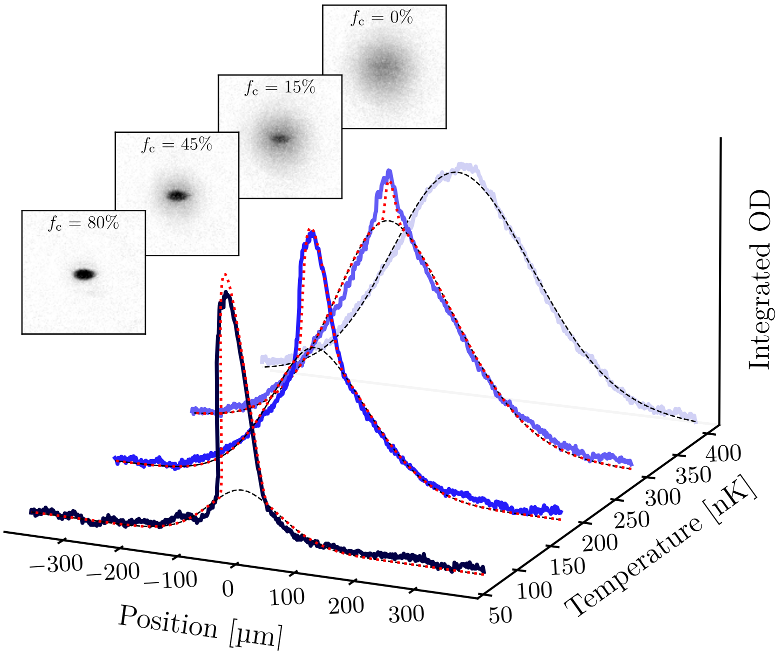

**Figure 2.6** – Absorption pictures and integrated density profiles after TOF at different moments of the evaporation ramps. As the power of the dipole traps is lowered, the temperature of the cloud decreases and, at the critical temperature, Bose-Einstein condensation is reached, clearly seen in the absorption images by the appearance of a bimodal structure. Solid blue lines are the integrated density profile of the absorption images shown in the insets. The black dashed lines are a fit to the thermal part using a Bose distribution, which allows us to extract the temperature shown in the axis. The dotted red line allows us to extract the condensed fraction shown in the insets and results from a bimodal fit taking into account the contribution of the thermal distribution and the Thomas-Fermi profile of the condensed part.

been measured in Kitagawa et al. (2008) and in Borkowski et al. (2017). Its value is $a = 105a_0$, with $a_0 \simeq 5.3 \times 10^{-11}\,\text{m}$ the Bohr radius. At the end of evaporation the trapping frequencies are $(\omega_x, \omega_y, \omega_z) = 2\pi \times (80, 240, 250)\,\text{Hz}$. The BEC peak density is $n_0 = 9 \times 10^{14}\,\text{atoms/cm}^3$ and the in-trap Thomas-Fermi radii are $(R_x, R_y, R_z) = (7.9, 2.7, 2.5)\,\mu\text{m}$. Finally, the chemical potential $\mu = gn_0 = h \times 3600\,\text{Hz} \gg \hbar\omega_k$, which justifies the Thomas-Fermi approximation, as discussed in section 1.1.3.

### 2.1.6 Absorption imaging

This section briefly describes the method of absorption imaging that we employ to extract information on the atoms. The line employed for imaging the ground state is the $^1\text{S}_0 \rightarrow {}^1\text{P}_1$ transition, with $\lambda_\text{b} = 398.9\,\text{nm}$ and $\Gamma_\text{b} = 2\pi \times 29\,\text{MHz}$. The procedure used to image atoms in the $^3\text{P}_0$ state will be described later in chapter 3.

The idea behind absorption imaging is the following: A resonant pulse is sent to the atomic cloud. Some of the photons will be absorbed and scattered in all directions, thus not reaching the camera. The atomic signal then appears as a shadow on the recorded image. This shadow allows one to extract information on the atomic column density through the Beer-Lambert law:

$$\frac{\mathrm{d}I}{\mathrm{d}z} = -n\sigma(I)I, \tag{2.9}$$

where $\sigma(I) = \sigma_0/(1 + I/I_{\mathrm{sat}})$ is the effective cross section with the effect of saturation taken into account and $z$ is the direction in which the imaging beam propagates. The bare resonant cross section is given by $\sigma_0 = 3\lambda^2/(2\pi)$ and the saturation intensity by $I_{\mathrm{sat}} = \hbar\Gamma\omega_{\mathrm{b}}^3/(12\pi c^2)$ with $\omega_{\mathrm{b}} = 2\pi c/\lambda_{\mathrm{b}}$. Integration leads to the following expression for the optical depth of the sample (OD):

$$\mathrm{OD}(\boldsymbol{\rho}) = \sigma_0 \int n(\boldsymbol{r})\,\mathrm{d}z = -\ln\left(\frac{I(\boldsymbol{\rho})}{I_0(\boldsymbol{\rho})}\right) + \frac{I(\boldsymbol{\rho}) - I_0(\boldsymbol{\rho})}{I_{\mathrm{sat}}}, \tag{2.10}$$

with $\boldsymbol{\rho} = (x, y)$. The first term in the right hand side corresponds to the optical density $\Delta(\boldsymbol{\rho})$. We see then, that for intensities well below $I_{\mathrm{sat}}$ the optical depth coincides with the optical density and we have $I(\boldsymbol{\rho}) = I_0(\boldsymbol{\rho})\exp[-\mathrm{OD}(\boldsymbol{\rho})]$.

Experimentally, the intensities $I$ and $I_0$ are obtained by taking two successive images: the first one in the presence of the atomic cloud, from which we extract $I$, and another one, the *reference* image, recorded once the atoms have left the camera field of view, which corresponds to $I_0$. Once the images are recorded, the OD is determined from equation (2.10). The column density $n(\boldsymbol{\rho}_k)$ and the total atom number $N_0$ are obtained as follows:

$$n(\boldsymbol{\rho}_k) = \frac{\mathcal{A}}{\mathcal{M}\sigma_0}\mathrm{OD}(\boldsymbol{\rho}_k), \qquad N_0 = \sum_{\boldsymbol{\rho}_k} n(\boldsymbol{\rho}_k), \tag{2.11}$$

where $\mathcal{A}$ is the pixel area and $\mathcal{M}$ the magnification of the optical setup. A method to extract the magnification of an imaging setup is presented in section 2.2.5.

Detailed features in the density profiles are sensitive to interferences on the imaging light (the so-called *imaging fringes*), which appear as a periodic modulation in the pictures. Also, intensity fluctuations during the time between the two images $I$ and $I_0$ are taken can occur and are detrimental because they might blurr or hide real atomic information. We remove these artifacts by employing a fringe-removal algorithm well-known in image processing and adapted to ultracold atoms experiments by several groups (Ockeloen et al. 2010). We will refer to this technique as *best-reference picture* in the following. The basic idea is to take an ensemble of reference images (what we called $I_0$ in the previous paragraph) and then generate an *ideal* reference picture for each image by performing a linear combination of all of them. The *best reference image* is the one that is closer to the picture with atoms in a region with no atoms, i.e., the one that minimizes the pixel difference between the generated reference picture and the region with no atoms. More details on the algorithm and its performance concerning our image treatement can be found in Bouganne (2018).

A last important detail to consider is the exposition time, i.e., for how long will the atoms be exposed to the imaging beam. There are mainly two effects to take into account:

1. Doppler effect: Each time an atom absorbs a photon, the atom recoils and acquires a velocity $v_{\mathrm{b}} = \hbar k_{\mathrm{b}}/M$. Then, after absorbing many photons, the atom

will be driven out of resonance and will not contribute to the OD anymore. In order to avoid this, the Doppler shift $\Delta\omega$ after the absorption of $N_{\mathrm{ph}}$ photons, $\Delta\omega = N_{\mathrm{ph}} k_{\mathrm{b}} v_{\mathrm{b}}$ should be smaller than the linewidth of the transition $\Gamma_{\mathrm{b}}$, which limits this to $N_{\mathrm{ph}} \leq 2000\,\mathrm{photons/atom}$. The number of absorbed photons is on the other hand given by $N_{\mathrm{ph}} \simeq \Gamma_{\mathrm{sp}}\tau$, with $\Gamma_{\mathrm{sp}} \simeq \Gamma_{\mathrm{b}}/4$ (Metcalf et al. 1999) for a saturation $s \simeq 1$ and $\tau$ the exposition time. The previous condition is then satisfied for $\tau \leq 200\,\mu\mathrm{s}$.

2. Heating: Upon each absorption-spontaneous emission of a photon, the atom is heated. The induced transverse heating (Grimm et al. 2000) after absorbing $N_{\mathrm{ph}}$ photons is $E_{\perp} = N_{\mathrm{ph}} E_{\mathrm{r}}/3$, with $E_{\mathrm{r}} = \hbar^2 k_{\mathrm{b}}^2/(2M)$. This is associated to a transverse diffusion $\Delta p_{\perp} = \hbar k_{\mathrm{b}}\sqrt{N_{\mathrm{ph}}/3}$. We make now a simplification and assume $\Delta x \simeq \Delta p\tau/M$. We then require that the displacement $\Delta x$ associated to this diffusion be smaller than the pixel size $p_{\mathrm{s}}$ during the time $\tau$ of exposition. The condition is then $\tau^{3/2} \leq \sqrt{3}Mp_{\mathrm{s}}/(\hbar k_{\mathrm{b}}\sqrt{\Gamma_{\mathrm{sp}}})$. For a pixel size $p_{\mathrm{s}} = 4.65\,\mu\mathrm{m}$ this leads to $\tau \leq 35\,\mu\mathrm{s}$.

The images shown and analyzed in this manuscript correspond to beam intensities on the order or smaller than $I_{\mathrm{sat}}$, with exposition times of $10 - 35\,\mu\mathrm{s}$ (i.e. $N_{\mathrm{ph}} \simeq 500 - 1500\,\mathrm{photons/atom}$). The best-reference picture algorithm is applied whenever fine details on the density profiles are needed (e.g. for extracting visibility of the interference patterns generated by atoms released from an optical lattice).

## 2.2 Loading and characterization of an optical lattice

As detailed in section 1.2.2, interacting bosons in an optical lattice are described by the Bose-Hubbard Hamiltonian. In this section, we illustrate the experimental scheme and the techniques used to produce and characterize a system governed by such a Hamiltonian. In particular, the loading procedure we employ will allow us to prepare a pile of independent 2D lattices, where the dynamics of each stack is given by the following 2D single band Bose-Hubbard Hamiltonian:

$$\hat{H}_{\mathrm{BH}} = -J\sum_{\langle i,j\rangle}(\hat{a}_i^{\dagger}\hat{a}_j + \hat{a}_j^{\dagger}\hat{a}_i) + \frac{U}{2}\sum_i \hat{n}_i(\hat{n}_i - 1) + \frac{M}{2}\sum_i(\Omega_x^2 x_i^2 + \Omega_y^2 y_i^2)\hat{n}_i. \tag{2.12}$$

In the following, we discuss in details how we calibrate the lattice depth $V_0$, allowing us to compute $J$ and $U$, the external frequencies $\Omega_i$ and how to prepare experimentally the ground state of a system described by equation (2.12). This is done by means of a scheme that relies on the adiabatic transfer of the BEC into the lattice potential. We then report on the observation of the superfluid to Mott insulator transition and discuss how its experimental signature can be related to a first order correlation function and therefore to the degree of phase coherence present in the sample. We then calibrate the on-site interaction energy by doing a collapse and revival experiment, and we perform noise-correlations analysis from a set of images of Mott insulators recorded after TOF.

## 2.2.1 Experimental considerations and calibrations

### Generation of the optical lattice and characterization techniques

We generate optical lattices by retro-reflecting optical Gaussian beams. This produces a standing wave modulated by the Gaussian envelope of the beams, that creates a dipole potential of the form (Bloch et al. 2008):

$$V(\boldsymbol{r}) = -V_0 \cos^2(k_\mathrm{L} z)\, \mathrm{e}^{-2\rho^2/w^2(z)}. \tag{2.13}$$

Here, $k_\mathrm{L} = 2\pi/\lambda_\mathrm{L}$, $\lambda_\mathrm{L}$ is the wavelength of the light employed to create the lattice and, as before, $V_0 = 4P\mathrm{Re}[\alpha(\lambda)]/(\pi\epsilon_0 c w_0^2)$ is the trap depth (the factor of 4 with respect to the single dipole trap is due to the constructive interference of the forward and reflected optical waves). As discussed in section 1.2.1, this picture is extended to several dimensions by intersecting several standing waves in different directions. If these waves do not interfere with each other, the total potential is given by the incoherent sum of each individual standing wave. For three orthogonal beams, we showed in section 1.2.1 that the physics in the lowest band could be described by an effective potential on top of the lattice [see equation (1.38) and the corresponding discussion], where this effective potential has the form of a harmonic confinement:

$$V_\mathrm{eff}(\boldsymbol{r}) = \sum_{\mu=x,y,z} \frac{1}{2} m \Omega_\mu^2 \mu^2. \tag{2.14}$$

To characterize the optical lattice, we need to determine the depths $V_{0,\mu}$ (which we will use to compute $J$ and $U$) and the external trapping frequencies $\Omega_\mu$. In practice, the external frequencies are on the order of several tens of Hz. We infer them experimentally by measuring center of mass oscillations of the BEC in the potential generated by one of the beams from the CDT and a lattice beam with the retro-reflection blocked. The CDT trapping frequencies are known, which allows us to extract $\Omega_\mu$.

In order to calibrate the lattice depth $V_0$, several methods exist (Morsch et al. 2006). The one we use is known as *Kapitza-Dirac diffraction* (Kapitza et al. 1933; Ovchinnikov et al. 1999), which has the advantage of needing short interaction times with the lattice (about $30 - 50\,\mu\mathrm{s}$). It consists in pulsing the optical lattice onto the BEC, which afterwards evolves freely in TOF. An absorption image is then recorded and shows a series of peaks [see figure 2.7(a)]. An interpretation of this phenomenon is the following: The BEC, initially prepared in a state of well-defined momentum $p \simeq 0$, virtually absorbs photons from one of the lattice beams and then, by stimulated emission, releases them into the other beam. Then, the atom acquires a net momentum equal to $2\hbar k_\mathrm{L}$, which explains the observed equidistant density peaks. The population of each one of the diffraction orders oscillates at rates that are proportional to the lattice depth and therefore, this kind of measurements can be used to extract $V_0$. In more details, the evolution is computed as follows (Denschlag et al. 2002): Prior to the lattice pulse, the BEC is well described by a plane wave $|p = 0\rangle$, which can be expressed in the Bloch basis as a linear combination of states $|n, q = 0\rangle$. Then, once the lattice is switched on, each one of the Bloch states picks up a phase $\sim \exp[-\mathrm{i}E(n, q = 0)t/\hbar]$ during the time $t = t_\mathrm{pulse}$ the atoms interact with the lattice. Finally, the sudden switch off of the lattice, projects the state back onto the plane-wave basis, where each

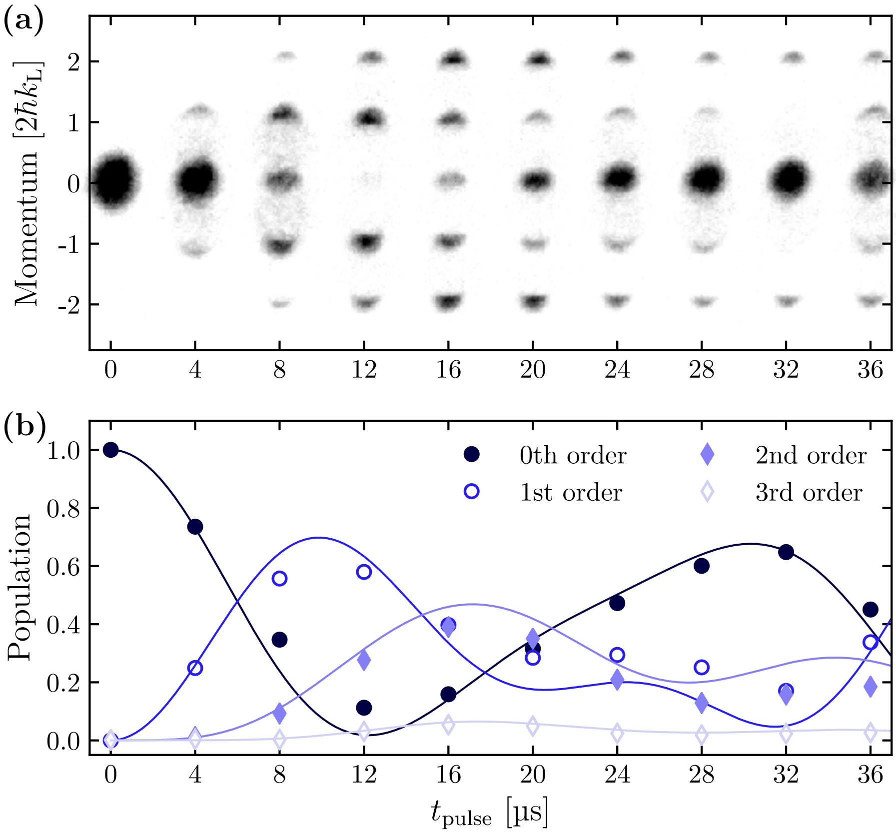

**Figure 2.7** – Calibration of the lattice depth through Kapitza-Dirac diffraction. **(a):** Absorption images after TOF of the atoms after having interacted with the lattice during a time $t_{\text{pulse}}$. We see diffraction peaks appearing at integer values of the lattice reciprocal vectors. **(b):** As time evolves, the population of each diffraction order changes, the oscillation rates are governed by the Bloch energies $E(n,q)$, which depend on the lattice depth $V_0$. A fit to the data employing the procedure described in the text can then be used to extract the lattice depth.

Bloch state can be decomposed as a linear combination of $|p = 2m\hbar k_L\rangle$, with $m \in \mathbb{Z}$ the diffraction order. The evolution of each order $m$ oscillates at a rate given by $E(n,q) = f(V_0)$, numerically computed, and this is what we use to extract the lattice depth. An example of a typical measurement and the fit using this procedure is shown in figure 2.7(b).

### Experimental aspects

Here, we give some information on the experimental lattice setup we use to generate cubic lattices. All three optical lattice beams are derived from the same source: a 5 W laser[32] at $\lambda_L = 759\,$nm, (see chapter 3). The optical beam is split in three paths: one for each axis of the lattice. To avoid crossed interferences between each axis of the lattice, the frequency of each beam is then shifted by means of an AOM. Labeling the horizontal axis $x$ and $y$ and the vertical one $z$, the shifts are $(\delta_x, \delta_y, \delta_z) = 2\pi \times (80, -80, 110)$ MHz. By doing so, the residual modulation is much faster than the external dynamics of

---

[32] Titanium-sapphire laser: SolsTiS. M Squared Lasers. The laser is pumped by a 16 W laser at 532 nm (Finesse. Laser Quantum).

the atoms and therefore, the interference between different beams can be neglected. To clean the optical mode, each beam is subsequently coupled into a polarization-maintaining optical fiber. Polarization fluctuations are minimized thanks to a half-wave plate in front of each fiber. At the output of the fibers, a polarizing beamsplitter is used to select the polarization . The polarizations of each lattice beam are linear and oriented orthogonal to each other: $\boldsymbol{\varepsilon}_x = \hat{\boldsymbol{e}}_z$ , $\boldsymbol{\varepsilon}_y = \hat{\boldsymbol{e}}_x$ and $\boldsymbol{\varepsilon}_z = \hat{\boldsymbol{e}}_y$, reducing further the possibility of crossed interferences. This beamsplitter also allows to convert possible remaining polarization fluctuations into power fluctuations, easier to suppress with a feedback system.

Each beam is then focused and aligned to match the atomic position. The waists are $(w_x, w_y, w_z) = (115, 125, 150)\,\mu\mathrm{m}$. Around 600 mW are available for the vertical arm and 400 mW for the horizontal ones. Retro-reflection is performed by a 0° mirror and aligned by re-coupling the beam into the same optical fiber. Polarization changes during propagation would result in a smaller interference term and, in some experiments, the use of a quarter-waveplate is necessary to compensate for possible polarization changes caused by the mirror (typically a dielectric one). So far, we have not noticed this to be an issue in our experimental setup and the polarization of the retro-reflected beam is not corrected. Power stabilization, essential for adiabatic loading and preventing heating mechanisms, is assured by a feedback loop that, through a photodiode, monitors the power and corrects possible deviations from the set-point by adjusting the diffraction efficiency of the AOMs. Concerning the alignment of the lattice beams, the radial position is controlled by means of a mirror mount with a piezoelectric actuator[33]. The axial position is adjusted by means of a lens. Finally, to improve mechanical stability, the retro-reflection mirrors mounts for the horizontal lattices are clamped on an Invar block, which assures its stability against thermal fluctuations.

Finally, the trap depths are measured by the Kapitza-Dirac technique and the external frequencies by recording collective mode oscillations as described in the previous paragraph. As an example: For $(P_x, P_y, P_z) = (0.4, 0.4, 0.6)\,\mathrm{W}$, we obtain $(V_{0,x}, V_{0,y}, V_{0,z}) = E_\mathrm{r} \times (24.0, 25.6, 27.0)$, with $E_\mathrm{r} = \hbar^2 k_\mathrm{L}^2/(2M) \simeq h \times 2\,\mathrm{kHz}$, the recoil energy at $\lambda_\mathrm{L} = 759\,\mathrm{nm}$. The residual confinement is $(\Omega_x, \Omega_y, \Omega_z) = 2\pi \times (42, 38, 33)\,\mathrm{Hz}$.

### 2.2.2 Adiabatic loading of the optical lattice

Once the lattice is calibrated and aligned, we need to load the atoms in such a way that we can prepare the ground state of the system, described by the Bose-Hubbard Hamiltonian in equation (2.12). As described in section 1.2.5, the most common method is to transfer the BEC previously prepared in the CDT into the lattice by slowly increasing the lattice depth.

We meet the criteria described in section 1.2.5 using the following experimental procedure:

1. Exponential ramp-up of the vertical lattice: with the CDT still on, the vertical lattice is ramped up in $t_z = 20\,\mathrm{ms}$ to its maximum depth ($V_z = 27E_\mathrm{r}$). This is necessary to freeze the vertical motion and hold atoms against gravity (ytterbium

---

[33] Picomotor Piezo Center Mount, Newport.

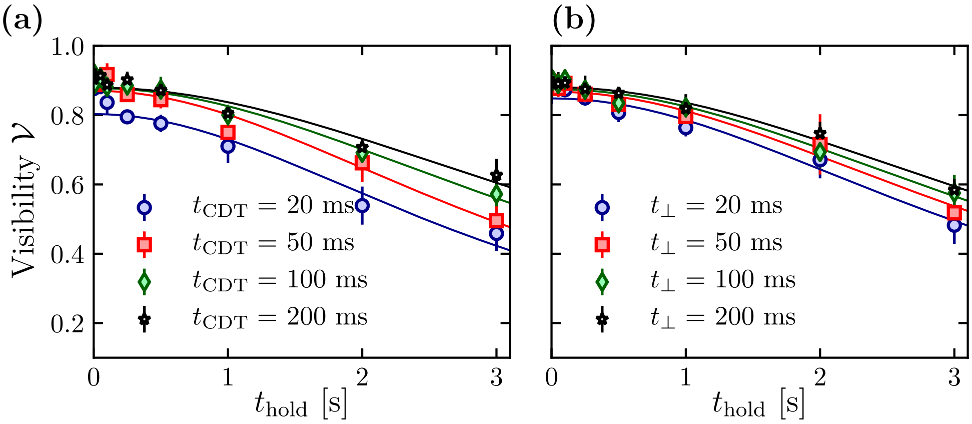

**Figure 2.8** – Characterization of the lattice loading. **(a)** and **(b):** Lifetime of the visibility of the diffraction peaks. Each data set corresponds to a different extinction speed of the CDT **(a)** or the rising up of the horizontal lattices **(b)**. The solid lines are Lorentzian fits to the data. The FWHM of each Lorentzian is associated to the lifetime of the visibility.

can only be optically trapped). Adiabaticity with respect to the band structure is then satisfied and the in-plane density is still mainly determined by the CDT.

2. Adiabatic extinction of the CDT: in order to reduce the density and mitigate three-body losses at later stages, the CDT is smoothly decompressed in a time $t_{\mathrm{CDT}}$. In this way, we create a stack of independent two dimensional BECs held by the vertical lattice alone.

3. Adiabatic loading of the horizontal lattices: finally, the horizontal lattice arms are slowly ramped to their final values $V_{\perp}$ in a time $t_{\perp}$.

With this loading scheme, we end up with a vertical collection of almost independent 2D horizontal lattices.

Experimentally, we optimize the decompression time $t_{\mathrm{CDT}}$ of the CDT and the ramp up time $t_{\perp}$ of the horizontal lattices following the procedure described in Gericke et al. (2007): We produce a superfluid at $6\,E_{\mathrm{R}}$ at a given ramp time and then measure how the visibility of the diffraction peaks (see next section), which characterizes phase coherence, evolves in the lattice by measuring it at different times $t_{\mathrm{hold}}$. We then increase the ramp times and repeat the procedure until the visibility lifetimes do not change anymore [see figure 2.8]. We finally work at $t_{\mathrm{CDT}} \simeq t_{\perp} \simeq 100\,\mathrm{ms}$.

We note that, although the adiabaticity criteria given in 1.2.5 do not apply in a strict sense for the decompression stage of the CDT, the same timescales are needed (Band et al. 2002) so that collective oscillations are not excited during the extinction of the trap. These oscillations would lead to heating during the loading of the horizontal lattice and reduce the visibility lifetime. Therefore, the optimization of the decompression speed can also be performed by looking at the visibility of the diffraction peaks once the whole lattice is loaded.

Finally, once adiabaticity is ensured, the remaining effects we need to take into account are the following:

1. Heating generated by spontaneous emission due to the lattice beams: This heating is given by $\Gamma_{\mathrm{heat}} = 2\Gamma_{\mathrm{sc}} E_{\mathrm{r}}$ (Grimm et al. 2000) and it is negligible (on the order of $0.04\, E_{\mathrm{r}}/\mathrm{s}$ for $P = 400\,\mathrm{mW}$).

2. Heating due to power fluctuations, which could explain the decay of the visibility observed at long times in figure 2.8.

### Model for the loading

We now detail the model that we use to numerically compute the equation of state of the sample, prepared by performing the loading procedure previously presented. The BEC, initially prepared in the CDT is well described in the Thomas-Fermi regime and its density distribution $n_{\mathrm{TF}}(\boldsymbol{r})$ takes the form of an inverted parabola [see equation (1.16)]. In particular, the radius of the BEC in the vertical direction within this framework reads:

$$R_z = \sqrt{\frac{2\mu}{M\omega_z^2}}, \tag{2.15}$$

We model the loading of the vertical lattice by performing a *sudden* approximation in which we project the BEC density in the periodic potential generated by the optical lattice. The number of populated planes is $N_{\mathrm{planes}} = 2R_z/d$ with $d = \lambda_{\mathrm{L}}/2$. For a given total atom number $N$, the atom number in each plane $j$ is given by:

$$N_z(j) = \int_{z_j-d/2}^{z_j+d/2} \int n_{\mathrm{TF}}(\boldsymbol{r})\,\mathrm{d}^2\rho\,\mathrm{d}z \simeq \frac{15Nd}{16R_z}\left[1-(jd/R_z)^2\right]^2 \quad \text{for} \quad R_z \gg d. \tag{2.16}$$

We show in figure 2.9 the atom number distribution in each plane for $N = 8\times10^3$ and $N = 8\times10^4$ atoms.

After this, we need to describe the switching off of the CDT and the horizontal lattices ramp up. We model this two steps as an adiabatic process, i.e., starting from distribution predicted by equation (2.16) we consider that (i) each plane is independent of the rest and (ii) that after ramping up the horizontal lattices, the system is described by the ground state of the Bose-Hubbard Hamiltonian. This ground state is calculated by using the Gutzwiller ansatz presented in section 1.2.3. The presence of the trap, leading to an inhomogeneous density profile, is introduced by making a local density approximation, i.e., we first find the equation of state $\bar{n}[\mu, V_\perp]$ and then interpolate to find the equation of state in each plane $j$ for the trapped system $\bar{n}_{\mathrm{tr}}(\boldsymbol{\rho}, j) = \bar{n}[\mu_j - V(\boldsymbol{\rho}), V_\perp]$. The chemical potential in each plane is found self-consistently by imposing

$$\int \bar{n}_{\mathrm{tr}}(\boldsymbol{\rho}, j)\,\mathrm{d}^2\rho = N_z(j). \tag{2.17}$$

Examples of the obtained density profiles are shown in figure 2.10 for different lattice depths and different atom numbers.

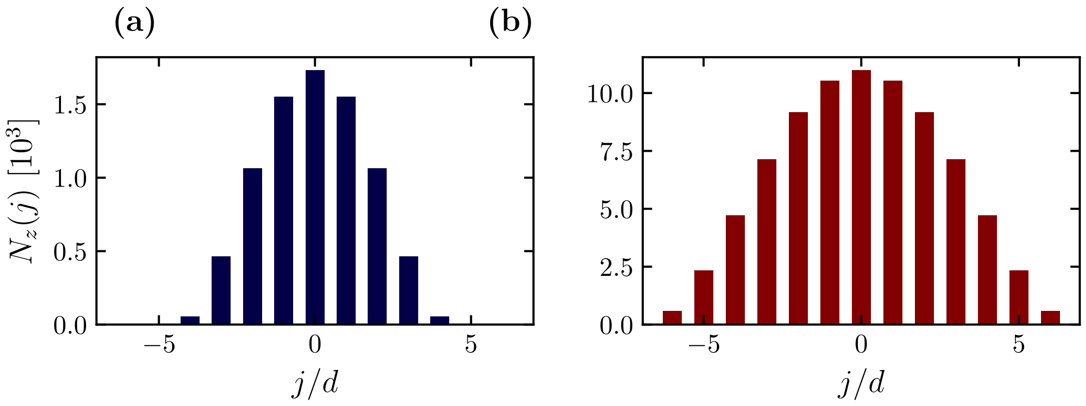

**Figure 2.9** – Atom distribution in the vertical lattice for $V_z = 27E_\mathrm{r}$. **(a)** for $N = 8 \times 10^3$ atoms and **(b)** for $N = 8 \times 10^4$ atoms predicted by equation (2.16).

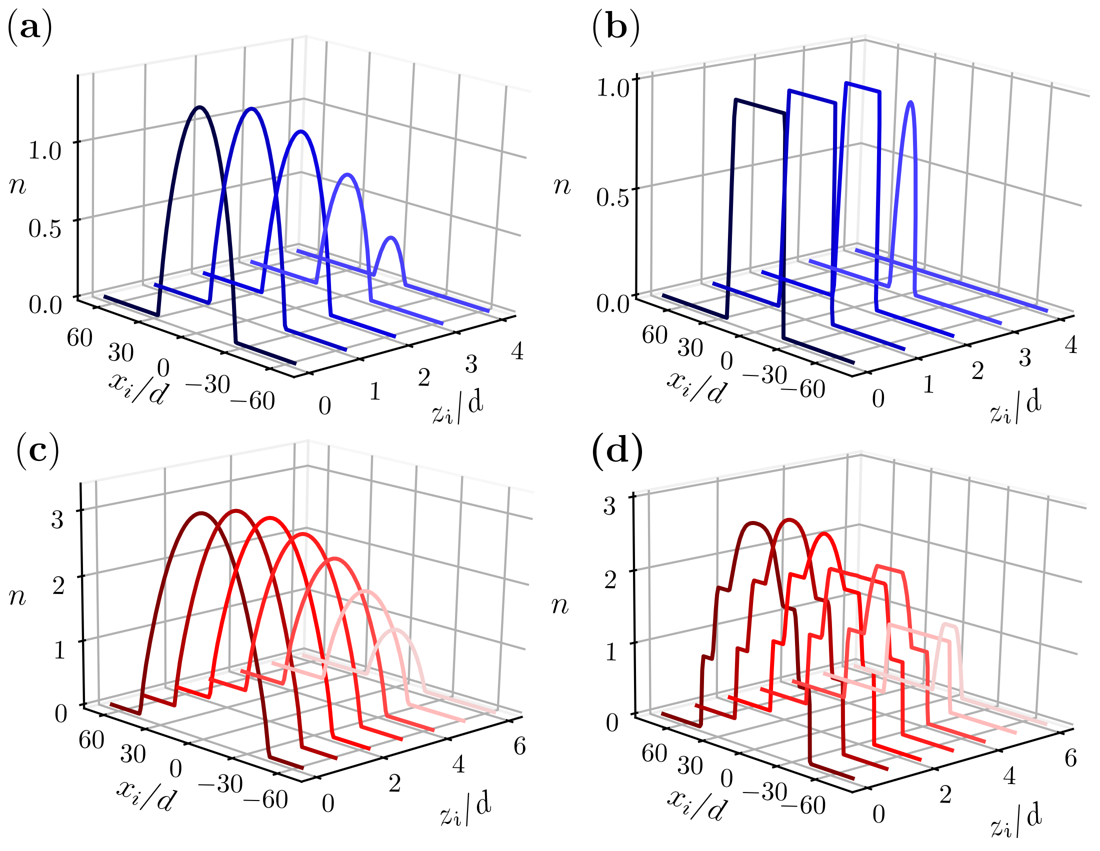

**Figure 2.10** – Density distribution in each vertical plane using the numerical model described in the text for $V_\perp = 6E_\mathrm{r}$ (left column) and $V_\perp = 14E_\mathrm{r}$ (right column). Figures **(a)** and **(b)** show the density profiles for an initial atom number $N = 8 \times 10^3$ atoms and **(c)** and **(d)** are the equivalent density distributions for $N = 8 \times 10^4$ atoms.

### 2.2.3 Observation of the superfluid to Mott insulator transition

#### Experimental signature

In an ideal situation, the initial state produced after evaporation is a BEC with negligible thermal fraction. Then, the adiabatic transfer realizes to a good approximation

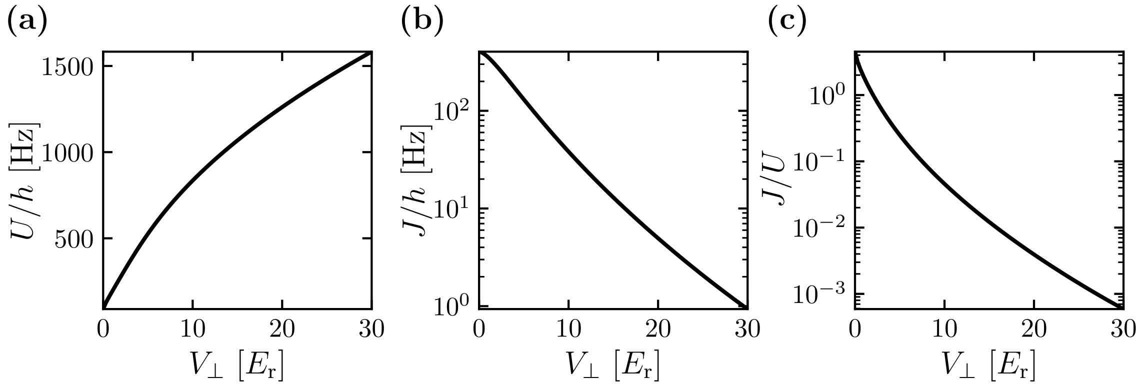

**Figure 2.11** – Bose-Hubbard parameters as a function of the lattice depth **(a):** On-site interaction energy. **(b):** Tunneling energy. **(c):** Ratio $J/U$. For all calculations $V_z = 27\,E_\mathrm{r}$.

the ground state of the Bose-Hubbard Hamiltonian. The nature of this ground state depends on whether the tunneling or the interactions dominate (see section 1.2.3), that is, it depends on the ratio $J/U$. The tunneling amplitude, $J$, is related to the height of the Wannier wave functions, and decreases exponentially with the lattice depth $V_\perp$. On-site interaction energies $U$, however, are related to the width of the Wannier functions and increase slowly with $V_\perp$. This allows us to tune the ratio $J/U$ over several orders of magnitudes by only changing the power of the lattice beams (see figure 2.11).

As pointed in section 1.2.3, a first experimental signature of this transition is the disappearance of interference peaks as one increases the lattice depth (Greiner et al. 2002b). Indeed, the existence of diffraction peaks is linked to the presence of a significant amount of atoms within a well-defined momentum class. The distribution in TOF reflects the *in situ* momentum distribution [see Gerbier et al. (2008) or appendix A]: $\mathcal{N}(\boldsymbol{k}) = \langle \hat{n}(\boldsymbol{k}) \rangle = \langle \hat{\Phi}^\dagger(\boldsymbol{k}) \hat{\Phi}(\boldsymbol{k}) \rangle$, with $\hat{\Phi}(\boldsymbol{k})$ the Fourier transform of the field operator. In the lattice, it reads:

$$\hat{\Phi}(\boldsymbol{k}) \propto \int \left( \sum_{j=1}^{L} w_\perp(\boldsymbol{\rho} - \boldsymbol{\rho}_j)\, \hat{a}_j \right) \mathrm{e}^{-\mathrm{i}\boldsymbol{k}\cdot\boldsymbol{\rho}}\, \mathrm{d}^2\rho = \tilde{w}_\perp(\boldsymbol{k}) \sum_{j=1}^{L} \mathrm{e}^{-\mathrm{i}\boldsymbol{k}\cdot\boldsymbol{\rho}_j} \hat{a}_j, \tag{2.18}$$

with $\tilde{w}_\perp(\boldsymbol{k})$ the Fourier transform of the Wannier function. The *in situ* momentum distribution can then be written as $\mathcal{N}(\boldsymbol{k}) = \mathcal{W}_\perp(\boldsymbol{k})\mathcal{S}(\boldsymbol{k})$, where $\mathcal{W}_\perp(\boldsymbol{k}) = |\tilde{w}_\perp(\boldsymbol{k})|^2$ is a smooth envelope function and $\mathcal{S}(\boldsymbol{k})$ the *structure factor* defined as:

$$\mathcal{S}(\boldsymbol{k}) = \sum_{i,j=1}^{L} \mathrm{e}^{\mathrm{i}\boldsymbol{k}\cdot(\boldsymbol{\rho}_i - \boldsymbol{\rho}_j)} \langle \hat{a}_i^\dagger \hat{a}_j \rangle. \tag{2.19}$$

Note that $S(\boldsymbol{k})$ is just the Fourier transform of the first-order correlation function $g(i,j) = \langle \hat{a}_i^\dagger \hat{a}_j \rangle$ (Naraschewski et al. 1999) introduced in section 1.2.3. The structure factor determines then the shape of the interference pattern, which characterizes the phase coherence along the lattice. The two equilibrium phases of the Bose-Hubbard Hamiltonian, can then be distinguished using the interference pattern (Zwerger 2003; Bloch et al. 2008):

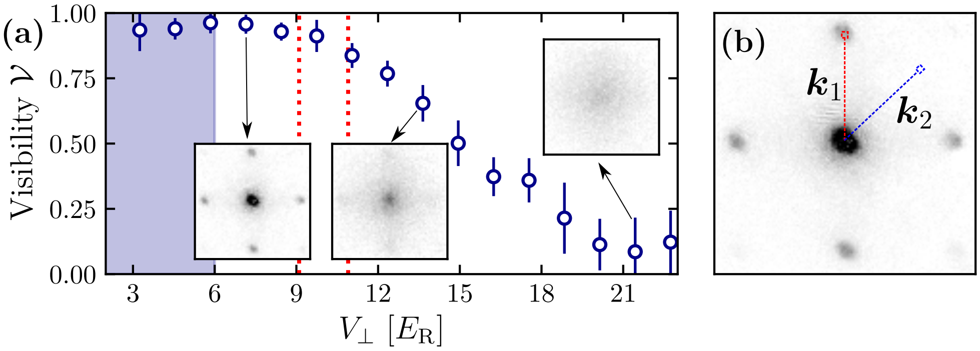

**Figure 2.12** – **(a):** Experimental signature of the superfluid to Mott insulator transition. The data shows how the measured visibility decays as the lattice depth is increased. This is seen in absorption pictures after TOF through the vanishing of the interference peaks (insets). The blue shaded region shows the region in which the Bose-Hubbard regime does not apply. The red dotted lines correspond to the depths at which the transition to the insulating phase is expected for $\bar{n} = 1$ and for $\bar{n} = 2$ in a 2D system. **(b):** Methodology to extract the visibility (see text): The maximum density is measured performing a pixel-sum centered at the interference peak (red square). The minimum density is extracted by a pixel sum along a diagonal at the same distance (blue square).

1. In the deep superfluid regime, with $J \gg U$, we have $g(i,j) = \alpha_i^* \alpha_j \simeq \bar{n}$. Phase coherence extends then over the whole lattice and:

   $$\mathcal{S}_\mathrm{SF}(\boldsymbol{k}) = \bar{n} \sum_{i,j=1}^{L} \mathrm{e}^{\mathrm{i}\boldsymbol{k}\cdot(\boldsymbol{\rho}_i - \boldsymbol{\rho}_j)}. \tag{2.20}$$

   All the terms of the sum are then added coherently, and the sum vanishes for all $\boldsymbol{k}$ except in the privileged directions for which $\boldsymbol{k} \cdot (\boldsymbol{\rho}_i - \boldsymbol{\rho}_j) = 2\pi m$, with $m \in \mathbb{Z}$ (i.e. when $\boldsymbol{k}$ is a reciprocal lattice vector $2\boldsymbol{k}_\mathrm{L}$), where sharp peaks appear. These peaks are usually referred to as *Bragg peaks* in analogy to the diffraction experiments performed in crystallography (Ashcroft et al. 1976).

2. Deep in the Mott insulator phase, with $U \gg J$, we have $g(i,j) \simeq n_0\, \delta_{ij}$, with $\delta_{ij}$ the Kronecker delta. Phase coherence is restricted to $i = j$, so:

   $$S_\mathrm{MI}(\boldsymbol{k}) = \sum_{i=1}^{L} n_0 = L n_0 = N, \tag{2.21}$$

   which is featureless.

We have observed this transition experimentally, the result is shown in figure 2.12(a), where we plot the visibility of the interference peaks as a function of the lattice depth. Each measurement corresponds to the average of 3 independent images. The visibility $\mathcal{V}$ is defined as proposed in Gerbier et al. (2005):

$$\mathcal{V} = \frac{\mathcal{N}(\boldsymbol{k}_1) - \mathcal{N}(\boldsymbol{k}_2)}{\mathcal{N}(\boldsymbol{k}_1) + \mathcal{N}(\boldsymbol{k}_2)}, \tag{2.22}$$

where $\boldsymbol{k}_1 = (0, 2k_\mathrm{L})$ corresponds to the center of the second Brillouin zone (i.e. at the diffraction peak position) and $\boldsymbol{k}_2 = (\sqrt{2}k_\mathrm{L}, \sqrt{2}k_\mathrm{L})$ is taken along a diagonal at the same distance [see figure 2.12(b)]. By defining visibility in this way, only the interference term $\mathcal{S}(\boldsymbol{k})$ matters in the calculation of the visibility, canceling out the contribution of $\mathcal{W}_\perp(\boldsymbol{k})$, assumed isotropic. In practice, we perform the pixel sum of each one of the four possible positions and their corresponding diagonals and then average.

The finite width of the peaks shown in the absorption images of figure 2.12 is mainly due to the finite TOF (21 ms) under which these images are taken. In fact, the *real* structure factor after a TOF is [see appendix A]:

$$S(\boldsymbol{k}) = \sum_{i,j} \mathrm{e}^{\mathrm{i}[\boldsymbol{k}\cdot(\boldsymbol{r}_i - \boldsymbol{r}_j) - M(\boldsymbol{r}_j^2 - \boldsymbol{r}_i^2)/(2\hbar t)]}, \tag{2.23}$$

with $\boldsymbol{k} = M\boldsymbol{r}/(\hbar t)$ and the expression given in equation (2.19) corresponds to a *far field* approximation. Reaching the pure far field regime (which corresponds to neglect the quadratic terms in the phase of $S$) requires long TOFs (Gerbier et al. 2008; Toth et al. 2008) on the order of $t_\mathrm{FF} \gg m\ell_\mathrm{c}R_0/\hbar \simeq 300\,\mathrm{ms}$, with $R_0 \simeq \ell_\mathrm{c} \simeq 10\,\mu\mathrm{m}$ the size of the cloud and the coherence length in the superfluid regime. Such long free fall times are impracticable in almost all experimental setups and only recently have been reached combined with single-particle detection in the far field regime (Nogrette et al. 2015; Cayla et al. 2018). Interaction effects during TOF can also broaden the peaks, but their effect can be neglected. This is due to the fact that the lattice frequencies $\omega_\mathrm{lat} \propto (V_0 E_\mathrm{r})^{1/2}$ (around 10 kHz) are bigger than the on-site interaction energy $U/h$ (on the order of the kHz) and the ballistic regime is achieved in a few periods (see appendix A).

An important remark is that the disappearance of the interference peaks is just a signature of the superfluid to Mott insulator transition and not a direct proof. The featureless structure factor in equation (2.21) would also appear for a high temperature ensemble. Therefore, a key point is to check that the loss of coherence is not due to heating, or to a non-adiabatic ramping of the lattice. We have verified that this is not the case with the following experimental sequence: we prepare a system in the deep insulating regime and then ramp down the power of the lattice beams driving the system back to the superfluid regime in 10 ms. After this, we have seen the diffraction peaks reappear, which shows that the disappearance of coherence is a reversible effect.

### 2.2.4 Calibrating on-site energies: collapse and revival experiments

The precision to which one can calculate the on-site energy $U$ by using equation (1.45) is limited by the uncertainties of the parameters involved in the overlap integral $\int |w(\boldsymbol{r})|^4 \,\mathrm{d}^3r$, most of them obtained from single-particle arguments. An independent method to extract the on-site interaction is therefore desirable. The collapse and revival method (Greiner et al. 2002a), which only assumes that the system can be described by the Bose-Hubbard Hamiltonian in equation (2.12), can be used to this end.

This method consists in the following: We prepare the system in the superfluid regime, where each site is well described by a coherent state $|\alpha\rangle_k$. In this situation, the order parameter is $\langle \hat{a} \rangle \simeq \sqrt{\bar{n}}$, phase coherence extends along the whole lattice and sharp peaks appear in TOF. The lattice is then *quenched*: we ramp up the depth of the lattice fast enough (in 75 µs) so that tunneling does not have time to redistribute the atoms to the new potential. Therefore, right after the quench, the order parameter has not changed and long-range phase coherence is still present, and the system is still described by a coherent state:

$$|\alpha\rangle_j = \mathrm{e}^{-|\alpha_j|/2} \sum_{n=0}^{\infty} \frac{\alpha_j^n}{\sqrt{n!}} |n\rangle_j. \tag{2.24}$$

After the quench, the coherent state is no longer an eigenstate of the new Hamiltonian $\sum_k U \hat{n}_k (\hat{n}_k - 1)/2$. By quenching the lattice, one creates then a non-equilibrium situation where each site evolves independently during a time $t$:

$$|\alpha\rangle_j(t) = \mathrm{e}^{-|\alpha_j|/2} \sum_{n=0}^{\infty} \frac{\alpha_j^n}{\sqrt{n!}} \mathrm{e}^{\mathrm{i}Un(n-1)t/\hbar} |n\rangle_j. \tag{2.25}$$

The order parameter evolves in time as:

$$\langle \hat{a} \rangle (t_{\mathrm{hold}}) = \sqrt{\bar{n}} \exp\left[\bar{n}\left(\mathrm{e}^{-\mathrm{i}Ut_{\mathrm{hold}}/\hbar} - 1\right)\right]. \tag{2.26}$$

For short times, the dephasing of Fock states with different atom numbers leads to a vanishing order parameter in a time $t_{\mathrm{col}} = \hbar/(\sqrt{\bar{n}}U)$. Within the Gutwiller approximation, the vanishing of the order parameter directly implies the disappearance of the interference peaks observed in TOF [figure 2.13(a)], i.e., a clear signature that phase coherence is lost. However, after a time $t_{\mathrm{rev}} = h/U$, the phase shift acquired by each Fock state is a multiple of $2\pi$ and the initial state is recovered up to a non-important global phase. Consequently, global phase coherence is restored. This is seen in TOF absorption images by the revival of the interference pattern (Greiner et al. 2002a). We have performed this experiment by loading a superfluid in a lattice at $V_\perp = 5\,E_\mathrm{r}$ and $V_z = 27\,E_\mathrm{r}$. We then quench $V_\perp$ to $26\,E_\mathrm{r}$ in 75 µs. We let the atoms interact with the lattice for a time $t_{\mathrm{hold}}$. Then, abruptly, we switch off the lattice beams and image the atoms after TOF. The evolution of the visibility extracted from these images is plotted in figure 2.13(b) for different interaction times. A model-free fit is performed by a sum of equidistant Gaussians. This allows us to account for the observed damping, which is a consequence of the residual confinement and does not modify the extracted value of $U$ (the error committed in assuming $U$ uniform along the lattice is smaller than 1%). The time at which the interference pattern reappears allows us to extract the on-site interaction energy $U = h \times 1475(25)$ Hz.

### 2.2.5 Noise-correlation experiments

In this section we perform an analysis of density noise-correlations of Mott insulators imaged after TOF. As predicted by Altman et al. (2004) and experimentally shown in Fölling et al. (2005) the apparently *featureless* density distribution from equation (2.21) still contains information that one can extract from noise analysis.

In the previous section, we argued that the TOF density distribution is related to the *in situ* momentum distribution. Density correlations in time of flight will then be given

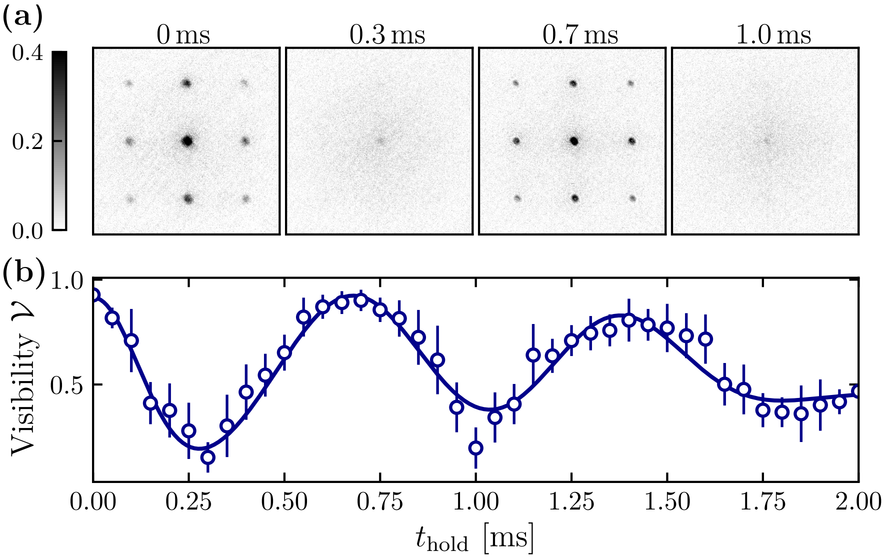

**Figure 2.13** – Collapse and revival experiment. Atoms are first prepared in the superfluid regime with $V_\perp \simeq 5\,E_\mathrm{r}$ and $V_z \simeq 27\,E_\mathrm{r}$. The horizontal lattice is then quenched to $V_\perp \simeq 26\,E_\mathrm{r}$ and the atoms are let to evolve. **(a):** Absorption images after TOF of the atoms after having evolved for a time $t_{\mathrm{hold}}$ in the quenched lattice. **(b):** Visibility of the interference peaks extracted from the absorption images for different evolution times $t_{\mathrm{hold}}$. The revival time of the visibility is associated to the on-site interaction energy (see text). We fit a periodic sum of Gaussians to the data to extract this time and we infer $U = h \times 1475(25)$ Hz. Figure adapted from Bouganne et al. (2017).

by $\langle \hat{n}(\boldsymbol{\rho})\hat{n}(\boldsymbol{\rho}')\rangle \propto \langle \hat{n}(\boldsymbol{k})\hat{n}(\boldsymbol{k}')\rangle$. These correlations can be related to *in situ* second-order correlations in momentum space[34]:

$$g_2(\boldsymbol{k},\boldsymbol{k}') = \frac{\langle \hat{n}(\boldsymbol{k})\hat{n}(\boldsymbol{k}')\rangle}{\langle \hat{n}(\boldsymbol{k})\rangle\langle \hat{n}(\boldsymbol{k}')\rangle} = 1 + \frac{1}{L^2}\sum_{i,j=1}^{L} \mathrm{e}^{-\mathrm{i}(\boldsymbol{k}-\boldsymbol{k}')\cdot(\boldsymbol{\rho}_i-\boldsymbol{\rho}_j)}. \tag{2.27}$$

The previous expression predicts that sharp peaks will appear in $g_2(\boldsymbol{k},\boldsymbol{k}')$ whenever $(\boldsymbol{k}-\boldsymbol{k}')\cdot(\boldsymbol{\rho}_i-\boldsymbol{\rho}_j) = 2\pi m$, with $m \in \mathbb{Z}$ (i.e., whenever $\boldsymbol{k}-\boldsymbol{k}'$ is equal to a reciprocal lattice vector). This indicates that Mott insulator states have long-range order in the second-order correlation function $g_2(\boldsymbol{k},\boldsymbol{k}')$. These kind of experiments have been interpreted in terms of the Hanbury-Brown and Twiss effect (Brown et al. 1956), and the observed peaks are sometimes referred to as *bunching peaks* in analogy.

We have performed this analysis following the procedure described in Fölling et al. (2005) on a set of 50 independent absorption images of a Mott insulator after a free expansion of 21 ms. In figures 2.14(a)-(b) we show an example of a single absorption image and a 1D cut through the center. As expected, the signal is apparently featureless. However, we see that density fluctuations are present. Through a noise-correlation analysis of such images, we can generate figure 2.14(c), where we see the appearance of several peaks at the positions predicted by equation (2.27). A strong peak is present

---

[34] see appendix A for a review of the derivation of this term.

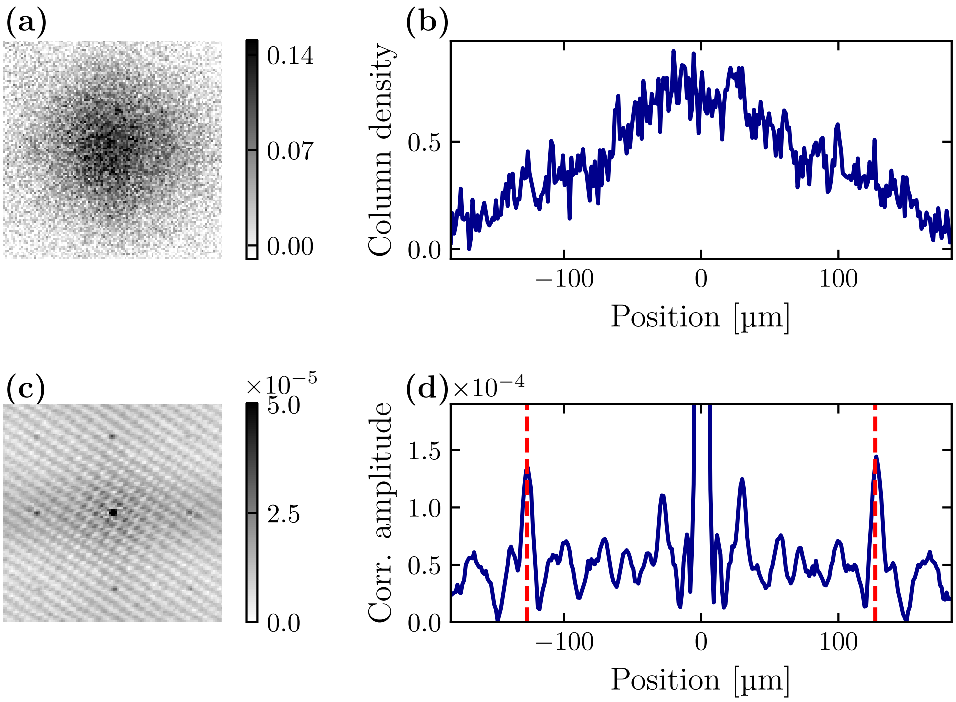

**Figure 2.14** – Noise correlations in a Mott insulator **(a):** Single absorption picture of a Mott insulator. **(b):** Cut through the center of the density profile where density fluctuations can be seen. **(c):** Density-density correlation function obtained following the procedure described in Fölling et al. (2005). **(d):** Cut through the center of the spatial noise correlation function. The red dashed lines correspond to the position of the peaks predicted by equation (2.27).

at $\boldsymbol{r} - \boldsymbol{r}' = 0$, which corresponds to an autocorrelation term not shown in equation (2.27) (see appendix A).

It is interesting to note that no *far field* approximation is needed to derive the phase term in equation (2.27) (see appendix A). The observed peaks should in principle be arbitrarily narrow and, as a consequence, the finite TOF cannot be responsible for the broadening of the peaks, which is actually due to the finite resolution of the imaging setup (Fölling et al. 2005). In the next section, we use these peaks to estimate the resolution of our imaging system.

### 2.2.6 Characterizing an imaging system with an optical lattice

#### Using a superfluid to extract the magnification

We can use the recorded images of a superfluid released from an optical lattice to extract the magnification of the optical system. Indeed, the density distribution observed in TOF $\mathcal{N}(\boldsymbol{\rho})$ reflects, up to a factor, the *in situ* momentum distribution $\mathcal{N}(\boldsymbol{k})$ with the substitution $\boldsymbol{\rho} = \boldsymbol{v}_{\mathrm{r}} t_{\mathrm{TOF}} = \hbar \boldsymbol{k} t_{\mathrm{TOF}}/M$. In the superfluid regime, equation (2.20) shows that a peak appears each time that $\boldsymbol{k} = 2\boldsymbol{k}_{\mathrm{L}}$, which, in TOF, corresponds to spatial separations:

$$\boldsymbol{\rho} - \boldsymbol{\rho}' = 2\frac{h}{\lambda M} t_{\mathrm{TOF}}. \tag{2.28}$$

The density distribution after TOF is subsequently recorded on a CCD thanks to an imaging setup that performs the transformation $\mathcal{N}(\boldsymbol{\rho}) \mapsto \mathcal{N}(\mathsf{x}_i, \mathsf{y}_i)$. In particular, a distance of $(\mathsf{x}_i - \mathsf{x}_j)$ pixels on the CCD represents a distance $\mathcal{M} \times (x - x')$ of the TOF distribution, with $\mathcal{M}$ the magnification of the setup. Each pixel on the CCD has an area $\mathcal{A} = d^2$, usually on the order of several $\mu\mathrm{m}^2$. Therefore, by locating the position of the peaks in an image, one can easily extract the magnification:

$$\mathcal{M} = \frac{\lambda M d(\mathsf{x}_i - \mathsf{x}_j)}{2ht_{\mathrm{TOF}}}. \tag{2.29}$$

The uncertainties on the wavelength $\lambda$ the mass $M$ and the pixel-size $p_{\mathrm{s}}$ are negligible, the experimental uncertainty on the TOF is on the order of $10^{-3}$ ms, and the center of the peaks can be pointed within a precision on the order of the pixel. All this combined allows us to extract a magnification with at least two or three significant digits.

### Using a Mott-insulator to extract the resolution

In an imaging system, the recorded distribution results from a convolution of the real density distribution with the point spread function (PSF) of the system, which takes into account the finite imaging resolution:

$$n_{\mathrm{CCD}}(x, y) = \int \mathrm{PSF}(\boldsymbol{x}) n(\boldsymbol{x} - \boldsymbol{x}')\, \mathrm{d}^2 x. \tag{2.30}$$

Let us now focus on a 1D-cut through one of the peaks. The shape of the peak is given by a Gaussian: $n_{\mathrm{peak}}(x) = A \exp\left[-x^2/(2\Delta x^2)\right]$, with $\Delta x$ the rms-width of the peak, infinitely narrow in principle. We then approximate the PSF by a Gaussian: $\mathrm{PSF}(x) = B \exp\left[-x^2/(2\sigma_x^2)\right]$, with $\sigma$ approximately the resolution of the imaging system. Because of the convolution, the measured peak on the CCD will also be a Gaussian of width $W_x = [\Delta x^2 + \sigma_x^2]^{1/2} \simeq \sigma_x$. The width of the recorded peaks is therefore directly linked to the resolution of the imaging setup.

Then, by using equation (2.29), and knowing the size of the pixel (6.45 µm) we extract a magnification $\mathcal{M} = 5.30$ by using figure 2.12(b). Finally, by analyzing one of the peaks in the noise-correlation analysis we can estimate the resolution of the setup. From a Gaussian fit performed on the cut through the center of one of such peaks allows us to extract a resolution $\sigma_x \simeq 4\,\mu\mathrm{m}$.

## 2.3 Summary and perspectives

In this chapter I have presented our experimental setup together with the main steps leading us to the reliable preparation of BECs and their subsequant adiabatic loading into an optical lattice. All this combined, allows us to prepare in a systematic way the ground state of the Bose-Hubbard Hamiltonian.

In the short term, we are planning several experimental upgrades. The first step we plan to implement is the loading of *only* a single plane of the 2D-lattice, instead of working with a pile of independent 2D-lattices. For this, we will first load the atoms in an intermediate trap. This trap consists of an optical lattice generated by a pair of beams at $\lambda = 532$ nm crossing with an angle, resulting in a lattice with a spacing

$d \simeq R_{\mathrm{TF}}/2 \simeq 4\,\mu\mathrm{m}$. Thanks to this large spacing, we will vetically compress the BEC, and then load a single vertical plane of the magic lattice.

We are also working to prepare a homogeneous system, i.e. to partially suppress the residual confinement of the lattice beams. We plan to achieve this by means of an auxiliary beam, properly tailored thanks to a spatial light modulator. We will use this correcting beam on top of the lattice ones so that the sum of the two leads to an approximately flat potential.

Finally, we will install a microscope objective. We have built a home-made objective that we will incorporate in the vertical axis to perform *in situ* images of the single plane. The tests performed so far with this microscope lead to a resolution on the order of 500 nm with light at $\lambda_{\mathrm{b}} = 400\,\mathrm{nm}$.

All of these future upgrades have been tested independently and are ready to be installed in the main experiment. Appart from this, we are considereng the possibility to implement in the long-term a *non-destructive* imaging setup, enhanced by a high-finesse cavity (Vallet et al. 2017). In a few words, the probe beam, largely detuned ($\delta_{\mathrm{L}} \gg \Gamma$), acquires a phase shift after going through the atomic cloud, where all the relevant information is stored. This signal can be arbitrarily amplified by means of a high-finesse cavity. Then, the probe beam is compared to a stable reference, from which the signal is read-out. Since these kind of measurements operate far from resonance, the number of scattered photons is quite low and the method is non-destructive. Moreover, these methods are supposed to drastically increase the signal-to-noise ratio.

# Part II

# Coherence and relaxation in few-body systems

# CHAPTER 3

# Single-particles in an optical lattice

Optical clock transitions constitute one of the main interest of alcaline-earth-like atoms. These transitions are free of spontaneous emission and have become an essential tool in many metrological applications, particularly in the community of frequency standards (Ludlow et al. 2015). They also offer a realistic experimental platform for precision measurement proposals, including schemes relying on clock interferometry to measure relativistic effects in quantum mechanics (Zych et al. 2011; Margalit et al. 2015) or as sensitive gravitational wave detectors (Graham et al. 2013). A few years ago, the relativistic time dilation between two aluminum ions, where one of them was submited to a harmonic velocity with an rms value on the order of 30 km/h, was measured by comparing frequency shifts on the clock transition on the order of $\delta f/f \simeq 10^{-15}$ (Chou et al. 2010).

Atoms with optical clock transitions have also become interesting for the study of many-body physics and as the main bricks for quantum simulation (Yi et al. 2008). For example, the SU($N$) symmetry obeyed by interacting atoms with $N = 2I+1$ internal components was observed in fermionic isotopes, for which the total spin $I > 1/2$, by performing spectroscopy in the clock transition (Scazza et al. 2014). This symmetry emerges because of the decoupling of the nuclear spin and the electronic orbital degrees of freedom (Gorshkov et al. 2010; Cazalilla et al. 2014), and such systems are good candidates for the simulation of the Kondo effect (Foss-Feig et al. 2010). Atoms featuring optical clock transitions are also well-suited for the emulation of artificial magnetism in optical lattices (Gerbier et al. 2010; Livi et al. 2016) and as the elementary pillars of quantum information protocols (Gorshkov et al. 2009; Daley 2011).

Many of these applications for quantum simulation rely on the coupling between the internal and the external degrees of freedom, a coupling provided by the recoil of the atom upon the absorption of a photon. When performing high precission spectroscopy measurements, however, it is better to decouple the external dynamics and drive the internal dynamics alone (Hu et al. 2017). This chapter and the following two are devoted to the dynamics of ultracold bosons driven on the clock transition in different experimental situations. In these chapters, I will present a study on the coherent dynamics of an ultracold quantum gas of ytterbium driven in the clock transition in different situations. These studies allowed us to identify some of the mechanisms, either technical or physical, that compete against this coherent driving.

In this first chapter, I will focus on the simple situation in which the atomic motion is frozen in a deep lattice, and the dynamics is purely internal. I will first describe our experimental setup to drive the clock transition and image the metastable state, and then present a technique commonly used to enable the driving of such clock transitions, known as magnetic mixing. After this, I will recall some key concepts on matter-light interaction in a periodic potential. For deep enough lattices one reaches the so-called Lamb-Dicke regime. A major interest of this framework is that the effect of the photon recoil is suppressed. As we will see in chapter 4, this decoupling between motional states and internal states is essential to reveal the spectroscopic signal of interacting particles in a lattice that would otherwise hidden in the Doppler-broadened profile. Finally, I will discuss the mechanisms that compete against this coherent control and display a series of experiments that allow us to give an estimation on the coherence time of our coupling laser.

## 3.1 The clock laser: Experimental setup and locking technique

We now present the main details concerning the optical setup and the locking technique that we use to generate a source that is narrow and stable enough to address the clock transition. A thorough report on the characterization of the ultra-low expansion (ULE) cavity and the performance of the frequency lock can be found in the PhD thesis of Alexandre Dareau (Dareau 2015).

**Experimental setup.** A scheme of the setup is shown in figure 3.1. Light at $\lambda_{\mathrm{cl}} \simeq 578\,\mathrm{nm}$ is generated by sum frequency generation. To this end, we use the light issued from an amplified fiber laser[35] at 1030 nm and a Nd:Yag[36] laser at 1319 nm. These two sources deliver about 5 W and 200 mW, respectively, and are focused to about 40 µm inside a non-linear crystal[37] after which 65 mW of yellow light at $\lambda_{\mathrm{cl}} \simeq 578\,\mathrm{nm}$ are available. This light is sent to a first AOM that will be used as fast actuator in the frequency locking scheme. After this, part of the light is sent to an iodine spectroscopy setup used to calibrate the absolute frequency of the cavity (Dareau 2015). The rest is sent through an optical fiber to the experiment (see figure 3.1). Here, the optical beam is split again: Part of it is sent to another AOM, which shifts the frequency before sending the light to the science chamber. This is the frequency seen by the atoms and we shall refer to this wavelength as $\lambda_{\mathrm{L}}$ on the following. The rest of the light is used to lock the laser in frequency. We send the light through an optical fiber to an ULE high finesse cavity[38]. This cavity is isolated from the environment through several stages: (i) The cavity is placed inside a vacuum chamber with a vacuum level on the order of $1 \times 10^{-8}$ mbar. (ii) This chamber is clamped on top of a an anti-vibration platform[39] which (iii) lies inside a home-made wooden box with acoustic foam in it.

---

[35] Koheras BoostiK Y10, NKT Photonics.

[36] Mephisto, Coherent.

[37] ppLN (*periodically poled lithium niobate*) crystal from Coherent.

[38] ATF-6301, Advanced Thin Films

[39] Nano-K 50 BM-10, Minus K Technology.

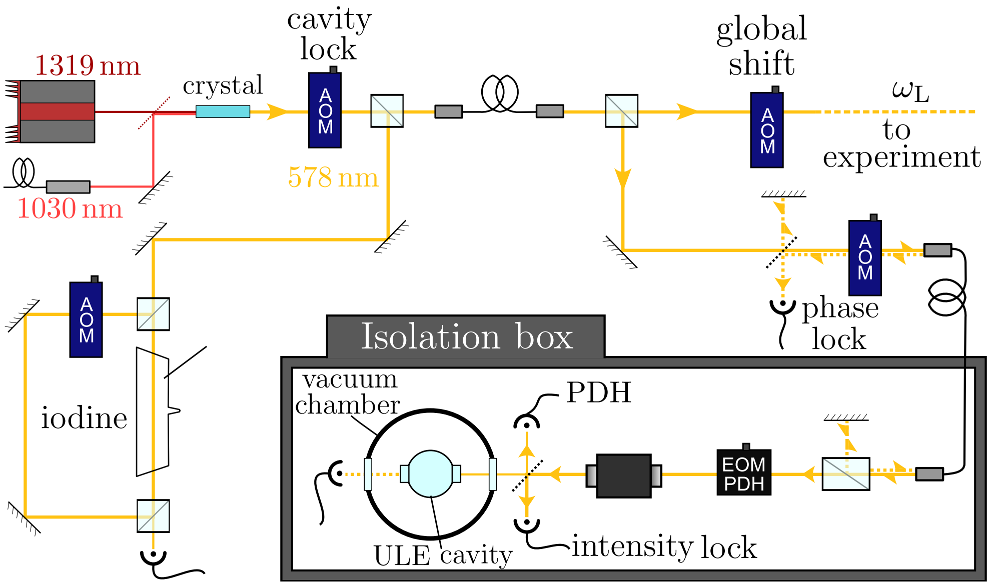

**Figure 3.1** – Schematics of the clock laser optical chain. Light at $\lambda_{\mathrm{cl}} = 578\,\mathrm{nm}$ is generated by frequency sum in an optical crystal and then split in two parts: One part is sent to an iodine spectroscopy setup, which is used to determine the absolute frequency of the ULE cavity. The rest is sent to the experiment table where it is again split in two paths. One is used to probe the atoms and the other is sent to an ULE cavity to frequency lock the laser. Part of this beam is previously sent back to the main optical table to correct for phase shifts in the optical fiber. Adapted from Dareau (2015)

Finally, (iv) the whole is placed into a sound-proof isolation box[40] (see figure 3.1). The heat generated inside the box is extracted thanks to a stream of regulated water at 19 °C circulating inside a metallic plate.

Once the light coming from the optical table reaches this platform, a small part of it is retro-reflected and sent back to the main optical table. Here it is used as the second arm of a Michelson interferometer, that we use to perform a phase lock. This is done in order to correct for phase changes inside the fiber mainly due to thermal or mechanical perturbations. Part of the remaining light is used for intensity stabilization before the ULE cavity and the rest is sent to the ULE cavity to perform the frequency lock.

**ULE cavity** The cavity consists of two high-reflectivity mirrors, a flat one and a concave one forming a Fabry-Perot cavity. These mirrors are separated of $L = 47.6\,\mathrm{cm}$ by a spherical ULE material. The ULE material is hold by two supports into a thermal shield, which is temperature regulated thanks to a Peltier element inside a feedback loop[41]. The finesse of the cavity $\mathcal{F} \simeq 257000$ has been deduced from the measurement of the cavity ring-down time $\tau_{\mathrm{rd}} \simeq 13\,\mu\mathrm{s}$ and the free spectral range $\Delta_{\mathrm{FSR}} = 2\pi \times 3\,144\,366(2)\,\mathrm{kHz}$ (Dareau et al. 2015) in good agreement with the specifications. The full width at half maximum of the cavity resonances is then $\delta\omega_{\mathrm{cav}} = \Delta_{\mathrm{FSR}}/\mathcal{F} \simeq 2\pi \times 12\,\mathrm{kHz}$.

---

[40] Built by the Keoda society

[41] LFI-3751. Wavelength Electronics

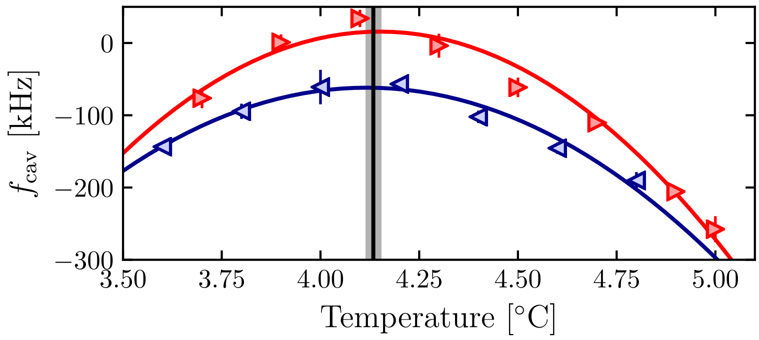

**Figure 3.2** – Determination of the zero-crossing point of the cavity. Two curves were taken, one by increasing the temperature (red curve, arrows pointing to the right) and one decreasing it (blue curve, arrows pointing to the left). The vertical line corresponds to the zero-crossing temperature $T_0 = 4.13(2)$ °C and the shaded region indicates one standard deviation.

The absolute frequency of the cavity is determined by comparing the free spectral range to the saturated absorption spectrum of the iodine molecule [see figure 3.1]. Iodine displays a resonance at about 10 GHz from the ytterbium clock transition. This allows us to track down the clock transition within a range of 40 kHz, accurate enough to subsequently locate in a reasonable amount of time the atomic $^{174}$Yb resonance by performing spectroscopy on a cold atomic cloud(Dareau 2015).

Finally, one of the main interests of ULE materials is the presence of a temperature for which a *zero-crossing point* in its dilation coefficient is reached. Here, temperature fluctuations have a much smaller effect on the length of the cavity and thus, on the resonance frequency. We have found this temperature experimentally at $T_0 \simeq 4.13(2)$ °C [see figure 3.2]. From the curvature $\kappa \simeq -2\pi \times 350\,\mathrm{kHz/K}^2$ we can infer the sensitivity to temperature fluctuations of the resonance frequency $\Sigma(T) \simeq 2\kappa(T - T_0)$ at a given temperature. We have measured the temperature stability of the thermal shield with an available probe outside of the temperature servo loop. This measurement shows fluctuations on the order or below a miliKelvin. We can estimate the impact on the frequency if we miss the zero-crossing by one standard deviation, i.e., if we set our temperature at 0.02 °C from $T_0$ [see shaded region in figure 3.2]. In this case $\Sigma \simeq 14\,\mathrm{kHz/K}$ and the measured temperature fluctuations translate into frequency variations with an rms smaller than 15 Hz. Nevertheless, despite the stability of the temperature of the cavity, we observe a dependence of the resonance frequency on the ambient temperature of the laboratory. In a few words, there are two additional factors that influence the resonance frequency: (i) The first one is the aging of the ULE material, which slowly changes the length of the cavity and thus its resonance frequency, translating into a slow drift which is constant from day to day if the surroundings of the cavity do not undergo any temperature change. We observe that the slope of this slow drift changes if the temperature of the surroundings of the cavity is modified, although with some time lag [we show this in figure 3.3, where we show the resonance frequency of the cavity during the last 6 years. From this we measure a drift of $\simeq -2.35\,\mathrm{kHz/day}$ over the last 3 years]. (ii) On top of this drift we also remark faster frequency deviations during the day, with a much stronger dependence on temperature. Due to these last fast drifts, we need to acquire several spectra per day in order to keep the cavity on resonance with the clock transition. A phenomenological model taking these aspects

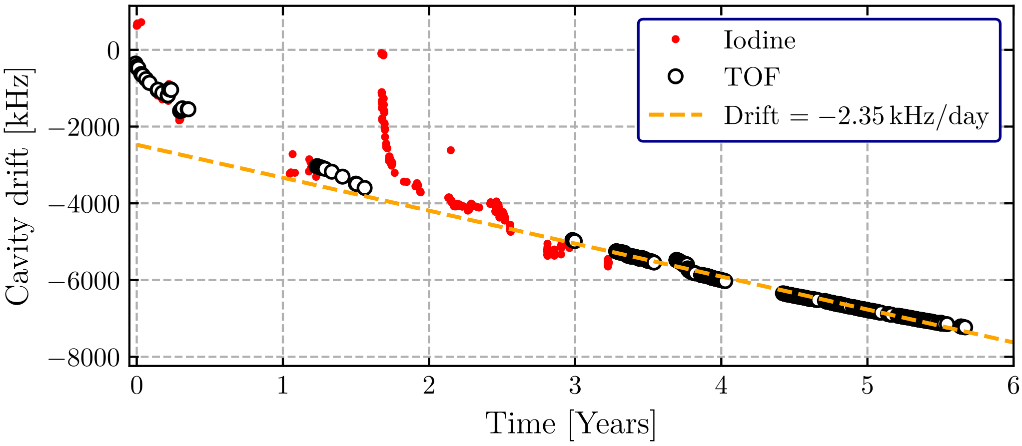

**Figure 3.3** – Drift of the ULE cavity with respect to $^{174}$Yb clock transition during the last 6 years. The black empty dots correspond to the measurement of the resonance of atoms in free space. The red dots are measurements using the iodine spectroscopy setup. The dashed line is a linear fit to the data over the last 3 years, which yields a slow drift of the resonance frequency of $-2.35\,\mathrm{kHz/day}$.

into account is presented in the PhD thesis of Raphaël Bouganne (Bouganne 2018).

**Locking technique.** The technique we use to lock the cavity is the Pound-Drever-Hall (PDH) technique (Drever et al. 1983). This technique relies on the measurement of the intensity reflected from the cavity, which arises from the interference between the part of the field directly reflected and the intra-cavity field transmitted by the in-coupling mirror[42]. The reflected intensity vanishes in resonance for a perfect resonator. In order to obtain an error signal, an EOM is located prior to the cavity. This EOM generates sidebands at $\Omega_{\mathrm{sb}} = 2\pi \times 4\,\mathrm{MHz}$. The frequency of these sidebands is much larger than the cavity bandwidth, $\Omega_{\mathrm{sb}} \gg \delta\omega_{\mathrm{cav}}$, and they are thus completely reflected. A fast photodiode[43] measures the beat between these sidebands and the reflected field generated by the carrier. The signal is then sent to a commercial lockbox[44] where it is demodulated and an error signal with a slope on the order of $1\,\mathrm{mV/Hz}$ subsequently used to lock the cavity is generated. The locking signal is split in two parts: a *fast* component sent to the driver[45] of the AOM right after the doubling crystal (see figure 3.1) and a *slow* one that is integrated another time and sent to a piezoelectric actuator located inside the Nd:Yag laser.

---

[42] In high finesse cavities, it is better to perform the lock on the reflection rather than on its transmission. This is due to the fact that the transmission field consists only of the leaking of the intracavity field. Thus, in order to observe the effect of a frequency variation, the intra-cavity field needs a time on the order of the cavity ring-down to build up and the bandwith is limited to a fraction of $\delta\omega_{\mathrm{cav}}$. However, the part of the field directly reflected from the cavity follows this change instantaneously.

[43] PDA8A, Thorlabs

[44] D2-125, Vescent Photonics

[45] E4400B, Agilent Technologies.

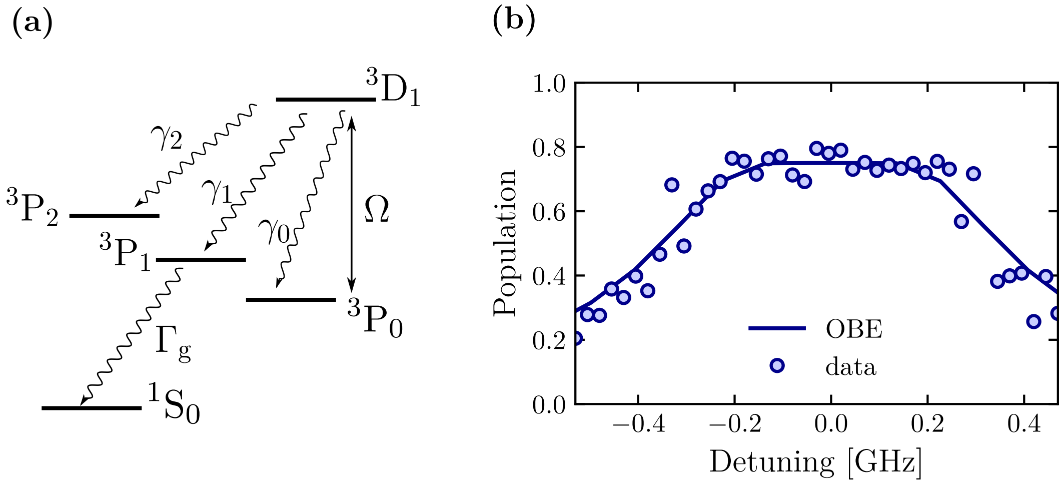

**Figure 3.4** – **(a):** Schematics of the energy levels involved in the repumping of the metastable state. The branching ratios are $b_0 = 0.6$, $b_1 = 0.3$, $b_2 = 0.1$. Typical spectrum of the repumping transition (blue dots) and the prediction by solving the optical Bloch equations (solid blue line) for a system equivalent to the one shown in **(a)** and the following parameters: $P = 5\,\mathrm{mW}$, $w_0 = 500\,\mu\mathrm{m}$ and $t_{\mathrm{rep}} = 500\,\mu\mathrm{s}$.

## 3.2 Imaging the metastable state

### Method

Atoms in the metastable $^3$P$_0$ state are not imaged directly. Instead, we repump them to the ground state $^1$S$_0$ and they are subsequently imaged through absorption imaginig on the $^1$P$_1$ transition. We achieve this by first transferring atoms in $^3$P$_0$ to another energy level at $\lambda_{\mathrm{rep}} = 1388.8\,\mathrm{nm}$ from the metastable state: 4f$^{14}$ 6s6 d − $^3$D$_1$. This state has a finite lifetime $\tau_{\mathrm{rep}} \simeq 380\,\mathrm{ns}$, i.e. $\Gamma_{\mathrm{rep}} = 2\pi \times 419\,\mathrm{kHz}$ (Bowers et al. 1996) and thus, atoms driven into this level decay back to the $^3$P$_J$ manifold with branching ratios $[b_i = \gamma_i/\Gamma_{\mathrm{rep}}]$: $b_0 = 0.6$, $b_1 = 0.3$ and $b_2 = 0.1$ (Bowers et al. 1996). The $^3$P$_0$ and $^3$P$_2$ states are metastable and thus, atoms fallen into $^3$P$_2$ exit the repumping cycle and are not detected. However, atoms ending in $^3$P$_1$ decay through spontaneous emission on the ground state at a rate $\Gamma_g$ [see figure 3.4(a)]. In figure 3.4(b) we show the measured and expected line shape for our experimental parameters: We send to the atoms approximately $5 - 6\,\mathrm{mW}$ of light at 1389 nm focused to 500 µm for a duration of $t_{\mathrm{rep}} = 500\,\mu\mathrm{s}$. The expected line shape is computed by solving the optical Bloch equations (OBE) for the system shown in figure 3.4(a). The OBE can be written as follows: The populations obey

$$\dot{P}_0 = \gamma_0 P_{\mathrm{rep}} - \Omega v, \tag{3.1}$$

$$\dot{P}_1 = \gamma_1 P_{\mathrm{rep}} - \Gamma_g P_1, \tag{3.2}$$

$$\dot{P}_2 = \gamma_2 P_{\mathrm{rep}}, \tag{3.3}$$

$$\dot{P}_{\mathrm{rep}} = -\Gamma_{\mathrm{rep}} P_{\mathrm{rep}} + \Omega v, \tag{3.4}$$

$$\dot{P}_g = \Gamma_g P_1, \tag{3.5}$$

where $P_0, P_1$ and $P_2$ are the populations of the $^3$P$_J$ manifold, with $J = 0, 1, 2$, respectively, whereas $P_g$ and $P_{\mathrm{rep}}$ are the populations of $^1$S$_0$ and $^3$D$_1$, respectively. The

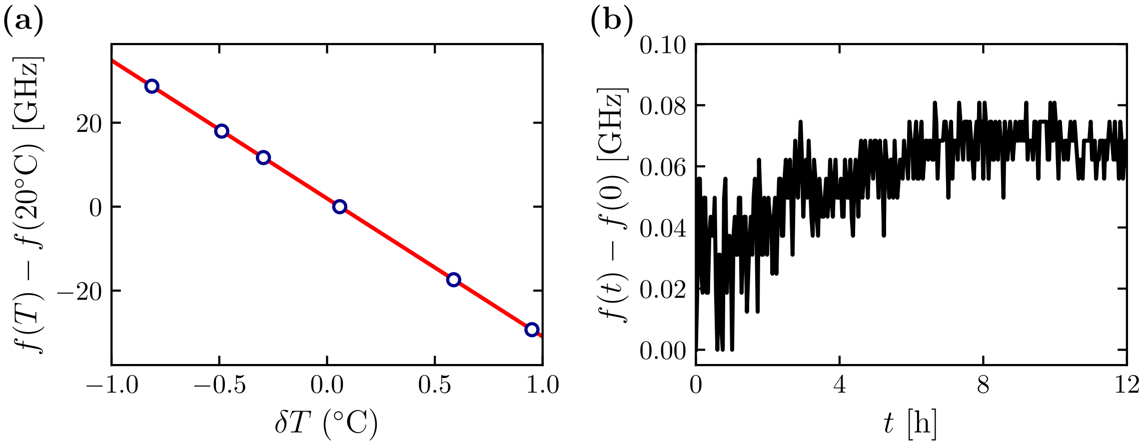

**Figure 3.5** – **(a):** Frequency dependence of the repumping laser on temperature (blue points). The fit (solid line) gives a temperature sensitivity of 33 GHz/°C. **(b):** Frequency stability of the repumping laser in working conditions (see text).

coherences between $^3\mathrm{P}_0$ and $^3\mathrm{D}_1$ are included in $v$ and $u$, which evolve as

$$\dot{v} = -\delta u - \frac{\Gamma_{\mathrm{rep}}}{2} v - \frac{\Omega}{2}(P_{\mathrm{rep}} - P_0), \tag{3.6}$$

$$\dot{u} = \delta v - \frac{\Gamma_{\mathrm{rep}}}{2} u. \tag{3.7}$$

We noted $\Omega$ the Rabi frequency and $\delta$ the detuning between $^3\mathrm{P}_0$ and $^3\mathrm{D}_1$.

The comparison of the OBE to the data agrees well, and we extract from this a repumping efficiency for the transfer of atoms in the metastable state to the ground state on the order of $\eta_{\mathrm{rep}} \simeq 0.8$. The resonance is broad and features a flat top on a frequency span of 400 MHz.

### Experimental setup

An interesting feature of the spectra shown in figure 3.4(b) is its plateau on the order of a several hundred MHz. This is of crucial importance for us because the repumping laser is not easily frequency locked[46]. We thus need a source that is passively stable enough, on the order of 100 MHz per day. The light at $\lambda_{\mathrm{rep}} = 1389$ nm is generated by a laser diode[47]. The laser diode is installed into a butterfly mount[48], and we use a current and temperature driver with a stability on the order of a few miliKelvin[49], which should be good enough since the measured dependency of the output frequency on temperature is on the order of 30 GHz/°C [see figure 3.5(a)]. Still, we remarked that the small temperature fluctuations and thermal drifts (a fraction of a degree per day) in the lab were leading to frequency variations with an amplitude on the order or larger than 500 MHz per day. To reduce this effect, we isolated the butterfly mount by putting it inside an aluminum shield with a Peltier element that passively maintains

---

[46] For this, one should first be able to transfer a substantial amount of atoms to the metastable $^3\mathrm{P}_0$ state and then perform saturated absorption spectroscopy on the $^3\mathrm{P}_0 \rightarrow {}^3\mathrm{D}_1$ transition.

[47] NLK1E5GAAA. NTT Electronics Corporation.

[48] LM14S2. Thorlabs.

[49] ITC510. Thorlabs.

the container at 12 °C. With this, we measure frequency drifts below 100 MHz per day [see figure 3.5(b)] and, in practice, we do not have to perform scans to find the resonance frequency for several months.

Once the laser wavelength is stable enough, we just need to adjust it to the atomic resonance frequency with an accuracy on the order of the GHz, so that we can then find the atomic line in a reasonable amount of time. This accuracy is usually within the specifications of commercial wavelength meters. However, the repumper wavelength is beyond the spectral bandwidth of our wavemeter[50]. We thus frequency double the repumper in a single-pass crystal to obtain a few µW of light at 695 nm, which is within the bandpass of the wavemeter. We then send this light into our wavelength meter, and use this frequency doubled light as our frequency reference.

## 3.3 Driving the clock transition

In this section we present the methods that allow us to excite the clock transition ($^1\mathrm{S}_0 \rightarrow {}^3\mathrm{P}_0$) from $^{174}$Yb . We first present the technique, known as *magnetic mixing* (Taichenachev et al. 2006) and then our experimental setup.

### Magnetic mixing

In principle, it is not possible to drive the $^1\mathrm{S}_0 \rightarrow {}^3\mathrm{P}_0$ transition since it would violate parity and spin conservation. This transition is thus strictly electric-dipole forbidden for the bosonic isotopes [see section 2.1.1]. However, Taichenachev et al. (2006) proposed a method to weakly enable the transition. The idea consists in using a static magnetic field $\boldsymbol{B}$ to couple a small fraction of the $^3\mathrm{P}_1$ state to the $^3\mathrm{P}_0$ state. Since the $^1\mathrm{S}_0 \rightarrow {}^3\mathrm{P}_1$ line is weakly allowed, the perturbed state becomes accessible too. This technique was demonstrated experimentally for $^{174}$Yb atoms in a lattice in Barber et al. (2006).

**Mixing $^3\mathrm{P}_1$ and $^3\mathrm{P}_0$.** The action of a static magnetic field $\boldsymbol{B} = B\boldsymbol{u}_z$ is described by the Hamiltonian $\hat{H}_B = -\hat{\boldsymbol{\mu}} \cdot \boldsymbol{B}$, with $\hat{\boldsymbol{\mu}}$ the magnetic dipole operator. At first order in perturbation theory, the ground state $|^1\mathrm{S}_0\rangle$ is not modified but the $|^3\mathrm{P}_0\rangle$ state becomes:

$$|^3\mathrm{P}_0{}'\rangle \simeq |^3\mathrm{P}_0\rangle + \sum_{j \neq {}^3\mathrm{P}_0} \frac{\langle \phi_j | -\hat{\boldsymbol{\mu}} \cdot \boldsymbol{B} | ^3\mathrm{P}_0\rangle}{E_{^3\mathrm{P}_0} - E_j} |\phi_j\rangle \simeq |^3\mathrm{P}_0\rangle + \frac{\Omega_\mathrm{B}}{\Delta} |^3\mathrm{P}_1\rangle, \tag{3.8}$$

with $\Delta = \omega_{^3\mathrm{P}_1} - \omega_{^3\mathrm{P}_0} \simeq 2\pi \times 21\,\mathrm{THz}$. The fraction of $^3\mathrm{P}_1$ in the perturbed state can be controlled via the magnetic field. The coupling strength, $\hbar\Omega_\mathrm{B}$, is given by (Taichenachev et al. 2006):

$$\hbar\Omega_\mathrm{B} = \langle ^3\mathrm{P}_0 | \hat{H}_B | ^3\mathrm{P}_1\rangle = \sqrt{\frac{2}{3}}\mu_\mathrm{B} B, \tag{3.9}$$

with $\mu_\mathrm{B} \simeq 9.27\,\mathrm{J/T}$ the Bohr magneton.

---

[50] WS6, High Finesse.

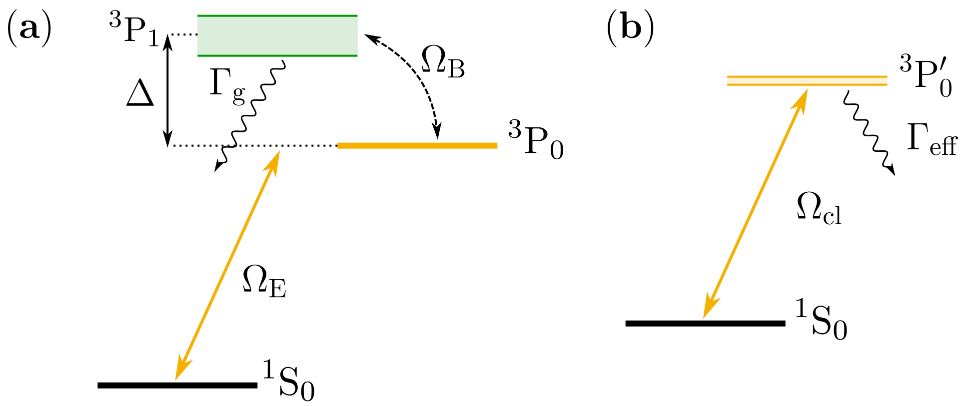

**Figure 3.6** – Magnetic mixing technique. **(a):** The bare atomic states $^3\mathrm{P}_0$ and $^3\mathrm{P}_1$ are coupled by the action of a static magnetic field $B$, with a coupling strength $\Omega_\mathrm{B}$. Since the $^3\mathrm{P}_1$ state has a decay rate $\Gamma_\mathrm{g}$, the new perturbed state, which consists mostly of the $^3\mathrm{P}_0$ state, can be coupled to the ground state by a laser, with a coupling strength $\Omega_\mathrm{E}$. **(b):** Effective two-level system. The coupled system is equivalent to a two-level atom in which the ground state $^1\mathrm{S}_0 \equiv g$ is coupled to the metastable excited state $^3\mathrm{P}_0{}' \equiv e$ with an effective strength $\Omega_\mathrm{cl} \propto \Omega_\mathrm{B}\Omega_\mathrm{E}$. Because of the magnetic mixing, the metastable state also acquires a finite width $\Gamma_\mathrm{eff}$ (negligible in practice).

**Effective Rabi frequency and linewidth.** We can now address the transition with a laser $\boldsymbol{E}_\mathrm{cl}$ resonant with the $^3\mathrm{P}_0$ transition. The coupling is given by:

$$\Omega_\mathrm{cl} = \langle {}^3\mathrm{P}_0{}' | \hat{\boldsymbol{d}} \cdot \boldsymbol{E}_\mathrm{cl} | {}^1\mathrm{S}_0 \rangle = \frac{\Omega_\mathrm{B}}{\Delta} \langle {}^3\mathrm{P}_1 | \hat{\boldsymbol{d}} \cdot \boldsymbol{E}_\mathrm{cl} | {}^1\mathrm{S}_0 \rangle. \tag{3.10}$$

Here $\hat{\boldsymbol{d}}$ is the electric dipole operator for the $^1\mathrm{S}_0 \rightarrow {}^3\mathrm{P}_1$ transition $\Omega_\mathrm{E}$ (Cohen-Tannoudji et al. 1992), related to the Rabi frequency by:

$$\Omega_\mathrm{E} = \sqrt{\frac{6\pi\Gamma_\mathrm{g} c^2}{\hbar\omega_\mathrm{g}^3}} \sqrt{I_\mathrm{cl}}. \tag{3.11}$$

with $\omega_\mathrm{g} = 2\pi c/\lambda_\mathrm{g}$ and $\Gamma_\mathrm{g}$, the frequency and linewidth of the intercombination transition, respectively, and $I_\mathrm{cl}$ the intensity of the electric field. Therefore, the clock transition can be addressed with an effective Rabi frequency:

$$\Omega_\mathrm{cl} = \frac{\Omega_\mathrm{B}\Omega_\mathrm{E}}{\Delta} = \alpha B \sqrt{I_\mathrm{cl}}, \tag{3.12}$$

with:

$$\alpha \simeq 2\pi \times 18.7 \, \frac{\mathrm{mHz}}{\mathrm{G}\sqrt{\mathrm{mW/cm}^2}}. \tag{3.13}$$

On the remaining, we will usually refer to the ground state $^1\mathrm{S}_0$ as $g$ and to the perturbed metastable excited state $^3\mathrm{P}_0{}'$ as $e$.

Note that the perturbed state also acquires a small effective linewidth, which leads to an spontaneous emission rate:

$$\Gamma_\mathrm{eff} \simeq \Gamma_\mathrm{g} \frac{\Omega_\mathrm{B}^2}{\Delta^2} = \gamma B^2, \tag{3.14}$$

with $\gamma = 2\pi \times 535\,\mathrm{pHz/G}^2$. This is usually completely negligible (see below).

**Differential light shift and quadratic Zeeman shift.** The presence of the magnetic field and the laser also leads to a shift of the resonance (Taichenachev et al. 2006). For the boson, the magnetic field causes a second order Zeeman shift which reads:

$$\delta_{\mathrm{B}} = -\beta B^2, \tag{3.15}$$

In addition, the probe itself induces a differential light shift given by:

$$\delta_{\mathrm{E}} = \kappa I_{\mathrm{cl}}. \tag{3.16}$$

The coefficients have been measured in atomic clocks and are $\beta = 2\pi \times 66\,\mathrm{mHz/G^2}$ and $\kappa = 2\pi \times 15\,\mathrm{mHz/(mW/cm^2)}$ (Barber et al. 2006; Barber et al. 2008). As we will see below, $\delta_{\mathrm{B}}$ is spatially uniform but $\delta_{\mathrm{E}}$ will depend on the shape of the beam driving the transition.

**Experimental parameters.** In the experiments presented in this thesis, the magnetic field is fixed at $B = 182\,\mathrm{G}$, which leads to a negligible spontaneous emission rate $\Gamma_{\mathrm{eff}}/(2\pi) \simeq 18\,\mu\mathrm{Hz}$. The probe consists of a Gaussian beam of peak intensity $I_{\mathrm{cl}} = 2P_{\mathrm{cl}}/(\pi w_{\mathrm{cl}}^2)$. The beam is focused on the atoms with a size of $w_{\mathrm{cl}} = 70\,\mu\mathrm{m}$ and the maximum power of the probe beam is $P_{\mathrm{cl}} = 18\,\mathrm{mW}$. We summarize the rest of parameters important for spectroscopy in table 3.1:

| **Magnitude** | **Value** |
|---|---|
| $\Omega_{\mathrm{cl}}/(2\pi)$ | 1650 Hz |
| $\delta_{\mathrm{B}}/(2\pi)$ | −2100 Hz |
| $\delta_{\mathrm{E}}/(2\pi)$ | 3500 Hz |

Table 3.1: Maximum values for the Rabi frequency, the Zeeman shift and the differential light shift for our experimental parameters: $B = 182\,\mathrm{G}$, $w_{\mathrm{cl}} = 70\,\mu\mathrm{m}$ and $P = 18\,\mathrm{mW}$.

## 3.4 Atom-light coupling in a periodic potential

The interaction of an atom in the single particle state $|\Phi\rangle = |\Phi_{\mathrm{int}}\rangle|\Phi_{\mathrm{ext}}\rangle$ with a laser $\boldsymbol{E}_{\mathrm{cl}}(\hat{\boldsymbol{r}}) = \boldsymbol{E}_0 \mathrm{e}^{\mathrm{i}\boldsymbol{k}_{\mathrm{cl}}\cdot\hat{\boldsymbol{r}}}$ couples the internal degrees of freedom of the atom $|\Phi_{\mathrm{int}}\rangle$ and the external ones $|\Phi_{\mathrm{ext}}\rangle$. If we consider a dipole interaction described by $\hat{V}_{\mathrm{AL}} = -\hat{\boldsymbol{d}} \cdot \boldsymbol{E}_{\mathrm{cl}}(\hat{\boldsymbol{r}})$, the coupling strength between the states $|\Phi\rangle$ and $|\Phi'\rangle = |\Phi'_{\mathrm{int}}\rangle|\Phi'_{\mathrm{ext}}\rangle$ is given by:

$$\Omega_{\mathrm{L}}(\boldsymbol{r}) = \langle\Phi'_{\mathrm{int}}| - \hat{\boldsymbol{d}} \cdot \boldsymbol{E}_0|\Phi_{\mathrm{int}}\rangle \cdot \langle\Phi'_{\mathrm{ext}}|\mathrm{e}^{\mathrm{i}\boldsymbol{k}_{\mathrm{cl}}\cdot\hat{\boldsymbol{r}}}|\Phi_{\mathrm{ext}}\rangle. \tag{3.17}$$

The first term leads to the Rabi frequency $\Omega_{\mathrm{cl}}$ defined in equation (3.12) in the presence of a static magnetic field $\boldsymbol{B}$. The second term is a matrix element between motional states that we will discuss in the following.

### 3.4.1 Atoms in free space

We can first see how the coupling between internal and external states works for a free particle. The initial state is described by a plane wave $|g; \boldsymbol{p} = \hbar\boldsymbol{q}\rangle$. The absorption of

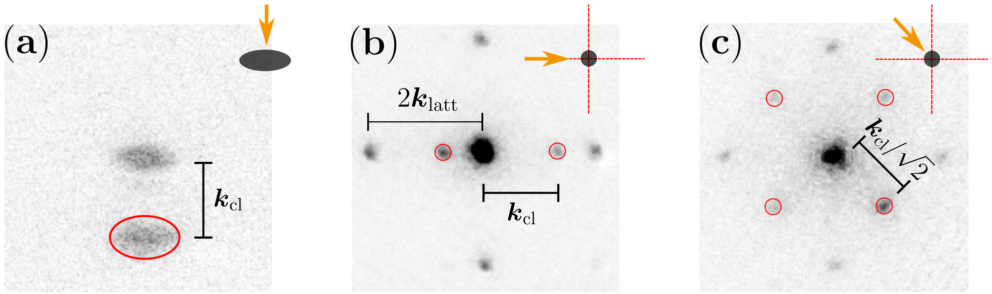

**Figure 3.7** – Coupling of the internal and external degrees of freedom. All images are recorded after a TOF of 21 ms and all situations correspond to $\pi/2-$pulses, i.e. half of the atoms are in the ground state and half in the excited state (red circles). **(a):** Atoms probed in free space. **(b):** Atoms released from an optical lattice at $V_\perp \simeq 6.5\,E_{\mathrm{r}}$ after being probed *in situ* by a laser propagating along one of the axis of the lattice. **(c):** Atoms released from an optical lattice at $V_\perp \simeq 6.5\,E_{\mathrm{r}}$ after being probed *in situ* by a laser propagating at 45° from the axis defined by the lattice.

a photon involves the following matrix element:

$$\langle \Phi'_{\mathrm{ext}} | \mathrm{e}^{\mathrm{i}\boldsymbol{k}_{\mathrm{cl}}\cdot\hat{\boldsymbol{r}}} | \Phi_{\mathrm{ext}} \rangle = \langle \boldsymbol{q}' | \boldsymbol{q} + \boldsymbol{k}_{\mathrm{cl}} \rangle = \delta_{\boldsymbol{q}+\boldsymbol{k}_{\mathrm{cl}}-\boldsymbol{q}'}, \tag{3.18}$$

which expresses momentum conservation. The only relevant state is thus $|\Phi'\rangle = |e; \boldsymbol{q} + \boldsymbol{k}_{\mathrm{cl}}\rangle$. The coupling strength in this case is the bare Rabi frequency $\Omega_{\mathrm{L}} = \Omega_{\mathrm{cl}}$. Moreover, due to energy conservation, the absorption frequency is shifted with respect to the bare frequency $\omega_0$ by the recoil frequency $\omega_{\mathrm{r}} = \hbar\boldsymbol{k}_{\mathrm{cl}}^2/(2M)$ and a Doppler shift contribution if $\boldsymbol{q} \neq 0$:

$$\hbar\omega_{\mathrm{L}} = \hbar\omega_0 + \frac{\hbar^2\boldsymbol{k}_{\mathrm{cl}}^2}{2M} + \frac{\hbar^2\boldsymbol{k}_{\mathrm{cl}}\cdot\boldsymbol{q}}{M}. \tag{3.19}$$

The coupling of internal and motional states can be seen experimentally by taking an image in TOF: In figure 3.7(a) we show a picture of a BEC in which half of the atoms have been transferred to the excited state. The pulse has been applied to an ensemble of atoms in free space and we see that the position after a TOF of those atoms transferred to the excited state is displaced by an amount $\boldsymbol{r} = \hbar\boldsymbol{k}_{\mathrm{cl}}t_{\mathrm{TOF}}/M$. By performing spectroscopy (see figure 3.9 below) we observe that the resonance frequency is shifted by $\omega_{\mathrm{r}}$, as expected.

### 3.4.2 Atoms in an optical lattice

The situation previously described is different when atoms are trapped in an optical lattice. Here, the allowed motional states $|\Phi_m\rangle$ are quantized and the coupling can only induce transitions between these bound levels. In such a case, the matrix element

$$V_{mn} = \langle \Phi_m | \mathrm{e}^{\mathrm{i}\boldsymbol{k}_{\mathrm{cl}}\cdot\hat{\boldsymbol{r}}} | \Phi_n \rangle = \int \Phi_m^*(\boldsymbol{r})\,\mathrm{e}^{\mathrm{i}\boldsymbol{k}_{\mathrm{cl}}\cdot\boldsymbol{r}}\,\Phi_n(\boldsymbol{r})\,\mathrm{d}^3 r, \tag{3.20}$$

gives the strength of the transition between a final bound state $|\Phi_m\rangle$ and the initial one $|\Phi_n\rangle$ shifted in momentum space by $\hbar\boldsymbol{k}_{\mathrm{cl}}$.

Let us focus on a situation in which the particles obbey also a dispersion relation $E(\boldsymbol{n}, \boldsymbol{q})$, given by the band structure of the lattice, which we suppose independent of the internal state[51]. As discussed in section 1.2.1, the eigenstates of the system are given by Bloch waves $|\boldsymbol{n}, \boldsymbol{q}\rangle$. We can decompose these states in the basis of plane waves (Ashcroft et al. 1976):

$$|\boldsymbol{n}, \boldsymbol{q}\rangle = \sum_{\boldsymbol{G}} C_{\boldsymbol{n},\boldsymbol{q}}(\boldsymbol{G}) |\boldsymbol{p} = \boldsymbol{G} + \boldsymbol{q}\rangle, \tag{3.21}$$

where the sum runs over all vectors $\boldsymbol{G}$ of the reciprocal lattice. Absorbing a laser photon changes the quasimomentum of the atom but can also induce transitions to other Bloch bands: $|g; \boldsymbol{q}, \boldsymbol{n}\rangle \to |e; \boldsymbol{q}', \boldsymbol{m}\rangle$. The matrix element of this process reads:

$$V_{\boldsymbol{m},\boldsymbol{n}}^{\boldsymbol{q}',\boldsymbol{q}} = \sum_{\boldsymbol{G},\boldsymbol{G}'} C^*_{\boldsymbol{m},\boldsymbol{q}'}(\boldsymbol{G}')\, C_{\boldsymbol{n},\boldsymbol{q}}(\boldsymbol{G}) \int \mathrm{e}^{\mathrm{i}(\boldsymbol{k}_{\mathrm{cl}}+\boldsymbol{q}-\boldsymbol{q}')\cdot\boldsymbol{r}}\, \mathrm{e}^{\mathrm{i}(\boldsymbol{G}-\boldsymbol{G}')\cdot\boldsymbol{r}}\, \mathrm{d}^3 r \tag{3.22}$$

$$= \sum_{\boldsymbol{G},\boldsymbol{G}'} C^*_{\boldsymbol{m},\boldsymbol{q}'}(\boldsymbol{G}')\, C_{\boldsymbol{n},\boldsymbol{q}}(\boldsymbol{G})\, \delta_{\boldsymbol{k}_{\mathrm{cl}}+\boldsymbol{q}+\boldsymbol{G},\boldsymbol{q}'+\boldsymbol{G}'}, \tag{3.23}$$

which manifests the conservation of quasimomentum, modulo a vector $\boldsymbol{G} - \boldsymbol{G}'$ of the reciprocal lattice. As in the case of a free particle, the momentum transfer and the conservation of quasimomentum can be directly seen by recording an image in TOF, i.e., by projecting back into the plane wave basis. We show this in figure 3.7 for a probe beam propagating along an axis of the lattice, $\boldsymbol{k}_{\mathrm{cl}} = (k_{\mathrm{cl}}, 0, 0)$, in figure 3.7(b) and at at $\theta = 45°$ with respect to the axis defined by the lattice, i.e. $\boldsymbol{k}_{\mathrm{cl}} = (k_{\mathrm{cl}} \sin\theta, k_{\mathrm{cl}} \cos\theta, 0)$ in figure 3.7(c). Energy conservation leads to an energy shift with respect to the bare frequency $\omega_0$ by a quantity that can be computed from the band structure:

$$\hbar\omega_{\mathrm{latt}}(\boldsymbol{q}, \boldsymbol{q}', \boldsymbol{n}, \boldsymbol{m}) = E(\boldsymbol{q}', \boldsymbol{m}) - E(\boldsymbol{q}, \boldsymbol{n}), \tag{3.24}$$

and this can be measured by performing spectroscopy (see figure 3.9 below). The total coupling strength is given by:

$$\Omega_{\mathrm{L}}(\boldsymbol{q}, \boldsymbol{q}', \boldsymbol{n}, \boldsymbol{m}) = V_{\boldsymbol{m},\boldsymbol{n}}^{\boldsymbol{q}',\boldsymbol{q}}\, \Omega_{\mathrm{cl}}. \tag{3.25}$$

### Approximations for deep lattices: Lamb-Dicke regime

As the lattice becomes deeper, the energy bands become flatter and, as a consequence, the change in quasimomentum upon the absorption of the photon has a smaller effect. In such a situation, it is more convenient to express the Bloch functions in the Wannier basis[52]:

$$|\boldsymbol{n}, \boldsymbol{q}\rangle = \left(\frac{d}{2\pi}\right)^{3/2} \sum_{\boldsymbol{i}} \mathrm{e}^{\mathrm{i}\boldsymbol{q}\cdot\boldsymbol{r}_i} |w_{\boldsymbol{n},\boldsymbol{i}}\rangle, \tag{3.26}$$

where the sum runs among all lattice sites. Let us then compute the strength of the transition in this new basis:

$$V_{\boldsymbol{m},\boldsymbol{n}}^{\boldsymbol{q}',\boldsymbol{q}} = \left(\frac{d}{2\pi}\right)^{3} \sum_{\boldsymbol{i},\boldsymbol{j}} \mathrm{e}^{\mathrm{i}(\boldsymbol{q}\cdot\boldsymbol{r}_i - \boldsymbol{q}'\cdot\boldsymbol{r}_j)} \int w^*_{\boldsymbol{m}}(\boldsymbol{r} - \boldsymbol{r}_j)\, \mathrm{e}^{\mathrm{i}\boldsymbol{k}_{\mathrm{cl}}\cdot\boldsymbol{r}} w_{\boldsymbol{n}}(\boldsymbol{r} - \boldsymbol{r}_j)\, \mathrm{d}^3 r \tag{3.27}$$

$$= \sum_{\boldsymbol{\varrho}} \mathrm{e}^{-\mathrm{i}\boldsymbol{q}\cdot\boldsymbol{\varrho}}\, \delta(\boldsymbol{q} + \boldsymbol{k}_{\mathrm{cl}} - \boldsymbol{q}') \int w^*_{\boldsymbol{m}}(\boldsymbol{r} + \boldsymbol{\varrho})\, \mathrm{e}^{\mathrm{i}\boldsymbol{k}_{\mathrm{cl}}\cdot\boldsymbol{r}} w_{\boldsymbol{n}}(\boldsymbol{r})\, \mathrm{d}^3 r, \tag{3.28}$$

---

[51] This is indeed the case when working at the magic wavelength $\lambda_{\mathrm{m}}$.

[52] We invert equation (1.33) and use the 3D identity $\sum_{\boldsymbol{j}} \mathrm{e}^{\mathrm{i}\boldsymbol{q}\cdot\boldsymbol{r}_j} = (2\pi/d)^3\, \delta(\boldsymbol{q})$, with $\boldsymbol{r}_j = \boldsymbol{j}d$.

where we have put $\boldsymbol{\varrho} = \boldsymbol{r}_i - \boldsymbol{r}_j$ and where quasimomentum conservation becomes also explicit. The interest of working in the Wannier basis arises when considering very deep lattices. Here, the overlap integral only takes significant values when $\boldsymbol{\varrho} = \boldsymbol{0}$ and we can approximate the matrix element as:

$$V_{\boldsymbol{m},\boldsymbol{n}}^{\boldsymbol{q}',\boldsymbol{q}} \simeq \eta_{\boldsymbol{mn}}\, \delta(\boldsymbol{q} + \boldsymbol{k}_{\mathrm{cl}} - \boldsymbol{q}'), \tag{3.29}$$

where we have defined the so-called *Lamb-Dicke* factor:

$$\eta_{\boldsymbol{mn}} = \int w_{\boldsymbol{m}}^{*}(\boldsymbol{r})\, \mathrm{e}^{\mathrm{i}\boldsymbol{k}_{\mathrm{cl}}\cdot\boldsymbol{r}} w_{\boldsymbol{n}}(\boldsymbol{r})\, \mathrm{d}^3 r. \tag{3.30}$$

As the lattice depth reaches a few recoils, the Wannier wave function becomes more and more localized in space and thus its Fourier transform gets broader. As a consequence, translating it by $\hbar\boldsymbol{k}_{\mathrm{cl}}$ is going to leave it nearly unchanged $\mathrm{e}^{\mathrm{i}\boldsymbol{k}_{\mathrm{cl}}\cdot\hat{\boldsymbol{r}}}|w_{\boldsymbol{0}}\rangle \simeq |w_{\boldsymbol{0}}\rangle$. Then, since Wannier functions corresponding to different bands are orthogonal, the overlap in (3.30) for very deep lattices is maximum for the so-called *carrier* or *zero-phonon* line $\boldsymbol{m} = \boldsymbol{n}$, a nomenclature that we adopt in the following, widely used in the ion comunity where the motional states are vibrational levels of an ion string. This framework is known as the *Lamb-Dicke regime* of light scattering, and occurs once the scatterer is confined to a region of size $\sigma \ll \lambda_{\mathrm{L}}$ (Wineland et al. 1979; Leibfried et al. 2003; Ludlow et al. 2015). In this limit, the effect of the recoil is completely suppressed for the carrier and the resonance frequency is given by the bare atomic resonance $\omega_0$.

At intermediate depths, transitions to other bands are partially suppressed but observable. Already at a few recoils $V_0 \geq 5\,E_{\mathrm{r}}$, the different bands are well resolved (see figure 3.9) and one can effectively suppress the recoil of the photon (thus decoupling the internal dynamics from the external ones) by driving the zero-phonon lines. The coupling strength in equation (3.17) takes the form:

$$\Omega_{\mathrm{L}}(\boldsymbol{m}, \boldsymbol{n}) = \eta_{\boldsymbol{mn}} \Omega_{\mathrm{cl}}. \tag{3.31}$$

In our experiment we typically load the atoms on the fundamental band and drive the zero-phonon line. If our laser was completely coherent, the spectra would be in this case Fourier-limited. However, there remain some broadening sources such as inhomogeneous coupling (due for instance to the spatial dependence of the Rabi frequency over the atomic cloud) or fluctuations of the laser frequency, that prevent us from observing arbitrarily narrow spectra. We will discuss this further below.

## 3.5 Spectroscopy of single particles in optical lattices

In the following sections, we are going to show a series of measurements in which we drive the clock transition of a degenerate ensemble of atoms loaded in 2D optical lattices. Here, we will be mostly concerned by single particle properties. For this, we prepare an $\bar{n} = 1$ Mott insulator in a deep lattice. In such a situation, interactions become irrelevant and the osberved dynamics correspond to those of single particles. By using the loading model described in section 2.2.2, we find that the maximum atom number to work in these conditions is $N \leq 8 \times 10^3$ atoms. For all data shown in this chapter, the vertical lattice depth is fixed at $V_z = 27\,E_{\mathrm{r}}$ and on the following we only indicate the depth of the horizontal ones $V_{\perp}$.

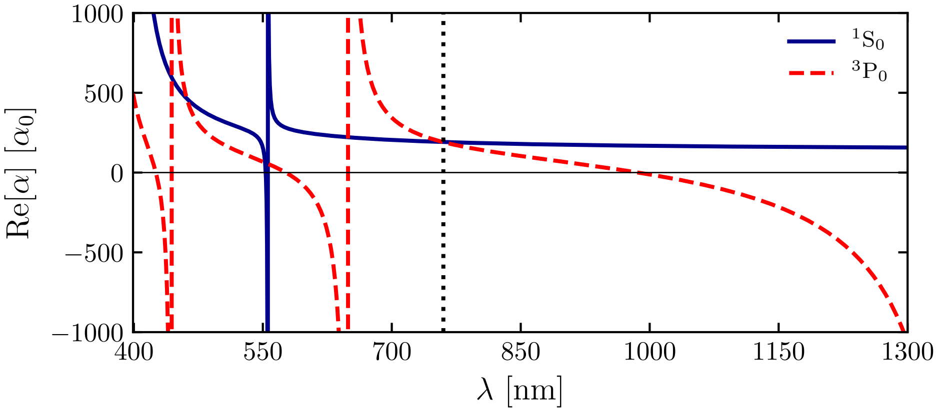

**Figure 3.8** – Real part of the polarizability for the ground state $^1$S$_0$ (solid blue line) and the excited metastable state $^3$P$_0$ (dashed red line). The magic wavelength for which $\mathrm{Re}[\alpha_g(\lambda_\mathrm{m})] = \mathrm{Re}[\alpha_e(\lambda_\mathrm{m})]$ corresponds to the vertical dotted line at $\lambda_\mathrm{m} \simeq 759.4\,\mathrm{nm}$.

### 3.5.1 A state-independent optical lattice: The *magic* wavelength

Let us then consider a single atom trapped in an optical lattice. As discussed in chapter 2, the potential felt by the atom depends on the wavelength of the light and the internal state of the atom. These two aspects [see equation (2.5)] are encoded in the real part of the polarizability $\alpha_j(\lambda)$ (Grimm et al. 2000). Although this offers interesting possibilities for quantum simulation, this differential light shift is often unwanted when performing precise measurements. Indeed, the different polarizabilities lead to different light shifts for each atomic state, which can be detected when performing spectroscopy. For instance, it leads to additional uncertainties to account for when carrying out error budgets in optical lattice clocks (Ludlow et al. 2015), as it requires both a good knowledge of the polarizability and the geometry of the trap. However, at certain wavelengths, called *magic* wavelengths, the polarizability is the same for two given states: $\mathrm{Re}[\alpha_g(\lambda_\mathrm{m})] = \mathrm{Re}[\alpha_e(\lambda_\mathrm{m})]$. For $^{174}$Yb clock states this wavelength corresponds to $\lambda_\mathrm{m} \simeq 759.353\,74(7)\,\mathrm{nm}$ (Barber et al. 2008). We show this in figure 3.8, where we plot the real part of the polarizability for the ground state and the metastable state. In all the rest of this work we use the magic wavelength $\lambda_\mathrm{m}$ to trap the atoms whenever we perform spectroscopy of the clock transition.

### 3.5.2 Spectroscopy in the Lamb-Dicke regime

#### Band resolved spectroscopy

At high lattice depths, the system is analog to an ensemble of harmonically trapped particles. By driving the zero-phonon line, the recoil of the photon is suppressed and the motion of the atoms is effectively decoupled from the internal dynamics. This dynamics can be driven coherently by exciting the system at the bare resonance frequency $\omega_0$. It is also possible to transfer atoms to the first *blue* excited band[53] shifted by a frequency

---

[53] If all atoms are initially in the fundamental band, we expect no *red* sideband coupling an atom in $|g; n = 1\rangle$ to $|e; n = 0\rangle$ at a frequency $\omega_0 - \omega_\mathrm{latt}$. By *blue* and *red* we mean plus or minus one quantum of vibration.

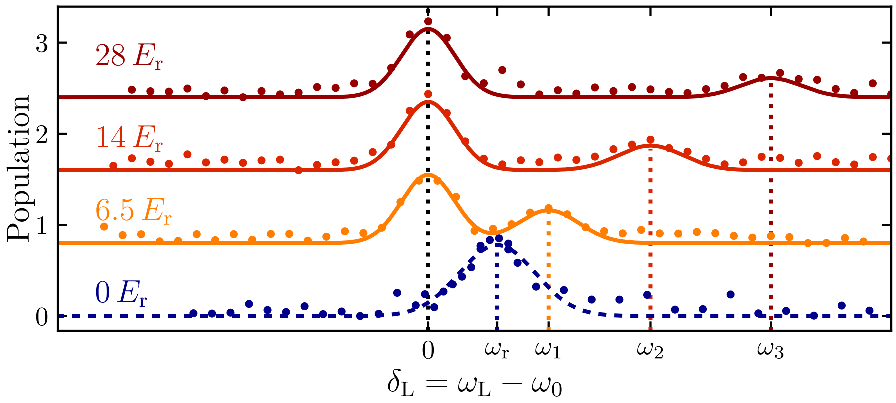

**Figure 3.9** – Band resolved spectroscopy in an optical lattice. Several spectra are taken at different lattice depths: from bottom to top $V_\perp = 0, 6.5, 14$ and $28\,E_\mathrm{r}$. Many aspects discussed in the main text can be observed: when atoms are probed in free space, the resonance frequency is blue shifted by $\omega_\mathrm{r}/(2\pi) \simeq 3.4\,\mathrm{kHz}$ with respect to the bare resonance frequency, corresponding to $\delta_\mathrm{L} = 0$. When the atoms are in the lattice we observe two peaks corresponding to the zero-phonon line (main transition at $\delta_\mathrm{L} = 0$) and the first blue sideband, which is well resolved for all spectra shown here. The solid line corresponds to a sum of two Gaussians fro which we extract the central frequency and the relative transfer. The sidebands are found at $\omega_1/(2\pi) \simeq 6.5\,\mathrm{kHz}$, $\omega_2/(2\pi) \simeq 12\,\mathrm{kHz}$, $\omega_3/(2\pi) \simeq 18.5\,\mathrm{kHz}$ for $V_\perp = 6.5, 14$ and $28\,E_\mathrm{r}$, respectively. The pulse duration is $T = 350\,\mu\mathrm{s}$, the bare Rabi frequency is set to $\Omega_\mathrm{cl}/(2\pi) \simeq 1450\,\mathrm{Hz}$ and the transition strengths are $\eta_{01} \simeq 0.42, 0.34$ and $0.28$ for $V_\perp = 6.5, 14$ and $28\,E_\mathrm{r}$, respectively. All spectra shown are Fourier limited and a vertical offset has been added for clarity.

$\hbar\omega_\mathrm{latt}$. Since these bands are well separated, the transition amplitude for each one is given by the usual Rabi formula for a two-level system:

$$P_e(\delta'_\mathrm{L}, t) = \frac{\Omega_\mathrm{L}^2}{\Omega_\mathrm{L}^2 + \delta'^2_\mathrm{L}} \sin^2\left(\frac{\sqrt{\Omega_\mathrm{L}^2 + \delta'^2_\mathrm{L}}}{2} t\right), \tag{3.32}$$

with $\delta'_\mathrm{L} = \delta_\mathrm{L} - \omega_\mathrm{latt}$ and $\Omega_\mathrm{L} = \eta_{m0}\Omega_\mathrm{cl}$ given by equation (3.31). We have performed this kind of spectroscopy in the following experimental conditions: Atoms are loaded in the fundamental band of a two-dimensional lattice at $\boldsymbol{q} \simeq \boldsymbol{0}$. The probe propagates in the plane defined by the lattice with an angle of $\theta = 45°$ with respect to the lattice arms [see figure 3.7(b)] and we record spectra at different depths $V_\perp$.

We show the results in figure 3.9 at different depths (and also in the absence of lattice, where the recoil shift appears). From these series of spectra, we extract (i) the resonance frequency and (ii) the transition amplitude for the first blue sideband, corresponding to the $n = 0 \to m = 1$ transition. We do this by performing a model-free fit with the sum of two Gaussians. We compare these values to the prediction from equations (3.24) and (3.31) in figure 3.10(a)-(b). The computed values agree well with the extracted parameters, validating our lattice and Rabi frequency calibrations.

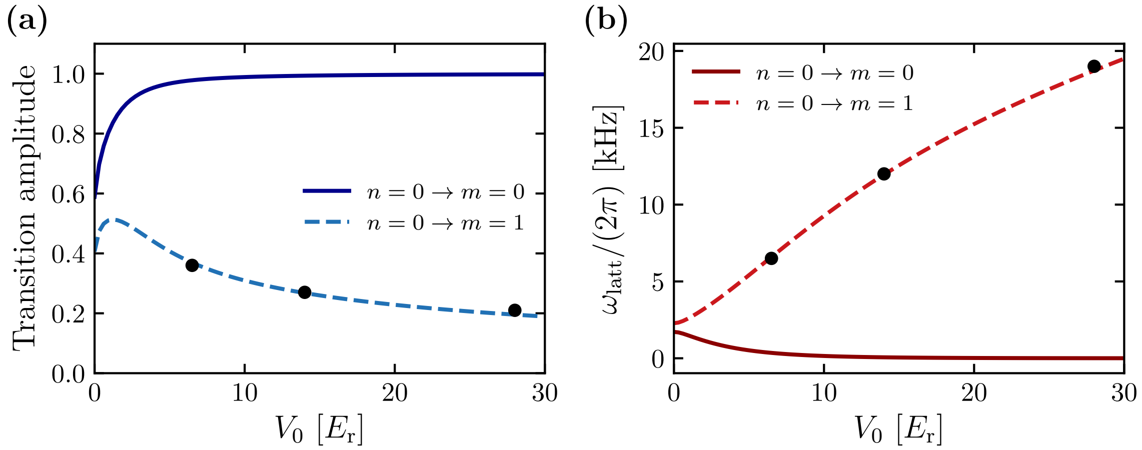

**Figure 3.10** – Band spectroscopy analysis. **(a):** Transition amplitudes and **(b):** frequency shifts computed by using equations (3.32) and (3.24), respectively. All curves correspond to $\boldsymbol{q} = \boldsymbol{0}$ and $\boldsymbol{q}' = (k_\mathrm{cl}/\sqrt{2}, k_\mathrm{cl}/\sqrt{2}, 0)$ and the legends indicate the initial and final band. The black dots correspond to the amplitudes and frequencies extracted from a Gaussian fit to the sidebands shown in figure 3.9.

### Driving the zero-phonon line: a first estimate of the laser linewidth

We have already discussed that the recorded spectra should in principle be Fourier broadened and that, if this is not the case, this is due to dephasing mechanisms, probably arising from the laser itself. In order to get a first evaluation of our laser linewidth, we performed spectroscopy on the zero-phonon line, with the idea that the narrowest observed spectrum should give a rough estimation of the linewidth of the clock laser. These experiments were performed in a lattice at $V_\perp = 24.5\,E_\mathrm{r}$, for which $\eta_{00} \simeq 0.9$. We show these spectra, taken at decreasing Rabi frequencies in figures 3.11(a)-(i). The solid lines are fits using equation (3.32) with only the resonance frequency as a free parameter. The data agrees well with the Fourier limited line shape given by the Rabi formula for full widths at half maximum down to $2\pi \times 150\,\mathrm{Hz}$. However, we note that for driving strengths on the order or below $\Omega_\mathrm{L}/(2\pi) \simeq 100\,\mathrm{Hz}$, important shot to shot fluctuations appear. Because of it, the spectra start being noisy and distorted and maximum transfer to the excited state is not always achieved. The next section is devoted to the discussion of the mechanisms that compete against the coherent driving and broaden the observed spectra, namely inhomogeneous dephasing and laser frequency fluctuations.

## 3.6 Characterization of the loss of coherence

Decoupling the internal dynamics from the motion of the atom by working in a very deep optical lattice should allow for a long coherent driving of the former. However, as we have seen in the previous section, we are not able to produce arbitrarily narrow spectra. In the absence of spontaneous emission, which is the case for the clock transition, we identify at least two important damping mechanisms:

1. Inhomogeneity of the probe over the atomic cloud.

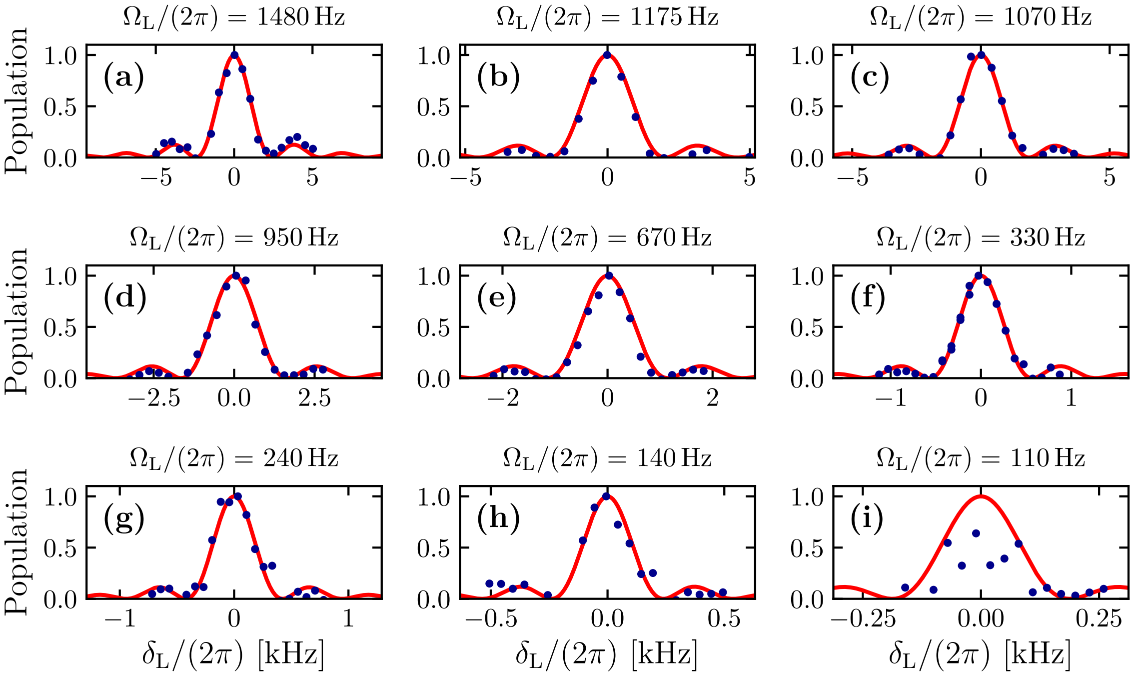

**Figure 3.11** – Examples of spectra recorded on the zero-phonon line at different Rabi frequencies in a lattice at $V_\perp \simeq 24.5\,E_r$. The pulse area is in all cases chosen such that $\Omega_L T = \pi$. The red solid line is a fit using equation (3.32) with only the resonance frequency left as a free parameter.

2. Frequency fluctuations of the probe.

In the next sections, we first present a discussion on these different dephasing mechanisms. Then, we characterize their importance experimentally by performing time-domain Rabi and Ramsey spectroscopy.

### 3.6.1 Inhomogeneity of the probe over the atomic cloud

As seen in the previous sections, the strength of the coupling of the zero-phonon line is given by $\Omega_L(\boldsymbol{r}) = \eta_{00}\Omega_{cl}(\boldsymbol{r})$. Here, we make explicit the dependence on position of the Rabi frequency. This spatial dependence arises from the Gaussian shape of the probe, whose intensity profile is given by

$$I_{cl}(\boldsymbol{\rho}) = I_{cl} f(\boldsymbol{\rho}) = I_{cl} \exp\left(-2\boldsymbol{\rho}^2/w_{cl}^2\right), \tag{3.33}$$

where $I_{cl} = 2P_{cl}/(\pi w_{cl}^2)$. As a consequence, atoms in different regions of the cloud will feel different Rabi frequencies and thus oscillate at uneven rates. Appart from this, we have seen that the presence of the probe induces a differential light shift $\delta_E(\boldsymbol{r}) = \kappa I_{cl}(\boldsymbol{\rho})$ [see section 3.3], resulting in an inhomogeneous detuning $\delta(\boldsymbol{r}) = \delta_L - \delta_E(\boldsymbol{r})$ over the sample, leading to another inhomogeneous broadening effect.

The recorded population in the excited state is thus given by the spatial average of equation (3.32) over the atomic cloud. For $N$ atoms, the average population is given by:

$$\bar{P}_e = \frac{1}{N} \int \frac{\Omega_{\mathrm{L}}^2(\boldsymbol{r})}{\Omega_{\mathrm{L}}^2(\boldsymbol{r}) + \delta^2(\boldsymbol{r})} \sin^2 \left( \frac{\sqrt{\Omega_{\mathrm{L}}^2(\boldsymbol{r}) + \delta^2(\boldsymbol{r})}}{2} t \right) \mathrm{d}^3 r \tag{3.34}$$

For a deep lattice prepared in the Mott isulator state, the effect of inhomogeneous broadening can be evaluated numerically by using the density profile calculated in section 2.2.2.

### Estimation of the inhomogeneities

An analytical estimation can also be carried on by performing a couple of approximations. First, since the extension of the atomic cloud is small compared to the size of the probe, we perform a parabolic approximation of the beam: $I_{\mathrm{cl}}(\boldsymbol{\rho}) \simeq I_{\mathrm{cl}}(1 - 2\boldsymbol{\rho}^2/w_{\mathrm{cl}}^2)$. Let us then estimate the order of magnitude of these effects for our experimental parameters:

$$\Delta\Omega = |\Omega_{\mathrm{L}}(0) - \Omega_{\mathrm{L}}(R)| \simeq \Omega_0 \frac{R^2}{w_{\mathrm{cl}}^2} \simeq 0.02\,\Omega_0, \tag{3.35}$$

$$\Delta\delta = |\delta_{\mathrm{L}}(0) - \delta_{\mathrm{L}}(R)| \simeq \Omega_0^2 \frac{2\kappa}{(\eta_{00}\alpha B)^2} \frac{R^2}{w_{\mathrm{cl}}^2} \simeq \Omega_0^2 \times 1 \times 10^{-5}\,\mathrm{s}. \tag{3.36}$$

Here $B$ is the strength of the static magnetic field and $\Omega_0 = \Omega_{\mathrm{L}}(0)$ is the Rabi frequency at the trap center. The numerical parameters $\alpha, \kappa$ have been given in section 3.3, and $\eta_{00} \simeq 0.9$. The previous estimations lead to $\Delta\Omega/(2\pi) \simeq 30\,\mathrm{Hz}$ and $\Delta\delta/(2\pi) \simeq 130\,\mathrm{Hz}$, respectively, for a Rabi frequency $\Omega_0/(2\pi) = 1400\,\mathrm{Hz}$.

### Estimation of the dephasing rate in Rabi oscillations

Generally, we are more interested in the contribution of the generalized Rabi frequency, rather than $\Delta\Omega$ or $\Delta\delta$ itself. This contribution reads:

$$\Omega_{\mathrm{L}}^2(\boldsymbol{r}) + \delta^2(\boldsymbol{r}) \simeq \Omega_0^2 + \delta_0^2 - 2\Omega_0^2 \left[ 1 - \frac{2\delta_0\kappa}{(\eta_{00}\alpha B)^2} \right] (\rho/w_{\mathrm{cl}})^2 + \mathcal{O}(\rho/w_{\mathrm{cl}})^4, \tag{3.37}$$

with $\delta_0 = \delta_{\mathrm{L}} - \delta_{\mathrm{E}}(0)$ the detuning at the center of the trap. In resonance, $\delta_0 = 0$, and we have $\Omega_{\mathrm{L}}^2(\boldsymbol{r}) + \delta^2(\boldsymbol{r}) \simeq \Omega_0^2[1 - 2(\rho/w_{\mathrm{cl}})^2]$. We then see that atoms located at the center of the trap oscillate as $\cos(\Omega_0 t)$, and atoms at the edges do it as $\cos[\Omega_0 t - \Omega_0 (R/w_{\mathrm{cl}})^2 t]$, with $R$ the longitudinal radius of the sample. From this, we estimate a dephasing due to the inhomogeneous profile of the clock beam at a rate proportional to this frequency difference:

$$\gamma_{\mathrm{d}}^{\mathrm{inh}} \simeq a\Omega_0 \frac{R^2}{w_{\mathrm{cl}}^2}, \tag{3.38}$$

with $a$ a numerical factor. We thus see that this effect can be mitigated by working at small Rabi frequencies and by reducing the atom number (thereby decreasing $R$). We note that this estimate holds provided the beam is well centered, otherwise this effect is amplified. However, since this would also entail a reduction of the measured Rabi frequency, that we do not observe, we disregard the misalignment effect as a dephasing source in our system.

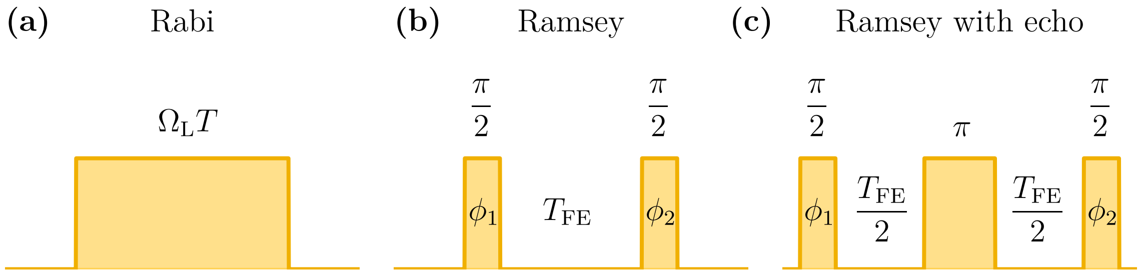

**Figure 3.12** – Schematics of the different spectroscopy techniques used in this chapter. **(a):** Rabi spectroscopy. A single pulse of varying area $\Omega_L T$ is applied to the atoms. **(b):** Ramsey spectroscopy. A first pulse of area $\pi/2$ and phase $\phi_1$ is applied to the atoms. The light is then switched off during a time of free evolution $T_{FE}$ after which another $\pi/2-$pulse with phase $\phi_2$ is applied. **(c):** Ramsey spectroscopy with echo. The sequence is the same as for Ramsey spectroscopy, but with a $\pi-$pulse inserted in the middle of the free evolution time.

### Frequency fluctuations of the probe

Even in a situation in which the inhomogeneous dephasing mechanisms would not play a significant role anymore, we would still be limited at some point by the possible frequency fluctuations of the probe laser. Apart from the frequency amplitude of this noise, it is important to identify the frequency spectrum of these fluctuations. In other words, in order to estimate their effect, it is essential to know how fast these fluctuations are with respect to, at least, the two following timescales: (i) the probing time within an experimental sequence $T$ (usually ranging from a few hundreds of µs up to a few tens of ms) and (ii) the time in between two experimental sequences $T_{seq} \gg T$ (on the order of 15-20 s). We can picture the instantaneous laser frequency as a classical but fluctuating quantity:

$$\omega_L(t) = \bar{\omega}_L + \Delta\omega_L(\Omega_{noise}) = \bar{\omega}_L + \sum_{\Omega_{noise}} \delta\omega_L(\Omega_{noise}) \cos\left(\Omega_{noise} t + \phi_{noise}\right). \tag{3.39}$$

Here we have decomposed the noise as a sum of contributions at different frequencies, but we do not try to give any details on the kind of noise. We can then distinguish the following cases:

1. Fast fluctuations, where $\Omega_{noise} \gg T^{-1}$: Here, the laser frequency undergoes fast changes during a pulse, which end up averaging out, in the sense that there is no shift of the line but the phase is randomized. This leads to the damping of Rabi oscillations. In such a framework maximum transfer of atoms to the excited state cannot be achieved and this is equivalent to incoherent spectroscopy.
2. Slow fluctuations, where $T_{seq}^{-1} \simeq \Omega_{noise} \ll T^{-1}$: In this case, maximum transfer can be achieved but the center frequency is random from one shot to another, and this leads to important shot-to-shot fluctuations and to a reduced contrast after averaging over many repetitions. These fluctuations could be due, for instance, to thermal drifts of the cavity environment.

We will now present a series of measurements using two different spectroscopy methods (see figure 3.12) at lattice depths $V_\perp \simeq 24.5\, E_r$. All experiments are performed at resonance $\delta_L \simeq 0$. To ensure that the laser drifts are compensated, we systematically record a spectrum before each run and correct the laser frequency accordingly.

### 3.6.2 Time-domain Rabi spectroscopy

We first present the results on time-domain Rabi spectroscopy. Here, the population of atoms transferred to the excited state is measured as a function of the pulse time $T$ (or pulse area $\Omega_L T$) [see figure 3.12(a)]. We have performed these experiments for different Rabi frequencies and we show them in figure 3.13. The data is then fitted by an heuristic function consiting of an exponentially damped sinusoidal from where we extract a damping rate $\gamma_d$. A first observation from these curves is that the damping rates decrease with decreasing Rabi frequency. From the previous discussion, this points to damping due to the inhomogeneous dephasing, which could be caused by the Gaussian profile of the probe. To extract more quantitative information from this observation, we plot the extracted damping rates as a function of the Rabi frequency in figure 3.15(a), and we observe a linear dependence as expected from equation (3.38). We perform a linear fit $\gamma_d = \gamma_0 + a\Omega_L(R/w_{cl})^2$ from which we find $a = 0.50(1)$. We also see that, at vanishing Rabi frequency, the interception with the $y-$axis is not zero. We interpret this as the dephasing set by the noise of the laser frequency alone. From the linear fit we extract $\gamma_0 = 34(3)\,\mathrm{s}^{-1}$.

### 3.6.3 Ramsey spectroscopy and echoes

#### The method

The method of Ramsey spectroscopy (Ramsey 1986) is based on the following idea [see figure 3.12(b)]:

1. Preparation: A first pulse of area $\Omega_L T = \pi/2$ and phase $\phi_1$ is used to prepare a coherent superposition of $g$ and $e$ [equator of the Bloch sphere].
2. Free evolution: The probe is then switched off during a variable time $T_{FE}$.
3. Measurement: A second pulse of area $\Omega_L T = \pi/2$ and phase $\phi_2$ is then sent and the $g$ population is measured.

In the case in which the first pulse is exactly at resonance, the coherent superposition remains with the same initial relative phase during the free evolution[54] and if the second pulse has $\phi_2 = \phi_1$ all atoms are sent to the excited state. As one scans $\phi_2$ all the meridian of the Bloch sphere is sampled and the ground state population oscillates with a $2\pi$ period with full contrast. This ideal picture is modified if (i) there are inhomogeneous dephasing sources or (ii) there is a phase jump of the laser during $T_{FE}$. The effect of inhomogeneous dephasing can be understood as follows: atoms in different positions of the cloud feel a different light shift during the excitation and thus dephase at distinct rates during the free evolution stage [there is a *spread* in the equatorial

---

[54] In the case in which the first pulse is detuned, a relative phase between $e$ and $g$ equal to $-\delta_L T_{FE}$ is acquired during the free evolution.

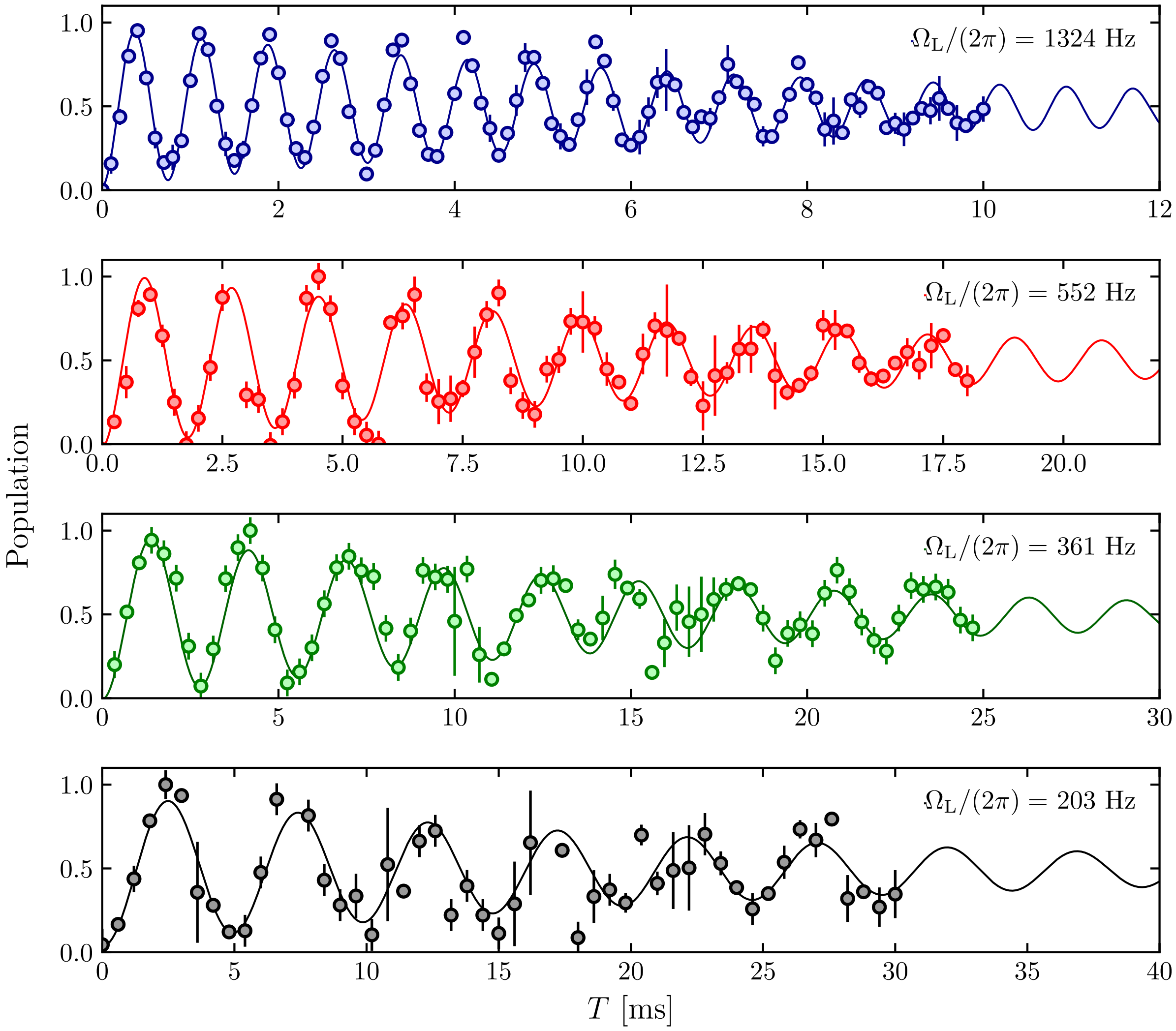

**Figure 3.13** – Rabi oscillations driven on the zero-phonon line in a lattice at $V_\perp = 24.5\, E_\mathrm{r}$. The solid lines are fits to an exponentially damped sinusoidal. From largest to smallest Rabi frequency, the extracted damping rates from these fits are $\gamma_\mathrm{d} = 120(10), 71(9), 60(10)$ and $40(10)\,\mathrm{s}^{-1}$, respectively.

plane of the Bloch sphere]. As a consequence, the effect of the second $\pi/2-$pulse will be different for each of atom and the contrast of the fringe gets reduced due to ensemble averaging.

### The echo

The interest of Ramsey spectroscopy is that one can get rid of the inhomogeneous dephasing by performing an *echo* (Hahn 1950), which consists in applying a $\pi-$pulse in the middle of the free evolution stage [see figure 3.12(c)]. The effect of adding a $\pi-$pulse in the middle of the free evolution, is equivalent to a $t \to -t$ transformation [180° rotation in the Bloch sphere] and thus, all inhomogeneous dephasing sources end up canceled with this technique. Therefore, Ramsey spectroscopy with an echo is a good technique to estimate the effect that frequency fluctuations alone have on the coherent driving.

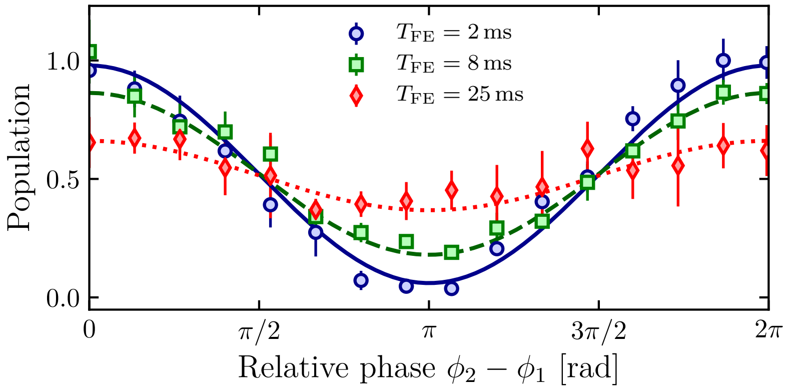

**Figure 3.14** – Ramsey fringes with echo for atoms driven on the zero-phonon line. We show the data for three different free evolution times $T_{\mathrm{FE}} = 2, 8$ and $25\,\mathrm{ms}$ corresponding to blue dots, green squares and red diamonds, respectively. The Rabi frequency is set to $\Omega_{\mathrm{L}}/(2\pi) \simeq 1.2\,\mathrm{kHz}$ and $V_\perp = 24.5\,E_{\mathrm{r}}$. The solid lines are a sinusoidal fit to the data.

### Experimental results

In figure 3.14 we show some Ramsey fringes recorded with the echo technique at different free evolution times $T_{\mathrm{FE}}$ for a Rabi frequency $\Omega_{\mathrm{L}}/(2\pi) \simeq 1200\,\mathrm{Hz}$. In figure 3.15(b) we show the contrast of the fringes as a function of the free evolution time for a set of data in which we have not performed an echo (red squares) and another one where it has been applied (blue circles), and we can see that the difference is drastic. By performing an exponential fit to the data, we find that the damping rate is reduced by almost an order of magnitude, from $\gamma_{\mathrm{d}}^{\mathrm{no-echo}} = 340(10)\,\mathrm{s}^{-1}$ without the echo to $\gamma_{\mathrm{d}}^{\mathrm{echo}} = 39(7)\,\mathrm{s}^{-1}$ with the echo.

This observation points to dephasing mechanisms occurring in between the two $\pi/2-$pulses. This could be due on the one hand to the inhomogeneous detuning induced by the probe, which leads to an inhomogeneous dephasing during the free evolution time. On the other hand, this could also point to frequency fluctuations such that $\Omega_{\mathrm{noise}} \simeq T_{\mathrm{seq}}^{-1}$. These fluctuations are indeed detrimental for the experiments performed without an echo [if the detuning changes from one sequence to the other the phase accumulated during the free evolution changes], but would be corrected by performing it thanks to the $\pi-$pulse. Moreover, we see that the decay rate $\gamma_{\mathrm{d}}^{\mathrm{echo}}$ agrees within the error bars with the interpolation at zero Rabi frequency $\gamma_0$ of the Rabi spectroscopy experiments, from which we infer a coherence time of the laser of $\tau_{\mathrm{coh}} \simeq 30\,\mathrm{ms}$.

## 3.7 Conclusion

In this chapter I have presented one of our main experimental tools: a narrow laser driving coherently an optical clock transition. I have first introduced the experimental setup that we use to probe the clock transition and I also described the laser system and procedure used to image the metastable state. Then, I reminded the technique used to enable the clock transition and the basic concepts of atom-light interaction in a periodic potential.

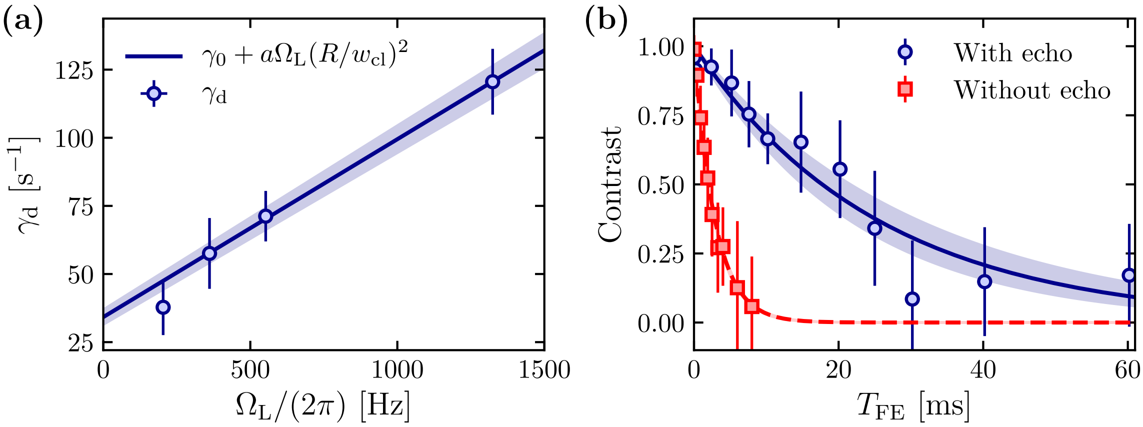

**Figure 3.15** – **(a):** Decay rates as a function of the Rabi frequency extracted from the fits to the data shown in figure 3.13. The solid line is a linear fit: $\gamma_d = \gamma_0 + a\Omega_L(R/w_{cl})^2$, from which we extract the numerical factor $a = 0.50(1)$ and $\gamma_0 = 34(3)\,\mathrm{s}^{-1}$. **(b):** Contrast of the fringes from a series of Ramsey spectroscopy measurements with (blue dots) and without (red squares) echo. The solid lines are exponential fits to the data from which we extract a decay rate of the contrast of $\gamma_d^{\text{no-echo}} = 340(10)\,\mathrm{s}^{-1}$ in the absence of echo and $\gamma_d^{\text{echo}} = 39(7)\,\mathrm{s}^{-1}$ with the echo. The shaded regions represent the $1-\sigma$ confidence regions.

After this, I have presented a series of measurements performed in an optical lattice with a small atom filling $\bar{n} \simeq 1$. Here, I have shown that we can use the clock transition to further characterize the lattice potential. Thanks to the high momentum imparted by the optical photons, we are able to transfer atoms to other zones of the first Brillouin zone and to higher energy bands.

By increasing the lattice depth, these lattice bands become well resolved and the situation becomes conceptually plainer: The lattice can be thought of as an ensemble of single particles in disconnected wells. I have shown that in this regime we can decouple the external degrees of freedom from the internal ones, by driving the zero-phonon line.

In the regime of deep lattices, I have displayed a series of measurements using different spectroscopy techniques, namely Rabi and Ramsey spectroscopy. We have taken advantadge of these results to infer the dephasing mechanisms that are present in our experiments. We have recognized inhomogeneous dephasing due to the spatial profile of the probe and possibly slow frequency fluctuations of the laser as the main sources. These experiments have allowed us to give an answer from atomic measurements to the question *«for how long can we drive the clock transition in a coherent manner?»*: on the order of $\Delta\omega^{-1} \simeq 30\,\mathrm{ms}$, limiting our Rabi oscillations and Ramsey experiments with echo. On top of this, the central frequency $\bar{\omega}_L$ slowly drifts in a scale much larger than the probing time and on the order of the duration of a sequence (see figure 3.16), which we think is the main dephasing source in the Ramse experiments without an echo.

The next steps in orther to better characterize these sourecs require a careful characterization of the eventual slow drifts of the ULE cavity. With this and some assumptions on the noise of the laser, one can then infer a quantitative relationship between the observed dephasing rate and the frequency noise spectral density of the laser (Domenico

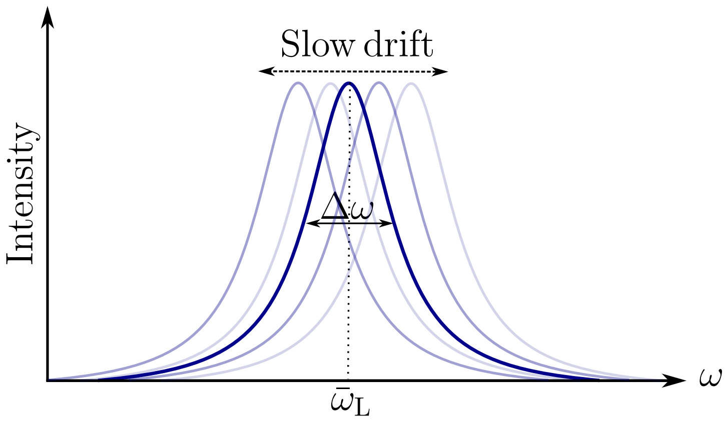

**Figure 3.16** – Scheme of the processes determining the laser frequency: On the one hand, fast fluctuations, occurring in the time scale the atoms are probed, give an effective width $\Delta\omega$ to the laser. On the other hand, slower drifts on the order of the time of a whole experimental sequence, change the central frequency $\bar{\omega}_{\mathrm{L}}$ from one shot to another.

et al. 2010). This study is currently being performed in our team by Alexis Ghermaoui and more details will be given in his PhD thesis.

# CHAPTER 4

# Interacting pairs in an optical lattice

In this chapter, I will focus on the physics of interacting atom pairs coherently driven on the clock transition. In the first section I will use spectroscopy to characterize the elastic and inelastic interactions between particles, either in the same or in different internal states. These measurements allowed us to infer the corresponding scattering lengths, unknown at the time we performed the experiments (Bouganne et al. 2017). Similar measurements were performed in parallel by the ytterbium team at LENS, in Florence, finding results which are compatible with ours (Franchi et al. 2017).

From these analyses we extracted a large value for the inelastic loss rate between two atoms in the excited state. Such processes are harmful for most experimental purposes since, on top of the losses, which end up limiting the signal-to-noise ratio, they constitute a potential source of entropy and decoherence. Therefore, finding an experimental procedure preventing the excitation to such states is desirable. In the second section of this chapter, I will show that the transfer to these lossy states can actually be strongly suppressed in certain conditions due to the presence of the losses itself, which is a manifestation of so-called quantum Zeno effect (Misra et al. 1977).

The quantum Zeno effect was initially proposed by Misra et al. (1977) in the context of quantum measurements, where they predicted that repeatedly measuring the state of a driven quantum system should freeze its coherent evolution. More than a decade after this, their idea was first verified experimentally in a system of ions by Itano et al. (1990). Since then, our understanding of the Zeno effect has been refined (Facchi et al. 2008) and many experiments taking advantage in some manner of the quantum Zeno effect have been performed.

In the context of quantum information, the quantum Zeno effect is used to prepare systems of qubits in the so-called decoherence-free subspaces (Beige et al. 2000). In the ultracold atom community, quantum Zeno dynamics have been observed by using a BEC in Streed et al. (2006). Also, the role of inelastic losses as an equivalent to the effect of a measurement has been investigated. In Syassen et al. (2008); Yan et al. (2013) and Zhu et al. (2014) an ensemble of molecules was loaded in an optical lattice with unit filling. Tunneling could eventually generate sites with double occupancies. In the occurrence of such events, molecules would undergo recombination processes leading to strong inelastic losses. However, these experiments showed that coherent tunneling was partially suppressed, and that the stronger the losses, the longer the ensemble lived. The system was actually driven into a strongly correlated state in which bosons behave as free fermions (García-Ripoll et al. 2009), showing that strong inelastic losses play a similar role as elastic interactions, and can drive a 1D system into a Tonks-Girardeau gas (Tonks 1936; Girardeau 1960). In an equivalent framework with fermionic atoms, Sponselee et al. (2019) observed that inelastic losses led the system into a highly-correlated state (Foss-Feig et al. 2012) where the atom loss perishes. Losses have also been locally induced in a BEC. Here, the dynamics reach a regime in which the number of lost atoms decreases as the strength of the dissipation is increased (Barontini et al. 2013). Tomita et al. (2017) observed that, while driving a system from the Mott insulator to the superfluid regime in an optical lattice, the growth of phase coherence induced by tunneling was delayed in the presence of strong dissipation. This delay was interpreted as a quantum Zeno suppression of coherent tunneling, preventing the atoms to delocalize, thus minimizing the dissipation.

In the second part of this chapter, I will show how the presence of two-body losses in our system freezes the coherent dynamics induced by the coupling. This second section is organized as follows: After a brief reminder of the key concepts concerning the evolution of an open quantum system and its connection to the quantum Zeno effect, I present an effective non-Hermitian Hamiltonian that describes the dynamics of atom pairs coupled by a laser and in the presence of losses. I will show that most of the observed effects and the emergence of a reduced-loss subspace can be directly linked to the spectrum of this non-Hermitian Hamiltonian, whose structure I compare in the last part of the chapter to our experimental data.

## 4.1 Spectroscopy of interacting atom pairs

### 4.1.1 Framework and experimental setup

We now focus on the dynamics of bosonic pairs in disconnected wells of an optical lattice. For this, we transfer into the optical lattice a BEC with $N \simeq 8 \times 10^4$ atoms, which is enough to prepare a Mott insulator with doubly-occupied sites present [see figure 4.1(a) and the discussion below]. The lattice is loaded following the procedure described in section 2.2.2, so that we end up with a stack of 2D independent horizontal lattices, with the atoms loaded in the fundamental bands, with different proportions of singly- and doubly-occupied sites. The atoms are then probed on the clock transition by a laser propagating in the plane defined by the lattices. The probe propagates at 45° with respect to the axis defined by the lattice beams [see figure 4.1(a)].

While driving these atoms on the clock transition, a first striking difference that we observe [see figure 4.1(b), where Rabi oscillations are being performed] with respect to the coherent dynamics of single particles shown in chapter 3 is the very strong decay on the order of the first hundreds of µs. This reduction is then followed by long-lived Rabi oscillations. We interpret the initial collapse of the atom number as a signature of strong inelastic two-body losses, emptying all doubly-occupied sites. The dynamics is then followed by the coherent evolution of the singly-occupied sites alone. The goal of the following sections is to determine the rate of these inelastic collisions, $\gamma_{eg}, \gamma_{ee}$,

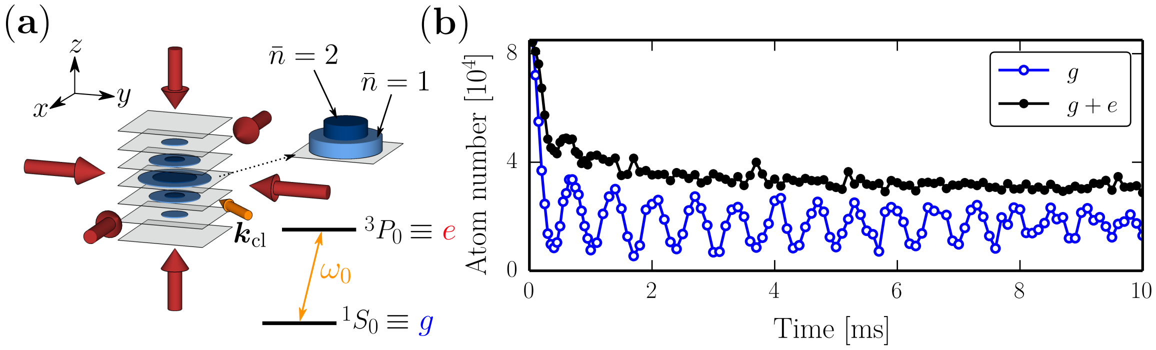

**Figure 4.1** – **(a)** Sketch of the three-dimensional lattice geometry. The drawing also illustrates the density profile of the Mott insulator and the level scheme of the ultra-narrow clock transition connecting the ground state $g$ and the metastable excited state $e$. **(b)** Coherent driving on the clock transition in the deep Mott insulator regime. A coupling laser resonant on the clock transition is switched on at time $t = 0$ with a Rabi frequency $\Omega_{\mathrm{L}}/(2\pi) \simeq 1500\,\mathrm{Hz}$. Closed (respectively open) symbols represent the remaining total atom number (resp. the population in the ground state $g$). Figure reproduced from Bouganne et al. (2017).

as well as to characterize the intra- and inter-species scattering lengths $a_{eg}$ and $a_{ee}$ describing the elastic interactions between atom pairs.

### The method

The method we employ is schematized in figure 4.2. It is based on the fact that, due to interactions, doubly-occupied sites are energy shifted with respect to the singly-occupied sites, and these shifts should emerge when performing spectroscopy. Since we set the optical lattice at the magic wavelength, the Wannier functions in different internal states are equal and the on-site energy shifts are given by:

$$U_{ij} = \frac{4\pi\hbar^2}{M} a_{ij} \int |w(\boldsymbol{r})|^4 \, \mathrm{d}^3 r. \tag{4.1}$$

Here, $i, j = \{e, g\}$ and $a_{ij}$ are the scattering lengths characterizing the elastic collisions between an atom in state $i$ and another in $j$.

The different interaction strengths translate into an energy shift with respect to a lattice site with two atoms in $g$. For a lattice with one atom in $g$ and one atom in $e$ this shift is $\hbar\delta_1 = U_{eg} - U_{gg}$. At the same time, this state is displaced by $\hbar\delta_2 = U_{ee} - U_{eg}$ with respect to the situation in which the two atoms are in $e$. Besides these energy shifts, atoms in such states are likely to decay via two-body inelastic processes. Two atoms in $g$ are stable, but the other two configurations will eventually lead to atom losses at rates that we denote as $\gamma_{eg}$ and $\gamma_{ee}$, respectively. These decay rates are related to the imaginary part of the scattering length through the two-body loss rate coefficient $\beta_{ij} = -(8\pi\hbar/M)\mathrm{Im}[a_{ij}]$ and we can write (see appendix B):

$$\gamma_{ij} = \beta_{ij} \int |w(\boldsymbol{r})|^4 \, \mathrm{d}^3 r. \tag{4.2}$$

Performing spectroscopy, thereby allows one to determine the elastic scattering lengths thanks to the additional peaks that appear on top of the $g \to e$ single-particle resonance

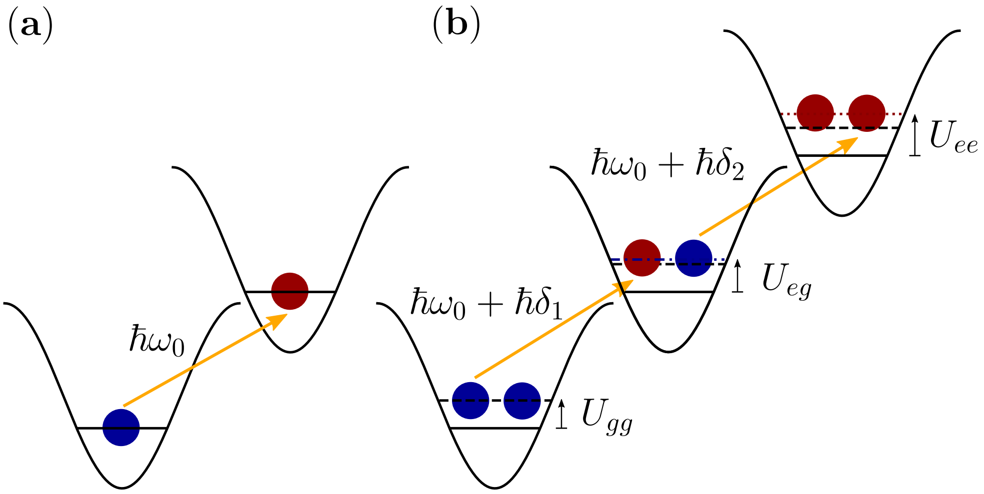

**Figure 4.2** – Schematics of the method to measure the interaction shifts by performing spectroscopy. **(a)** Atoms in singly-occupied sites show a resonant peak at the bare resonance frequency $\omega_0$. **(b)** Atoms in doubly occupied sites experience an interaction energy shift $U_{ij} \propto a_{ij}$ which depends on the internal state of the atom. These shifts can then be measured by performing spectroscopy.

at $\delta_\mathrm{L} = 0$. These peaks correspond to the $gg \to eg$ transition (one-photon process) and to the $gg \to ee$ transition (two-photon process), and are located at the following detunings:

$$\delta_\mathrm{L} = \delta_1 = \frac{U_{eg} - U_{gg}}{\hbar}, \qquad \delta_\mathrm{L} = \frac{\delta_1 + \delta_2}{2} = \frac{U_{ee} - U_{gg}}{2\hbar}, \tag{4.3}$$

respectively. The decay rates $\gamma_{ij}$ can be inferred by transferring atoms either into the *eg* or *ee* states and performing a lifetime measurement, i.e., by recording the remaining population at different holding times.

### Experimental setup and determination of the Mott shells

**Experimental setup.** All the measurements shown in this chapter are performed in an optical lattice at the magic wavelength and at fixed lattice depths, measured by the Kapitza Dirac technique described in section 2.2.1: The vertical lattice is at $V_z = 27\,E_\mathrm{r}$ and the horizontal ones are set at $(V_x, V_y) \simeq (24, 25.4)\,E_\mathrm{r}$, deep in the Mott insulator regime. It is then safe to neglect tunneling, on the order of $\hbar/J \simeq 70\,\mathrm{ms}$ , compared to the timescale of the experiments presented in this section, which are on the order of a few ms. We can thus consider the lattice sites as independent. The on-site interaction shift $U_{gg}/h = 1475(25)\,\mathrm{Hz}$ for two atoms in the ground state, has been measured by the method of collapse and revival exposed in section 2.2.4. Atoms are then probed on the zero-phonon line with the geometry shown in figure 4.1(a).

In the following sections we will refer to experiments in which we either measure (i) the total population of atoms in $g$, achieved by regular absorption imaging, (ii) the total atom number $e+g$, which we obtain by repumping atoms in $e$ back to the ground state and then using absorption imaging and finally (iii) only atoms in $e$. For this last one, we first send an intense beam, resonant with the ${}^1\mathrm{S}_0 \to {}^1\mathrm{P}_1$ transition to remove the population of $g$ atoms (we call this the *blasting* procedure), and then we repump

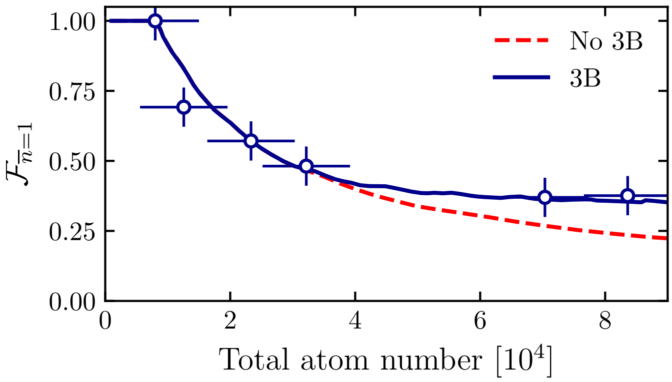

**Figure 4.3** – Normalized population $\mathcal{F}_{\bar{n}=1}$ of the Mott shell with single occupancy as a function of the total atom number $N_{\mathrm{at}}$. Data points are extracted from the asymptotic behavior of coherent oscillations such as the one shown in figure 4.1(b), for different initial atom numbers. The dashed line is the prediction from our loading model assuming adiabaticity and zero temperature (see section 2.2.2). The solid line numerically accounts for three-body collisions: We consider that sites with triple occupancy are quickly emptied by three-body events. Figure adapted form Bouganne et al. (2017)

the atoms in $e$ back to $g$ and image them.

**Determination of the Mott shells.** The long-time asymptote $N_\infty$ in the $e$+$g$ curve in figure 4.1(b) corresponds to the number of sites with only one atom. This kind of measurements can thus be used to extract the initial fraction of singly-occupied sites $\mathcal{F}_{\bar{n}=1}$. Assuming our lattice contains only singly- and doubly-occupied sites [see below], the initial total atom number can be written as $N_0 = L(\mathcal{F}_{\bar{n}=1} + 2\mathcal{F}_{\bar{n}=2})$, with $L$ the total number of sites and $\mathcal{F}_{\bar{n}=2}$ the fraction of doubly occupied sites, so that $\mathcal{F}_{\bar{n}=1} + \mathcal{F}_{\bar{n}=2} = 1$. The asymptote corresponds to $N_\infty = L\mathcal{F}_{\bar{n}=1}$ since, at long times, all doubly-occupied sites have decayed. Combining these two equations, the fraction of singly occupied sites can be expressed as:

$$\mathcal{F}_{\bar{n}=1} = \frac{2N_\infty}{N_0 + N_\infty}. \tag{4.4}$$

This offers a way to test the loading model presented in section 2.2.2, by comparing the predicted density distribution to the one we infer experimentally. We do this by driving Rabi oscillations at different initial atom numbers and we extract for each measurement the fraction of singly-occupied sites, $\mathcal{F}_{\bar{n}=1}$, thanks to the asymptotic value. We show the inferred fractions in figure 4.3. Here, the dashed line corresponds to the predicted fraction of $\bar{n} = 1$ sites using our loading model described in section 2.2.2: For a small atom number of $N = 8 \times 10^3$ atoms our model predicts only a plateau with $\mathcal{F}_{\bar{n}=1} = 1$, which agrees well with the data. However, for larger atom numbers our model predicts several insulating plateaus (including filling fractions $\bar{n} > 2$) and the $\bar{n} = 1$ fraction that we measure is actually underestimated by the model. As an example, for $N = 8 \times 10^4$ atoms we predict the following fractions: $\mathcal{F}_{\bar{n}=\{1,2,3\}} = (0.25, 0.39, 0.36)$. We think this disagreement arises from three-body losses[55] occurring during the loading of the lattice. By taking the losses heuristically into account (basically, we suppose that at

---

[55] The three body loss rate $K_3 \simeq 7 \times 10^{-30}\,\mathrm{cm}^6/\mathrm{s}$ (Kitagawa et al. 2008) leads to a loss rate $\tau_3 \simeq 100\,\mathrm{ms}$ at $20\,E_{\mathrm{r}}$, which is comparable to our loading times.

the end of the loading all triply-occupied sites have disappeared, which corresponds to the solid line in figure 4.3) we find a good agreement with our measurements. For $N = 8 \times 10^4$ atoms we obtain $\mathcal{F}_{\bar{n}=\{1,2,3\}} = (0.36, 0.64, 0)$. Therefore, from now on, we use the loading model presented in section 2.2.2 together with the three-body suppression whenever we need to determine our density distribution.

---

*The content presented in sections 4.1.2-4.1.5, denoted by $*$, has been published in Bouganne et al. (2017) and is exposed here without major modifications. Only a few notations have been changed and some footnotes and references to within the manuscript have been added.*

---

### 4.1.2 Model (∗)

The dynamics of single particles in isolated wells driven in the clock transition considered in the previous chapter is well described by the Hamiltonian:

$$\hat{H}^{(1)} = \hbar \begin{pmatrix} 0 & \dfrac{\Omega_\mathrm{L}}{2} \\ \dfrac{\Omega_\mathrm{L}}{2} & -\delta_\mathrm{L} \end{pmatrix}, \tag{4.5}$$

with $\Omega_\mathrm{L}$ and $\delta_\mathrm{L} = \omega_\mathrm{L} - \omega_0$ the Rabi frequency and the detuning, respectively.

We will now consider the dynamics of doubly-occupied sites driven by the coupling laser, which differs from singly-occupied sites in several aspects. First, due to bosonic enhancement, the coupling strength is $\sqrt{2}$ times higher for double than for single occupancy. Second, the three possible symmetric states $|gg\rangle$, $|eg\rangle$ and $|ee\rangle$ have in general different interaction energies, characterized by Hubbard parameters $U_{gg}$, $U_{eg}$ and $U_{ee}$, the last two being unknown. Finally, the states $|eg\rangle$ and $|ee\rangle$ are prone to inelastic decay via principal quantum number changing collisions. We model this inelastic process by adding an imaginary term $-\mathrm{i}\hbar\gamma_{e\alpha}/2$ to the Hamiltonian, with $\alpha = e, g$. This results in a dynamics captured by a non-Hermitian effective Hamiltonian [see the discussion in section 4.2.1 below]:

$$\hat{H}_\mathrm{eff}^{(\overline{n}=2)} = \begin{pmatrix} 0 & \dfrac{\hbar\Omega_\mathrm{L}}{\sqrt{2}} & 0 \\ \dfrac{\hbar\Omega_\mathrm{L}}{\sqrt{2}} & U_{eg} - U_{gg} - \mathrm{i}\dfrac{\hbar\gamma_{eg}}{2} - \hbar\delta_\mathrm{L} & \dfrac{\hbar\Omega_\mathrm{L}}{\sqrt{2}} \\ 0 & \dfrac{\hbar\Omega_\mathrm{L}}{\sqrt{2}} & U_{ee} - U_{gg} - \mathrm{i}\dfrac{\hbar\gamma_{ee}}{2} - 2\hbar\delta_\mathrm{L} \end{pmatrix} \tag{4.6}$$

in the $\{|gg\rangle, |eg\rangle, |ee\rangle\}$ basis.

We numerically solve the generalized Schrödinger equation using the effective Hamiltonian in equation (4.6) with initial condition $|\Psi^{(2)}\rangle = |gg\rangle$. We also solve the Schrödinger equation for singly-occupied sites using equation (4.5) with initial condition $|\Psi^{(1)}\rangle = |g\rangle$. This gives transition probabilities denoted $P_\alpha^{(2)} = |\langle\alpha|\Psi^{(2)}\rangle|^2$ with $\alpha = gg, eg, ee$ and $P_\beta^{(1)} = |\langle\beta|\Psi^{(1)}\rangle|^2$ with $\beta = g, e$. We then sum the contributions of doubly- and

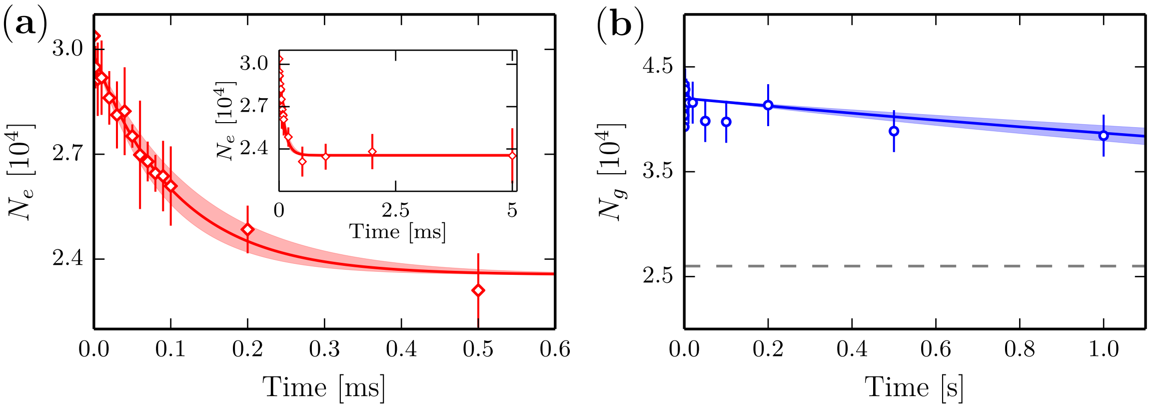

**Figure 4.4** – **(a)** Lifetime measurement for a sample with only atoms in $e$. Doubly-occupied sites quickly decay through inelastic collisions. The inset shows the plateau of remaining singly-occupied sites for longer times. **(b)** Absence of inelastic collisions involving $g$ and $e$. The dashed line shows the asymptote expected for a complete decay of $e-g$ pairs. In **(a)** and **(b)**, solid lines are exponential fits to the data, with the shaded area reflecting the 68 % confidence intervals. Figure reproduced from Bouganne et al. (2017).

singly-occupied sites to obtain the average populations $\overline{N}_g$ and $\overline{N}_e$. For example, we have[56]

$$\frac{\overline{N}_e}{N_{\mathrm{at}}} = \eta_e \mathcal{F}_{\overline{n}=1} P_e^{(1)} + \eta_e \mathcal{F}_{\overline{n}=2} \left( P_{ee}^{(2)} + \frac{1}{2} P_{eg}^{(2)} \right). \tag{4.7}$$

We assume the repumping efficiency $\eta_e$ to be independent from the filling factor for simplicity.

### 4.1.3 Lifetime of doubly-occupied sites (∗)

In this section we measure the inelastic loss rates $\gamma_{ee}$ and $\gamma_{eg}$. We first investigate the role of $e-e$ inelastic collisions. After a coupling laser pulse of area $\Omega_{\mathrm{L}} T \simeq \pi$ [$\Omega_{\mathrm{L}}/(2\pi) \simeq 1500\,\mathrm{Hz}$] in order to obtain a substantial population of $|ee\rangle$, we apply a removal pulse (see section 4.1.1) to get rid of remaining atoms in state $g$. We are then left with a collection of singly- and doubly-occupied sites where all atoms are in the excited state $e$. We show in figure 4.4(a) the measured lifetime of this sample. We detect a fast exponential decay at short times which we interpret as the consequence of inelastic $e-e$ collisions. For longer times, we observe a plateau corresponding to the remaining $e$ atoms in singly-occupied sites. The exponential decay rate is a direct measurement of $\gamma_{ee} = 9300(100)\,\mathrm{s}^{-1}$ [see appendix B].

A similar technique is used to investigate the role of $e-g$ inelastic collisions. We apply a coupling laser pulse of area $\Omega_{\mathrm{L}} T \simeq \pi/2$ [$\Omega_{\mathrm{L}}/(2\pi) \simeq 1500\,\mathrm{Hz}$] in order to obtain a substantial population of $|eg\rangle$. We measure the atom number in the ground state

---

[56] For atoms in the ground state, we have a similar relation:

$$\frac{\overline{N}_g}{N_{\mathrm{at}}} = \mathcal{F}_{\overline{n}=1} P_g^{(1)} + \mathcal{F}_{\overline{n}=2} \left( P_{gg}^{(2)} + \frac{1}{2} P_{eg}^{(2)} \right).$$

$g$ which is expected to decay as $\dot{N}_g/N_{\text{at}} = -\gamma_{eg}\mathcal{F}_{\overline{n}=2}P_{eg}^{(2)}/2$. Figure 4.4(b) shows a typical measurement, where almost no losses occur even after one second. In order to extract a damping rate, we fix the initial populations using the model in section 4.1.1. An exponential fit to the data, with a rate $\gamma$ as the only free parameter, yields $\gamma = 0.5(1)\,\text{s}^{-1}$. The projected asymptote of the decay is represented with the dashed line in figure 4.4(b). We measure a similar lifetime for atoms in $g$ in the absence of the coupling laser. Hence the measured damping rate $\gamma$ is only an upper bound for $\gamma_{eg}$.

### 4.1.4 Spectroscopy of elastic interactions (∗)

We now turn to the determination of elastic interaction parameters $U_{eg}$ and $U_{ee}$. To this end, we perform spectroscopic experiments probing doubly-occupied sites. The method is illustrated in figure 4.5(a)-(b), and the measurements shown in figure 4.5(c)-(d).

The determination of $U_{eg}$ is best performed in a perturbative limit, where the pulse area and the population of $|ee\rangle$ remain small [figure 4.5(a)]. The time evolution of $|\Psi^{(2)}\rangle$ then reduces to that of a two-level system resonant for $\hbar\delta_{\text{L}} = U_{eg} - U_{gg}$. This resonance is well-resolved provided that the Rabi frequency is much smaller than $(U_{eg} - U_{gg})/\hbar$.

In order to extract the interaction strength $U_{ee}$, one could in principle use a two-photon resonance directly linking $|gg\rangle$ and $|ee\rangle$. This requires a weak enough Rabi frequency $\Omega_{\text{L}} \ll \Delta$ and $\delta'_{\text{L}} \ll \Delta$, where $\hbar\Delta = U_{eg} - (U_{ee} + U_{gg})/2$ is an interaction shift and where $\delta'_{\text{L}} = \delta_{\text{L}} - (U_{ee} - U_{gg})/(2\hbar)$ is the two-photon detuning. Under these conditions, the intermediate state $|eg\rangle$ can be adiabatically eliminated, and the dynamics reduces to that of an effective two-level system. The difference $(U_{ee} - U_{gg})/2$ can therefore be directly measured from the location of the two-photon resonance. Practically, this idealized experiment is difficult to perform for weak coupling due to the strong loss rate $\gamma_{ee}$, which gives a substantial width to the two-photon resonance. In order to circumvent this issue, we perform the experiment at a larger Rabi frequency, and make use of the losses by measuring $N_g + N_e$ after a clock pulse of area $\Omega_{\text{L}}T = 2\pi$ [figure 4.5(b)]. The background signal from singly-occupied sites is minimized near resonance, whereas doubly-occupied sites show a pronounced feature due to $e - e$ losses located at $\hbar\delta_{\text{L}} \simeq (U_{ee} - U_{gg})/2$. Even for large Rabi frequencies, we find that the loss spectral feature in the total signal is only weakly affected by the intermediate $|eg\rangle$ state [inset of figure 4.5(b)].

The experimental results are presented in figures 4.5(c)-(d). Data is centered so that $\delta_{\text{L}} = 0$ corresponds to the single-atom resonance. The measurement of $U_{eg}$ [figure 4.5(c)] is done with a weak Rabi frequency $\Omega_{\text{L}}^{\text{weak}}/(2\pi) \simeq 150\,\text{Hz}$ and displays a shoulder near $\delta_{\text{L}}/(2\pi) \simeq -300\,\text{Hz}$. This corresponds to the signal from doubly occupied sites. On the other hand, the measurement of $U_{ee}$ [figure 4.5(d)], performed at strong Rabi frequency $\Omega_{\text{L}}^{\text{strong}}/(2\pi) \simeq 1500\,\text{Hz}$, shows a loss peak almost coincident with $\delta_{\text{L}}/(2\pi) \simeq 0\,\text{Hz}$, or equivalently $U_{ee} \simeq U_{gg}$. To extract quantitative values, we fit the prediction of the model from section 4.1.2 to the experimental spectra [solid and dashed lines in figures 4.5(c)-(d)]. We fix the normalized populations $\mathcal{F}_{\overline{n}=1,2}$, the loss rates $\gamma_{ee}$, $\gamma_{eg}$ and the initial atom number $N_{\text{at}}$ to their measured values and leave the Rabi frequencies $\Omega_{\text{L}}^{\text{weak}}$, $\Omega_{\text{L}}^{\text{strong}}$, the interaction energies $U_{ee}$, $U_{eg}$ and the repumping efficiency $\eta_e$ as free parameters. The prediction of the model has been further con-

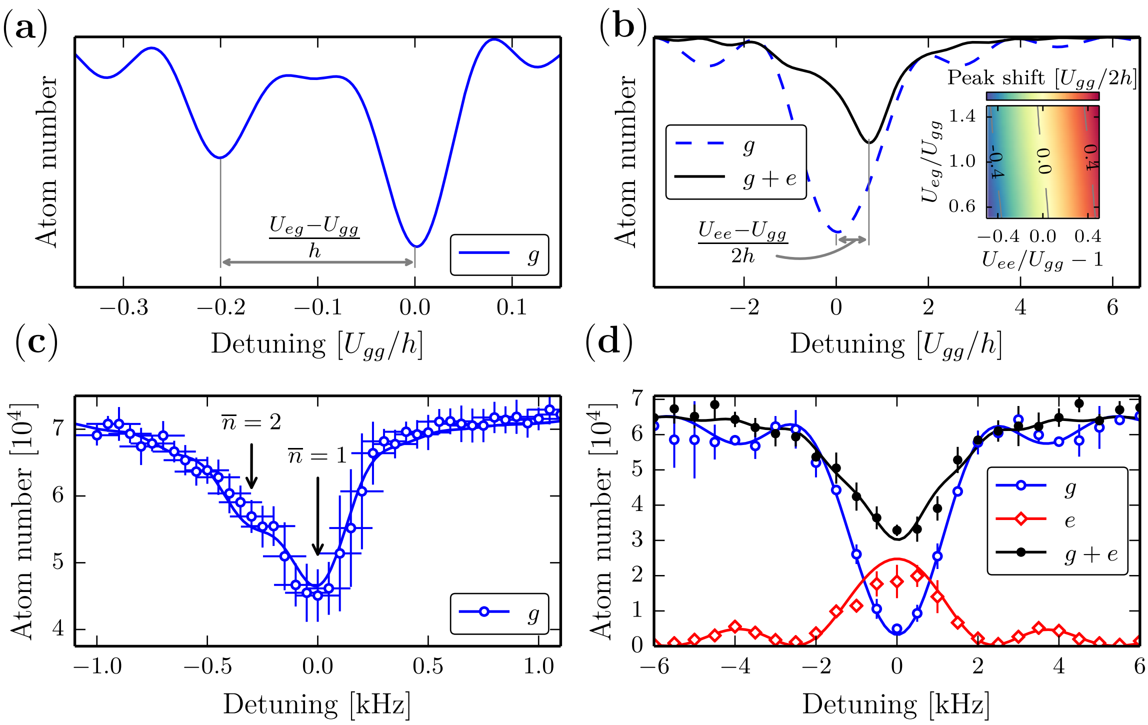

**Figure 4.5** – Determination of $U_{eg}$ and $U_{ee}$, (a-b) illustrate the methods, (c-d) show the measurements. **(a)** Method for measuring $U_{eg}$. The number of atoms in $g$ is plotted with respect to detuning, with a pulse area $\Omega_{\mathrm{L}}T = \pi$. Singly-occupied sites are excited on the single-atom resonance near $\delta_{\mathrm{L}} = 0$, with $\delta_{\mathrm{L}}$ the laser detuning. Interactions shift the resonance for doubly-occupied sites to $\delta_{\mathrm{L}} = (U_{eg} - U_{gg})/\hbar$. This interaction sideband can be resolved with sufficiently weak Rabi frequency $\Omega_{\mathrm{L}} \ll |U_{eg} - U_{gg}|/\hbar$. For illustrative purposes, $\Omega_{\mathrm{L}}/(2\pi) = 70\,\mathrm{Hz}$ and $U_{eg} = 0.8\,U_{gg}$ in this plot. **(b)** Method for measuring $U_{ee}$. For strong Rabi frequencies and pulse area $\Omega_{\mathrm{L}}T = 2\pi$, the total population of doubly occupied sites has decreased due to inelastic collisions (black solid line). This loss resonance is shifted with respect to the single-atom resonance (dashed blue line, pulse area $\Omega_{\mathrm{L}}T = \pi$) by $(U_{ee} - U_{gg})/(2\hbar)$, with weak dependence on $U_{eg}$ (see inset). For illustrative purposes, $\Omega_{\mathrm{L}}/(2\pi) = 1500\,\mathrm{Hz}$ and $U_{ee} = 2.5\,U_{gg}$ in this plot. **(c)** Experimental determination of $U_{eg}$ with $\Omega_{\mathrm{L}}T \simeq \pi$. The shoulder near $\delta_{\mathrm{L}}/(2\pi) \simeq -300\,\mathrm{Hz}$ indicates the excitation of doubly occupied sites. **(d)** Experimental determination of $U_{ee}$. The open symbols show $N_g$ for the reference measurement with $\Omega_{\mathrm{L}}T \simeq \pi$ locating the single-atom resonance. The closed ones correspond to $N_g + N_e$ for the loss measurement with $\Omega_{\mathrm{L}}T \simeq 2\pi$. The loss curve is almost centered on the single-atom resonance. A common fit to all data sets in **(c)** and **(d)** (solid and dashed lines) yields best fit parameters $U_{ee} = 0.97(23)\,U_{gg}$ and $U_{eg} = 0.82(8)\,U_{gg}$ (see text). The quoted error bars are statistical 68 % confidence intervals obtained by the bootstrap method. In all plots, zero detuning corresponds to the single-atom resonance. Figure reproduced from Bouganne et al. (2017).

volved with a Gaussian function to account for frequency jitter of the clock laser, the width $\sigma$ being left as an extra free parameter. We obtain $\Omega_{\mathrm{L}}^{\mathrm{weak}}/(2\pi) = 145(13)\,\mathrm{Hz}$, $\Omega_{\mathrm{L}}^{\mathrm{strong}}/(2\pi) = 1470(70)\,\mathrm{Hz}$ and $\eta_e = 68(6)\,\%$, consistent with our calibrations. The width of the convolving Gaussian $\sigma = 100(40)\,\mathrm{Hz}$, is consistent with the narrowest spectrum we could observe, as discussed in section 3.5.2. Finally we extract

$(U_{ee} - U_{gg})/h = -40(340)\,\mathrm{Hz}$ and $(U_{eg} - U_{gg})/h = -270(120)\,\mathrm{Hz}$, in agreement with the qualitative discussion above. The error bars represent statistical 68 % confidence intervals on the optimal values of $U_{eg}$ and $U_{ee}$, obtained by the bootstrap method.

### 4.1.5 Determination of atomic parameters (∗)

The ratio of the elastic interaction parameters $U_{eg}$ and $U_{ee}$ to $U_{gg}$ is directly proportional to the ratio of the respective scattering lengths. From our calibration of $U_{gg}$ (see section 2.2.4) we get:

$$a_{eg} - a_{gg} = -19(11)\,a_0, \tag{4.8}$$

$$a_{ee} - a_{gg} = -3(25)\,a_0. \tag{4.9}$$

The error bars do not account for possible systematic errors (for instance, in determining $U_{gg}$). Combining our measurements and the value $a_{gg} = 105\,a_0$ from Kitagawa et al. (2008), we obtain the scattering lengths $a_{eg} = 86(11)\,a_0$, $a_{ee} = 102(25)\,a_0$. We thus find all scattering lengths involving the clock states of $^{174}$Yb equal within 20 %. The near-equality of the scattering lengths is somewhat surprising. These observations differ markedly from the fermionic $^{173}$Yb isotope, where the equivalent scattering lengths have been found very different from one another (Cappellini et al. 2014; Scazza et al. 2014).

We also extract from the loss rate $\gamma_{ee}$ the two-body loss rate constant $\beta_{ee}$ that enters into the rate equation $\mathrm{d}\langle\hat{\Psi}_e^\dagger\hat{\Psi}_e\rangle/\mathrm{d}t = -\beta_{ee}\langle\hat{\Psi}_e^\dagger\hat{\Psi}_e^\dagger\hat{\Psi}_e\hat{\Psi}_e\rangle$ [the relation between the two is $\hbar\gamma_{ee}/U_{gg} = M\beta_{ee}/(4\pi\hbar a_{gg})$, see appendix B]. We find:

$$\beta_{ee} = 2.6(3) \times 10^{-11}\,\mathrm{cm}^3/\mathrm{s}. \tag{4.10}$$

This value is in line with comparable measurements in strontium or fermionic ytterbium (Scazza et al. 2014; Traverso et al. 2009; Ludlow et al. 2011). As noted in section 4.1.3, we can only give an upper bound on the rate constant $\beta_{eg} \leq 10^{-15}\,\mathrm{cm}^3/\mathrm{s}$. Low $e - g$ inelastic loss rates were also observed for fermionic $^{173}$Yb (Scazza et al. 2014) and $^{87}$Sr (Bishof et al. 2011).

Similar experiments have been performed by the ytterbium team at LENS in Florence (Franchi et al. 2017). Their results agree with ours within the uncertainties.

### 4.1.6 Summary and conclusion

In this section, I have shown a series of spectroscopic measurements performed on bosonic pairs in an optical lattice. The strong initial decay observed during Rabi oscillations experiments, which is a signature of strong inelastic two-body losses, has allowed us to verify our lattice loading model thanks to the asymptotic values of these decays. In order to reproduce our data, we have seen that three-body losses during the loading stages need to be taken into account.

The two-body loss rates responsible for the initial decay while performing Rabi oscillations have been determined by performing lifetime experiments. Finally, by recording spectra at both low and high Rabi frequencies we have measured the interaction spectroscopic shifts giving access to the intra- and inter-state scattering lengths. The extracted values are summarized in table 4.1 below. In the same table, we also show the values measured by the LENS team (Franchi et al. 2017). Their values for the scattering lengths are more precise than ours and we use these in the rest of the manuscript.

| Quantity | LKB (Bouganne et al. 2017) | LENS (Franchi et al. 2017) |
|---|---|---|
| $a_{eg}$ $[a_0]$ | 86(11) | 94.7(1.6) |
| $a_{ee}$ $[a_0]$ | 102(25) | 126.7(2.3) |
| $\beta_{eg}$ $[\mathrm{cm}^3/\mathrm{s}]$ | $\leq 1 \times 10^{-15}$ | $\leq 1 \times 10^{-14}$ |
| $\beta_{ee}$ $[\mathrm{cm}^3/\mathrm{s}]$ | $2.5(1) \times 10^{-11}$ | $1.3(7) \times 10^{-11}$ |

Table 4.1: Intra- and inter-state scattering lengths together with the two-body loss rates measured in this work and comparison with te values reported in Franchi et al. (2017). The ground state scattering length has been measured in Kitagawa et al. (2008) and is $a_{gg} \simeq 105\, a_0$, with $a_0$ the Bohr radius.

## 4.2 Quantum Zeno dynamics of «dressed» pairs in a deep optical lattice

In the previous section, we have seen that all the measured interaction strengths, either elastic $(U_{eg}, U_{ee})$ or inelastic $(\hbar\gamma_{ee})$, are close to the on-site interaction strength $U_{gg}$. This leads to very small frequency shifts for the transitions $|gg\rangle \to |eg\rangle$ and $|gg\rangle \to |ee\rangle$. Moreover, due to inelastic losses and the broadening sources discussed in section 3.6 these transitions are not easily resolved, even at small Rabi frequencies. In particular, this means that driving the transition $|gg\rangle \to |eg\rangle$ without populating the lossy $|ee\rangle$ state will be a challenging task.

In this section we show that, by performing adiabatic passages for weak coupling strengths $(\Omega_\mathrm{L} \ll \gamma_{ee})$, the transfer to the lossy state $|ee\rangle$ is strongly suppressed. The stronger the losses, the stronger the transfer rate is reduced, leading to a longer lifetime of the samples. This is reminiscent to the observation of a *quantum Zeno effect* where, the presence of strong losses in the $|ee\rangle$ state would act as a continuous measurement preventing the coherent driving towards this state. This arises naturally when considering non-Hermitian Hamiltonians as the one in equation (4.6), as we show in the following.

### 4.2.1 The quantum Zeno effect

**Open quantum systems and the Lindblad equation**

In quantum mechanics, one frequently faces the problem concerning the relaxation dynamics of a small system $\mathcal{S}$ coupled to an environment or large *reservoir* $\mathcal{R}$ (an *open* quantum system). In general, because of this coupling, the dynamics of $\mathcal{S}$ alone are no longer unitary due to the correlations arising between $\mathcal{S}$ and $\mathcal{R}$. Still, under some approximations, even in this case, one can derive an effective equation of motion for the small system $\hat{\rho}_\mathcal{S}$ by tracing over the many modes of the environment, i.e. $\hat{\rho}_\mathcal{S} = \mathrm{tr}_\mathcal{R}[\hat{\rho}_\mathcal{S} \otimes \hat{\rho}_\mathcal{R}]$.

It can be shown that the evolution of $\mathcal{S}$ can be cast as the sum of a unitary evolution given by the free Hamiltonian of $\mathcal{S}$ and a *dissipator* $\mathcal{L}[\hat{\rho}_{\mathcal{S}}]$, characterizing the relaxation mechanisms of the small system. These dynamics are given by a master equation, which in the so-called *Lindblad* form reads (Breuer et al. 2007; Haroche et al. 2013):

$$\frac{\mathrm{d}}{\mathrm{d}t}\hat{\rho}_{\mathcal{S}}(t) = \frac{1}{\mathrm{i}\hbar}[\hat{H}_{\mathcal{S}}, \hat{\rho}_{\mathcal{S}}(t)] + \mathcal{L}[\hat{\rho}_{\mathcal{S}}(t)] \tag{4.11}$$

$$= \frac{1}{\mathrm{i}\hbar}[\hat{H}_{\mathcal{S}}, \hat{\rho}_{\mathcal{S}}(t)] + \sum_{\mu} \gamma_{\mu} \left[\hat{L}_{\mu}\,\hat{\rho}_{\mathcal{S}}(t)\hat{L}_{\mu}^{\dagger} - \frac{1}{2}\hat{L}_{\mu}^{\dagger}\hat{L}_{\mu}\,\hat{\rho}_{\mathcal{S}}(t) - \frac{1}{2}\hat{\rho}_{\mathcal{S}}(t)\hat{L}_{\mu}^{\dagger}\hat{L}_{\mu}\right], \tag{4.12}$$

describing the irreversible evolution of an open quantum system. Here $\hat{L}_{\mu}$ depends on the nature of the dissipative process (i.e. the effect of the environment) and $\gamma_{\mu}$ characterizes the strength of such events.

### Generalized *indirect* frequent measurements and their connection to dissipation

These same equations arise in the general theory of quantum measurements (Breuer et al. 2007), where one wishes to extract information of an observable $\hat{\mathcal{A}}$ of a given system $\mathcal{S}$ *indirectly*, by coupling it to a measuring device (a *probe*) previously prepared in a given state. As in the previous description, correlations arise among the probe and the system because of this coupling.

Then, one uses an apparatus which performs a projective measurement of an observable of the probe, yielding an *approximate* measurement of $\hat{\mathcal{A}}$, because of the correlations built during its interactions with the probe. It can be shown [see e.g. Breuer et al. (2007) for a detailed derivation] that, if the measurements are not read, the density matrix of the system being measured $\hat{\rho}_{\mathcal{S}}$ follows an evolution given by equation (4.12).

In this case, the Lindblad operator $\hat{L}_{\mu}$ is given by the indirectly measured operator $\hat{\mathcal{A}}$ and its strength $\gamma_{\mu}$ is proportional to the *rate* $\gamma$ of the measurement of $\hat{\mathcal{A}}$ (Breuer et al. 2007). Therefore, indirect frequent measurements can have an irreversible effect on the evolution of the original system, which establishes a link between measurements and dissipative processes.

### The quantum Zeno effect

A beautiful consequence of what has been discussed in the previous section is that the coherent evolution of a system can actually be frozen by performing arbitrarily frequent measurements.

To see this (Breuer et al. 2007), let us consider a two-level system consisting of discrete states $|a\rangle$ and $|b\rangle$, coupled with a strength $\Omega/2$, i.e. described by the free Hamiltonian $\hat{H}_{\mathcal{S}} = \Omega\hat{\sigma}_x/2$ (which generates Rabi oscillations between the two levels). Imagine that we now want to perform somehow an indirect measurement telling us if the atom is either on state $|a\rangle$ or in state $|b\rangle$ (i.e. to measure $\hat{\mathcal{A}} = \hat{\sigma}_z$). A possible measurement protocol for such a measurement is schematized in figure 4.6(a). The master equation reads:

$$\frac{\mathrm{d}}{\mathrm{d}t}\hat{\rho}_{\mathcal{S}}(t) = \frac{\Omega}{2\mathrm{i}}[\hat{\sigma}_x, \hat{\rho}_{\mathcal{S}}(t)] + \frac{1}{\tau_{\mathrm{Z}}}\left[\hat{\sigma}_z\,\hat{\rho}_{\mathcal{S}}(t)\hat{\sigma}_z^{\dagger} - \frac{1}{2}\hat{\sigma}_z^{\dagger}\hat{\sigma}_z\,\hat{\rho}_{\mathcal{S}}(t) - \frac{1}{2}\hat{\rho}_{\mathcal{S}}(t)\hat{\sigma}_z^{\dagger}\hat{\sigma}_z\right], \tag{4.13}$$

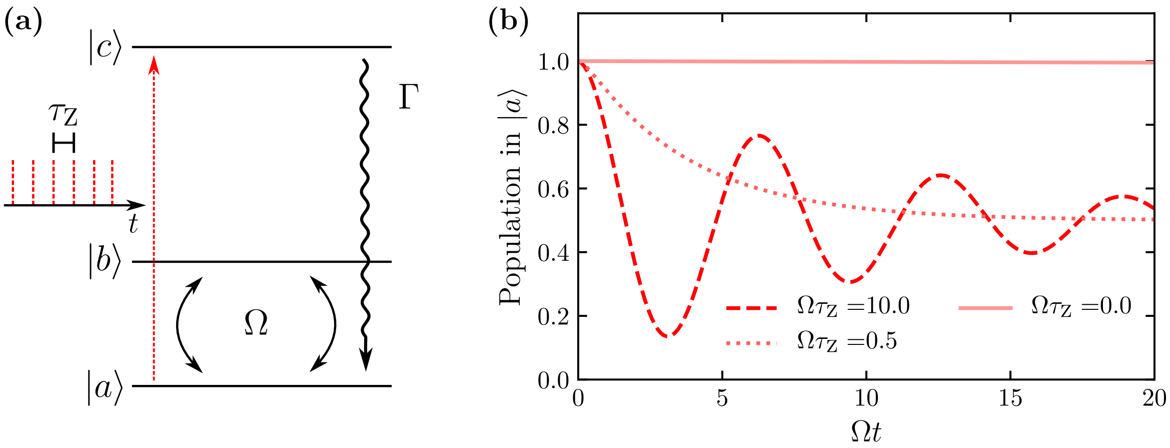

**Figure 4.6** – Quantum Zeno effect. **(a)** Schematics of the model proposed in the main text to observe the quantum Zeno effect: two levels $|a\rangle$ and $|b\rangle$ are coherently driven. The population in one of these states is measured at intervals given by $1/\tau_Z$ by coupling $|a\rangle$ to another state $|c\rangle$. The population in the ground state is shown for different measurement rates $1/\tau_Z$, showing that increasing the rate of measurements in a given interval slows down the dynamics.

where the inverse of the measurement rate has been denoted by $\tau_Z$, the so-called *Zeno time*. By mapping the 2-level system onto a pseudo-spin 1/2, we can write this evolution in terms of the components of the spin vector $\boldsymbol{s} = (u, v, w)$, with:

$$u = 2\mathrm{Re}[\rho_{ab}], \qquad v = 2\mathrm{Im}[\rho_{ba}], \qquad w = \rho_{aa} - \rho_{bb}, \tag{4.14}$$

which allows us to rewrite equation (4.13) as:

$$\dot{u} = -\frac{2}{\tau_Z}u, \qquad \dot{v} = \Omega w - \frac{2}{\tau_Z}v, \qquad \dot{w} = \Omega v. \tag{4.15}$$

Let us now assume that the system is initially prepared in $|a\rangle$, i.e. $w(0) = 1$, and that $v(0) = u(0) = 0$. The population difference evolves thus as:

$$w(t) = \frac{1}{\lambda_- - \lambda_+}\left(\lambda_- \mathrm{e}^{-\lambda_- t} - \lambda_+ \mathrm{e}^{-\lambda_+ t}\right), \quad \text{with} \quad \lambda_\pm = \frac{1}{\tau_Z} \pm \Omega\sqrt{\frac{1}{(\Omega\tau_Z)^2} - 1}. \tag{4.16}$$

The evolution of the ground state population is then given by $p_a(t) = [1 + w(t)]/2$. In the case $\Omega\tau_Z \ll 1$, these solutions correspond to damped Rabi oscillations with an oscillation frequency $\sim \Omega$. However, for $\Omega\tau_Z \gg 1$, one finds $p_a(t) = [1 + \mathrm{e}^{-\gamma_{\text{eff}} t}]/2$ with

$$\gamma_{\text{eff}} = \Omega^2 \tau_Z / 2. \tag{4.17}$$

This vanishes in the limit of $\tau_Z \to 0$, i.e. the population in the ground state is frozen $p_a(t) \simeq 1\,\forall t$ if the measurement rate is large enough. This can be seen figure 4.6(b) where we show the solution of equations (4.13) for different values of $\tau_Z$. This scaling as $\Omega^2\tau_Z = \Omega^2/\gamma$ is usually recognized as a clear signature of the quantum Zeno effect in a system.

These limits of large and small $\tau_Z$ can be easily understood in the case of projective measurements. For large $\tau_Z \gg \Omega^{-1}$, the system undergoes Rabi oscillations until the measurement is performed. Here, the system is found either in $|a\rangle$ or $|b\rangle$ with a probability given by the usual Rabi formula and the wave function is then projected. However, if the measurement is performed at times $\tau_Z \ll \Omega^{-1}$, the probability of being found in the ground state can be expanded as $p_a(\tau_Z) \simeq 1 - \Omega^2\tau_Z^2 \simeq 1$ if $\tau_Z \to 0$. The system is then projected with high probability onto $|a\rangle$.

If we consider now $n$ such measurements in a time interval $t = n\tau_Z$, we find that the probability of remaining in $|a\rangle$ is given by:

$$p_a(t = n\tau_Z) \simeq (1 - \Omega^2 t^2/n^2)^n \simeq 1 - \Omega^2 t^2/n \to 1 \quad \text{if}\, n \to \infty. \tag{4.18}$$

That is, we find again that the dynamics are slowed down and even effectively frozen if the system is frequently measured at a rate faster than its internal dynamics. This freezing under a frequent or continuous observation is usually referred to as the quantum Zeno effect (Misra et al. 1977).

In the previous paragraph, we have established an analogy between quantum measurements and dissipative processes. If we push this analogy further, we see that the role of the measurement rate $1/\tau_Z$ is equivalent to the strength of the dissipation parameters $\hat{L}_\mu$. Thus, by this reasoning, one expects strong losses to freeze the evolution of the system too.

This inhibition of the coherent dynamics under frequent measurements was actually shown for the first time by Itano et al. (1990) in an experiment with beryllium ions, following an earlier proposal by Cook (1988). The principle of the experiment is shown in figure 4.6(a): two long-lived hyperfine levels $|a\rangle$ and $|b\rangle$ are coupled by an RF field, which induces Rabi oscillations between them. Then, one of these states, say $|a\rangle$, is connected to an unstable state $|c\rangle$ via an allowed optical transition. Since this state is unstable, photons are scattered at a rate proportional to its width $\Gamma$, which constitutes a possible measurement for discerning if the atom was actually in $|a\rangle$ or not. Itano et al. then sent $n$ pulses resonant with the $|a\rangle \to |c\rangle$ line during the first RF $\pi-$pulse. Their key observation was that the transfer to state $|b\rangle$ was arbitrarily reduced as the number of pulses $n$ increased, which constituted an experimental confirmation of the quantum Zeno effect.

### Effective Hamiltonian and quantum jumps

The master equation (4.12) can be rewritten in terms of the evolution under an effective non-Hermitian Hamiltonian and a quantum jump[57]:

$$\frac{\mathrm{d}}{\mathrm{d}t}\hat{\rho}_{\mathcal{S}}(t) = \frac{1}{\mathrm{i}\hbar}[\hat{H}_{\text{eff}}, \hat{\rho}_{\mathcal{S}}(t)] + \mathcal{J}[\hat{\rho}_{\mathcal{S}}(t)], \tag{4.19}$$

where we have defined:

$$\hat{H}_{\text{eff}} = \hat{H}_{\mathcal{S}} - \sum_\mu \mathrm{i}\frac{\hbar\gamma_\mu}{2}\hat{L}_\mu^\dagger\hat{L}_\mu \qquad \text{and} \qquad \mathcal{J}[\hat{\rho}_{\mathcal{S}}] = \sum_\mu \gamma_\mu \hat{L}_\mu \hat{\rho}_{\mathcal{S}}(t)\hat{L}_\mu^\dagger. \tag{4.20}$$

It was shown in Dalibard et al. (1992); Dum et al. (1992) and (Carmichael 1993) that the evolution in terms of the density matrix is equivalent to a description in terms of

---

[57] We use that if $\hat{A}$ is a non-Hermitian operator, then $[\hat{A}, \hat{\rho}] = \hat{A}\rho - \rho\hat{A}^\dagger$.

states $|\Phi\rangle$ evolving under the non-Hermitian Hamiltonian $\hat{H}_{\text{eff}}$. In a few words, the evolution of the system in a small time interval $\delta t$ is given by the following Schrödinger equation:

$$\mathrm{i}\hbar \frac{\mathrm{d}}{\mathrm{d}t}|\Phi(t)\rangle = \hat{H}_{\text{eff}}|\Phi(t)\rangle, \tag{4.21}$$

interrupted by a *quantum jump* with a probability given by

$$p_\mu = \gamma_\mu \delta t \langle \Phi(t)|\hat{L}_\mu \hat{L}_\mu^\dagger|\Phi(t)\rangle, \tag{4.22}$$

which projects the state towards $\hat{L}_\mu|\Phi(t)\rangle$. Averaging this over many realizations (the so-called *quantum trajectories*) is equivalent to solving the Lindblad master equation (4.12). This techinique is known as the *Monte-Carlo wave function approach* (Dalibard et al. 1992; Plenio et al. 1998).

The quantum jump term $\mathcal{J}[\hat{\rho}_{\mathcal{S}}]$ is usually also referred to as the *feeding* term. For some kind of dissipative processes, e.g. atom losses, atoms are continuously *fed* into smaller-number Fock states and eventually the vacuum state (the steady-state), which does not participate into the dynamics anymore.

Let us specialize this to our experimental situation: We deal with the coherent coupling of atom pairs enduring two-body losses. In each lattice site, the effective dynamics of the reduced density matrix is projected onto a subspace where only the $\hat{P}_0 = |0\rangle\langle 0|$ and $\hat{P}_2 = |2\rangle\langle 2|$ subspaces play a role. If we were only measuring a single lattice site then, in the Monte Carlo wave function point of view, the state of the atomic pair would evolve under $\hat{H}_{\text{eff}}$ and at some point there would be a quantum jump projecting the state onto $|0\rangle$, stopping the dynamics. In the experiments, we have thousands of lattice sites where these dynamics are taking place. Since we only measure atom pairs that have not decayed, we can project onto the subspace concerning $\hat{\rho}_{\mathcal{S},2}$ alone.

In this case, the evolution on the subspace of doubly-occupied sites is completely governed by the non-Hermitian effective Hamiltonian and we can either use the master equation *or* equation (4.21) directly [i.e. with no need to keep track of the feeding term (or the quantum jumps)] to describe our observations, as we have done in section 4.1.

Let us then summarize the main ideas that have appeared in the previous discussion:

1. The frequent measurement of a system inhibits its coherent dynamics [see equation (4.18)].
2. The effect of dissipation is analogous to a measurement.
3. The evolution of a dissipative system can be fully described by an effective non-Hermitian Hamiltonian *if* the subspace spanned by the quantum jump is not measured and does not participate into the dynamics anymore [in such a case, we can use equation (4.21) to compute the evolution of the system].

### 4.2.2 Dressed states, exceptional points and reduced-loss subspace at weak coupling

#### Non-Hermitian Hamiltonian

Let us now focus in our particular situation, i.e., atomic pairs in independent harmonic wells, driven by the laser and where two particles in the excited state undergo inelastic collisions and are lost. This is well described by the effective non-Hermitian Hamiltonian in equation (4.6), that we rewrite here in a more compact form:

$$\hat{H}^{(2)} = \hbar \begin{pmatrix} 0 & \dfrac{\Omega_\mathrm{L}}{\sqrt{2}} & 0 \\ \dfrac{\Omega_\mathrm{L}}{\sqrt{2}} & \eta - \delta_\mathrm{L} & \dfrac{\Omega_\mathrm{L}}{\sqrt{2}} \\ 0 & \dfrac{\Omega_\mathrm{L}}{\sqrt{2}} & \chi - 2\delta_\mathrm{L} - \mathrm{i}\dfrac{\Gamma}{2} \end{pmatrix}, \tag{4.23}$$

where we have put $\gamma_{eg} \simeq 0$, $\Gamma = \gamma_{ee} \simeq 2\pi \times 1500\,\mathrm{Hz}$ and defined $\hbar\eta = U_{eg} - U_{gg} \simeq -h \times 140\,\mathrm{Hz}$ and $\hbar\chi = U_{ee} - U_{gg} \simeq 2h \times 150\,\mathrm{Hz}$, which are determined by the lattice depth and fixed in all this section. Now, instead of focusing on the evolution of the bare states $\{|gg\rangle, |eg\rangle, |ee\rangle\}$ as we did in the previous sections, we consider the eigenstates and eigenvalues of $\hat{H}^{(2)}$:

$$\hat{H}^{(2)}|\lambda_k\rangle = \hbar\lambda_k|\lambda_k\rangle \qquad \text{with} \qquad \lambda_k = \omega_k - \mathrm{i}\frac{\gamma_k}{2}. \tag{4.24}$$

These eigenvalues and eigenvectors depend on the given Rabi frequency and detuning, $\lambda_k = \lambda_k(\Omega_\mathrm{L}, \delta_\mathrm{L})$, but we do not explicit the dependency to alleviate the notation. We note that, since $\hat{H}^{(2)}$ is not an Hermitian operator, in principle one should compute the right and left eigenvectors in order to write it in its diagonal form (see appendix E). However, if the Hamiltonian is symmetric, it is sufficient to specify its right (or left) eigenvectors (Moiseyev 2011) and, from now on, we keep our discussion referring only to the right eigenvectors.

Another consequence of the non-Hermiticity of the Hamiltonian is that its eigenvalues are complex: the real part $\omega_k$ corresponds to the eigenfrequency of the eigenstate, and the parameter $\gamma_k$ in the imaginary part gives the lifetime of the eigenstate $|\lambda_k\rangle$. Let us show this last statement: Under the action of $\hat{H}^{(2)}$, the state of the system at a given time $t_0$ is given by a superposition of the eigenstates:

$$|\psi(t_0)\rangle = \sum_j \alpha_k(t_0)|\lambda_k\rangle. \tag{4.25}$$

The evolution of the system expressed in the eigenbasis is given by:

$$|\psi(t)\rangle = \sum_k \mathrm{e}^{(-\mathrm{i}\omega_k - \gamma_k/2)t}\alpha_k(t_0)|\lambda_k\rangle, \tag{4.26}$$

and therefore, the population of each eigenstate at a time $t > t_0$ reads:

$$P_k(t) = |\langle\lambda_k|\psi(t)\rangle|^2 = \mathrm{e}^{-\gamma_k t}P_k(t_0), \tag{4.27}$$

i.e., because of the effective non-Hermitian description of the problem, probabilities are not conserved. The imaginary part of each complex eigenvalue is proportional to the population of $|ee\rangle$ in $|\lambda_k\rangle$ at the given $\Omega_{\mathrm{L}}$ and $\delta_{\mathrm{L}}$, i.e.

$$\gamma_k = \gamma_{ee}\Pi_k^{ee}(\Omega_{\mathrm{L}}, \delta_{\mathrm{L}}), \tag{4.28}$$

with $P_k = \Pi_k^{gg} + \Pi_k^{eg} + \Pi_k^{ee}$ and where the $\Pi_k^{j}$ are the populations of the bare states in each dressed state $|\lambda_k\rangle$. We are going to show next that, in the weak coupling regime, this population $\Pi_k^{ee}$ is strongly reduced for some eigenstates with respect to what one would expect by diagonalising $\hat{H}^{(2)}$ in the absence of losses, that is: $\Pi_k^{ee}(\Gamma = \gamma_{ee}) \ll \Pi_k^{ee}(\Gamma = 0)$. This effective inhibition of the transfer to the lossy state becomes more drastic as $\Gamma \gg \Omega_{\mathrm{L}}$, resulting in smaller loss rates $\gamma_k$ as one increases the value of the losses $\Gamma$, as opposed to what one would naively expect.

### Dressed states

Let us compute the spectrum of $\hat{H}^{(2)}$. We note that, for non-Hermitian Hamiltonians there is no unique way of ordering the eigenstates (one can choose to label them according to decreasing real or imaginary parts of the eigenvalues, for instance) (Ibáñez et al. 2014). We have chosen to label the eigenstates so that the eigenvectors and eigenvalues are continuous functions of $\delta_{\mathrm{L}}$ at a given $\Omega_{\mathrm{L}}$. In the following we denote the eigenstates as $|\lambda_i\rangle$ and we call $|\lambda_1\rangle$ the eigenstate that at large *negative* detunings corresponds to $|gg\rangle$ and $|\lambda_3\rangle$ the one that corresponds to $|gg\rangle$ at large *positive* detunings.

We display the result of this diagonalisation in figures 4.7 and 4.8 in the strong and weak coupling limits, for $\Omega_{\mathrm{L}}/(2\pi) \simeq 1500$ and $150\,\mathrm{Hz}$ respectively. We show the real and imaginary parts of the eigenvalues on the top rows and the bare-state composition of each dressed state on the bottom rows. From these diagonalisations we observe the following features: in the strong coupling limit, the energy levels are well separated and except for the non-zero imaginary parts, one obtains a spectrum which is very similar to the one that would be obtained by setting $\Gamma = 0$, with the usual avoided crossings. However, at weak coupling, and as it can be seen in figure 4.8(b), two interesting features appear: on the one hand, there are level crossings in the real parts and, on the other hand, regions where the losses are strongly reduced ($\gamma_k \ll \Gamma$) emerge.

### Exceptional points: The boundary between the weak and strong coupling regimes

An interesting feature of non-Hermitian Hamiltonians is that, for certain values of the control parameters ($\Omega_{\mathrm{L}}$ and $\delta_{\mathrm{L}}$ in our case), the real *and* imaginary parts of two or more eigenvalues become equal and, in this point, the corresponding eigenstates *coalesce* and become parallel. These points of the parameter space where the Hamiltonian cannot be diagonalised are known as *exceptional points* (EP) (Heiss 2012). For our physical parameters (i.e. $U_{ij}$ and $\gamma_{ee}$) there is no physical situation for which the three eigenstates coalesce (i.e. there is no *third order* EP). However, for some values of $(\Omega_{\mathrm{L}}, \delta_{\mathrm{L}})$ it can happen that two of them do. We show this in figure 4.9, where eigenstates $|\lambda_1\rangle$ and $|\lambda_2\rangle$ coalesce at $(\Omega_{\mathrm{EP}}^{1\leftrightarrow 2}, \delta_{\mathrm{EP}}^{1\leftrightarrow 2}) \simeq 2\pi \times (450, 530)\,\mathrm{Hz}$. Another second order EP (not shown) appears at $(\Omega_{\mathrm{EP}}^{2\leftrightarrow 3}, \delta_{\mathrm{EP}}^{2\leftrightarrow 3}) \simeq 2\pi \times (610, 10)\,\mathrm{Hz}$, where $|\lambda_2\rangle$ and $|\lambda_3\rangle$ coalesce.

Systems featuring either losses or gain, i.e. systems that can be described by non-

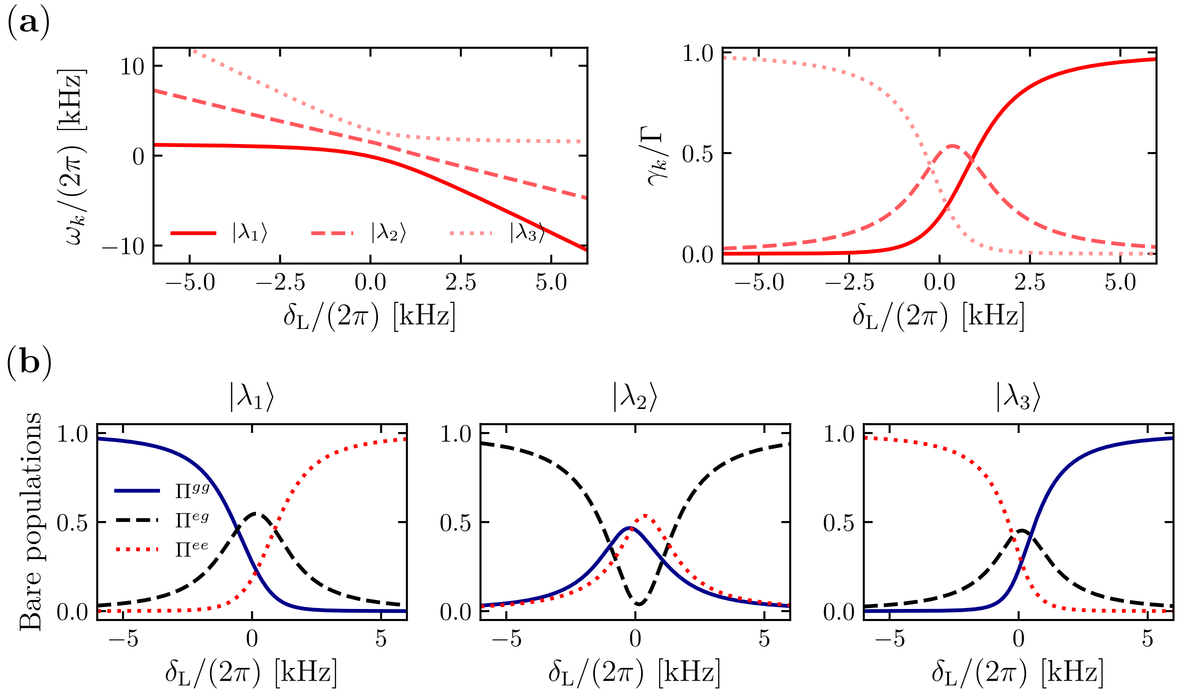

**Figure 4.7** – Spectrum of $\hat{H}^{(2)}$ in the strong coupling limit. **(a):** Real **(left)** and imaginary parts **(right)** of the eigenvalues.**(b):** Bare state composition of each dressed state.

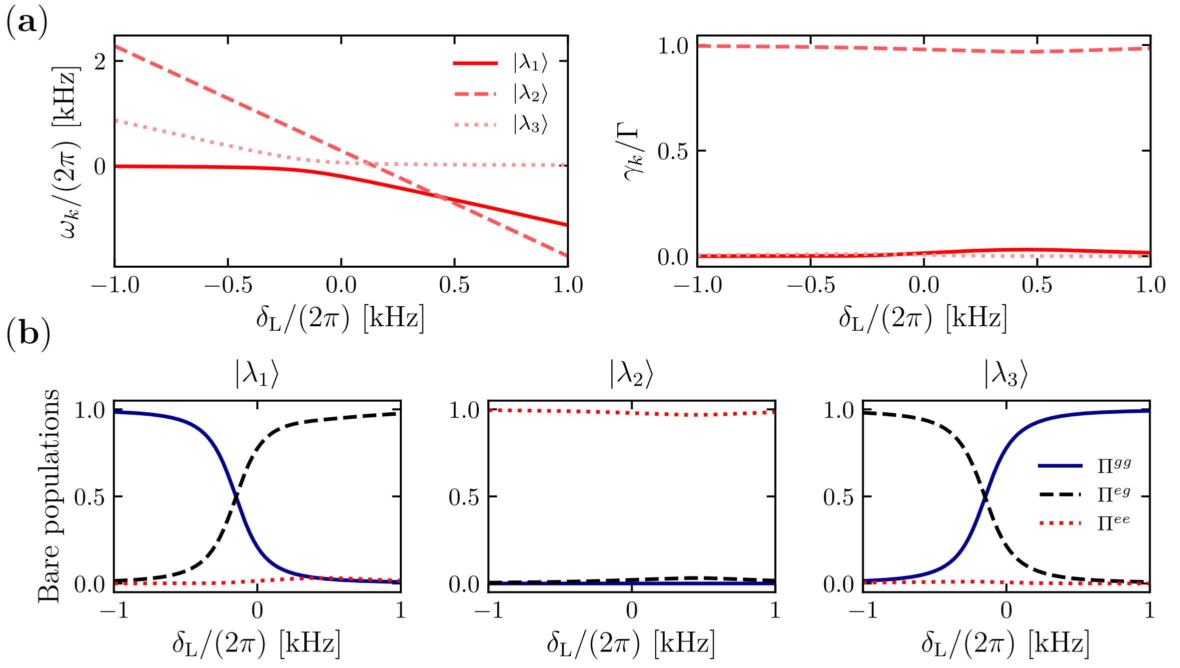

**Figure 4.8** – Spectrum of $\hat{H}^{(2)}$ in the weak coupling limit. **(a):** Real **(left)** and imaginary parts **(right)** of the eigenvalues. **(b):** Bare state composition of each dressed state. In this case, we see the appearance of crossings in the real part spectrum and the emergence of a subspace in which the loss rate is strongly reduced for all detunings.

Hermitian Hamiltonians, are well suited for the study of EPs. Encircling such points leads to new and sometimes counter-intuitive phenomena (Heiss 2012). The question

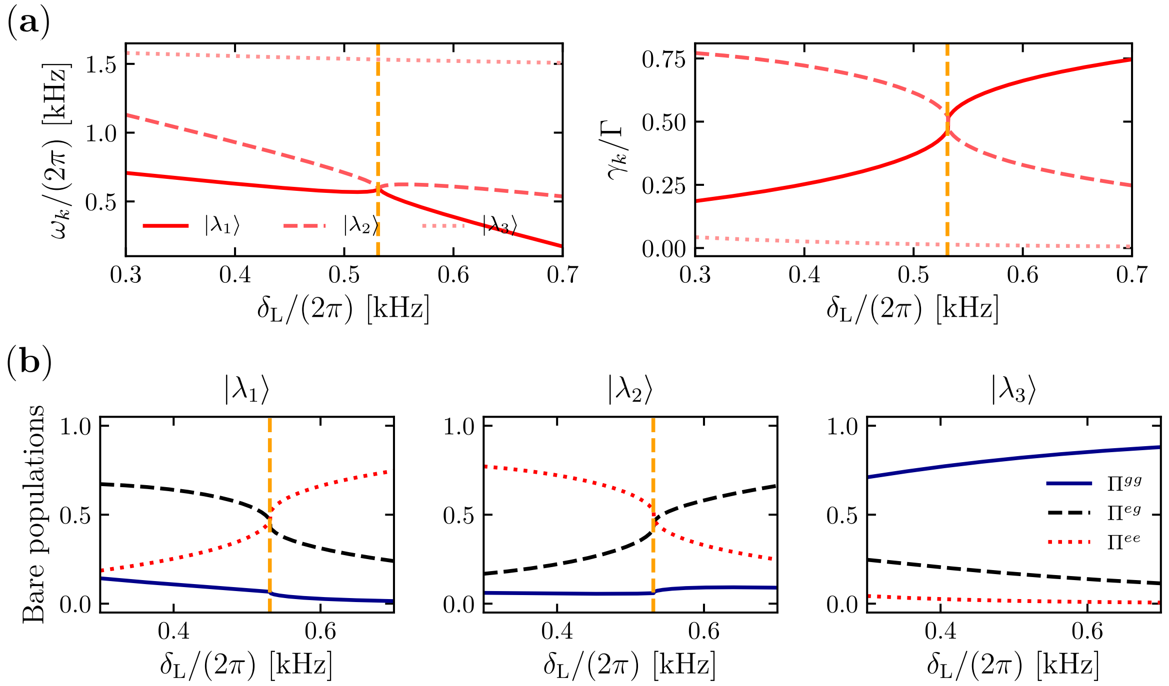

**Figure 4.9** – Spectrum of $\hat{H}^{(2)}$ at $\Omega_{\text{L}} = \Omega_{\text{EP}}^{1\leftrightarrow 2}$. **(a):** Real **(left)** and imaginary parts **(right)** of the eigenvalues. **(b):** Bare state composition of each dressed state. The vertical dashed line is located at $\delta_{\text{L}} = \delta_{\text{EP}}^{1\leftrightarrow 2}$, where $|\lambda_1\rangle$ and $|\lambda_2\rangle$ coalesce.

of adiabaticity by performing a loop around an EP has been studied in Milburn et al. (2015), and it has been shown to depend on the chirality of the loop around these points (Doppler et al. 2016). Other effects such as unidirectional invisibility have been observed (Lin et al. 2011b; Feng et al. 2013) and the role of EPs in enhanced sensing schemes has also been proved (Chen et al. 2017). In the field of quantum simulation of open quantum systems, the presence of EPs offers new frames to address quantum phase transitions (Nakagawa et al. 2018).

Unfortunately, so far, we have not been able to observe experimentally any of these features supposed to occur when encircling these points. A closed loop around an EP inevitably goes through the strong coupling region, where atom losses are sizable, and our signal-to-noise ratio is not sufficient. Still, these points mark the boundary between what we are calling weak coupling and strong coupling regimes, since the reduced-loss subspace emerges once the Rabi frequencies become $\Omega_{\text{L}} < \Omega_{\text{EP}}$.

### Reduced-loss subspace

We are interested in preparing our system in one of the eigenstates whose imaginary eigenvalues belong to this reduced-loss subspace. We achieve this by performing adiabatic passages. In our experiments we always start with all the atoms in the ground state, and thus $|\Psi(t_0)\rangle = |gg\rangle$. Then, depending on whether we ramp our clock laser starting from negative or positive enough detunings, we will be following approximately the states that we have labeled as $|\lambda_1\rangle$ or $|\lambda_3\rangle$ [see figure 4.8(a)]. The question of adiabaticity in the non-Hermitian case is more involved than the Hermitian one: In a few words, adiabaticity can only be fulfilled in principle for the *least dissipative* eigenstate,

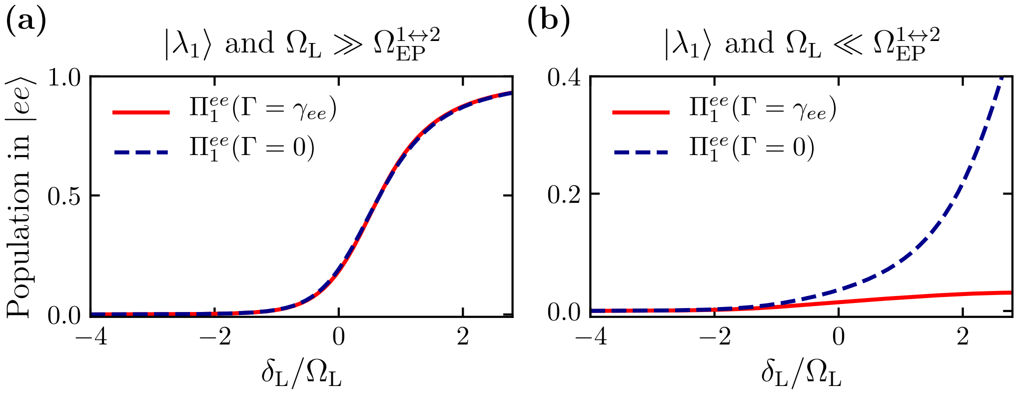

**Figure 4.10** – Suppression of the coherent transfer to the excited state during an adiabatic passage. **(a):** In the strong coupling limit, the transfer to the excited state population for $\Gamma = \gamma_{ee}$ is not modified with respect to the observed transfer in the absence of losses ($\Gamma = 0$). **(b):** However, this transfer is strongly suppressed in the weak-coupling limit.

and this, as usual, provided the rate of change of the Hamiltonian is slow compared to the Bohr frequencies involved (Nenciu et al. 1992; Ibáñez et al. 2014). This notion, known as *quasi-adiabaticity* is discussed in more details in appendix E. When quasi-adiabaticity holds, there is a global loss of population, but the proportions of each bare state in each dressed state are conserved.

We have already discussed that the imaginary part of the eigenvalues, giving the population loss rate of each eigenstate, is related to the contribution of the bare state $|ee\rangle$. In figure 4.10 we show more explicitly that by following, for example, the state $|\lambda_1\rangle$ in the weak coupling regime and in the presence of the losses it is indeed expected to observe a suppression of the transfer to the excited state, and therefore a reduced loss rate.

We are now going to derive an effective Hamiltonian for this reduced-loss subspace. To do this, we can first split the Hamiltonian in (4.23) as $\hat{H}^{(2)} = \hat{H}_0 + \hat{V}$, with:

$$\hat{H}_0 = \hbar \begin{pmatrix} 0 & 0 & 0 \\ 0 & \eta - \delta_\mathrm{L} & 0 \\ 0 & 0 & \chi - 2\delta_\mathrm{L} - \mathrm{i}\dfrac{\Gamma}{2} \end{pmatrix}, \qquad \hat{V} = \hbar \begin{pmatrix} 0 & \dfrac{\Omega_\mathrm{L}}{\sqrt{2}} & 0 \\ \dfrac{\Omega_\mathrm{L}}{\sqrt{2}} & 0 & \dfrac{\Omega_\mathrm{L}}{\sqrt{2}} \\ 0 & \dfrac{\Omega_\mathrm{L}}{\sqrt{2}} & 0 \end{pmatrix}. \tag{4.29}$$

Here, we see that, due to the large imaginary part of $E_{ee} = U_{ee} - \mathrm{i}\hbar\gamma_{ee}/2$ we have $|E_{ee}| \gg |E_{gg}, E_{eg}|$ and thus, this state is energetically far from the other two in $\hat{H}_0$. The method of the *effective Hamiltonian* (Cohen-Tannoudji et al. 1992) is well suited for such a situation. We can first split the Hilbert space into two complementary subspaces $\mathcal{H} = \mathcal{H}_P \oplus \mathcal{H}_Q$, with $\hat{P} = |gg\rangle\langle gg| + |eg\rangle\langle eg|$ and $\hat{Q} = \mathbb{1} - \hat{P} = |ee\rangle\langle ee|$. The method consists now in in finding a Hamiltonian $\hat{H}_\mathrm{eff}$ sharing the same eigenvalues in the subspace $\mathcal{H}_P$ as the full Hamiltonian $\hat{H}$ in $\mathcal{H}$. That is, we require that, for a given state $|\psi\rangle \in \mathcal{H}_P$: $\hat{H}_\mathrm{eff}|\psi\rangle = E|\psi\rangle$ provided $\hat{H}|\varphi\rangle = E|\varphi\rangle$ for $|\varphi\rangle \in \mathcal{H}$.

In the weak coupling situation, we can perform a perturbative expansion to derive the effective Hamiltonian for the dynamics in $\mathcal{H}_P$. To second order in $\hat{V}$, it reads (Cohen-Tannoudji et al. 1992):

$$\hat{P}\hat{H}_{\text{eff}}\hat{P} \simeq \hat{P}(\hat{H}_0 + \hat{V})\hat{P} - \hat{P}\hat{V}\hat{Q}\frac{1}{\hat{Q}\hat{H}_0\hat{Q}}\hat{Q}\hat{V}\hat{P}. \tag{4.30}$$

We obtain the following effective Hamiltonian:

$$\hat{P}\hat{H}_{\text{eff}}\hat{P} = \hbar \begin{pmatrix} 0 & \dfrac{\Omega_{\text{L}}}{\sqrt{2}} \\ \dfrac{\Omega_{\text{L}}}{\sqrt{2}} & \delta_{\text{eff}} - \mathrm{i}\dfrac{\gamma_{\text{eff}}}{2} \end{pmatrix}, \tag{4.31}$$

with an effective light-shift and a reduced loss rate $\gamma_{\text{eff}}$ given by:

$$\delta_{\text{eff}} = \eta - \delta_{\text{L}} - \frac{2\Omega_{\text{L}}^2}{4(\chi - 2\delta_{\text{L}})^2 + \Gamma^2} \quad \text{and} \quad \gamma_{\text{eff}} = \frac{2\Omega_{\text{L}}^2}{4(\chi - 2\delta_{\text{L}})^2 + \Gamma^2}\Gamma. \tag{4.32}$$

From this, we see that the presence of dissipation freezes the dynamics of the three-level system by projecting it onto a subspace with only two states $|gg\rangle$ and $|eg'\rangle \simeq |eg\rangle$, the latter having a finite lifetime $\gamma_{\text{eff}} \ll \Gamma$.

For detunings $\delta \simeq \chi/2$ this effective loss rate becomes $\gamma_{\text{eff}} \propto \Omega^2/\Gamma$, which is exactly the same behavior observed in equation (4.17), and is a clear signature of the quantum Zeno effect. This scaling explains the tendency observed in figure 4.10, where an increase of the loss rate, actually reduces the transfer to the excited state, and thus the effective loss rate. We also see that, in the weak-coupling limit, an increase of the loss rate has an effect which is similar to increasing the detuning with respect to the transition to the lossy state (or, equivalently, moving away the $|gg\rangle \to |ee\rangle$ resonance by setting $|U_{ee}| \gg U_{gg}, U_{eg}$).

### 4.2.3 Experimental results

#### Adiabatic following and lifetimes

Here we show the experimental results obtained by performing a lifetime experiment after following either $|\lambda_1\rangle$ or $|\lambda_3\rangle$ with a Rabi frequency $\Omega_{\text{L}} \ll \Omega_{\text{EP}}$, and in the region where each one has the smaller imaginary part, so that we can be quasi-adiabatic during the passage [see appendix E]. Experimentally, we proceed as follows:

1. We first ramp up the Rabi frequency from 0 to $2\pi \times 150\,\text{Hz}$ at a rate of $10\,\text{Hz/ms}$ with the detuning fixed at $\delta_{\text{L}}(0)/(2\pi) = \mp 1.5\,\text{kHz}$ [see figure 4.11(a)].
2. The detuning is then ramped from $\delta_{\text{L}}(0)$ to the final chosen value with a fixed speed of $10\,\text{Hz/ms}$ [see figure 4.11](a).
3. Once the final detuning is reached, we let the coupling laser on at this value for a variable hold time and measure the total population of the dressed states after a TOF [see figure 4.11(a)-(b)].

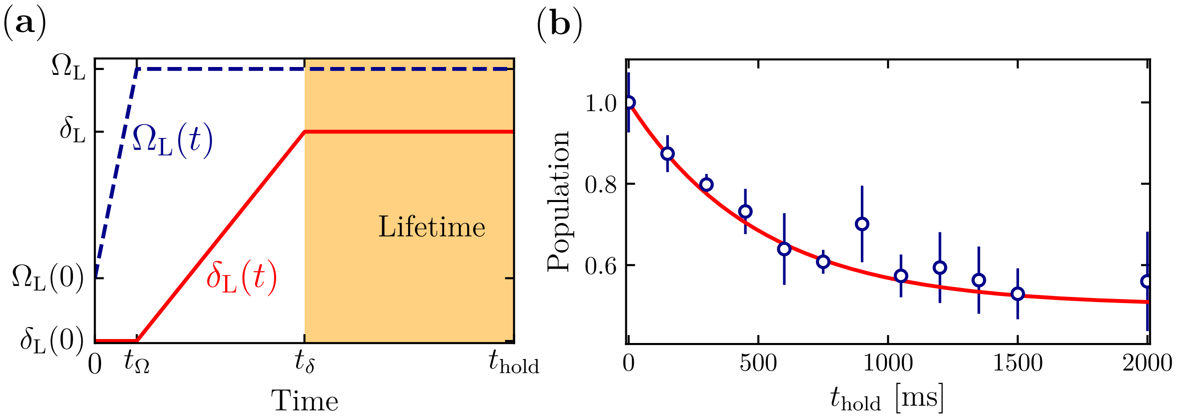

**Figure 4.11** – **(a):** Schematics of the ramps for the passages: First, the Rabi frequency is ramped and then the detuning. Finally, a lifetime of the dressed states (shaded area) is performed by letting the clock laser on at the final detunings and Rabi frequencies. **(b)** Example of lifetime measurement. The data corresponds to an experiment following $|\lambda_1\rangle$ at the final detuning $\delta_\mathrm{L} = 2\pi \times -650\,\mathrm{Hz}$. The solid line is a fit to an exponential decay.

We then perform a fit to an exponential decay and we plot the extracted lifetimes in figure 4.12. We compare these lifetimes to the ones extracted by diagonalising the Hamiltonian in equation (4.23) with ($\Gamma = \gamma_{ee}$) and also to the naive loss rate that would be expected if the suppression was not present, i.e. $\gamma_{ee}\Pi^{ee}(\Gamma = 0)$. As discussed, our experiments confirm that the presence of losses strongly inhibits the transfer to the lossy state.

### Measuring the $|eg\rangle$ population

By performing lifetime experiments, it is also possible to infer the actual population of the state $|eg\rangle$, $\Pi^{eg}$ in a given eigenstate at a given $(\delta_\mathrm{L}, \Omega_\mathrm{L})$. As explained in section 4.1.1, experimentally, we can only access either the total population, that we call $N_{e+g}$, or the total atom number in $g$ or $e$, that we call $N_g$ or $N_e$, respectively. But when we record an image we cannot distinguish which atoms belonged to doubly- or singly-occupied sites (note that in the previous discussion we have ignored the singly-occupied sites, which are of course present in our measurements but do not participate into the dissipative dynamics). A method to infer $\Pi^{eg}$ is schematized in figure 4.13(a). It consists on recording two lifetime measurements: (i) One measuring the total population $N_{e+g}$, from which we extract $A = N_{gg}^{(2)} + N_{eg}^{(2)} + N_{ee}^{(2)} + N_g^{(1)} + N_e^{(1)}$ at $t = 0$ and $C = N_g^{(1)} + N_e^{(1)}$ at long times, once all doubly occupied sites have decayed and (ii) another one measuring just $N_g$: Here $B = N_g^{(1)} + N_{gg}^{(2)} + N_{eg}^{(2)}/2$ at $t = 0$ and $D = N_g^{(1)}$ at long times. Then, if we assume $N_{ee}^{(2)} \simeq 0$ [which is indeed the case if the passage is adiabatic, see figure 4.8(a)], the population of the $|eg\rangle$ state can be computed as:

$$\Pi^{eg} = \frac{2[(A - B) - (C - D)]}{A - C}. \tag{4.33}$$

We have performed these measurements following $|\lambda_1\rangle$ and we show the results in figure 4.13(b). We see that we are able to prepare samples with a large population $|eg\rangle$, whose lifetime are twice as large as would be expected in the absence of this suppression. By

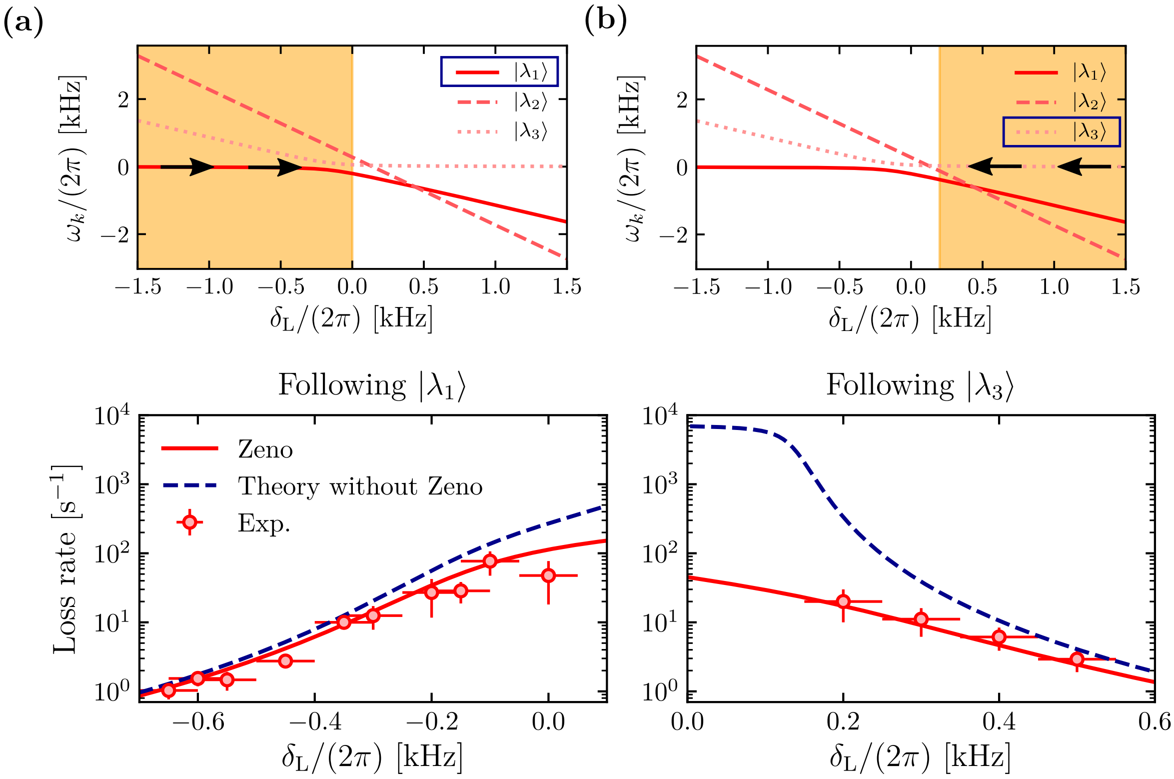

**Figure 4.12** – **(Top):** Schematics of the passage. The shaded regions corresponds to the region of explored detunings during the sweeps. **(Bottom):** Decay rates extracted from performing a lifetime experiment (see main text) after an adiabatic passage following either $|\lambda_1\rangle$ [starting at $\delta/(2\pi) = -1.5\,\mathrm{kHz}$] in **(a)** or $|\lambda_3\rangle$ [starting at $\delta/(2\pi) = +1.5\,\mathrm{kHz}$] in **(b)**. In both cases the final Rabi frequency is $\Omega_{\mathrm{L}}/(2\pi) = 150\,\mathrm{Hz}$ and the final detuning of the ramp is indicated in the $x-$axis. The red solid line corresponds to the loss rate extracted by diagonalising equation (4.23) with $\Gamma = \gamma_{ee}$. The blue dashed line corresponds to a diagonalisation with $\Gamma = 0$. As discussed in the main text, this measurements confirm that transfer to the excited state is strongly suppressed in the presence of losses.

performing the same measurements following state $|\lambda_3\rangle$ we should observe a similar behavior, but with a stronger suppression.

### 4.2.4 Perspectives and conclusion

In this second section, I have given experimental evidence that the presence of a strongly dissipative state can slow down the coherent transfer towards this state, and interpreted this observation in terms of the quantum Zeno effect. I have shown this for a conceptually simple experimental situation: atomic pairs in independent harmonic wells. Here, the dynamics governing the internal states is well-captured by a $3 \times 3$ non-Hermitian Hamiltonian. By diagonalising this Hamiltonian in the weak coupling regime, one already sees the emergence of a slowly decaying manifold. I have then derived an effective Hamiltonian describing the dynamics in this subspace, which shows the typical scaling of the quantum Zeno suppression mechanism.

This has been verified experimentally, by performing an adiabatic following of such

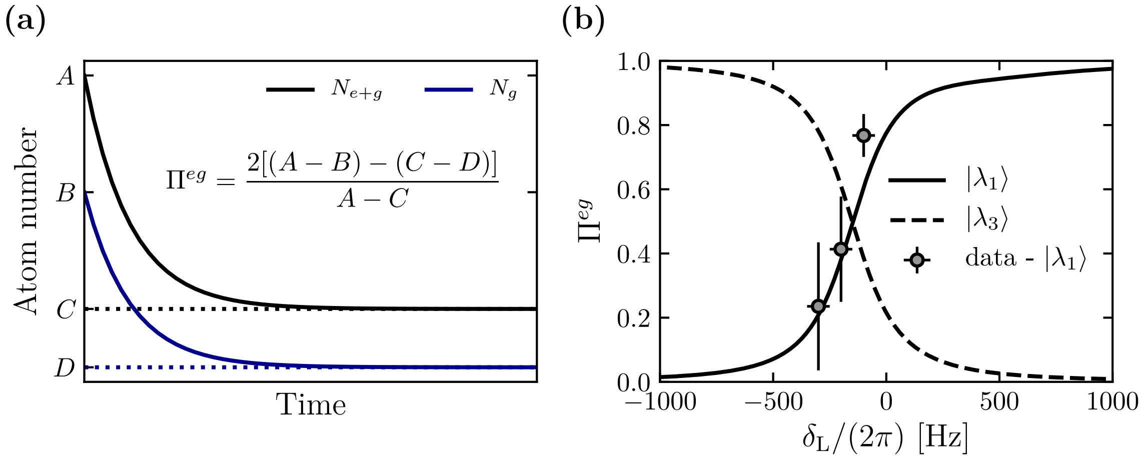

**Figure 4.13** – **(a):** Method to measure the $|eg\rangle$ population by performing lifetime measurements. **(b):** Measured $|eg\rangle$ population obtained by applying the method shown in **(a)**. The ramp is performed at $\Omega_L/(2\pi) = 150\,\mathrm{Hz}$ by following $|\lambda_1\rangle$ from $\delta_L(0)/(2\pi) = -1.5\,\mathrm{kHz}$ to the detuning indicated in the $x$-axis. The solid and dashed lines correspond to the population obtained by diagonalising equation (4.23) for our experimental parameters.

slowly decaying states. We have measured loss rates which are reduced by orders of magnitude with respect to the ones that one would be naively expected if this suppression was not present. Finally, I have also shown that this allows us to remain in a dressed state in which we have coherently transferred a large part of the population to the $|eg\rangle$ state while keeping the $|ee\rangle$ state depleted.

This suppression mechanism would work much better if we could increse the loss rate, which can in principle be achieved by increasing the lattice depth[58] or by reducing the Rabi frequency. Here we face the problem that the times needed for the ramps become long ($> 1\,\mathrm{s}$), and we start being limited by the dephasing mechanisms discussed in section 3.6. Also, for such long ramps, the hypothesis of independent pairs would not really hold anymore, since the ramps cover several tunneling cycles.

Inelastic two-body losses in the excited state are prone to be problematic in experiments involving the two clock states. Such losses constitute a source of entropy and eventually could prevent from reaching the ground state when preparing specific Hamiltonians (Baur et al. 2010). Thus, mechanisms such as the one presented in this section could prove useful for quantum simulation protocols when using alkaline-earth like atoms, suffering in general from strong inelastic losses in the excited state.

---

[58] We note, however, that $\hbar\gamma_{ee} \simeq U_{gg} \propto g \int |w(\boldsymbol{r})|^4 \mathrm{d}^3 r$, and thus increases slowly ($\propto V^{3/4}$) with the lattice depth.

# Part III

# Coherence and relaxation in many-body systems

# CHAPTER 5

# Non-linear dynamics of a bulk Bose-Einstein condensate

In chapter 4 I have shown a set of experiments in which, by performing spectroscopy on the clock transition, we were able to extract the interaction strength between an atom in the ground state and another in the excited state and between two atoms in the excited state, leading to a measure of $a_{eg}$ and $a_{ee}$, respectively. These experiments were performed in a deep optical lattice, where the Lamb-Dicke regime applies and the motion of the atoms is frozen. In such a situation, I have shown in chapter 3 that we are able to drive the internal dynamics in a coherent way for tens of ms, mostly limited by the drifts of and the linewidth of the laser and its inhomogeneous profile over the atomic sample.

In this chapter I present the experimental results and a study on the coherent driving of a bulk BEC, trapped in a harmonic potential and driven on the clock transition. I show in figure 5.1(b)-(c) an example of the two kind of experiments that will be studied in this chapter: Spectroscopy in time domain [figure 5.1(b)] on the form of Rabi oscillations and spectroscopy in frequency domain [figure 5.1(c)].

The high momentum imparted by the optical photon, $\hbar \boldsymbol{k}_{\mathrm{L}}$, couples in this case the internal dynamics to the external ones and the BEC, initially prepared in a narrow wave packet of zero momentum, is transferred to the excited state, described by a wave packet centered around $\hbar \boldsymbol{k}_{\mathrm{L}}$. The absence of spontaneous emission allows us to study the relaxation mechanisms competing against this coherent driving, from which we identify Doppler broadening, mean-field interactions and strong inelastic losses as the main ones. In the first introductory section, I present an overview of different spectroscopic techniques used to probe quantum gases. These techniques share common features with the single-photon clock transition, such as state dependent interaction shifts and momentum transfer depending on the kind of spectroscopy.

The experimental results are subsequently presented in two different sections: First, I discuss the spectroscopy in frequency domain in the irreversible weak coupling regime, analyzing the expected shape of the spectra depending on whether interactions or Doppler broadening prevails. This section follows closely the description of the two-photon spectroscopy experiments performed on hydrogen (Killian 2000), or on Bragg

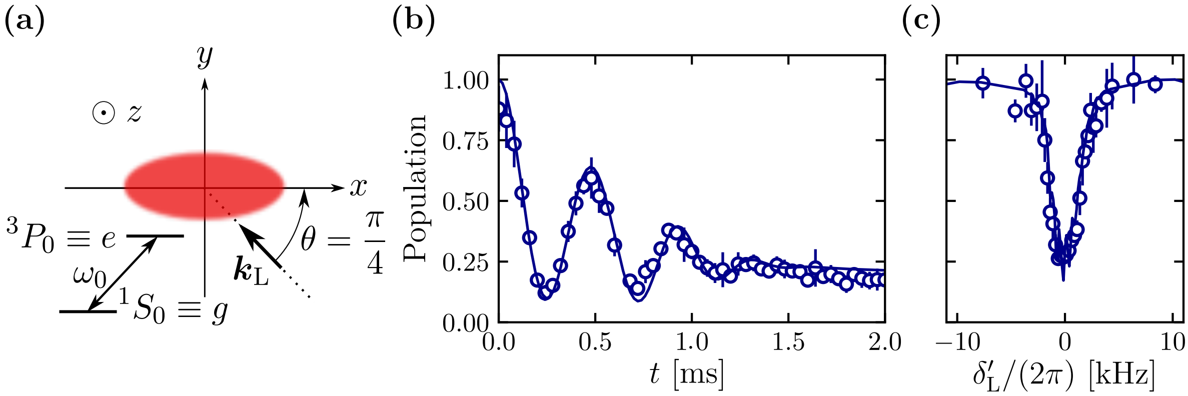

**Figure 5.1** – **(a)** Schematics of the experiment. A BEC trapped in an elongated harmonic trap with $\omega_x \ll \omega_{y,z}$ is probed on the clock transition $^1\mathrm{S}_0 \rightarrow {}^3\mathrm{P}_0$ by a laser propagating in the $x-y$ plane at 45° with respect to the weak axis. **(b)** Rabi oscillation at strong coupling. **(c)** Spectroscopy in frequency domain. The blue solid lines in figures **(b)** and **(c)** correspond to a GP simulation in the experimental conditions described in the main text.

scattering experiments (Zambelli et al. 2000). I then present a study on the relaxation dynamics of a BEC undergoing coherent Rabi oscillations. I present a minimal model that allows us to understand the behavior observed in the limits of very strong and very weak coupling. Throughout this chapter, in order to go beyond the empirical and approximate models, the experimental data is systematically compared with the result of numerical simulations based on a pair of coupled dissipative GPEs. The results shown in this chapter were published in Bosch Aguilera et al. (2018).

## 5.1 Introduction

### 5.1.1 Spectroscopy of ultracold quantum gases

Spectroscopy has become a major tool to investigate and reveal many-body phenomena in materials. Already more than half a century ago, inelastic neutron scattering experiments confirmed the predictions of Landau (Landau 1941) and Feynman (Feynman 1955) showing the existence of a roton minimum in superfluid $^4$He (Palevsky et al. 1958; Yarnell et al. 1959). In these experiments, neutrons act as a probe of density fluctuations and the response of the system, provided interactions with the neutrons are weak enough, is embodied in the so-called dynamic structure factor $S(\boldsymbol{q}, \omega)$, directly linked to two-body correlations and the elementary excitations of the ensemble (Nozières et al. 1999).

More recently, two-photon Bragg spectroscopy experiments[59] have been performed on ultracold quantum gases and share many analogies with neutron scattering. In weakly interacting Bose gases, the spectrum of elementary excitations, given by the Bogoliubov

---

[59] In Bragg experiments, atoms are exposed to two beams of nearly resonant frequencies $\omega_1$ and $\omega_2$ and wave vectors $\boldsymbol{k}_1$ and $\boldsymbol{k}_2$, separated by an angle $\theta$. Atoms can absorb photons from one beam and emit it into the other, ending up in the same internal state but with an energy difference $\delta\omega = \omega_1 - \omega_2$ that can create excitations in the gas and having acquired a net momentum $\hbar\delta k = \hbar|\boldsymbol{k}_1 - \boldsymbol{k}_2| \simeq 2\hbar k_\mathrm{L} \sin(\theta/2)$.

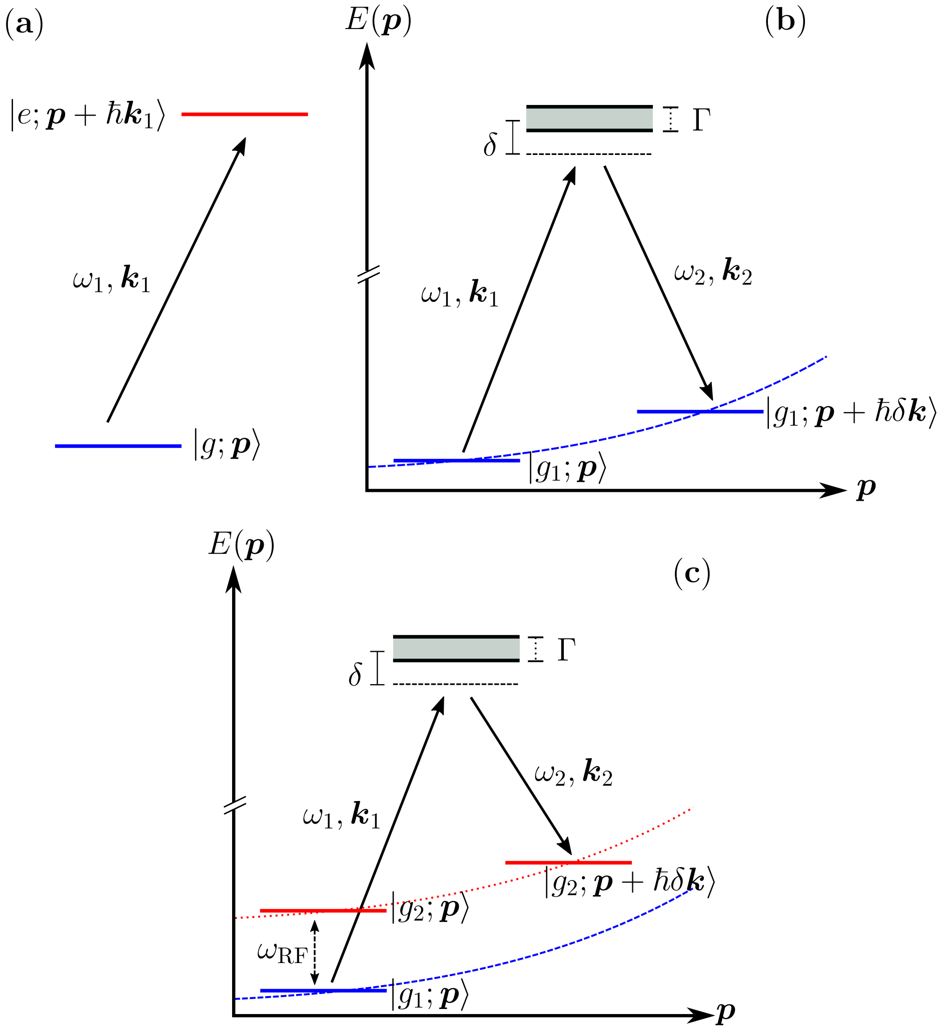

**Figure 5.2** – Different spectroscopic techniques discussed in the main text. **(a):** Optical spectroscopy. **(b):** Bragg spectroscopy. **(c):** Raman and RF spectroscopy. The states are labeled as $|a, \boldsymbol{p}\rangle$, where $a$ denotes the internal state and $\boldsymbol{p}$ the motional state. In **(a)** the transition occurs between two different electronic states $g, e$. In **(b)** and **(c)** the transitions occur between hyperfine states, denoted as $g_1$ and $g_2$, within the ground-state manifold. The detuning with respect to the excited state has been denoted by $\delta$ and the width of the excited state by $\Gamma$.

dispersion relation, was successfully measured with this technique at low (Stamper-Kurn et al. 1999; Vogels et al. 2002) and high momenta (Stenger et al. 1999; Steinhauer et al. 2002). These experiments were performed using condensates trapped in harmonic potentials, and showed that the confinement had a strong influence on the measured structure factor (Zambelli et al. 2000). More recently, Bragg spectroscopy has been applied in a periodic potential (Clément et al. 2009; Ernst et al. 2010) and also in homogeneous systems (Gotlibovych et al. 2014), observing a Heisenberg-limited momentum response. Moreover, it has been used to probe quantum gases in the strongly interacting regime, measuring deviations with respect to the Bogoliubov spectrum (Papp et al. 2008; Lopes et al. 2017) and, not long ago, a signature of the roton mode has been witnessed with this technique in a dipolar quantum gas (Petter et al. 2019). Bragg spectroscopy has also been applied to probe fermionic systems where, for instance, the structure factor was measured in a Fermi gas during the BEC-BCS crossover (Veeravalli et al. 2008).

Quantum gases experiments use many other kinds of spectroscopy techniques. For example, the existence of a cold collision shift in bosonic systems (Harber et al. 2002; Görlitz et al. 2003) and its absence in fermionic ones (Gupta et al. 2003; Zwierlein et al. 2003) was demonstrated by using microwave and RF spectroscopy, where atoms are transferred between two different ground-state hyperfine levels without momentum transfer [see figure 5.2(c)]. A review of how these different spectroscopic techniques have been employed in fermionic systems can be found in Törmä (2014); Tarruell (2014) and Törmä (2016).

This chapter is devoted to the spectroscopy of a bulk BEC driven on an optical clock transition. In such a situation, the absorption of the photon changes (i) the internal state and (ii) the motional state of the atom because of the high momentum imparted. Two-photon optical spectroscopy was essential to reveal Bose-Einstein condensation of spin-polarized hydrogen (Fried et al. 1998; Killian et al. 1998) through the mean-field collisional shift with respect to a thermal gas. Such a shift has also been observed by using ultra-narrow transitions. For instance, in Ytterbium (Yamaguchi et al. 2010) and metastable Helium (Rooij et al. 2011), where it has also been used to measure inter-state scattering lengths (Notermans et al. 2016) and the difference between the spectrum of a BEC and a degenerate Fermi gas. These experiments were all performed in an irreversible, weak-coupling regime.

We summarize the main effect of these different spectroscopic techniques in table 5.1:

| **Technique** | **State** | **Momentum transfer** | **Resonance shift** |
|---|---|---|---|
| RF/Microwave | $g_1 \to g_2$ | $\delta \boldsymbol{k} = 0$ | $(g_{21} - g_{11})n_g$ |
| Bragg | $g_1 \to g_1$ | $\delta \boldsymbol{k} = \boldsymbol{k}_1 - \boldsymbol{k}_2$ | $\hbar\omega(\delta \boldsymbol{k})$ |
| Raman | $g_1 \to g_2$ | $\delta \boldsymbol{k} = \boldsymbol{k}_1 - \boldsymbol{k}_2$ | $(g_{21} - g_{11})n_g + \hbar\omega(\delta \boldsymbol{k})$ |
| Optical | $g \to e$ | $\delta \boldsymbol{k} = \boldsymbol{k}_1$ | $(g_{eg} - g_{gg})n_g$ |

Table 5.1: Characteristics of the different spectroscopic techniques of common use in BEC experiments, in the weak coupling regime. Here $g_{\alpha\beta}$ denotes the mean-field interaction strength between atoms in states $\alpha$ and $\beta$ and $\hbar\omega(\delta \boldsymbol{k})$ corresponds to the particular dispersion relation of the excitations.

### 5.1.2 Resonance shifts and broadening sources

Let us focus on optical spectroscopy. In the present description, we will only consider weak excitations so that the population in the excited state can be neglected at all times. The optical spectrum of a bulk BEC in a magic harmonic trap is mainly determined by:

1. The inhomogeneous mean-field interactions $\propto gn(\boldsymbol{r})$.
2. The finite momentum width $\Delta p \simeq \hbar/R$ of the BEC.

We can already see the importance of interactions and the Doppler effect from a semi-classical argument. A ground state atom with momentum $\boldsymbol{p}$ at position $\boldsymbol{r}$ has an energy $E_\mathrm{i} = E_g + \boldsymbol{p}^2/(2M) + V_\mathrm{tr}(\boldsymbol{r}) + g_{gg} n_g(\boldsymbol{r})$, with $E_g$ the internal energy of the atom, $V_\mathrm{tr}(\boldsymbol{r})$ the trap potential, and $g_{gg} n(\boldsymbol{r})$ the interaction in the mean-field approximation. The absorption of a photon from the laser promotes the atom to the excited state, changing its atomic momentum to $\boldsymbol{p}' = \boldsymbol{p} + \hbar \boldsymbol{k}_\mathrm{L}$ and its energy energy to $E_\mathrm{f} = E_e + \boldsymbol{p}'^2/(2M) + V_\mathrm{tr}(\boldsymbol{r}) + g_{eg} n_g(\boldsymbol{r})$. Thus, the resonance condition becomes:

$$\hbar\omega_\mathrm{L} = E_\mathrm{f} - E_\mathrm{i} = \hbar\omega_0' + \boldsymbol{v}_\mathrm{r} \cdot \boldsymbol{p} + (g_{eg} - g_{gg})\, n_g(\boldsymbol{r}), \tag{5.1}$$

with $\boldsymbol{v}_\mathrm{r} = \hbar k_\mathrm{L}/M$ the recoil velocity. Three contributions appear here: The first term is the bare resonance frequency $\omega_0 = E_e - E_g$, which is corrected by the recoil frequency $\omega_\mathrm{r} = \hbar \boldsymbol{k}_\mathrm{L}^2/(2M)$, with $\omega_0' = \omega_0 + \omega_\mathrm{r}$. The second term indicates that the line is Doppler-sensitive, i.e., the resonance is shifted by a quantity proportional to the momentum with respect to an atom at rest. The third term corresponds to the collisional shift due to the different mean-field interactions. Because of the inhomogeneous density profile, the resonance condition becomes position-dependent:

$$\delta_\mathrm{L}'(\boldsymbol{r}) = \omega_\mathrm{L} - \omega_0' = \frac{1}{\hbar}\boldsymbol{v}_\mathrm{r} \cdot \boldsymbol{p} + \frac{1}{\hbar}\chi g_{gg} n_g(\boldsymbol{r}), \tag{5.2}$$

where we have put

$$\chi = (g_{eg}/g_{gg} - 1). \tag{5.3}$$

Besides, due to the confinement within a finite size $R_i$, the trapped BEC acquires a momentum width $\Delta p_i \simeq \hbar/R_i$, with $R_i$ the Thomas-Fermi radius in direction $i$. We can now estimate the contribution of each of the two broadening sources:

(i) Doppler broadening: $$\delta_\mathrm{D} \propto \frac{1}{\hbar}\boldsymbol{v}_\mathrm{r} \cdot \Delta\boldsymbol{p} \propto \frac{v_\mathrm{r}\sin\theta}{R_y}. \tag{5.4}$$

(ii) Mean-field broadening: $$\delta_\mathrm{int} \propto \frac{1}{\hbar}\chi g_{gg}[n(0) - n(R)] = \frac{\chi\mu}{\hbar}. \tag{5.5}$$

with $\theta$ the angle between the probe and the most confining axis of the trap, the $y-$axis in our experimental situation and $\mu = g_{gg} n(0)$ in the Thomas-Fermi regime. In table 5.1 we give the expected shift in the weak coupling regime for the different kinds of spectroscopies previously discussed.

### 5.1.3 Spin-orbit coupled systems

It is interesting to note that the system under study, i.e., a bulk BEC driven on an optical transition, represents a form of spin-orbit coupled (SOC) system (Goldman et al. 2014). We can show that this is indeed the case already in a simplified situation: We consider a 2-level atom moving in 1D being driven by a laser of frequency $\omega_\mathrm{L}$ and wave vector $\boldsymbol{k}_\mathrm{L} = k_\mathrm{L}\boldsymbol{u}_x$. In order to change its internal state, atoms need to exchange energy and momentum with the laser field. The Hamiltonian describing the interaction of the atom with the laser can be written as:

$$\hat{H}(t) = \frac{\hat{p}_x}{2M} + \frac{\hbar\omega_0}{2}\left(\hat{\mathbb{1}} + \hat{\sigma}_z\right) + \hbar\Omega_\mathrm{L}\cos(\omega_\mathrm{L} t - k_\mathrm{L}\hat{x})\,\hat{\sigma}_x \tag{5.6}$$

In a frame rotating at the laser frequency $\omega_\mathrm{L}$ and under the RWA, the Hamiltonian becomes time-independent:

$$\hat{H}' = \frac{\hat{p}_x^2}{2M} - \frac{\hbar\delta_\mathrm{L}}{2}\hat{\sigma}_z + \frac{\hbar\Omega_\mathrm{L}}{2}\left(\mathrm{e}^{-\mathrm{i}k_\mathrm{L}\hat{x}}\hat{\sigma}_+ + \mathrm{e}^{\mathrm{i}k_\mathrm{L}\hat{x}}\hat{\sigma}_-\right) \tag{5.7}$$

By performing a gauge transformation $\hat{\Lambda} = \exp(\mathrm{i}k_\mathrm{L}\hat{x}\hat{\sigma}_z)$, the Hamiltonian can be brought into the usual form of a SOC system:

$$\hat{\mathcal{H}}_\mathrm{SOC} = \frac{1}{2M}(\hat{p}_x - \hat{\mathcal{A}})^2 + \frac{\hbar\delta_\mathrm{L}}{2}\hat{\sigma}_z + \frac{\hbar\Omega_\mathrm{L}}{2}\hat{\sigma}_x, \tag{5.8}$$

with $\hat{\mathcal{A}} = \hbar k_\mathrm{L}\hat{\sigma}_z$. Spin-orbit coupling with ultracold atoms has been previously achieved by using two-photon Raman transitions with alkali atoms (Lin et al. 2011a). The technique is similar to Bragg scattering, but the frequency difference of the beams is enough to promote atoms into an excited hyperfine state within the ground state manifold [see figure 5.2(c)]. Although the Raman transition was largely detuned from the excited state, these experiments were mostly limited by the induced spontaneous emission. The same technique has been used to generate spin-orbit coupling in fermionic ytterbium in an optical lattice, using the internal hyperfine degree of freedom as both a pseudo-spin and a synthetic spatial dimension (Mancini et al. 2015). Also with fermionic ytterbium, spin-orbit coupling using the clock transition has been observed in an optical lattice (Livi et al. 2016). The relaxation mechanisms identified in the following give some perspective on the detrimental effects limiting the stability of spin-orbit coupled bulk systems with bosonic alkaline-earth like atoms.

## 5.2 Experimental setup

The experiments that will be shown in this chapter are performed with a BEC trapped in an CDT at the magic wavelength $\lambda_\mathrm{m} \simeq 759.4\,\mathrm{nm}$. Previously, the BEC has been prepared in the CDT described in chapter 2 and then adiabatically transferred into this other trap at $\lambda_\mathrm{m}$.

The $\lambda_\mathrm{m}$-CDT consists of a vertical beam, focused at a waist $w_\mathrm{v} \simeq 100\,\mu\mathrm{m}$ and with a power $P_\mathrm{v} = 800\,\mathrm{mW}$. The horizontal beam has a waist $w_\mathrm{h} \simeq 11\,\mu\mathrm{m}$ and we set its power among one of the following three values $P_\mathrm{h} = 10, 20$ or $30\,\mathrm{mW}$. For each power we have measured the following trapping frequencies through center of mass oscillations: $(\omega_x, \omega_y, \omega_z)_{10} = 2\pi \times (20, 264, 275)\,\mathrm{Hz}$, $(\omega_x, \omega_y, \omega_z)_{20} = 2\pi \times (22, 450, 450)\,\mathrm{Hz}$ and $(\omega_x, \omega_y, \omega_z)_{30} = 2\pi \times (23, 570, 580)\,\mathrm{Hz}$, respectively. For the typical atom numbers employed in this chapter, $N_0 \simeq 10^4$, this corresponds to interaction strengths on the interval $\mu/h \simeq 1 - 2\,\mathrm{kHz}$.

The atoms are then probed by a laser resonant with the ${}^1\mathrm{S}_0 \to {}^3\mathrm{P}_0$ transition for a duration $t$. The coupling laser propagates in the $x - y$ plane with a wave vector $\boldsymbol{k}_\mathrm{L}$ making an angle $\theta = \pi/4$ with the weak axis ($x$-axis) of the trap [see figure 5.1(a)]. The magic CDT is switched off immediately after the pulse. The cloud then expands in TOF for 12 ms and we record an image of the remaining atoms in $g$ by using the ${}^1\mathrm{S}_0 \to {}^1\mathrm{P}_1$ transition. For the remaining of the chapter we focus on the atomic population $P_g$, i.e., the total atomic number normalized to 1.

## 5.3 Theoretical description of the driving

### 5.3.1 Framework

The trapped BEC, coherently driven in the clock transition, can be described in second quantisation via the following many-body Hamiltonian:

$$\hat{H} = \hat{H}_{\text{sp}} + \hat{H}_{\text{int}} + \hat{V}_{\text{AL}}. \tag{5.9}$$

The single-particle contribution is given by:

$$\hat{H}_{\text{sp}} = \sum_{\alpha=g,e} \int \left[ -\frac{\hbar^2}{2M} \hat{\Psi}^\dagger_\alpha(\boldsymbol{r}) \boldsymbol{\nabla}^2 \hat{\Psi}_\alpha(\boldsymbol{r}) + V_{\text{tr}}(\boldsymbol{r}) \hat{\Psi}^\dagger_\alpha(\boldsymbol{r}) \hat{\Psi}_\alpha(\boldsymbol{r}) + E_\alpha \hat{\Psi}^\dagger_\alpha(\boldsymbol{r}) \hat{\Psi}_\alpha(\boldsymbol{r}) \right] \mathrm{d}^3 r. \tag{5.10}$$

where $V_{\text{tr}}(\boldsymbol{r})$ is the trapping potential and $\hat{\Psi}_\alpha(\boldsymbol{r})$ destroys an atom in state $\alpha$ at a point $\boldsymbol{r}$. We consider that atoms interact through mean-field collisions described by a contact potential:

$$\hat{H}_{\text{int}} = \frac{1}{2} \sum_{\alpha,\beta} \int g_{\alpha\beta}\, \hat{\Psi}^\dagger_\alpha(\boldsymbol{r}) \hat{\Psi}^\dagger_\beta(\boldsymbol{r}) \hat{\Psi}_\alpha(\boldsymbol{r}) \hat{\Psi}_\beta(\boldsymbol{r})\, \mathrm{d}^3 r. \tag{5.11}$$

Here, $g_{\alpha\beta} = 4\pi\hbar^2 a_{\alpha\beta}/M$ is the interaction strength between an atom in a state $\alpha$ and another in $\beta$. Finally, the coupling between the $g$ and $e$ states induced by the laser is described through the coupling with a classical field of frequency $\omega_{\text{L}}$ and wave vector $\boldsymbol{k}_{\text{L}}$. Under the rotating-wave approximation, the coupling potential $\hat{V}_{\text{AL}}$ reads:

$$\hat{V}_{\text{AL}} = \frac{\hbar\Omega_{\text{L}}}{2} \int \left[ \hat{\Psi}^\dagger_e(\boldsymbol{r}) \hat{\Psi}_g(\boldsymbol{r})\, \mathrm{e}^{\mathrm{i}(\boldsymbol{k}_{\text{L}}\cdot\boldsymbol{r} - \omega_{\text{L}} t)} + \text{h.c} \right] \mathrm{d}^3 r, \tag{5.12}$$

From now on, we set $E_g = 0$ and $E_e = \hbar\omega_0$ with $\omega_0 = 2\pi c/\lambda_0$ the bare frequency of the atomic transition. The time-dependency in the Hamiltonian can be removed by changing to a frame rotating at $\omega_{\text{L}}$, which transforms the field operator in the excited state as $\hat{\Psi}_e \rightarrow \hat{\Psi}_e \exp(-\mathrm{i}\omega_{\text{L}} t)$. This leads to $\hat{H} \rightarrow \hat{H} - \hbar\omega_{\text{L}}$. We can absorb this term in $\hat{H}_{\text{sp}}$ and write $E_e = -\hbar\delta_{\text{L}}$ with $\delta_{\text{L}} = \omega_{\text{L}} - \omega_0$ the detuning.

As we have seen in chapter 4, atoms in the excited state undergo two-body inelastic collisions leading to atom losses. In order to take this into account, we describe the dynamics of the system with a Lindblad master equation for the density matrix $\hat{\rho}$ (Haroche et al. 2013):

$$\frac{\mathrm{d}\hat{\rho}}{\mathrm{d}t} = \frac{1}{\mathrm{i}\hbar}[\hat{H}, \hat{\rho}] + \mathcal{L}[\hat{\rho}], \tag{5.13}$$

where $\mathcal{L}[\hat{\rho}]$ is the Lindblad operator defined as:

$$\mathcal{L}[\hat{\rho}] = \frac{\beta_{ee}}{2} \int \left[ \hat{C}(\boldsymbol{r}) \hat{\rho} \hat{C}^\dagger(\boldsymbol{r}) - \frac{1}{2} \hat{C}^\dagger(\boldsymbol{r}) \hat{C}(\boldsymbol{r}) \hat{\rho} - \frac{1}{2} \hat{\rho} \hat{C}^\dagger(\boldsymbol{r}) \hat{C}(\boldsymbol{r}) \right] \mathrm{d}^3 r, \tag{5.14}$$

with $\hat{C}(\boldsymbol{r}) = \hat{\Psi}^2_e(\boldsymbol{r})$.

### 5.3.2 GPE simulations

#### Derivation of the lossy GPE

A set of GPEs taking into account the inelastic losses can be derived from the previous master equation (5.13). A convenient way to perform this derivation is to compute the evolution of the expectation value of the field operator $\langle\hat{\Psi}_\alpha(\boldsymbol{r})\rangle$ and perform at the end the symmetry breaking approximation $\langle\hat{\Psi}_\alpha(\boldsymbol{r})\rangle = \Phi_\alpha(\boldsymbol{r},t)$, with $\Phi_\alpha(\boldsymbol{r},t)$ the order parameter (Pitaevskii et al. 2003) [see section 1.1.3]. This leads to:

$$\frac{\partial\langle\hat{\Psi}_g(\boldsymbol{r})\rangle(t)}{\partial t} = \frac{1}{\mathrm{i}\hbar}\mathrm{tr}\left(\hat{\Psi}_g(\boldsymbol{r})[\hat{H}\,,\hat{\rho}\,]\right), \tag{5.15}$$

$$\frac{\partial\langle\hat{\Psi}_e(\boldsymbol{r})\rangle(t)}{\partial t} = \frac{1}{\mathrm{i}\hbar}\mathrm{tr}\left(\hat{\Psi}_e(\boldsymbol{r})[\hat{H}\,,\hat{\rho}\,]\right) + \mathrm{tr}\left(\hat{\Psi}_e(\boldsymbol{r})\mathcal{L}[\hat{\rho}\,]\right). \tag{5.16}$$

The first term in the RHS of the two previous equations is equal to $-\mathrm{i}\langle[\hat{\Psi}_\alpha(\boldsymbol{r})\hat{H}]\rangle/\hbar$ and leads to the usual time-dependent GPE equations (Pitaevskii et al. 2003) with a coupling term:

$$\mathrm{i}\hbar\frac{\partial\Phi_g}{\partial t} = \left[\hat{h} + g_{gg}|\Phi_g|^2 + g_{ge}|\tilde{\Phi}_e|^2\right]\Phi_g + \frac{\hbar\Omega_\mathrm{L}}{2}\tilde{\Phi}_e, \tag{5.17}$$

$$\mathrm{i}\hbar\frac{\partial\tilde{\Phi}_e}{\partial t} = \left[\hat{h} + \boldsymbol{v}_\mathrm{r}\cdot\hat{\boldsymbol{p}} - \hbar\delta'_\mathrm{L} + g_{ge}|\Phi_g|^2 + g_{ee}|\tilde{\Phi}_e|^2\right]\tilde{\Phi}_e + \frac{\hbar\Omega_\mathrm{L}}{2}\Phi_g. \tag{5.18}$$

where we have put $\tilde{\Phi}_e(\boldsymbol{r},t) = \Phi_e(\boldsymbol{r},t)\exp(-\mathrm{i}\boldsymbol{k}_\mathrm{L}\cdot\boldsymbol{r})$, $\delta'_\mathrm{L} = \delta_\mathrm{L} - E_\mathrm{r}$ and defined the single-particle Hamiltonian $\hat{h} = \hat{\boldsymbol{p}}^2/(2M) + V_\mathrm{tr}$ with $\hat{\boldsymbol{p}} = -\mathrm{i}\hbar\boldsymbol{\nabla}$.

The second term in equation (5.16) does not conserve the atom number and leads to:

$$\mathrm{tr}\left(\hat{\Psi}_e(\boldsymbol{r})\mathcal{L}[\hat{\rho}\,]\right) = -\frac{\beta_{ee}}{2}|\Phi_e(\boldsymbol{r},t)|^2\Phi_e(\boldsymbol{r},t). \tag{5.19}$$

The contribution of the losses can be absorbed in the GPE equations by making the substitution:

$$g_{ee} \to g'_{ee} = \frac{4\pi\hbar^2}{M}a_{ee} - \mathrm{i}\frac{\hbar\beta_{ee}}{2}. \tag{5.20}$$

These mean-field equations, describe a non-Hermitian evolution taking into account all the effects discussed so far: coherent driving, inter- and intra-state interactions, atomic motion and inelastic losses[60].

We note that the $\beta_{ee}$ coefficient appearing in this equations corresponds to the parameter used in the inelastic loss rate equation $\partial\langle\hat{\Psi}_e^\dagger\hat{\Psi}_e\rangle/\partial t = -\beta_{ee}\langle\hat{\Psi}_e^\dagger\hat{\Psi}_e^\dagger\hat{\Psi}_e\hat{\Psi}_e\rangle$. For a BEC, this equation reduces to $\dot{n}_e = -\beta_{ee}n_e^2$, with $n_e = \langle\hat{\Psi}_e^\dagger\hat{\Psi}_e\rangle$ the mean density in $e$ (Kagan et al. 1985) [see appendix B].

In the following, the data is sistematically compared to the solution of these GPE equations. The equations are solved by first writing them in a dimensionless form,

---

[60] For the simulations, we use the most accurate parameters for the scattering terms, namely $a_{eg} \simeq 0.9\,a_{gg}$, $a_{ee} \simeq 1.2\,a_{gg}$ and $\beta_{ee} \simeq 2.6\times10^{-11}\,\mathrm{cm}^3/\mathrm{s}$ [see chapter 3 or Bouganne et al. (2017); Franchi et al. (2017)]

using harmonic oscillator units with respect to the smallest trapping frequency $\omega_x$. We use a Cartesian grid of size $40 \times 40 \times 40$, and the size of the grid in *each* direction corresponds to $4R_i$ with $R_i$ $(i = x, y, z)$ the initial Thomas-Fermi radius of the condensate. The time-step for the evolution is set according to $\Delta\mathtt{t}_k = 1/(100\omega_y)$, with $\omega_y$ the highest trapping frequency. The lossy GPEs are finally evolved using a split-step Fourier method (Javanainen et al. 2006) where the kinetic energy and the local terms are propagated separately and locally in momentum and position spaces, respectively. Finally, the term coupling $g$ and $e$ is implemented exactly by performing explicitly a SU(2) rotation whose parameters are determined by the local position-dependent detuning and the Rabi frequency.

## 5.4 Spectroscopy of a trapped BEC

In this section, we discuss the frequency domain spectroscopy experiments we have perfomed on a trapped BEC. We consider an atomic BEC prepared in the electronic ground state in various conditions, apply a pulse of length $t$ to transfer part of the atoms to the excited state, and record the number of remaining ground state atoms as we vary the laser detuning for a fixed pulse length. An example of such a spectum together with the prediction of a dissipative two-component GP model is shown in figure 5.1(c).

In the next sections we discuss the main physical effects determining the shape, the center and the width of the spectra, namely inhomogeneous interactions and Doppler broadening. We consider in all case pulses long enough so that Fourier broadening can be neglected. We have also tested in our GP numerical simulations that the effect of the Gaussian shape of the clock beam does not lead to a significant broadening[61] for the experiments presented in this chapter.

### 5.4.1 Analysis of the broadening sources

In order to compute the number of atoms transferred to the excited state (or, equivalently, remaining in the ground state) we now turn to a quantum description of the excitation process. If we consider long and weak excitations, the shape of the spectrum (i.e. the number of excited atoms at a given detuning and momentum transfer) can be computed in terms of Fermi's golden rule (Cohen-Tannoudji et al. 1992):

$$A(\boldsymbol{q}, \omega_{\mathrm{L}}) \propto \sum_j \eta_j \delta(\hbar\omega_{\mathrm{L}} - E_j + E_0), \tag{5.21}$$

with $\boldsymbol{q} = \hbar\boldsymbol{k}_{\mathrm{L}}$ the momentum imparted by the probe and $\eta_j = |\langle j|\Omega_{\mathrm{L}} \mathrm{e}^{\mathrm{i}\boldsymbol{k}_{\mathrm{L}}\cdot\boldsymbol{r}}|0\rangle|^2$ the overlap factor among motional states. Here, $\Phi_0(\boldsymbol{r}) = \langle \boldsymbol{r}|0\rangle$ is the initial wave function of the BEC and $\phi_j(\boldsymbol{r}) = \langle \boldsymbol{r}|j\rangle$ are the possible excited motional states from $\hat{H}_{\mathrm{sp}} + \hat{H}_{\mathrm{int}}$ in equation (5.9). Computing $A(\boldsymbol{q}, \omega)$ is in general a complicated task (we usually do not know how to compute the spectrum of excited states). However, there are two limit situations in which a calculation is feasible and we present them in the next paragraphs, following closely the discussion in Killian (2000).

---

[61] As discussed in chapter 3, the inhomogeneous profile leads to a non-uniform Rabi frequency $\Omega_{\mathrm{L}}$ over the cloud. Moreover, this also induces a position-dependent differential light shift and, therefore, an inhomogeneous detuning and both effects broaden the resonance.

### Doppler broadening

We start by neglecting mean-field interactions between $g$ and $e$ atoms, i.e., we put $\chi = 0$. In this situation the $\phi_j$ are just harmonic oscillator wave functions. However, because the momentum imparted to the particles is substantial ($\simeq \hbar k_{\mathrm{L}}$), the excited state atoms behave nearly as free particles and one can approximate the $\phi_j$ by plane waves. Then, the shape of the spectrum is given by:

$$A_{\mathrm{D}}(\boldsymbol{q}, \omega_{\mathrm{L}}) = \int \mathcal{N}(\boldsymbol{p})\, \delta\left(\hbar\omega_{\mathrm{L}} - \frac{(\boldsymbol{p}-\boldsymbol{q})^2}{2M} + \frac{\boldsymbol{p}^2}{2M}\right) \mathrm{d}^3 p, \tag{5.22}$$

with $\mathcal{N}(\boldsymbol{p})$ the momentum density distribution of the trapped BEC. We can specialize this to our experimental situation in which $\boldsymbol{q} = \hbar k_{\mathrm{L}}(\cos\theta, \sin\theta, 0)$. Then, $\boldsymbol{p}\cdot\boldsymbol{q} \simeq q_x p_x + q_y p_y$ and since $p_x \simeq \hbar R_x^{-1} \ll p_y \simeq \hbar R_y^{-1}$ we can write $\boldsymbol{p}\cdot\boldsymbol{q} \simeq p_y \hbar k_{\mathrm{L}} \sin\theta$ and:

$$A_{\mathrm{D}}(\boldsymbol{q}, \delta'_{\mathrm{L}}) \simeq \frac{M}{\hbar k_{\mathrm{L}} \sin\theta} \int \mathcal{N}\left(p_x, \frac{M\delta'_{\mathrm{L}}}{k_{\mathrm{L}}\sin\theta}, p_z\right) \mathrm{d}p_x\, \mathrm{d}p_z. \tag{5.23}$$

The peak of the spectrum coincides with $\delta'_{\mathrm{L}} \simeq 0$ (Zambelli et al. 2000). In order to extract useful information such as the broadening of the spectrum, one can evaluate numerically equation 5.23, with $\mathcal{N}$ given by the Fourier transform of the Thomas-Fermi profile. However, a simple estimate is obtained by performing a Gaussian expansion around $\delta'_{\mathrm{L}} = 0$. The rms-width $\Delta_{\mathrm{D}}$ of this Gaussian is (Zambelli et al. 2000):

$$\Delta_{\mathrm{D}} = \sqrt{\frac{8}{3}}\delta_{\mathrm{D}} \simeq 1.63 \frac{v_{\mathrm{r}} \sin\theta}{R_y}. \tag{5.24}$$

### Interaction broadening

The other limiting case consists in neglecting the Doppler effect. In the weak coupling situation, atoms transferred to the excited state can be treated in the Hartree-Fock approximation (Goldman et al. 1981), and we can look for the single-particle wave functions under the following effective potential:

$$V_{\mathrm{eff}}(\boldsymbol{r}) = V_{\mathrm{tr}}(\boldsymbol{r}) + g_{eg} n_g(\boldsymbol{r}) = \mu + \chi g_{gg} n_g(\boldsymbol{r}). \tag{5.25}$$

It has been shown in Killian (2000) that the line-shape is given by:

$$A_{\mathrm{int}}(\boldsymbol{q}, \delta'_{\mathrm{L}}) \propto \int n(\boldsymbol{r}) \delta\left(\delta'_{\mathrm{L}} - \frac{V_{\mathrm{eff}}(\boldsymbol{r}) - \mu}{\hbar}\right) \mathrm{d}^3 r \propto \frac{\hbar\delta'_{\mathrm{L}}}{\chi\mu}\sqrt{1 - \frac{\hbar\delta'_{\mathrm{L}}}{\chi\mu}}. \tag{5.26}$$

In order to estimate the spectral broadening due to interactions, we can calculate the rms-frequency width of the previous expression, which reads:

$$\Delta_{\mathrm{int}} = \sqrt{\frac{8}{147}}\delta_{\mathrm{int}} \simeq 0.23 \frac{\chi\mu}{\hbar}. \tag{5.27}$$

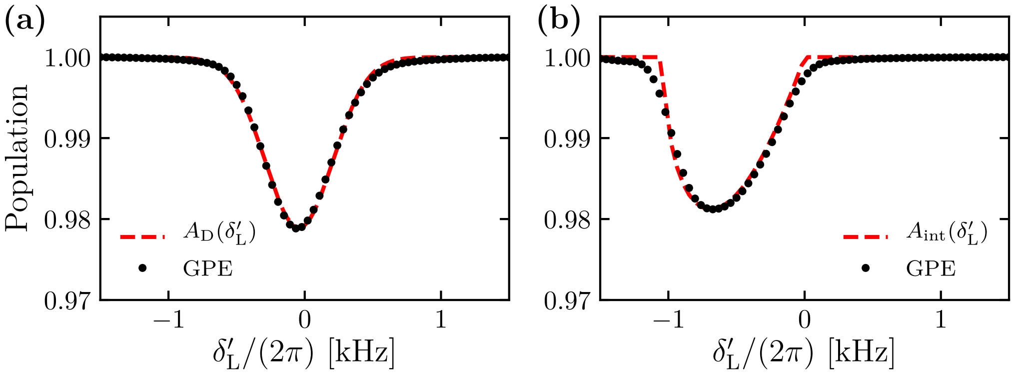

**Figure 5.3** – Example of spectra generated by using the GP model (see text below). **(a)** In the Doppler broadening regime with $\chi = 0$. **(b)** In the interaction broadening regime, by neglecting $\nabla^2\Phi_0$ in the GPE simulation. In both cases we have put $\beta_{ee} = 0$. The red dashed lines correspond to a fit using the simplified models presented in the text: **(a)** A Gaussian expansion around $\delta'_L \simeq 0$ of equation (5.23) and **(b)** using equation (5.26). The rms-width of the fitted Gaussian $\sigma$ for the Doppler broadened situation in **(a)** coincides with $\Delta_D$ in equation (5.24) and the rms-width of the profile shown in **(b)** coincides with $\Delta_{int}$ in equation (5.27). The simulation parameters are $\Omega_L = 2\pi \times 25\,\mathrm{Hz}$, the pulse length is $t = 3.5\,\mathrm{ms}$ and the trapping frequencies $(\omega_x, \omega_y, \omega_z) = 2\pi \times (10, 100, 100)\,\mathrm{Hz}$, with a chemical potential $\mu/h \simeq 2\,\mathrm{kHz}$.

### GPE simulations

We can test the validity of these two limit situations by generating some data using the dissipative GPEs (see above). In particular, we consider a situation at weak coupling strength $\Omega_L \simeq 2\pi \times 25\,\mathrm{Hz}$ with pulses of $t = 3.5\,\mathrm{ms}$, i.e., shorter than a quarter of the period of the confining potential used in the simulation, $(\omega_x, \omega_y, \omega_z) = 2\pi \times (10, 100, 100)\,\mathrm{Hz}$, so that the motion of the atoms is essentially the same as in free space, but long enough to neglect Fourier broadening [on the order of $1/(2\pi t) \simeq 50\,\mathrm{Hz}$]. The chosen chemical potential is $\mu/h = 2\,\mathrm{kHz}$. The result of these simulations is shown for $\chi = 0$ (i.e. in the Doppler broadening regime) in figure 5.3(a). A Gaussian fit to the simulated data leads to an rms width $\Delta/(2\pi) \simeq 236\,\mathrm{Hz}$ which agrees well with the weak-coupling prediction in equation (5.24): $\Delta_D/(2\pi) \simeq 250\,\mathrm{Hz}$. In order to test the interaction broadening regime prediction, we generate data by using $\chi = 0.5$ and neglecting the term in $\nabla^2\Phi_0$ in the GPE evolution. We show this in figure 5.3(b). By fitting the data with equation (5.26) we obtain an rms-width $\Delta \simeq \Delta_{int} = 2\pi \times 240\,\mathrm{Hz}$.

### Heuristic formula for the effect of both contributions

In an actual experiment, both effects need to be in principle taken into account. For this, in analogy with the previous work on Bragg spectroscopy (Zambelli et al. 2000), we model the experimental spectra by a Gaussian of rms-width $\sigma$ which we take to be given by:

$$\sigma = \sqrt{\Delta_D^2 + \Delta_{int}^2}. \tag{5.28}$$

For our typical experimental values we have $\mu/h \simeq 1.0 - 2.5\,\mathrm{kHz}$, $R_y \simeq 0.7 - 1.4\,\mu\mathrm{m}$ and $\theta = \pi/4$. As shown in chapter 3, for $^{174}$Yb the intra-species interaction strength is $g_{eg} = 0.9\,g_{gg}$, i.e., $\chi = 0.1$. Using equations (5.24) and (5.27) we see that the interaction

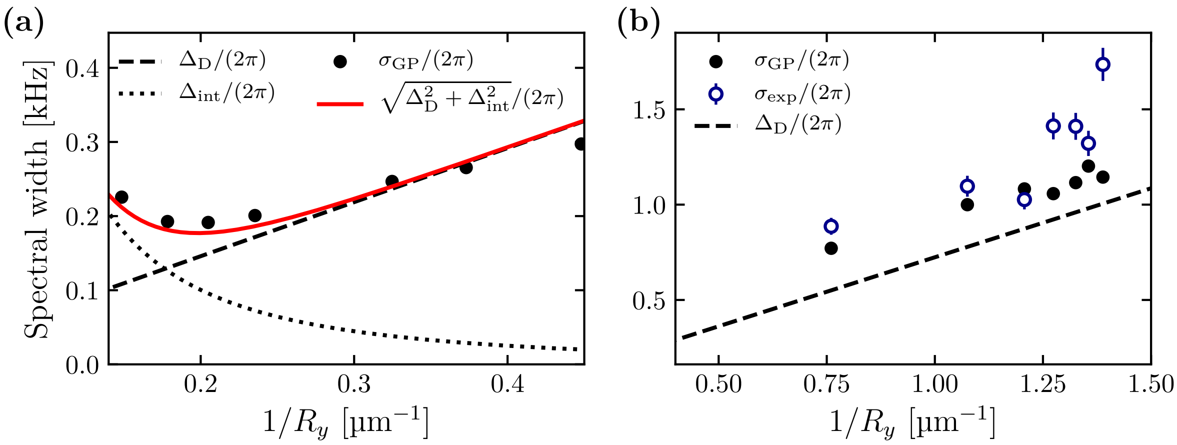

**Figure 5.4** – Spectrum width as a function of the inverse of the Thomas-Fermi radius $R_y$ in the $y-$direction. **(a):** Simulation - Black dashed and dotted lines correspond to the interaction and Doppler widths in equations (5.24) and (5.27), respectively. The red solid line is the quadratic average of both contributions. The points correspond to the rms of a Gaussian fit to spectra simulated via the GP equations. The parameters for the simulation are: $\Omega_{\mathrm{L}} = 2\pi \times 25\,\mathrm{Hz}$, $t = 3.5\,\mathrm{ms}$, $(\omega_x, \omega_y, \omega_z) = 2\pi \times (10, 100, 100)\,\mathrm{Hz}$ and $\chi$ is set to $\chi = 0.2$. The Thomas-Fermi radius is varied by changing the atom number from $N = 2 \times 10^4$ atoms to $N = 5 \times 10^6$ atoms. **(b)** Experiment and simulation - The black dashed line corresponds to the width predicted by equation (5.24). Empty points correspond to the rms width of a Gaussian fitted to the experimental data. Filled points correspond to the rms of a Gaussian fit to spectra simulated via the GP equations in the same experimental conditions. The experimental parameters are $\Omega_{\mathrm{L}} = 2\pi \times 150\,\mathrm{Hz}$ and the pulse length $t = 20 - 30\,\mathrm{ms}$. The Thomas-Fermi radius is varied by using different trapping frequencies and atom numbers. Figure adapted from Bosch Aguilera et al. (2018).

broadening $\Delta_{\mathrm{int}}/(2\pi) \simeq 25 - 60\,\mathrm{Hz}$ is negligible compared to the Doppler broadening $\Delta_{\mathrm{D}}/(2\pi) \simeq 500 - 1000\,\mathrm{Hz}$, which is the main source of broadening and dephasing in our experiments.

To test the validity of this Gaussian approximation we compute spectra using the GPE, again considering weak excitations. For these simulations, we have chosen a trap confinement and probe pulse length accordingly to the reasons exposed in the previous paragraph. The results are shown in figure 5.4(a), and we find a good agreement between the GPE simulation and the heuristic model in equation (5.28).

### 5.4.2 Comparison with the experiments

We now investigate to which extent the previous models can be used to describe our experimental data. We have recorded several spectra in different conditions by changing either the confining potential depth or the atom number. By doing so, we are able to explore a regime of interactions on the range $\mu/h \simeq 1 - 2\,\mathrm{kHz}$. Still, as previously stated, because of the small difference between the strengths $g_{gg}$ and $g_{eg}$, the shape of the spectra is mainly determined by Doppler broadening. The recorded spectra are thus fitted with a Gaussian, from which we extract an rms-width $\sigma_{\mathrm{exp}}$. An example of these spectra is given in figure 5.1(c). In figure 5.4(b) we show the extracted widths

$\sigma_{\text{exp}}$ and compare them to the expected Doppler width. The calculated width $\Delta_{\text{D}}$ underestimates by approximately a factor 2 experimental widths. We attribute this mismatch to the following reasons:

1. Although working at relatively small Rabi frequencies ($\Omega_{\text{L}} = 2\pi \times 150\,\text{Hz}$), the pulses are long and the depletion of the ground state becomes important (on the range of $40 - 60\%$). In this case, we cannot consider that we are in the perturbative regime and both the losses in the excited state and the interactions need to be accounted for, which lacks in the previous models.
2. The duration of the pulse is much larger than the period of the trap along the most confined axis. The in-trap dynamics are not included in the previous models either and therefore, the movement of the atoms in the trap, which can also lead to a broadening of the resonance due to the Doppler effect, is not accounted for.

In order to gain some insight into this mismatch, we have produced a series of spectra in the same experimental conditions using the GPE, which accounts for all these effects. We have extracted an rms-width $\sigma_{\text{GP}}$ from each generated curve by performing a Gaussian fit to the data, which we also show in figure 5.4(b). The width extracted from these simulations agrees well with $\sigma_{\text{exp}}$ at small interaction strengths (i.e. small $1/R_y$). A possible first reason to explain the small mismatch between $\sigma_{\text{exp}}$ and $\sigma_{\text{GP}}$ are the fast frequency fluctuations of the probe laser [see section 3.6], which can have significant effect at these Rabi frequencies considering the long times employed [20-30 ms]. However, as interactions increase, the experimental width is systematically about a 30% larger compared to the simulations. We will address this inconsistency appearing at large interactions in section 5.5.3.

## 5.5 Non-linear Rabi oscillations and relaxation of a bulk BEC

We now turn to the time-domain spectroscopy of a trapped BEC. For this, we perform Rabi oscillations, i.e., we fix the laser detuning[62] $\delta'_{\text{L}}$ and record the remaining ground state atoms for different pulse durations $t$. In this section, we do not limit to weak excitations and we explore the physics between the strong coupling regime, where the Rabi frequency is the largest energy scale in the experiment, to the weak coupling regime, where the broadening sources become larger than the Rabi frequency. Thus, the coherent driving, which transfers the BEC into a superposition of states of different internal and external quantum numbers, competes against a series of relaxation processes: Doppler broadening and inhomogeneous elastic and inelastic mean-field interactions. An example of this is shown in figure 5.5 where we can observe a crossover with decreasing driving strength $\Omega_{\text{L}}$ from a coherent regime with underdamped oscillations 5.5(a)-(c), to an incoherent one where relaxation takes over 5.5(d)-(f).

---

[62] Before recording Rabi oscillations, a spectrum is acquired in order to determine the resonance frequency $\delta'_{\text{L}}$ and correct for eventual cavity drifts.

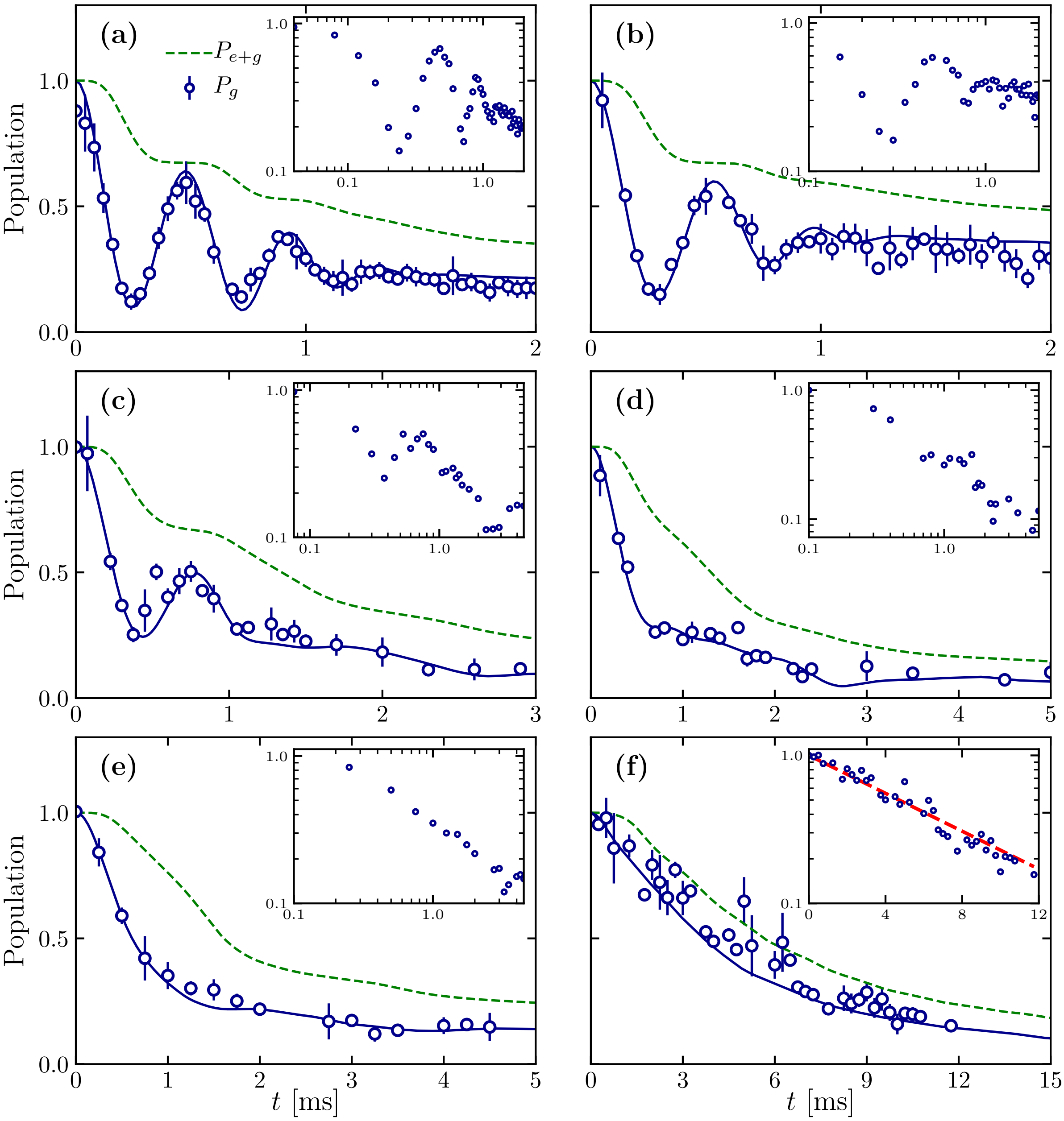

**Figure 5.5** – Population dynamics as a function of the pulse duration $t$ for varying Rabi frequencies: $\Omega_{\mathrm{L}}/(2\pi) \simeq 2.1\,\mathrm{kHz}$ **(a)**, $1.8\,\mathrm{kHz}$ **(b)**, $1.1\,\mathrm{kHz}$ **(c)**, $750\,\mathrm{Hz}$ **(d)**, $540\,\mathrm{Hz}$ **(e)**, $185\,\mathrm{Hz}$ **(f)**. Blue circles show the measured population in $g$ normalized to the total atom number, noted $P_g$. The solid blue lines show fits to the lossy GPE model (see text below), with only the driving strength $\Omega_{\mathrm{L}}$, the initial atom number and the detuning $\delta'_{\mathrm{L}}$ as free parameters. The green dashed lines show the evolution of the total atom number extracted from the GPEs, normalized to the initial one, noted $P_{e+g}$. The insets in **(a)**-**(e)** show the same data in double-logarithmic scale. For the inset in **(f)** only the vertical axis is in logarithmic scale. The red dashed line in **(f)** shows an exponential fit to the data with a 1/e decay rate of $\simeq 150\,\mathrm{s}^{-1}$ in good agreement with $\Omega_{\mathrm{L}}^2/(2\Delta_{\mathrm{D}})$, where $\Delta_{\mathrm{D}}/(2\pi) \simeq 600\,\mathrm{Hz}$. For all data shown in this figure, the trap frequencies are $(\omega_x, \omega_y, \omega_z) \simeq 2\pi \times (20, 264, 275)\,\mathrm{Hz}$ and the BEC chemical potential is $\mu/h \simeq 1\,\mathrm{kHz}$. Figure adapted from Bosch Aguilera et al. (2018).

### 5.5.1 Phenomenological analysis

This observation is reminiscent of the textbook quantum optics situation of a driven two-level system undergoing relaxation at a rate $\Gamma$. Here, one expects a crossover from exponentially underdamped oscillations when $\Omega > \Gamma$ towards a purely exponential decay at a rate $\propto \Omega^2/\Gamma$ for $\Omega < \Gamma$, analogous to the Wigner-Weisskopf decay expected when a discrete level is coupled to a continuum of spectral width $\Gamma$ (Cohen-Tannoudji et al. 1992) [see appendix C]. This picture also holds in a similar fashion for an ensemble of Doppler-broadened non-interacting particles: In a uniform system, the coherent driving would only couple two single states: $|g, \mathbf{0}\rangle$ and $|e, \boldsymbol{k}_\mathrm{L}\rangle$ of momenta 0 and $\hbar \boldsymbol{k}_\mathrm{L}$, respectively. The presence of the trap in our experimental situation couples instead two wave packets of width $\sim \hbar/R$ centered around these same momenta. As we have seen, this leads to a Doppler broadening $\Delta_\mathrm{D}$ which plays the role of the spectral width $\Gamma$. Therefore, averaging over the atomic cloud, induces a decay of the $g - e$ coherences because of ensemble dephasing. The contrast of the oscillations gets reduced during the evolution with an asymptote at 1/2 of the total initial population.

Such an exponential decay is only observed for the weakest coupling employed in our experiments [inset of figure 5.5(f)]. Indeed, for larger driving strengths we find a much slower algebraic decay [see insets in log-log scale in figures 5.5(a)-(e)], which means that the picture of an ensemble of two-level Doppler-broadened independent BECs cannot explain our data.

Before going into a more quantitative analysis and in order to gain some intuition, we start by describing the crossover between the two regimes by fitting our data with the following heuristic function:

$$P_g(t) = \frac{A(t)}{1+C}\left[1 + C\cos(\Omega_\mathrm{L} t)\,\mathrm{e}^{-t/\tau_2}\right], \tag{5.29}$$

where $A(t) = (1 + t/\tau_1)^{-1}$ is a smooth envelope describing the global decay of the population in $g$, $\tau_2$ corresponds to the damping time of the oscillations and $C$ is the contrast of these oscillations.

We show in figure 5.6 the best parameters as a function of the calculated Rabi frequency that result from fitting this empirical model to the experimental data using equation (3.10). The data corresponds to the oscillations shown in figure 5.5 and other oscillations taken in similar experimental conditions, i.e., with $\mu/h \simeq 1\,\mathrm{kHz}$ and where $\Delta_\mathrm{D}/(2\pi) \simeq 600\,\mathrm{Hz}$. The measured frequency of the oscillations agrees well with the calculated one [solid line in figure 5.6(a)] and, as expected, the contrast of the oscillations decreases with decreasing Rabi frequency [figure 5.6(b)]. We have enforced $C = 0$ in the fits for all Rabi frequencies $\Omega_\mathrm{L} \leq \Delta_\mathrm{D}$ where no oscillation is visible (shaded regions in figure 5.6). This absence of oscillations is coherent with what one would expect in the weak coupling regime [see appendix C]. We also show the inverse decay times for the populations [5.6(c)] and the coherences [5.6(d)]. It is interesting to note that, at weak coupling, the decay rate follows the trend $\Omega_\mathrm{L}^2/(2\Delta_\mathrm{D})$ [solid line in 5.6(c)] predicted for an ensemble of Doppler-broadened non-interacting two-level systems.

In the next section, we show on the one hand that this non-linear relaxation can be attributed to the strong inelastic losses that atoms in the excited state undergo. On the

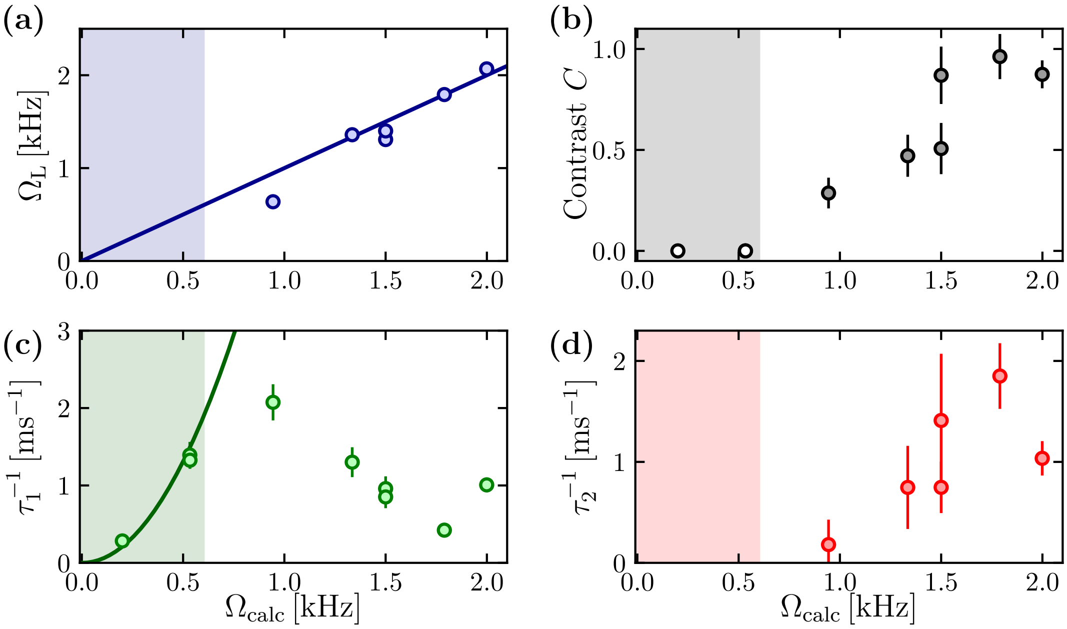

**Figure 5.6** – Results of the empirical fits using equation (5.29). **(a)** Measured oscillation frequency $\Omega_L$, **(b)** contrast of the oscillations $C$ **(c)** amplitude damping rate $1/\tau_1$ and **(d)** coherence damping rate $1/\tau_2$ as a function of the calculated rabi frequency $\Omega_{calc}$. The solid line in **(a)** shows the expected oscillation frequency for vanishing detuning. The solid line in **(c)** shows the predicted decay rate for weak driving $\Omega^2/(2\Delta_D)$. We have enforced $C = 0$ in the fitting procedure for $\Omega_{calc} \leq \Delta_D \simeq 2\pi \times 600\,\mathrm{Hz}$ (shaded regions) where no oscillation is visible. All fit parameters are extracted from Rabi oscillations performed in a BEC whose trap frequencies are $(\omega_x, \omega_y, \omega_z) \simeq 2\pi \times (20, 264, 275)\,\mathrm{Hz}$ and the BEC chemical potential is $\mu/h \simeq 1\,\mathrm{kHz}$. Figure adapted from Bosch Aguilera et al. (2018).

other hand, we also show that for very weak couplings one expects indeed to recover the exponential decay.

## 5.5.2 Dephasing and damping sources: a toy model

To go beyond the phenomenological model shown in the previous paragraph and point the mechanisms that are responsible for the observed dephasing on the one hand, and the shape of the decay in the data shown in figure 5.5 on the other hand, we present here a minimal model solvable in the regimes of strong and weak driving.

### Evolution of the 1-body density matrix in the mean-field approximation

Let us focus on the evolution of the one-body density matrix

$$\rho_{\alpha\beta}(\boldsymbol{r}, \boldsymbol{r}') = \langle \hat{\Psi}^\dagger_\alpha(\boldsymbol{r}) \hat{\Psi}_\beta(\boldsymbol{r}') \rangle. \tag{5.30}$$

We will only consider internal correlations at the same position $\boldsymbol{r} = \boldsymbol{r}'$. Moreover, we will systematically perform a mean-field approximation to reduce expectation values involving four field operators to:

$$\langle \hat{\Psi}^\dagger_\alpha(\boldsymbol{r}) \hat{\Psi}^\dagger_\beta(\boldsymbol{r}) \hat{\Psi}_\gamma(\boldsymbol{r}) \hat{\Psi}_\delta(\boldsymbol{r}) \rangle \simeq \langle \hat{\Psi}^\dagger_\alpha(\boldsymbol{r}) \hat{\Psi}_\gamma(\boldsymbol{r}) \rangle \langle \hat{\Psi}^\dagger_\beta(\boldsymbol{r}) \hat{\Psi}_\delta(\boldsymbol{r}) \rangle = \rho_{\alpha\gamma}\rho_{\beta\delta}. \tag{5.31}$$

With this, the evolution of the one-body density matrix under the master equation (5.13) becomes (we omit the spatial dependence in the notation):

$$\dot{\rho}_{gg} = \dot{\rho}_{gg}\big|_{\mathrm{kin}} + \mathrm{i}\frac{\Omega_{\mathrm{L}}}{2}(\rho_{eg} - \rho_{ge}), \tag{5.32}$$

$$\dot{\rho}_{eg} = \dot{\rho}_{eg}\big|_{\mathrm{kin}} + \mathrm{i}\frac{\Omega_{\mathrm{L}}}{2}(\rho_{gg} - \rho_{ee}) - \mathrm{i}\delta_{\mathrm{L}}\rho_{eg} - \frac{\beta_{ee}}{2}\rho_{ee}\rho_{eg} + \frac{\mathrm{i}}{\hbar}[\Delta_1\rho_{gg} - \Delta_2\rho_{ee}]\rho_{eg}, \tag{5.33}$$

$$\dot{\rho}_{ee} = \dot{\rho}_{ee}\big|_{\mathrm{kin}} - \mathrm{i}\frac{\Omega_{\mathrm{L}}}{2}(\rho_{eg} - \rho_{ge}) - \beta_{ee}\rho_{\mathrm{ee}}^2. \tag{5.34}$$

In the previous set of equations, we have put $\Delta_1 = g_{eg} - g_{gg}$ and $\Delta_2 = g_{ee} - g_{eg}$. The terms $\dot{\rho}_{\alpha\beta}\big|_{\mathrm{kin}}$ contain the motional evolution of the one-body density matrix due to $\hat{H}_{\mathrm{sp}}$. This term is not local and, because of it, these equations are hard to solve (even numerically) and some approximations are needed.

### Weak coupling regime

First of all, we consider the case in which $\hbar\Omega_{\mathrm{L}}$ is the smallest energy scale. We will treat the motional evolution approximately, under the following two assumptions:

1. We are in the weak coupling regime and the population of $e$ atoms is small. We can therefore neglect their motion and also their effect through mean-field collisions on $g$ atoms. With this:

$$\dot{\rho}_{gg}\big|_{\mathrm{kin}} = \dot{\rho}_{ee}\big|_{\mathrm{kin}} = 0. \tag{5.35}$$

2. The main effect of the motion is to shift the resonance frequency due to the recoil and to damp the coherences between $g$ and $e$ atoms. In order to obtain an analytical solution, we treat this effect in a similar fashion as a driven atom undergoing background collisions with a residual gas (Cohen-Tannoudji et al. 1992), and we write:

$$\dot{\rho}_{eg}\big|_{\mathrm{kin}} \simeq \left(-\frac{1}{\mathrm{i}\hbar}E_{\mathrm{r}} - \Delta_{\mathrm{D}}\right)\rho_{eg}. \tag{5.36}$$

With these simplifications, the equations are now local and are just a non-linear version of the standard optical Bloch equations. Working in the weak coupling limit allows for further approximations. In particular, except for the decay term $-\beta_{ee}\rho_{ee}^2$, we can neglect all terms involving $\rho_{ee}$. In such a situation, $\rho_{gg}$ changes at a much slower pace compared to $\rho_{eg}$ which evolves at a rate $\propto \Delta_{\mathrm{D}}^{-1}$. The coherences reach their stationary state much faster and follow the slow variable $\rho_{gg}$. We can thus perform an adiabatic elimination of the coherences (Cohen-Tannoudji et al. 1992) and their steady state value reads:

$$\rho_{eg}^{(\mathrm{ss})} = \frac{\mathrm{i}\Omega_{\mathrm{L}}}{\Delta_{\mathrm{D}} + \mathrm{i}\delta'_{\mathrm{L}} - \mathrm{i}\Delta_1\rho_{gg}/\hbar}\rho_{gg}, \tag{5.37}$$

where $\delta'_{\mathrm{L}} = \delta_{\mathrm{L}} - E_{\mathrm{r}}$. The population of the ground state evolves under:

$$\dot{\rho}_{gg} \simeq -\frac{\Omega_{\mathrm{L}}^2\Delta_{\mathrm{D}}}{2\left[\Delta_{\mathrm{D}}^2 + (\delta'_{\mathrm{L}} - \Delta_1\rho_{gg}/\hbar)^2\right]}\rho_{gg} \tag{5.38}$$

As previously discussed, the term $\Delta_1 = g_{eg} - g_{gg}$ is small compared to the Doppler broadening $\Delta_{\rm D}$ and we also neglect it for this discussion. For $\delta'_{\rm L} = 0$, the population in the ground state follows the simple equation $\dot{\rho}_{gg} \simeq -\Omega_{\rm L}^2 \rho_{gg}/(2\Delta_{\rm D})$, so that:

$$\rho_{gg}(t) = \rho_0 \, \mathrm{e}^{-t/\tau_2}, \tag{5.39}$$

with $1/\tau_2 = \Omega_{\rm L}^2/(2\Delta_{\rm D})$, i.e., the population in the ground state decays exponentially due to the broadening introduced by the movement of the atoms, and there is no oscillation; which is indeed what we observe at the smallest drivings [see solid line in figure 5.6(c)].

### Strong coupling regime

We now turn to the opposite limiting situation in which $\hbar\Omega_{\rm L}$ and $\hbar\beta_{ee}n_0$ are the largest energy scales, with $\Omega_{\rm L} > \beta_{ee}n_0$. In this case the dephasing mechanisms play a minor role at short times and the system undergoes Rabi oscillations with a slowly decaying envelope $\varrho(t)$ due to the losses in the excited state: $\dot{\varrho}(t) = -\beta_{ee}\varrho(t)^2$. We can thus write $\rho_{gg} \simeq \varrho(t)\cos^2(\Omega_{\rm L}t/2)$ and $\rho_{ee} \simeq \varrho(t)\sin^2(\Omega_{\rm L}t/2)$. Averaging over a period we find that the envelope function decays as:

$$\dot{\varrho}(t) \simeq -\frac{3}{4}\beta_{ee}\varrho(t)^2. \tag{5.40}$$

In the particular case of a uniform system, we can write $\varrho = N/L$, and the averaged population $\bar{P}_g$ evolves as:

$$\bar{P}_g(t) = \frac{1}{1 + t/\tau_1}, \tag{5.41}$$

with $1/\tau_1 = 3\beta_{ee}\varrho(0)/4$. Therefore, the expected dynamics at strong coupling correspond to underdamped Rabi oscillations around an average value decaying algebraically as $\sim 1/t$. This is indeed what we observe experimentally for strong driving [see figures 5.5(a)-(e)].

Therefore, we conclude that in the weak coupling limit, due to the Doppler relaxation, $\Delta_{\rm D}$, the decay of the ground state population should be exponential with no oscillations. This decay is due to the damping of the coherences. However, for strong couplings, this single-particle picture no longer holds and the population decays algebraically because of the inelastic two-body collisions.

### GPE analysis

To go beyond this analysis, we have solved the lossy GPE equations (5.17) and (5.18) numerically and fitted the numerical solution to the experimental data with only the following free parameters: the initial atom number $N_0$, the coupling strength $\Omega_{\rm L}$ and the detuning $\delta'_{\rm L}$. The GPE fit corresponds to the solid lines shown in figure 5.5. For all this data, which corresponds to a value of the interactions $\mu/h \simeq 1\,\mathrm{kHz}$, we find a good agreement between the GPEs and the observed dynamics. The fitted Rabi frequencies agree within 10% with the calculated ones and the extracted detunings (on the order of $|\delta_{\rm L}|/(2\pi) \leq 300\,\mathrm{Hz}$) are compatible with our accuracy in finding the resonance.

### 5.5.3 Beyond GPE: other possible sources of dephasing

Until now, we have seen that the main sources of decoherence are Doppler broadening and strong inelastic losses. Although elastic mean-field collisions are present, they have not been essential to describe the data.

However, this is no longer the case once we drive oscillations in tighter traps: For this, we performed a set of experiments at chemical potentials up to $\mu/h \simeq 2\,\mathrm{kHz}$, an example of which can be seen in figure 5.7(a). We have used the empirical model in equation (5.29), and we show the result of the extracted contrasts in 5.7(b), which drop as interactions increase. At this stage, there is no evident way of telling if this reduction of the contrast is due to Doppler broadening or the stronger interactions. As before, we try to gain some insight by fitting the experimental data with the dissipative coupled GP model. As we can see in 5.7(a), the long-time decay of the population is well reproduced but the damping of the oscillations is underestimated. In figure 5.7(c) we show that this effect is systematic by quantifying the agreement between the GP model and the observations by a reduced $\chi^2$ factor:

$$\chi^2_\nu = \frac{1}{M} \sum_{i=1}^{M} \frac{[f(t_i) - P_g(t_i)]^2}{\sigma^2_{g,i}}, \tag{5.42}$$

i.e., the sum of the fit residuals $f(t_i) - P_g(t_i)$ weighted by the standard deviation $\sigma_{g,i}$ and normalized to the number $M$ of data points. We find that the reduced $\chi^2$ increases regularly with the initial chemical potential [see figure 5.7(c)]. This observation goes accordingly with the mismatch noticed in section 5.4.2, where the broadening of the experimental spectra for strong interactions is larger than the one predicted by the GPE [see figure 5.4(b)], and thus, a stronger damping of the oscillations is not surprising in this sense. A possible indication of this is that the mean-field description becomes insufficient. A first attempt to go beyond the previous model, although still under a mean-field description, is to heuristically include in the GPE other processes such as momentum relaxation collisions of the type

$$|g, \boldsymbol{0}\rangle + |e, \boldsymbol{k}_\mathrm{L}\rangle \rightarrow |g, \boldsymbol{q}\rangle + |e, \boldsymbol{k}_\mathrm{L} - \boldsymbol{q}\rangle. \tag{5.43}$$

It is possible to derive a rate $\gamma_\mathrm{coll}$ for such a process in the case of a uniform gas of density $n$. The rate in this case is [see appendix D]:

$$\gamma_\mathrm{coll} \simeq n \sigma_{ge} v_\mathrm{r}, \tag{5.44}$$

with $\sigma_{ge} = 4\pi a_{eg}^2$ the collisional cross-section. A numerical application for our typical densities $n \simeq 5\times10^{14}\,\mathrm{at/cm}^3$ of the experiments in figure 5.7 leads to $\gamma_\mathrm{coll}/(2\pi) \simeq 100\,\mathrm{Hz}$ which is too small with respect to the other damping contributions to have a significant effect [see red dotted line in figure 5.7(a)].

We note however, that this simple estimate does not account for any correlations between the particles. Additional effects such as thermal population of quasiparticles in the initial state, which could have been generated by excitations during the transfer from the initial CDT to the magic trap, are not included in the GP description and could also contribute to the relaxation of coherence. A similar argument was drawn in Gardiner et al. (2001) in order to try to explain the lack of understanding of two-photon

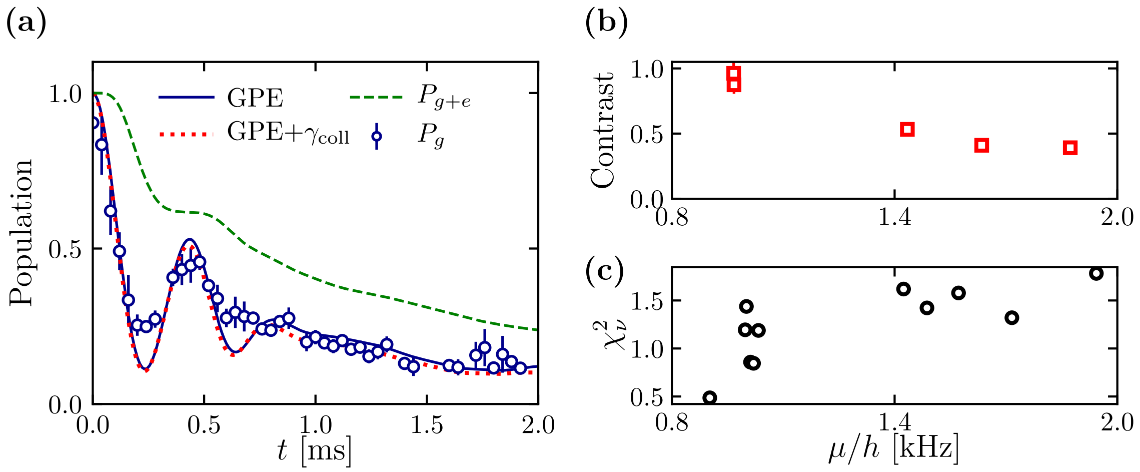

**Figure 5.7** – **(a):** Population dynamics for $\mu/h \simeq 2\,\text{kHz}$. The solid blue line corresponds to a fit to the dissipative GP model, showing a faster relaxation of the experimental points compared to the prediction. The dotted red line corresponds to a GPE simulation taking diffusive collisions into account. The trap frequencies are $(\omega_x, \omega_y, \omega_z) \simeq 2\pi \times (23, 570, 580)\,\text{Hz}$ for this measurement. **(b):** Contrast of the oscillations $C$ versus initial chemical potential $\mu$. All curves correspond to oscillations with $\Omega_\text{L}/(2\pi) \simeq 2\,\text{kHz}$, and $\delta'_\text{L} \simeq 0$. **(c):** Reduced $\chi^2$ of a fit to the two-component lossy GP model versus $\mu$. Figure adapted from Bosch Aguilera et al. (2018).

spectroscopy of atomic hydrogen (Fried et al. 1998; Killian et al. 1998). We have not investigated this issue further because of the complexity of a theoretical description in terms of quasiparticle dynamics.

## 5.6 Conclusion

In this chapter, I have presented a study on the relaxation dynamics of a driven BEC trapped in an harmonic potential at the magic wavelength. For our experimental parameters and due to the nature of $^{174}$Yb, the most important damping sources are Doppler broadening and inelastic losses between excited state atoms.

In a first part, I have studied a series of frequency spectroscopy experiments. Here, I have compared our experimental data to two theoretical models obtained in the weak coupling, irreversible regime (Killian 2000; Zambelli et al. 2000). I have shown that these predictions do not reproduce properly the experimental data, and this has been attributed mainly to two factors (i) the depletion of the condensate in our experiments is important and (ii) the movement of the atoms in the trap, which also needs to be accounted for. The data has then been compared to a pair of coupled, dissipative GPEs, which take these effects into account. The agreement between the simulations and the experimental data is good for small interactions. However, the result of these simulations underestimates some unidentified sources of decoherence in our experimental data as interactions are increased.

In the second part, I have investigated and identified some of the phenomena leading to the rich relaxation dynamics observed during the coherent driving of Rabi oscillations. In particular, instead of the exponential decay one would expect for an ensemble of non-interacting particles, I have shown with a simple analytical model that the presence of inelastic losses modifies this to a slower algebraic decay. Doppler broadening also contributes to the dephasing of the oscillations and the non-interacting prediction is recovered at small driving strengths. Here, I have also compared our observations to the GP prediction, which reproduces well the data at small values of the interactions. Again, a disagreement between the GP prediction and the experimental data at strong interactions has been identified.

The driven BEC presented in this chapter can be seen as a quenched spin-orbit coupled BEC (Goldman et al. 2014), with the spin corresponding to the internal states $g, e$. Due to their absence of spontaneous emission, alkaline-earth-like atoms, such as ytterbium, are attractive candidates to be used in the generation of artificial gauge fields. However, the relaxation sources presented in this chapter, and notably the strong inelastic losses, are of course detrimental for these kinds of experiments. For instance, if one were to prepare the ground state of a BEC dressed by the coupling say, by an adiabatic ramp of the Rabi frequency, the stability and the ability to follow the ground state of the system will be strongly limited by these relaxation mechanisms. This effects can be substantially reduced working in larger traps such as the state-of-the-art uniform potentials (Gaunt et al. 2013), with sizes of several tens of microns. This would reduce the Doppler broadening and eliminate all broadening contributions due to spatial dependent terms. Moreover, it would considerably slow-down the inelastic losses thanks to the smaller densities.

# CHAPTER 6

# Anomalous momentum diffusion in a dissipative many-body system

In this chapter, I focus on the interplay between interactions and decoherence in the form of spontaneous emission for an ensemble of atoms loaded in an optical lattice. Here, dissipation is artificially induced in a controlled manner by a continuous driving of the intercombination transition $^1\mathrm{S}_0 \to {}^3\mathrm{P}_1$, which leads to a series of absorption-spontaneous emission events. As is well known (Holland et al. 1996; Pichler et al. 2010) spontaneous emission is a source of dissipation which erases the coherences between the internal states. Besides, due to the recoil of the atom in a random direction after the spontaneous emission of a photon, it also destroys coherences between external states. More in detail, after spontaneously emitting a photon, the motional atomic degrees of freedom become entangled with the continuum of modes of the emitted photon. By tracing over these modes (i.e., *erasing* the information) an initially pure atomic state with well-defined momentum turns into a statistical mixture of momentum states. There is a spread in momentum space which entails the localization of the spatial coherence of the atom. These coherences vanish on a scale given by the wavelength of the spontaneously emitted photon, as experimentally shown in Pfau et al. (1994).

As we have already discussed in section 2.2.3 (see also appendix A) spatial phase coherence (i.e. the first order correlation function) and the momentum distribution are Fourier transforms of each other. Thus, a broadening of the one, causes a reduction of the other. In an optical lattice, spatial coherence is characterized by the visibility of Bragg peaks, which gets reduced as long-range order is lost. Yanay et al. (2014) showed that for non-interacting particles in a lattice, the effect of continuous absorption-spontaneous emission cycles was the exponential suppression of the spatial coherence. This exponential decay is associated to a random walk in momentum space, with a momentum width growing in a diffusive manner as $\Delta p \propto \sqrt{t}$. This evolution, ends up driving the system to a uniform distribution of quasimomenta.

In this chapter we show that, in the presence of strong interactions, the evolution dynamics towards the steady state develops in a non-trivial manner, drastically different from the exponential decay predicted for ideal systems. After an initial exponential loss of the coherence, a slow algebraic regime with residual coherence emerges. This regime, which features a subdifusive behavior ($\Delta p \propto t^{1/4}$), was predicted in Poletti et al. (2012) and Poletti et al. (2013) and steams from the competition between dissipation, trying to localize atoms in Fock space, coherent tunneling, trying to delocalize the atoms and interactions, promoting low occupation numbers by inhibiting transitions between states with different occupations and thus, different energies. The presence of interaction then disfavors reaching the steady state, thus partially allowing the remaining coherence to decay in a much slower way. Poletti et al. showed that this algebraic subdiffusive stage can be linked to the dynamics taking place in configuration space (Fock space). As it will be shown, the evolution of spatial coherence is locked to the evolution of the populations and thus follows the same algebraic dynamics.

The emergence of slow algebraic relaxations in the presence of interactions have also been predicted in dissipative many-body spin systems (Cai et al. 2013) and in a model of optical optical lattice clocks with dipole-dipole interactions (Henriet et al. 2019).

In a more general framework, understanding the interplay between dissipation and interactions is a key issue of open quantum systems (Müller et al. 2012), and the results shown in this chapter constitute an experimental evidence of the non-trivial role of interactions in dissipative systems.

This chapter is organized as follows: In the first section, the experimental results are shown and two different analyses are presented and discussed. Then, the model presented in Poletti et al. (2012) and Poletti et al. (2013) is depicted. Finally, an extension to this model which describes closer our experimental framework by taking into account atom losses and the inhomogeneous density profile is presented.

A more detailed exposition of the theory elements invoked in this chapter and on the eventual role of excited energy bands and collective effects can be found in the PhD thesis of Raphaël Bouganne (Bouganne 2018).

*The content presented in sections 6.1-6.4 and in appendix F, denoted by ∗∗, has been published in Bouganne et al. (2019) and is exposed here without major modifications. Only a few sections and paragraphs have been rearranged and others moved to appendix F. Some references to within the manuscript have been added.*

## 6.1 Main results and discussion (∗∗)

### 6.1.1 Framework and experimental setup

In our experiments, we create degenerate quantum gases of bosonic $^{174}$Yb atoms trapped in a stack of independent, two-dimensional optical lattices [figure 6.1(a)] (see section 2.2). For this, the vertical confinement along gravity $V_z \simeq 27\,E_\mathrm{r}$ is much stronger than the horizontal one, essentially freezing motion along $z$ and realizing a stack of independent two-dimensional quantum gases [see figure 6.1(a)]. Here, $\lambda_\mathrm{latt} = 2\pi/k_\mathrm{latt} \simeq 760\,\mathrm{nm}$ is the wavelength of the lattice lasers, $E_\mathrm{r} = h^2/(2M\lambda_\mathrm{latt}^2) \simeq h \times 1980\,\mathrm{Hz}$ the recoil energy, and $M$ the atomic mass. We calibrate the lattice depths along each axis independently using Kapitza-Dirac diffraction (Denschlag et al. 2002) [see section 2.2.1].

A (quasi-)condensate (Bloch et al. 2008) forms then in each plane for small lattice depth $V_\perp$. When $V_\perp$ is roughly above $6\,E_\mathrm{r}$, the quantum gases are well described by a single-band Bose-Hubbard Hamiltonian (Bloch et al. 2008) [see section 1.2.2],

$$\hat{H}_\mathrm{BH} \;=\; -J\sum_{\langle i,j\rangle}\hat{a}_i^\dagger\hat{a}_j+\sum_i\left[\frac{U}{2}\hat{n}_i(\hat{n}_i-1)+V_i\,\hat{n}_i\right]. \tag{6.1}$$

Here, $J$ is the tunneling energy between nearest neighbors, $U$ is the repulsive on-site interaction strength, $V_i$ is a harmonic potential arising from the Gaussian envelope of the lattice lasers (Zwerger 2003; Bloch et al. 2008), and $\hat{a}_i$ and $\hat{n}_i=\hat{a}_i^\dagger\hat{a}_i$ are the annihilation and number operators for lattice site $i$. A superfluid to Mott-insulator transition occurs as $V_\perp$ and the ratio $U/J$ increase (Bloch et al. 2008). The Mott insulator phase, where the atomic density is pinned at integer values, appears around $10\,E_\mathrm{r}$ for a filling of $\bar{n}=1$ atom per site. In this work, we explore a regime of lattice depths ranging from zero to $13\,E_\mathrm{r}$. The harmonic potential $V_i$ leads to an inhomogeneous spatial distribution with a maximum filling $\bar{n}\simeq 2.5$ atoms per site (Bouganne et al. 2017) [see section 2.2.2].

We expose the atomic cloud to dissipation by shining a near-resonant laser beam for a given duration $t$. The dissipation laser operates near the intercombination transition ${}^1\mathrm{S}_0-{}^3\mathrm{P}_1$, of frequency $\omega_0=2\pi/\lambda_0$ and wavelength $\lambda_0\simeq 556\,\mathrm{nm}$. The dissipation laser has wavevector $\boldsymbol{k}_\mathrm{L}$ and frequency $\omega_\mathrm{L}=ck_\mathrm{L}$, propagates vertically and is detuned by $\delta_\mathrm{L}=\omega_\mathrm{L}-\omega_0=+15\Gamma_0$ from resonance, with $\Gamma_0=2\pi\times 180\,\mathrm{kHz}$ the excited state linewidth. The laser polarization $\boldsymbol{\varepsilon}_\mathrm{L}$ is parallel to the uniform bias magnetic field $|\boldsymbol{B}|\simeq 1\,\mathrm{G}$ [see figure 6.1(a)]. The saturation parameter is $s\simeq\Omega_\mathrm{L}^2/(2\delta_\mathrm{L}^2)\simeq 10^{-3}$, with $\Omega_\mathrm{L}$ the Rabi frequency. The rate of spontaneous emission for a single atom in free space is then well-approximated by $\gamma_\mathrm{sp}\simeq s\Gamma_0/2$, we calibrated its value using Rabi oscillations (see figure F.1 in appendix F.1).

Our main observable is the momentum distribution after a 20 ms time-of-flight expansion. In the absence of dissipation, the momentum distribution corresponds to a multiple wave interference pattern, with sharp peaks at the Bragg positions where the matter waves interfere constructively (Bloch et al. 2008) [see section 2.2.3]. As shown in figure 6.1(b), the Bragg peaks vanish rapidly (on a time-scale around $0.4\,\mathrm{ms}\sim 0.2\,\gamma_\mathrm{sp}^{-1}$) when dissipation is enabled. However, a residual structure in the momentum distribution persists for much longer times up to a few milliseconds. Besides the relaxation of coherence, we also observe atom losses that we attribute to two-body, light-assisted inelastic collisions (Weiner et al. 1999). We focus first on the evolution of coherence, and discuss the role of losses later below. In the remainder, we normalize the momentum distribution to the instantaneous atom number $N(t)$.

### 6.1.2 Heuristic analysis of the diffusion process

In order to characterize the momentum diffusion and the associated decay of spatial coherence, we follow first a heuristic approach. We plot in figure 6.1(c) the amplitude of the central Bragg peak versus time. After an initial linear decay, the peak amplitude

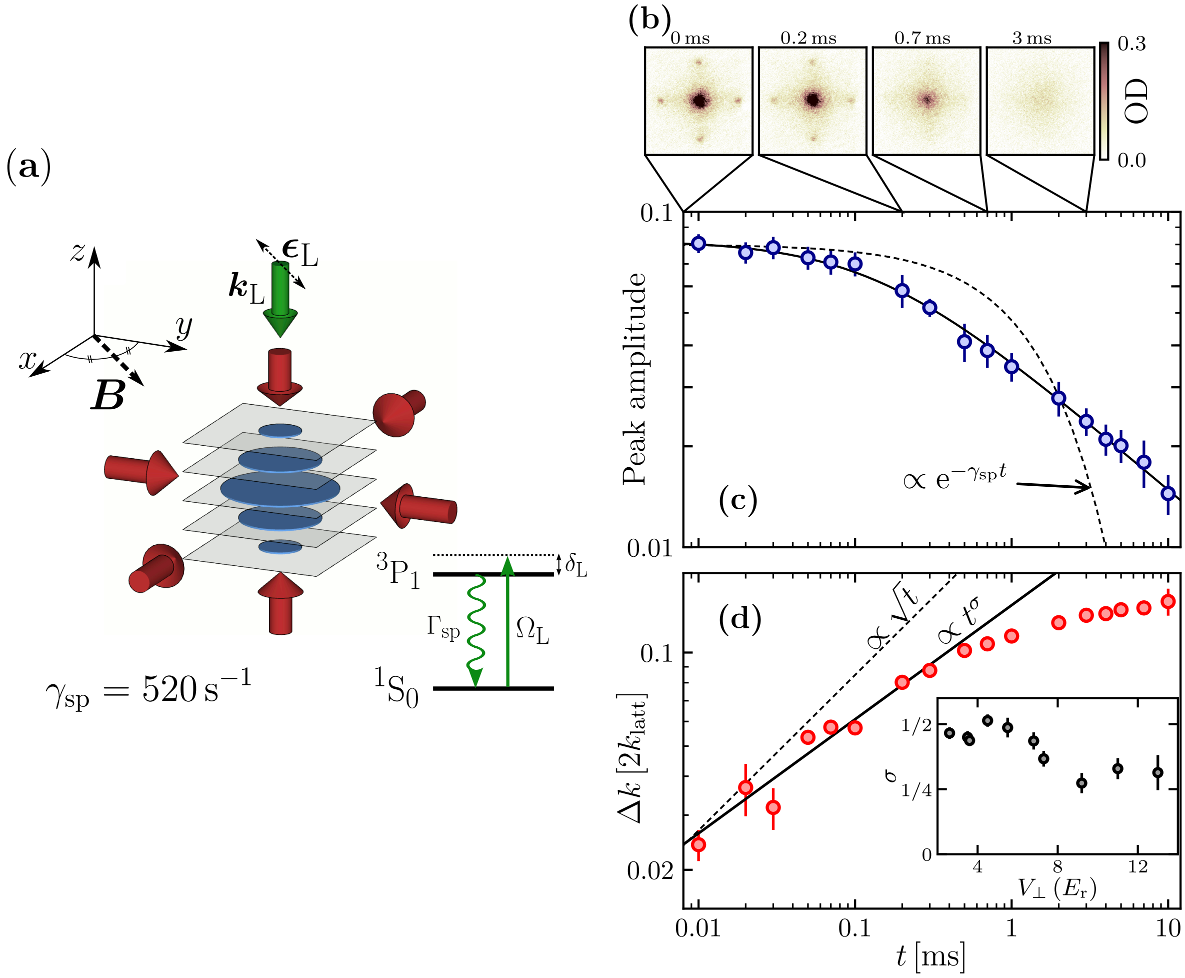

**Figure 6.1** – Observation of anomalous diffusion in momentum space. **(a):** An ultracold gas of $^{174}$Yb atoms is trapped in a stack of two-dimensional square optical lattices and exposed to dissipation by spontaneous emission. A laser close to an atomic resonance (green arrow) induces fluorescence cycles at a rate $\gamma_{sp} \simeq 520\,s^{-1}$. Random recoil of the atom destroys the initial spatial coherence. **(b):** Absorption pictures showing the vertically integrated optical density (OD) after time of flight, revealing the momentum distribution $\mathcal{N}(\boldsymbol{k})$, for several dissipation times. **(c):** Time evolution of the peak amplitude of the momentum distribution. The dashed line shows the exponential decay expected for non-interacting atoms [see equation (6.3)]. The solid line is a fit to $A/(1+\gamma_i t/\kappa)^\kappa$. **(d):** Time evolution of the momentum width $\Delta k$. The observed saturation results from the finite size of the integration area. The short-time evolution follows a power-law (solid line) whose exponent $\sigma$ varies with lattice depth (inset). The dashed line indicates normal diffusion with $\sigma = 1/2$. In **(c)** and **(d)** the in-plane lattice depth is $V_\perp \simeq 7.3\,E_r$. Each point corresponds to the mean over 3 realizations of the experiment. Error bars are standard deviations of the mean. Adapted from Bouganne et al. (2019).

settles to a power-law (*algebraic*) decay at long times. We show in figure 6.2(a) that this observation is valid for all lattice depths $V_\perp \geq 5\,E_r$.

The peak amplitude in figures 6.1(c) and 6.2(a) is estimated from $n_{peak} \equiv N_{peak}/N$, where the total atom number $N$ (respectively, population $N_{peak}$ of the central peak) is evaluated by counting the signal in a 480 µm-wide square region around the atomic cloud (resp., 25 µm-wide square in the centre of the image). For each $V_\perp$, we perform a fit using the phenomenological function

$$n_{\mathrm{peak}} = \frac{A}{(1+\gamma_{\mathrm{i}} t/\kappa)^{\kappa}}, \tag{6.2}$$

with $A$ the initial amplitude, $\gamma_{\mathrm{i}}$ the initial decay rate and $\kappa$ a decay exponent characterizing the long-time dynamics [solid lines in figures 6.1(c) and 6.2(a)]. The fit function decreases linearly at short times $\gamma_i t \ll 1$ and as a power law at long times $\gamma_i t \gg 1$. The crossover time between the two regimes $\sim \kappa/\gamma_{\mathrm{i}}$, typically $\sim 0.1 - 0.2\,\gamma_{\mathrm{sp}}^{-1}$, is related to the disappearance of long-ranged spatial coherence.

For non-interacting atoms (id), one would expect that the quasimomentum distribution $\mathcal{N}^{(\mathrm{id})}$ relaxes exponentially to a uniform distribution equal to the mean number of atoms per site $\bar{n}$ (Pichler et al. 2010; Yanay et al. 2014),

$$\mathcal{N}^{(\mathrm{id})}(\boldsymbol{k}, t) \simeq \mathcal{N}^{(\mathrm{id})}(\boldsymbol{k}, 0)\, \mathrm{e}^{-\gamma_{\mathrm{sp}} t} + \bar{n}\left(1 - \mathrm{e}^{-\gamma_{\mathrm{sp}} t}\right). \tag{6.3}$$

Equation (6.3) predicts a faster decay at long times than experimentally observed, and cannot explain the power-law.

Following the same heuristic approach, we plot in figure 6.1(d) the momentum growth $\Delta k = \sqrt{\Delta k_t^2 - \Delta k_{t=0}^2}$, where the root-mean-square momentum width

$$\Delta k_t^2 = \int_{1\mathrm{BZ}} k_x^2 \mathcal{N}(\boldsymbol{k}, t)\, \mathrm{d}^2 k, \tag{6.4}$$

is computed in the first Brillouin zone (1BZ). The exponential decay in equation (6.3) would lead to $\Delta k \propto \sqrt{t}$ at short times, close to what we observe for small lattice depths [inset of figure 6.1(d)]. However, in the Bose-Hubbard regime $V_\perp \geq 6\, E_{\mathrm{r}}$, we observe *subdiffusion* with a power-law behavior $\Delta k \propto t^{\sigma}$ with an exponent $\sigma \simeq 1/4$ [inset of figure 6.1(d)].

From the heuristic analysis, we conclude that the momentum distribtuion broadens more slowly than would be expected for non-interacting particles (equivalently, spatial coherence decays more slowly than expected). However, we also observe that the initially empty excited Bloch bands become gradually populated by spontaneous emission (Pichler et al. 2010), on a time scale roughly one order of magnitude longer than the decay of coherence in the fundamental band. The quantities studied in the heuristic analysis are averaged over all bands, which complicates their interpretation. In order to extract quantities related to the fundamental band of primary interest, we have implemented a more elaborate analysis where we fit a model distribution to the experimental momentum profiles.

### 6.1.3 Extracting the coherence from the momentum profiles

#### Analysis of the momentum profiles

Our model builds on the observed characteristics of the momentum distribution. In the algebraic regime observed in figure 6.2(a), the momentum distribution is indeed

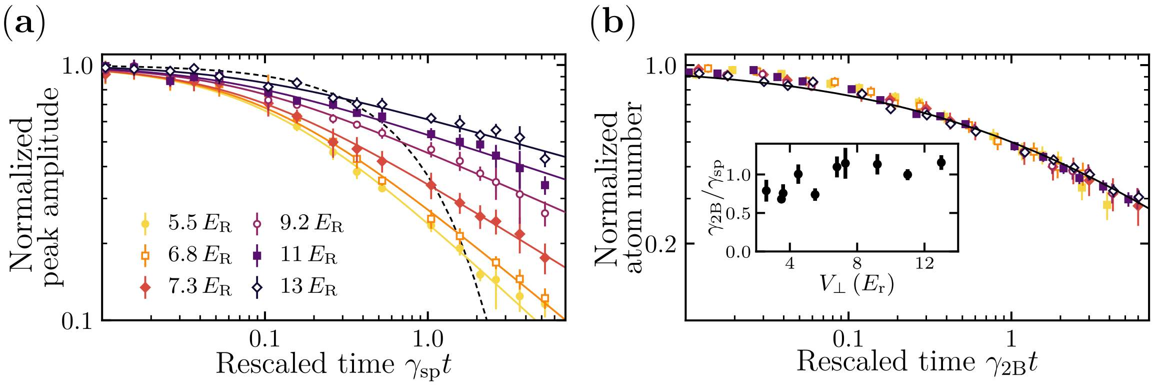

**Figure 6.2** – Decay of peak momentum amplitude and atom losses. **(a):** Time evolution of the peak amplitude of the momentum distribution. The solid lines are fits as in figure 6.1. The dashed line shows the exponential decay expected for non-interacting atoms [see equation (6.3)]. **(b):** Time evolution of the rescaled atom number $N/N_0$ versus rescaled time $x = \gamma_{2\mathrm{B}}t$. We extract the initial atom number $N_0$ and the two-body light-induced loss rate $\gamma_{2\mathrm{B}}$ (see inset) for each value of $V_\perp$ from a fit to $N_0/[1+x^\beta]$, with $\beta$ close to $1/2$ for all lattice depths (see figure F.6 in appendix F.4). The solid line is $1/(1+\sqrt{x})$. Each point corresponds to the mean over 3 realizations of the experiment. Error bars are standard deviations of the mean. Adapted from Bouganne et al. (2019).

characterized by a residual modulation on the scale of the first Brillouin zone, or equivalently by short-range spatial coherences before time of flight. Neglecting coherences beyond nearest neighbors, the lowest-band momentum distribution is approximately given by

$$\mathcal{N}(\boldsymbol{k}) \simeq \mathcal{W}(\boldsymbol{k}) \left[ 1 + \sum_{\boldsymbol{d}=\pm \boldsymbol{e}_{x/y}} C_{\mathrm{nn}} \cos(\boldsymbol{k}\cdot\boldsymbol{d}) \right]. \tag{6.5}$$

Here, the Wannier envelope $\mathcal{W}(\boldsymbol{k})$ –the form factor– reflects the on-site confinement, and the term between brackets –the structure factor– is the residual interference pattern [see section 2.2.3 or appendix A]. The quantity

$$C_{\mathrm{nn}} = 1/N \sum_{\boldsymbol{r}_i} \langle \hat{a}^\dagger_{\boldsymbol{r}_i+\boldsymbol{\delta}} \hat{a}_{\boldsymbol{r}_i} \rangle, \tag{6.6}$$

is a spatially-averaged correlation function of the bosonic field between two nearest-neighbor sites at positions $\boldsymbol{r}_i$ and $\boldsymbol{r}_i + \boldsymbol{\delta}$, with $\boldsymbol{\delta} = \boldsymbol{e}_{x/y}$ the basis vectors of the square lattice.

We use a multi-band expansion analogous to equation (6.5) to fit the measured momentum distributions and extract the fundamental band nearest-neighbor coherence $C_{\mathrm{nn}}$. In such a case the momentum distribution reads [see equation (F.11) in appendix F.3]

$$\mathcal{N}(\boldsymbol{k}) = \sum_{\text{bands}\,\boldsymbol{\nu}} \mathcal{S}_{\boldsymbol{\nu}}(\boldsymbol{k}) \mathcal{W}_{\boldsymbol{\nu}}(\boldsymbol{k}). \tag{6.7}$$

Here, the envelope function $\mathcal{W}_{\boldsymbol{\nu}}(\boldsymbol{k})$ is related to the Fourier transform of the Wannier function for each energy band labeled by $\boldsymbol{\nu}$. The normalized structure factor $\mathcal{S}_{\boldsymbol{\nu}}$ for

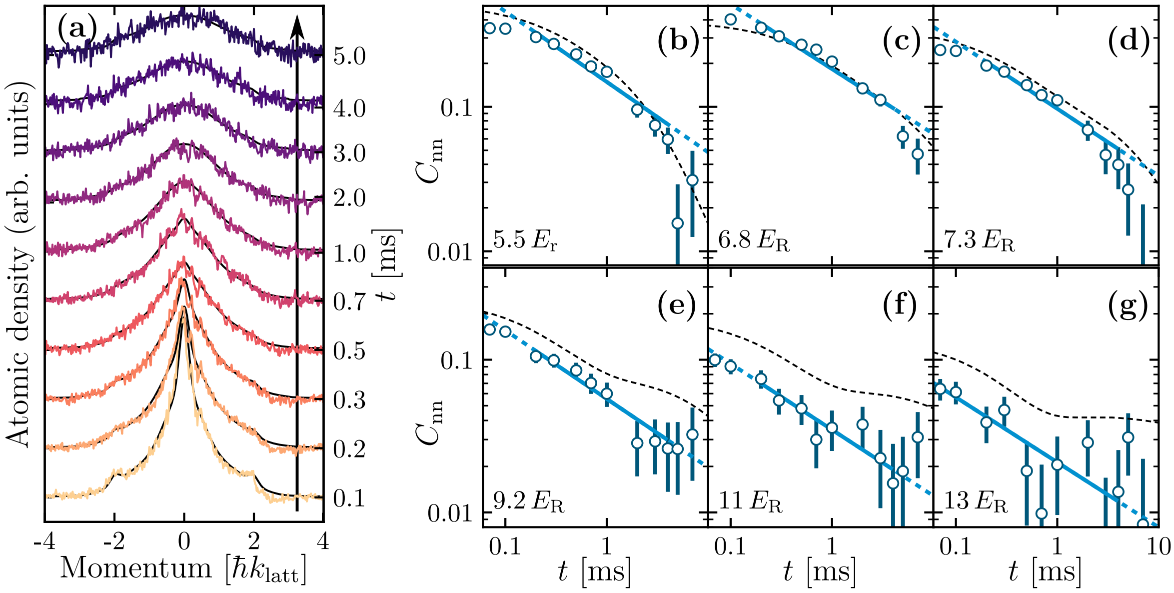

**Figure 6.3** – Decay of nearest-neighbour coherence. **(a):** One-dimensional momentum profiles $\mathcal{N}(\boldsymbol{k})$ for $\boldsymbol{k} = (k_x, 0)$ versus dissipation time for a lattice depth $V_\perp \simeq 7.3\,E_{\text{r}}$. The dissipation time $t$ increases from bottom to top. Solid lines are fits to a multi-band function from which we obtain the nearest-neighbor coherence $C_{\text{nn}}$. **(b)** to **(g)** Time evolution of $C_{\text{nn}}$ for various lattice depths $V_\perp$. Solid lines are a fit to a power-law decay with exponent $\alpha$, extracted in a chosen time window (see main text). The dots show an extrapolation of the fit outside this window. The dashed lines show the prediction of the model described in the main text, including dissipation due to spontaneous emission and two-body light-induced losses. Imaging noise limits the level of coherence that we are able to detect to $C_{\text{nn}} \gtrsim 0.015$. The plateaux reached at long times in **(d)-(g)** are compatible with this noise floor. Error bars are 1-sigma confidence intervals derived from a $\chi^2$ fitting procedure. Adapted from Bouganne et al. (2019).

band $\boldsymbol{\nu}$ is related to the correlation function $\langle \hat{a}^\dagger_{\boldsymbol{\nu},i} \hat{a}_{\boldsymbol{\nu},j} \rangle$,

$$\mathcal{S}_{\boldsymbol{\nu}}(\boldsymbol{k}) = \frac{1}{N} \sum_{i,j} \mathrm{e}^{\mathrm{i}\boldsymbol{k}\cdot(\boldsymbol{r}_i - \boldsymbol{r}_j)} \langle \hat{a}^\dagger_{\boldsymbol{\nu},i} \hat{a}_{\boldsymbol{\nu},j} \rangle. \tag{6.8}$$

We truncate this expansion to the lowest band and the first few excited bands to model our experimental signal (see appendix F.3 for a more detailed account). We verified that including more terms in the expansion leads to negligible corrections. For the fundamental band, we write the structure factor as the sum of a *coherent* component $\mathcal{S}_{0,\text{BEC}}(\boldsymbol{k})$ describing the condensate, and of an *incoherent* component $\mathcal{S}_0(\boldsymbol{k})$ with only short-ranged coherence modelled by equation (F.11). For the excited bands, which can be gradually populated by light scattering, we neglect coherence and take $\mathcal{S}_{\boldsymbol{\nu}\neq 0}(\boldsymbol{k}) = 1$.

### Evolution of the coherences

Once we have extracted the coherences $C_{\text{nn}}$ from the momentum profiles, in order to extract a reliable exponent from the evolution of $C_{\text{nn}}$, we perform a power-law fit in a specific time window $[t_1, t_2]$. The initial time $t_1$ is taken to be $t_1 = \kappa/\gamma_{\text{i}}$, i.e. the start of the algebraic decay found from the fits to the peak amplitude (see above). The final time is $t_2 = 2\,\gamma_{\text{sp}}^{-1}$. In this way, we exclude from the fit the data points

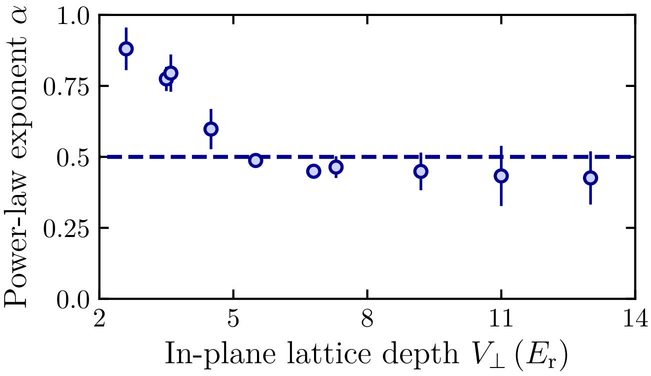

**Figure 6.4** – Decay exponent $\alpha$ of the nearest-neighbor coherence $C_\mathrm{nn}$. Exponents are extracted from fits $C_\mathrm{nn} \propto 1/t^\alpha$, as shown in figure 6.3(b)-(g), and error bars are 1-sigma confidence interval derived from statistical analysis of the fits. We observe a plateau with $\alpha \simeq 1/2$ for $V_\perp \geq 6\,E_\mathrm{r}$. Adapted from Bouganne et al. (2019).

clearly departing from the algebraic decay (for small $V_\perp$) or limited by imaging noise (mostly for high $V_\perp$). For the highest lattice depth [figure 6.3(g)], the algebraic decay starts almost immediately as there is very little coherence in the initial state, already in the Mott insulator regime. This also means that the signal reaches the imaging noise limit quickly, leaving only a few points for the fit. We still present the corresponding exponent in figure 6.4 to show that the decay is compatible with the expected $1/\sqrt{t}$ law.

Figure 6.3(a) shows typical momentum profiles and the corresponding fits (see also figure F.4 in appendix F.3). For lattice depths $V_\perp \geq 7\,E_\mathrm{r}$, we find that the nearest-neighbor coherence $C_\mathrm{nn}$ decays algebraically $\propto 1/t^\alpha$ [see figure 6.3(b)-(g)]. For lower lattice depths a departure from the power-law is observed at long times. The fitted exponent $\alpha$ shown in figure 6.4 settles to a value $\alpha \simeq 1/2$ as interactions increase. In the whole region where the Bose-Hubbard model is valid, $V_\perp \geq 6\,E_\mathrm{r}$, the exponent follows the plateau $\alpha \simeq 1/2$. We thus reach the same conclusions as in the heuristic approach, namely the emergence of algebraic time relaxation and anomalous momentum diffusion for a dissipative Bose-Hubbard system.

### 6.1.4 Interpretation of the results

The emergence of slowly-relaxing states is already seen in the simplest possible case with two atoms and two lattice sites [see appendix F.2]. A basis of the Hilbert space for two atoms is given by $\{|S\rangle, |I\rangle, |A\rangle\}$, with the two symmetric and antisymmetric combinations

$$|S/A\rangle = \frac{|2,0\rangle \pm |0,2\rangle}{\sqrt{2}} \qquad \text{and} \qquad |I\rangle = |1,1\rangle. \tag{6.9}$$

Here $|n,m\rangle$ denotes a Fock state with $n$ atoms in the first well and $m$ in the second. Without dissipation, the ground state of this minimal model is $|G\rangle \propto |I\rangle - (2J/U)|S\rangle$ to first order in $J/U \ll 1$.

Dissipation is conveniently treated in the quantum trajectory approach (Plenio et al. 1998; Daley 2014), where the dissipative dynamics is described as non-unitary evolution generated by an effective Hamiltonian interrupted at random times by quantum jumps.

In our case, the effective Hamiltonian $\hat{H}_{\text{eff}} = \hat{H}_{\text{BH}} - (\text{i}\hbar\gamma_{\text{sp}}/4)\hat{\Delta}^2$ and the jump operator $(\gamma_{\text{sp}}/2)\hat{\Delta}\hat{\rho}\hat{\Delta}$ are determined by the number difference operator $\hat{\Delta} = \hat{n}_1 - \hat{n}_2$. The imaginary part of the eigenvalues of $\hat{H}_{\text{eff}}$ determine the rate of quantum jumps (Plenio et al. 1998). In the limit of decoupled wells ($J \to 0$), the quantum state after a jump switches between $|S\rangle$ and $|A\rangle$, thereby randomizing the relative phase.

Treating tunneling as a small perturbation, the lowest energy eigenstate of $\hat{H}_{\text{eff}}$ is

$$|G'\rangle \propto |I\rangle - \frac{2J}{U - \text{i}\hbar\gamma_{\text{sp}}}|S\rangle, \tag{6.10}$$

with corresponding eigenvalue $E_{G'} \simeq -4J^2/(U - \text{i}\hbar\gamma_{\text{sp}})$. The rate of jumps $-2\text{Im}(E_{G'}) \simeq \gamma_{\text{sp}}\epsilon^2$ is much smaller than the natural dissipation rate $\gamma_{\text{sp}}$. Physically, the interaction energy mismatch $\sim U$ between states with different occupation numbers shifts the dissipative processes out of resonance and strongly suppresses the relaxation, a phenomenon termed *interaction-impeding of decoherence* in Poletti et al. (2013). In contrast, other eigenstates are mostly superpositions of $|S\rangle$ and $|A\rangle$ and decay at the natural rate $\gamma_{\text{sp}}$ (see the discussion in appendix F.2).

Poletti et al. have shown that this interaction-impeding of decoherence persists with many atoms and many sites. However, a crucial difference with the minimal model is that a large number of slowly-relaxing states participate in the long-time dynamics when $\hbar\gamma_{\text{sp}} \ll U$. This leads to an algebraic regime with power-law decay for many observables. In particular, one can show that $C_{\text{nn}}$ obeys the universal law (see section 6.3)

$$C_{\text{nn}} \simeq \frac{\eta}{\sqrt{z\gamma_{\text{sp}}t}}, \tag{6.11}$$

with $\eta \simeq 0.478$ a numerical factor and $z = 4$ the number of nearest neighbors. The time evolution $\propto 1/t^{1/2}$ in equation (6.11) agrees well with our observations in figure 6.4, even though the system is inhomogeneous due to the auxiliary trapping potential. A numerical calculation using Gutzwiller theory and the local density approximation also confirms the survival of the $C_{\text{nn}} \propto 1/t^{1/2}$ behavior in a trapped gas for high enough lattice depths (see section 6.4).

### 6.1.5 Adding losses to the model

We finally discuss the role of atom losses in more details. In figure 6.2(b), we show the time evolution of the normalized atom number $N(t)/N(0)$ for different lattice depths. We find that the data collapse onto the same curve $1/(1 + x^{\beta})$ with a scaling variable $x = \gamma_{2\text{B}}t$ [inset of figure 6.2(b)] and an exponent $\beta$ close to 1/2. This asymptotic scaling reflects the behavior of the two-body correlation function $\langle\hat{n}(\hat{n} - 1)\rangle/\bar{n}^2 \propto 1/t^{\beta}$ (see appendix F.4). At long times, we expect that inelastic losses generate a gas of hardcore bosons with $\langle\hat{n}(\hat{n} - 1)\rangle = 0$, consistent with our measurements and reminiscent of the inhibition of losses in a 1D gas of molecules (Syassen et al. 2008).

We have extended phenomenologically the theory of Poletti et al. (2013) by adding a two-body loss term to the master equation for $p(n)$ (see section 6.4). The characteristic two-body loss rate $\gamma_{2\text{B}}$ is a free parameter adjusted to best match the atom number decay (see appendix F.4). We find a fair agreement with our data for the correlation function $C_{\mathrm{nn}}$ (figure 6.3, black dashed lines) and for the atom number decay up to $\gamma_{\mathrm{sp}}^{-1}$. We conclude that the lossy dynamics preserves the anomalous slowing down, only suppressing it when the fraction of lost atoms becomes large (Sciolla et al. 2015). At long times, the model fails to capture the observed dynamics. This could be explained by additional effects neglected in the theory, such as inter-band transitions, the dynamical creation of correlations between different sites or collective effects in light-matter interaction. For lattice depths $V_\perp \geq 10\,E_{\mathrm{r}}$, the model also overestimates the initial coherence, which could be due to a finite temperature of the sample.

## 6.2 Theoretical background: description of light scattering (∗∗)

### Master equation for the ground state density matrix

We now turn to the theoretical description of our results. A first-principle description of the many-boson problem interacting with the quantized electromagnetic field is a difficult problem (Pichler et al. 2010), and solving it without approximations a formidable task. Poletti et al. have discussed a minimal single-band model where spontaneous light scattering is treated as a continuous, strictly local density measurement.

For non-interacting atoms, the model reduces to the exponential relaxation described by equation (6.3). Strong interactions drastically modify this relaxation process. The essence of the phenomenon can be traced back to the existence of states with low coherence but also low relaxation rates that dominate the long-times dynamics. In this section we give a simplified derivation of the model from Poletti et al. and explore its consequences for the on-site number distribution, the single-particle correlation function, and the momentum distribution.

We consider a quantum gas of ultracold atoms with two internal states $g$ and $e$. The $g-e$ transition is driven by an off-resonant laser. In general, the dynamics of the laser driven atomic ensemble is described by a quantum master equation for the atomic density matrix (Dalibard et al. 1985; Cohen-Tannoudji et al. 1992; Ellinger et al. 1994; Pichler et al. 2010). We consider here the experimentally relevant limit of large detunings and weak saturation of the excited state. In this limit, the population in $e$ is negligible at all times, and the excited state can be eliminated adiabatically (Dalibard et al. 1985; Cohen-Tannoudji et al. 1992; Ellinger et al. 1994). The evolution of the spatial coherences in the ground state is then governed by a master equation for the reduced ground state density matrix $\hat{\rho}$,

$$\frac{\mathrm{d}\hat{\rho}}{\mathrm{d}t} \simeq \frac{1}{\mathrm{i}\hbar}\left[\hat{H}_0 + \hat{V}_{\mathrm{dd}}, \hat{\rho}\right] + \mathcal{L}[\hat{\rho}]. \tag{6.12}$$

This describes the effect that off-resonant scattering of laser photons has on the quantized motional state of the gas.

The structure of equation (6.12) is that of a Lindblad master equation describing Markovian open systems (Haroche et al. 2013). The commutator describing the unitary evolution involves the Hamiltonian $\hat{H}_0$ in the absence of laser light (including atom-atom interactions). In the presence of laser light, a dipole-dipole interaction term

$V_{\mathrm{dd}}(\boldsymbol{r}-\boldsymbol{r}') \propto 1/|\boldsymbol{r}-\boldsymbol{r}'|^3$ also appears. Finally, the so-called Lindblad superoperator $\mathcal{L}$ describes relaxation of the atomic motional degrees of freedom due to spontaneous emission and collective effects. The dipole-dipole interaction $\hat{V}_{\mathrm{dd}}$ and the Lindblad dissipator are related to each other [see Pichler et al. (2010) and references therein]. Explicit expressions for these operators are given in Pichler et al. (2010), and their origin discussed in detail.

### Bose-Hubbard master equation

The Bose-Hubbard Hamiltonian in equation (6.1) is derived from a more general many-body Hamiltonian under the single-band and tight-binding assumptions (Bloch et al. 2008). Applying these assumptions to the ground state master equation (6.12) (Pichler et al. 2010), one finds a discretized version with the Hamiltonian $\hat{H}_0 \to \hat{H}_{\mathrm{BH}}$, and a Lindblad dissipator

$$\mathcal{L}[\hat{\rho}] \quad = \quad \frac{\gamma_{\mathrm{sp}}}{2} \sum_{i,j} \Lambda_{ij} \Big( 2\hat{n}_i \hat{\rho} \hat{n}_j - \hat{n}_i \hat{n}_j \hat{\rho} - \hat{\rho} \hat{n}_i \hat{n}_j \Big), \tag{6.13}$$

where $\hat{\rho}$ now denotes the projection on the fundamental band of the density matrix. The rates $\Lambda_{ij}$ are determined by the overlap integrals,

$$\Lambda_{ij} = \int F(\boldsymbol{r}-\boldsymbol{r}') |w(\boldsymbol{r}-\boldsymbol{r}_i)|^2 |w(\boldsymbol{r}'-\boldsymbol{r}_j)|^2 \, \mathrm{d}^3 r \, \mathrm{d}^3 r'. \tag{6.14}$$

The kernel involves the Fourier tranform

$$F(\boldsymbol{r}-\boldsymbol{r}') = \int D(\boldsymbol{u}) \, \mathrm{e}^{\mathrm{i}\Delta\boldsymbol{k}\cdot(\boldsymbol{r}-\boldsymbol{r}')} \, \mathrm{d}^2 u, \tag{6.15}$$

of the directional factor $D(\boldsymbol{u})$ describing the radiation pattern of the atomic dipole. This factor reads

$$D(\boldsymbol{u}) = \frac{3}{8\pi} \times [1 - (\boldsymbol{u} \cdot \boldsymbol{\varepsilon}_{\mathrm{L}})^2], \tag{6.16}$$

for our choice of $\pi$-polarization (see figure 6.1). In equation (6.15), the quantity $\Delta\boldsymbol{k} = \boldsymbol{k}_{\mathrm{L}} - k_0 \boldsymbol{u}$ describes a *momentum kick* after absorbing a laser photon of momentum $\hbar\boldsymbol{k}_{\mathrm{L}}$ and spontaneously emitting a photon of momentum $\hbar k_0 \boldsymbol{u}$, with $k_0 = 2\pi/\lambda_0$ and $\boldsymbol{u}$ a random unit vector corresponding to the direction of propagation.

Absorption-spontaneous emission cycles can be interpreted as weak, continuous measurements of the atoms' position at a rate $\gamma_{\mathrm{sp}}$ (Marte et al. 1993). The motional degrees of freedom of the gas become entangled with the electro-magnetic field when they interact, and erasing the information about the electro-magnetic field projects the atomic state into a state of ill-defined momentum, and therefore well-defined position by Heisenberg's principle. The function $F$ quantifies the resolution of this measurement: $F$ falls to zero for distances $\gg 1/k_0$, which is nothing but the diffraction limit associated with the optical detection of the atomic position.

### Zero-range model

The optical lattice spacing $d = \lambda_{\mathrm{latt}}/2$ and the range of $F$ are both on the order of an optical wavelength. In the Bose-Hubbard regime, the Wannier functions are localized on a much smaller scale. When calculating the on-site decay rate $\Lambda_{ii}$, one can approximate $F(\boldsymbol{r}-\boldsymbol{r}') \simeq F(\boldsymbol{0}) = 1$ and $\Lambda_{ii} \simeq F(\boldsymbol{0})$. Moreover, $F$ is maximal at the origin and the localization of Wannier functions near their respective centres implies that $|\Lambda_{i,j\neq i}| \ll |\Lambda_{ii}|$. This allows us to perform a so-called *zero-range approximation* in the following, where we retain only the on-site decay terms and neglect off-sites terms with $i \neq j$: $\Lambda_{ij} \simeq \delta_{ij}$. Such an approximation becomes exact in the limiting case where the Wannier functions become infinitely localized, similar to the Lamb-Dicke limit where inter-band transitions are supressed [see section 3.4]. In the same limit, dipole-dipole interactions are no longer relevant: off-site terms are negligible and the on-site term can be absorbed in the on-site interaction energy $U$ of the Bose-Hubbard Hamiltonian.

## 6.3 Analysis of a continuous measurement model (∗∗)

### 6.3.1 Single-band zero-range model

We now turn to the analysis of the many-body model defined by the Bose-Hubbard master equation. The Hamiltonian part $\hat{H}_0$ is the Bose-Hubbard model [equation (6.1)] and the dissipation superoperator is, combining the single-band and zero-range approximations,

$$\mathcal{L}[\hat{\rho}] = \frac{\gamma_{\mathrm{sp}}}{2}\sum_i 2\hat{n}_i\hat{\rho}\hat{n}_i - \hat{n}_i^2\hat{\rho} - \hat{\rho}\hat{n}_i^2. \tag{6.17}$$

This model was studied in detail by Poletti et al. We recall that collective effects (super or subradiance, light-induced dipole-dipole interactions) and inter-band transitions are neglected (Pichler et al. 2010). As a result, the model of Poletti et al. should be viewed as the minimal description of a dissipative Bose-Hubbard system submitted to continuous measurement by light scattering. Yet, as we argue in section 6.1 and below, the model captures the essential features of the non-trivial momentum diffusion observed in our experiments.

The density matrix can be represented in the Fock basis as

$$\hat{\rho} = \sum_{\boldsymbol{n},\boldsymbol{m}} \rho_{\boldsymbol{m}}^{\boldsymbol{n}} |\boldsymbol{n}\rangle\langle\boldsymbol{m}|, \tag{6.18}$$

where $\boldsymbol{n} = (n_1, \cdots, n_{N_{\mathrm{s}}})$ identifies a particular configuration of Fock states on the $N_{\mathrm{s}}$ sites. Statistical mixtures of Fock states are not affected by dissipation due to the particular structure of $\mathcal{L}$, and for finite tunneling there exists a unique asymptotic steady-state $\rho_{\boldsymbol{m}}^{\boldsymbol{n}} \propto \delta_{\boldsymbol{m},\boldsymbol{n}}$, a fully mixed state where all Fock state configurations are equally likely (Poletti et al. 2013).

A key observation of Poletti et al. is that the relaxation to the steady-state proceeds via three stages:

1. an initial stage governed by the time scale $\gamma_{\mathrm{sp}}^{-1}$, where the number distribution broadens and the long-range coherence potentially present in the initial state decays exponentially (Cohen-Tannoudji et al. 1992),

2. an intermediate stage, where relaxation slows down dramatically and an algebraic regime emerges. This regime corresponds to a state which essentially belongs to a decoherence-free subspace and does not decay. Finite tunneling amplitude partially restores coherence in this mixture of Fock states (*quantum fluctuations around the decoherence free subspace*) and allows relaxation to persist in a strongly modified manner,
3. a final stage where the system *thermalizes* towards the asymptotic steady-state.

The first regime where long-range coherence disappears can not be precisely described by the formalism of Poletti et al. (2012) and Poletti et al. (2013), and we did not attempt to do it theoretically. However, we provide an empirical discussion of the experimentally observed behavior in appendix F.3.2.

## 6.3.2 Anomalous diffusion in the algebraic regime

### Master equation for populations

In the second stage of the decay, coherence is already short-ranged. The density matrix is mainly diagonal with a weak contribution of the off-diagonal coherences $\rho_{\boldsymbol{n}}^{\boldsymbol{n}+\boldsymbol{e}_{i,j}}$ between configurations differing by one tunneling event with $i, j$ nearest-neighbors. The vector $\boldsymbol{e}_{i,j}$ with components $(\boldsymbol{e}_{i,j})_k = +1$ if $k = i$, $-1$ if $k = j$, and 0 otherwise indicates that we consider a process where one atom moved from site $j$ to site $i$. We neglect other off-diagonal matrix elements between configurations differing by two or more tunneling events.

Because of the large mismatch between interaction energy and damping rate, the rapidly-oscillating coherence can be expressed as a slave variable depending on the slowly-evolving populations. Following Poletti et al. (Poletti et al. 2013), the steady-state coherences are given by

$$\rho_{\boldsymbol{n}}^{\boldsymbol{n}+\boldsymbol{e}_{i,j}} \simeq \frac{J\sqrt{n_j(n_i+1)}}{U(n_i-n_j+1)+\mathrm{i}\hbar\gamma_{\mathrm{sp}}}\left(\rho_{\boldsymbol{n}}^{\boldsymbol{n}} - \rho_{\boldsymbol{n}+\boldsymbol{e}_{i,j}}^{\boldsymbol{n}+\boldsymbol{e}_{i,j}}\right). \tag{6.19}$$

Adiabatic elimination of the coherences leads to a set of closed equations of motion for the populations $\rho_{\boldsymbol{n}}^{\boldsymbol{n}}$ alone, valid in the limit $U, \hbar\gamma_{\mathrm{sp}} \gg J$ where the populations relax much more slowly than the coherences [equation 3S in the Supplementary Material of Poletti et al. (2013)].

An additional simplification comes from assuming a factorization ansatz for the dominant diagonal part of the density matrix,

$$\hat{\rho} \simeq \prod_i \left( \sum_{n_i=0}^{\infty} p_{n_i} |n_i\rangle_i\, {}_i\langle n_i| \right). \tag{6.20}$$

With this additional assumption, the complicated evolution equation for the diagonal matrix elements reduces to a difference equation obeyed by the on-site number distribution $p_n$ (Poletti et al. 2013),

$$\frac{\mathrm{d}p_n}{\mathrm{d}\tau} = W_{n+1}(p_{n+1}-p_n) - W_{n-1}(p_n - p_{n-1}). \tag{6.21}$$

Here we introduced the rescaled time $\tau = t/t^*$, with the characteristic interaction-enhanced time

$$t^* = \frac{1}{2z\gamma_{\mathrm{sp}}}\left(\frac{U\bar{n}}{J}\right)^2 \gg \gamma_{\mathrm{sp}}^{-1}, \tag{6.22}$$

and with $\bar{n}$ the average filling and $z$ the number of nearest neighbors. The master equation (6.21) is governed by the non-linear transition rates

$$W_{n+1} = \bar{n}^2 \sum_m g(n+1, m) p_{m-1}, \tag{6.23}$$

$$W_{n-1} = \bar{n}^2 \sum_m g(n, m+1) p_{m+1}, \tag{6.24}$$

where the function $g$ is defined as

$$g(x,y) = \frac{xy}{(x-y)^2 + (\hbar\gamma_{\mathrm{sp}}/U)^2}. \tag{6.25}$$

The characteristic time $t^*$ allows us to identify the three regimes described earlier: (i) $t \lesssim \gamma_{\mathrm{sp}}^{-1}$: initial relaxation of coherences, (ii) $\gamma_{\mathrm{sp}}^{-1} \lesssim t \ll t^*$: algebraic regime, (iii) $t \gtrsim t^*$: final relaxation to the steady-state.

### Scaling regime

Poletti et al. (Poletti et al. 2013) solved the master equation numerically using an array of Fock states as initial condition. They pointed out that the number distribution obeys scale invariance for specific conditions, namely in a *scaling window* $\gamma_{\mathrm{sp}}^{-1} \lesssim t \ll t^*$ such that $\Delta n(t) \ll \bar{n}$.

This scale invariance characterizes the algebraic regime and can be justified in the limit of large fillings $\bar{n} \gg 1$ and weak dissipation $\hbar\gamma_{\mathrm{sp}}/U \to 0$. This allows one to make a continuum approximation where the discrete variable $n$ is replaced by a continuous one $x = n/\bar{n} \in [0, \infty)$. The discrete occupation number distribution becomes continuous, $p_n \longrightarrow p(x)/\bar{n}$, and the master equation maps to a Fokker-Planck equation with a non-linear diffusion term (Poletti et al. 2012; Poletti et al. 2013). With an initial Fock state $p_n = \delta_{n,\bar{n}}$ $[p(x) \propto \delta(x-1)]$ and for weak dissipation, there exists a solution which exhibits scale invariance,

$$p(x) \simeq \frac{1}{\tau^\beta} f\left(u = \frac{x-1}{\tau^\beta}\right), \tag{6.26}$$

with a normalized time $\tau$ and a scaling exponent $\beta$ (Poletti et al. 2013). The scaling function is

$$f(u) = \frac{1}{4\Gamma(5/4)} \mathrm{e}^{-u^4/16}, \tag{6.27}$$

where $\Gamma$ denotes the Gamma function and where the scaling exponent is $\beta = 1/4$ (Poletti et al. 2013).

This scaling solution is only exact in the limit defined by $\hbar\gamma_{\mathrm{sp}}/U \ll 1$ and $\bar{n} \gg 1$. However, it remains relevant outside the high-filling limit provided two conditions are met. First, the average filling $\bar{n}$ must not be too small, and second, the number distribution must be peaked around $\bar{n}$ with small dispersion $\Delta n \ll \bar{n}$. With these conditions fulfilled, the numerical solutions of the master equation (6.21) approximately obey the scaling form until the second condition gets violated for times $t \simeq t^*$ (Poletti et al. 2013). This defines a *scaling window* in the time evolution, roughly determined by $\gamma_{\text{sp}}^{-1} \lesssim t \ll t^*$. The width of these windows shrinks with decreasing filling or increasing initial number fluctuations, until $\gamma_{\text{sp}} t^* \simeq 1$ and the scaling behavior essentially disappears. For a system described by the Bose-Hubbard model, number squeezing occurs even in the superfluid regime where $\Delta n \simeq 1$ as soon as $U \gtrsim J$. As a result, the scaling behavior starts being observable for fillings as low as $\bar{n} \gtrsim 1.5$. We discuss in the following section that this behavior, first noticed in Poletti et al. (2013) for the evolution of $p_n$, is also visible in the evolution of the spatial coherence.

### 6.3.3 Nearest-neighbor coherence

#### General formula in the algebraic regime

We now evaluate how phase coherence evolves in the algebraic regime. Initially, the gas could possess long-range correlations that decay in the first stage of the evolution. In the algebraic stage, correlations are short-ranged and dominated by the nearest-neighbor correlation function $C_{\pm 1} = \langle \hat{a}_{i\pm 1}^{\dagger} \hat{a}_i \rangle$. One can relate this correlation function to the density matrix elements,

$$C_{\pm 1} = \sum_{\boldsymbol{n}} \sqrt{n_i (n_{i\pm 1} + 1)} \rho_{\boldsymbol{n}}^{\boldsymbol{n} + \boldsymbol{e}_{i\pm 1, i}}. \tag{6.28}$$

Using the nearest-neighbor coherences in equation (6.19) and the factorization ansatz in equation (6.20), we find

$$C_{\pm 1} = \frac{J}{U} \sum_{m,n=0}^{+\infty} (n - m) g(m+1, n+1) [p_n p_{m+1} - p_{n+1} p_m], \tag{6.29}$$

the form we use for numerical calculations.

In figure 6.5 we show the solution of equation (6.29) for various initial occupation probability distributions. A true scaling regime, reaching the universal limit of equation (6.32), appears already for $\bar{n} > 1$ but only when $\Delta n \ll \bar{n}$.

#### Universal power-law decay for weak dissipation

We can derive an analytical prediction in the limit of high fillings ($\bar{n} \gg 1$) and weak dissipation ($\gamma_{\text{sp}}/U \to 0$). By taking the continuum limit in equation (6.29), we find that the nearest-neighbor coherence factors $C_{\pm 1}$ take the following form in the scaling regime:

$$C_{\pm 1} \simeq \frac{J \eta_0}{U \tau^{\alpha}}. \tag{6.30}$$

The nearest-neighbor coherence therefore inherits the scaling properties of the number distribution function $p$ but with a scaling exponent $\alpha = 2\beta = 1/2$ twice as large. The numerical factor $\eta_0 \simeq 0.676$ is

$$\eta_0 = \int \frac{f(u) f'(v) - f'(u) f(v)}{u - v} \, \mathrm{d}u \, \mathrm{d}v = \frac{2\Gamma(3/4)}{\Gamma(1/4)}, \tag{6.31}$$

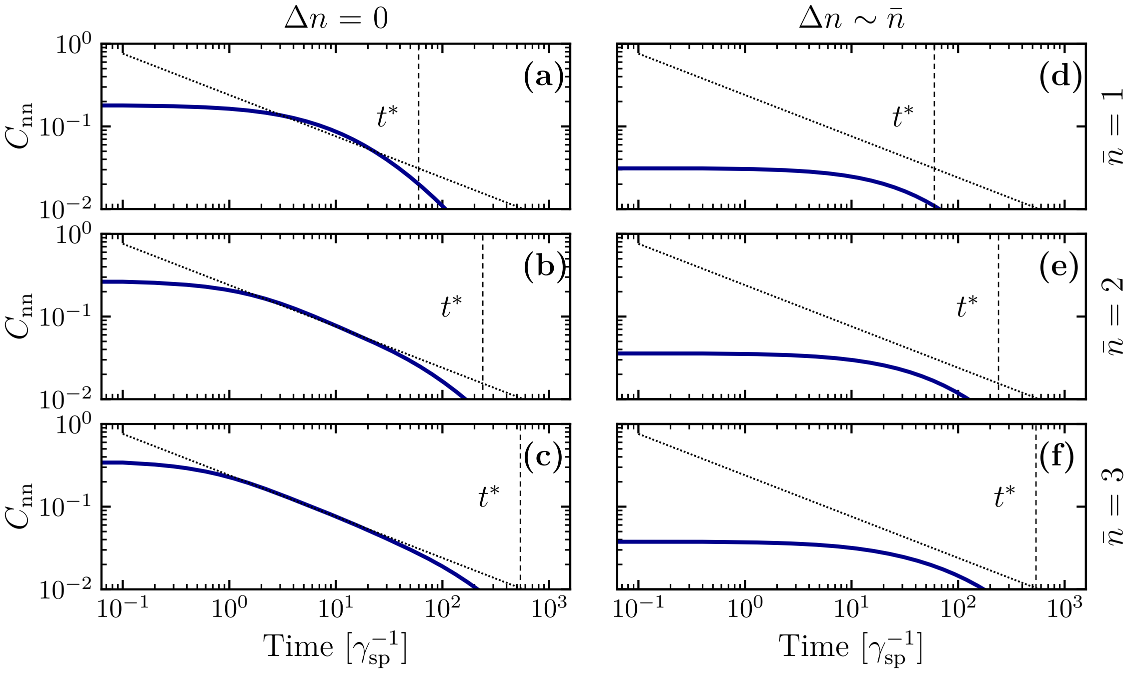

**Figure 6.5** – Emergence of a scaling regime in the dissipative Bose-Hubbard model. **(a)-(f):** Calculated time evolution of the nearest-neighbor coherence $C_{\mathrm{nn}}$ from equation (6.29) (solid line), for $\bar{n} = 1$, 2 and 3. The dotted line is the universal form of equation (6.32) valid for large fillings. The vertical dashed line shows the time $t^*$ from equation (6.22). The Bose-Hubbard parameters are calculated for $V_\perp = 10\,E_{\mathrm{r}}$. The initial distribution corresponds to a Fock state in **(a)-(c)** and to a coherent state in **(d)-(f)**. Adapted from Bouganne et al. (2019).

where $\Gamma$ denotes the Gamma function. The coherence factor can be rewritten in the universal form quoted in section 6.1,

$$C_{\mathrm{nn}} = \frac{C_{\pm 1}}{\bar{n}} \simeq \frac{0.478}{\sqrt{z\gamma_{\mathrm{sp}}t}}, \tag{6.32}$$

which is independent of the microscopic parameters $U$, $J$ or $\bar{n}$.

## 6.4 Extended model: External confinement and losses (∗∗)

In the experiment, the density distribution is inhomogeneous due to the auxiliary trapping potential provided by the lattice beams envelopes. Moreover the total atom number decreases with time, because of light-assisted inelastic losses [see appendix F.4]. For a faithful simulation of the actual dissipative dynamics, we take these two aspects into account.

### 6.4.1 Inhomogeneous density distribution

The model studied in Poletti et al. (2013) focuses on uniform systems prepared in a Mott insulator state with integer filling $\bar{n}$, whereas our experimental situation is more complex because of an additional harmonic potential created by the lattice beams [see section 1.2.1]. This leads to an inhomogeneous spatial distribution of $\bar{n}$ with a maximum value around 2.5 in the center of the cloud [see section 2.2.2]. Morever, we probe a many-body ground state which is not a Mott insulator state. We thus extend the model by taking into account the inhomogeneity and the initial ground state.

We use a similar approach as in Bouganne et al. (2017) to predict the initial equilibrium density distribution of atoms in the optical lattice [see section 2.2.2].

For each site, we solve the model from equation (6.21) using its initial occupation probability distribution. We then compute $C_{\mathrm{nn}}$ by averaging equation (6.29) over the spatial density profile. The final results are qualitatively the same as in the homogeneous case studied previously: The scaling regime and the associated universal law $C_{\mathrm{nn}} \propto 1/\sqrt{t}$ appear for a narrow enough occupation number distribution $\Delta n \ll \bar{n}$ and for a sufficiently high filling $\bar{n} \gtrsim 1.5$. To explain the survival of the scaling behavior of $C_{\mathrm{nn}}$ upon spatial averaging, we notice that (i) the less dense parts of the cloud where the scaling regime is never reached decay exponentially and their contribution to the correlation function quickly becomes negligible, and that (ii) the denser parts do obey scaling and follow equation (6.32) which is independent of the density.

### 6.4.2 Including atom losses

While the model of Poletti et al. (2013) captures the power-law behavior and the exponent observed experimentally, it also predicts a much slower decay than in the experiments. The timescale $t^* \propto (U/J)^2$ governing the duration of the scaling window with algebraic decay changes by several orders of magnitude when $V_\perp$ varies from 3 to 13 $E_\mathrm{r}$. In the experiments, we observe instead that the correlation function decays on a timescale $\sim \gamma_{\mathrm{sp}}^{-1}$ for all lattice depths (up to a numerical factor). We resolve this discrepancy by considering the effect of inelastic losses on the decay of coherence.

To include the observed two-body losses in the theory, we add another Lindblad superoperator

$$\mathcal{L}_{2\mathrm{B}}[\hat{\rho}] = \frac{\gamma_{2\mathrm{B}}}{2} \sum_i 2\hat{a}_i^2 \hat{\rho} \hat{a}_i^{\dagger 2} - \hat{a}_i^{\dagger 2} \hat{a}_i^2 \hat{\rho} - \hat{\rho} \hat{a}_i^{\dagger 2} \hat{a}_i^2 \tag{6.33}$$

to the master equation (6.12), with a two-body loss rate $\gamma_{2\mathrm{B}} \propto U$. $\mathcal{L}_{2\mathrm{B}}$ couples configurations with different atom numbers (unlike $\mathcal{L}$), making a direct extension of the theory not trivial. If $\gamma_{2\mathrm{B}}$ is smaller than the spontaneous emission rate, the coherences evolve essentially as in the lossless case, with a small correction due to inelastic decay. If we neglect this correction and apply the same procedure as without losses, we obtain a master equation for populations with an additional two-body loss term in the master equation (6.21),

$$\left.\frac{\mathrm{d}p_n}{\mathrm{d}t}\right|_{\mathrm{losses}} = -\gamma_{2\mathrm{B}} n(n-1) p_n + \gamma_{2\mathrm{B}} (n+2)(n+1) p_{n+2}. \tag{6.34}$$

We extended the model of section 6.3 using equation (6.34), even though the condition for such a treatment is not fully met for our experimental conditions ($\gamma_{2\mathrm{B}} \simeq \gamma_{\mathrm{sp}}$). A more complete analysis including both dephasing and losses from first principles is beyond the scope of this work, and of the theory developed in Poletti et al. (2013). We determined the two-body loss rate $\gamma_{2\mathrm{B}}$ directly from the experimental data, minimizing the $\chi^2$ between the model predictions and the measured atom number. Here $\gamma_{2B}$ is the only free parameter, and its best-fit value for each horizontal lattice depth $V_\perp$ is shown in figure F.6(b) from appendix F.4.

## 6.5 Conclusion

In this chapter, I have shown that the evolution of spatial coherence in a strongly interacting system shows a non-trivial dynamics consisting of an algebraic subdiffusive decay, as was predicted by Poletti et al. Our experimental data confirms their claim. We observe indeed that after a strong and fast decay of the coherence, a residual modulation in the momentum distribution persists. As we show, this modulation is as a signature that nearest-neighbor coherence is still present, and our measurements show that it survives for long times. This phenomenon has been called *interaction-impeded decoherence* and is sometimes referred to as an *interaction-induced Zeno effect* (as opposed to the *normal* quantum Zeno effect, as the one discussed in chapter 4), signaling the robustness, furnished by the interactions, of certain states against decoherence.

I have also presented an extended version of the model of Poletti et al. Here, we take into account two-body inelastic losses and the inhomogeneous density profile induced by the residual Gaussian confinement of the lattice beams. It has been shown that the subdiffusive regime still emerges provided the initial atom number distribution is narrow and the filling is large enough. The theory presented agrees well with the experimental data.

The measurements shown in this chapter confirm that the presence of strong interactions can protect the coherence of the system, allowing a residual coherence to remain for long times in a slowly decaying subspace. In other words, strong interactions delay reaching the completely decohered steady-state, allowing a short-range order to persist for much longer compared to the non-interacting case.

# Outlook

## Summary and conclusions

In this manuscript I have presented a series of experimental studies concerning the optical excitation of a quantum gas of bosonic ytterbium atoms. In all cases, the physics is rich due to the interplay between coherent quantum dynamics, dissipation (either from two-body losses or from spontaneous emission) and inter-atomic interactions.

In the first part of this work (I), I have introduced and characterized the experimental setup in which these experiments are performed. I have also discussed the main theoretical concepts appearing repeatedly in the remaining of the thesis. In particular, I have presented a detailed account of the validity of the adiabatic approximation for interacting particles, invariably used when one thinks of preparing a quantum gas in an optical lattice. Although the question is simple at first sight, the answer is in general not easy to find, especially when taking the auxiliary harmonic trap potential into account. I have presented a series of pragmatic criteria that allow one to give at least a minimal estimate, in good agreement with the times found experimentally.

In the second part (II), I have detailed the experimental techniques that we use to probe the clock transition. I have then shown a study performed on ensembles of independent systems with few (one or two) particles. These ensembles correspond to particles in deep optical lattices, where tunneling is negligible over the course of the experiment, allowing one to treat each lattice site independently of the others. Studying single atoms or atom pairs driven on the clock transition has allowed us to determine certain properties of the band structure of the optical lattice. Then, by probing the internal degrees of freedom in the zero-phonon line, we have been able to test and characterize the clock laser linewidth and to extract the elastic and inelastic collisional properties of the ground and metastable states of $^{174}$Yb.

From these measurements, we have inferred the existence of strong inelastic two-body losses between atoms in the metastable state. This has enabled us to study the dissipative preparation of a small open quantum system, where both interactions and dissipation, induced by the losses, are present. In such a situation, I have shown that by driving the system in the weak-coupling regime, the losses itself force the dynamics to take place in a slowly-decaying subspace. This has been interpreted as a manifestation of the quantum Zeno effect.

I have then presented in the third part (III) two different experimental studies in which dissipation takes place in a many-body framework. Firstly, in the weakly interacting regime, with a BEC in a harmonic trap, well described in the mean-field framework. Secondly, in the strongly interacting regime, with a quantum gas in an optical lattice.

In the weakly interacting regime, I have analyzed the mechanisms that lead to the relaxation of a driven bulk BEC. I have shown that, except for very weak couplings, where Doppler broadening dominates the damping of the internal coherences, the presence of inelastic two-body losses governs the total dynamics, leading to a non-linear decay of the overall signal. In the presence of stronger interactions, we have observed an additional source of relaxation, which could not be accounted for by a mean-field approach.

Finally, in an optical lattice, I have shown a series of measurements in which we drive the intercombination transition. In this case, the dissipation caused by spontaneous emission affects not only the internal dynamics but also the external ones. In particular, it destroys spatial coherences. Here, I have shown that the presence of strong enough interactions (basically, once the system reaches the Bose-Hubbard regime) helps to maintain a residual amount of short-range order, decaying in a much slower fashion compared to what is expected for non-interacting particles. In particular, we have proven with these experiments the emergence of anomalous momentum diffusion, caused by the interplay between interactions and dissipation.

# Outlook

## I. Dynamics in one-dimensional tubes

### ➟ Two-body decay of fermionized bosons in an optical lattice: More (but different) Zeno dynamics

In the atomic limit ($J = 0$), an optical lattice with unit filling where all particles are in the excited metastable state is expected to be stable. As tunneling is present, however, events in which two particles meet at the same site and are lost can occur. In the case in which interactions and dissipation are strong compared to the tunneling, the actual loss rate $\gamma_{\text{eff}}$ becomes much smaller than both the tunneling and the *bare* loss rate $\gamma_{ee}$, and is given by

$$\gamma_{\text{eff}} \propto \frac{J^2}{4U_{ee}^2 + \hbar^2\gamma_{ee}^2}\gamma_{ee}. \tag{O.1}$$

Syassen et al. (2008) and García-Ripoll et al. (2009) interpreted this in terms of the quantum Zeno effect, where both elastic and inelastic interactions would act as a continuous measurement, thus preventing tunneling events towards the lossy configuration. The dynamics of the gas confined to the lossless subspace is then equivalent to a system of hardcore bosons, also known as a Tonks-Girardeau gas (Tonks 1936; Girardeau 1960). In such systems, peculiar to one dimension, strong interactions make bosons similar to fermions by preventing double occupancies and thereby mimicking the Pauli principle.

We have performed these kind of measurements in a system of 1D Mott insulators for different lattice depths, and a preliminary result is shown in figure O.1. Comparing our data to the expected decay rate (dotted line) we see that the loss dynamics we observe is much slower and follows a different law at longer times.

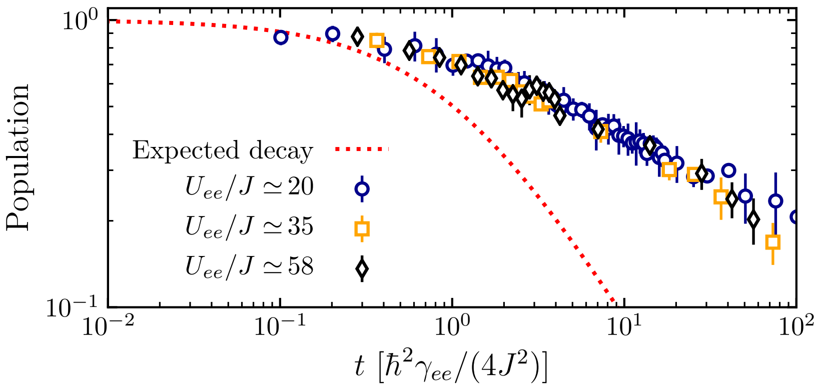

**Figure O.1** – Loss dynamics at different lattice depths of an ensemble of 1D Mott insulators where all particles are in the excited metastable state. The red dotted line is the expected decay according to the theory developed in García-Ripoll et al. (2009). The observed decay is much slower, which could be a hint of strong correlations arising in the system.

The theory developed by García-Ripoll et al. (2009) maps the bosonic system to a gas of hardcore bosons with a residual decay strongly suppressed by the Zeno effect. Experiments so far (Syassen et al. 2008; Yan et al. 2013; Zhu et al. 2014) have been compatible with a simplified version of their theory, which neglects all correlations and also assumes an initially flat density profile with one atom per site (a good approximation in the initial state when preparing the system in the MI regime). The markedly slower decay in our case points to the importance of possible initial deffects and correlations between neighboring sites, beyond the model presented in García-Ripoll et al. (2009). This could also point to dynamical correlations building up in time, effectively slowing down the decay.

We have started a collaboration with Leonardo Mazza (Université Paris-Sud) and Davide Rossini (University of Pisa) in order to develop a theory framework to explain these observations.

### ➟ Spin dynamics in the Mott insulator regime

A system of two-level atoms in an optical lattice is well suited for the study of spin dynamics, where both tunneling and interactions are present (Altman et al. 2003). Using the clock transition, by applying a $\pi/2$ pulse to a Mott insulator at unit filling, we can prepare a system where each site is described by a superposition

$$|\psi(\boldsymbol{k}_{\mathrm{cl}})\rangle_i = \frac{1}{\sqrt{2}}\left[|g\rangle + \mathrm{e}^{\mathrm{i}\phi_i(\boldsymbol{r})}|e\rangle\right], \tag{O.2}$$

with a spatially dependent phase $\phi_i(\boldsymbol{r}) = \boldsymbol{k}_{\mathrm{cl}} \cdot \boldsymbol{r}_i$. Such a system can be mapped onto a Heisenberg Hamiltonian. A similar configuration has been studied in Hild et al. (2014). Here, using local observables (the density-density correlation function), Hild et al. observe spin-diffusion within a time scale given by the *super-exchange*, $\hbar/J_{\mathrm{se}} = \hbar U/J^2$. Still, within a similar experimental framework, but measuring directly the total magnetization with Ramsey spectroscopy, we observe dynamics occurring in much faster timescales, on the order of $\hbar/J$. A complete description of the system should then resemble to a bosonic version of the so-called $t - J$ model, where in this context $t \mapsto J$ is the tunneling matrix element and $J \mapsto J_{\text{se}}$ is the super-exchange constant. In a perfectly ordered Mott insulator, the tunneling term should have very little effect, but as soon as a few defects (holes or *doublons*) are present due to the trap, imperfect preparation of the system, or finite temperature effects, the motion of this hole will be governed by the tunneling term and is susceptible to scramble the spin ordering by creating large scale entanglement in the system as it moves around in space. Moreover, the presence of interactions and inelastic losses could also modify this picture, and we are currently investigating these points.

## II. Towards artificial gauge fields

The next step in our experiment is the implementation of the protocol described in Gerbier et al. (2010) in order to generate an artificial gauge field using the clock states. In a few words, in this scheme atoms are trapped in a state-dependent lattice in one direction (e.g. atoms in $g$ are trapped on its nodes and atoms in $e$ in its anti-nodes)[1] and in a magic lattice in the other direction. If the lattice is deep enough, tunneling in the state-dependent direction is only feasible provided the atom changes its internal state. This can be achieved by sending a photon resonant with the clock transition, a process known as *laser-assisted tunneling*.

Upon this tunneling, the atom also changes its internal state and its full atomic state acquires a phase due to the recoil imparted by the photon. Tunneling in the magic direction occurs via regular tunneling and thus no phase is acquired. After a closed loop in the lattice, the particle has acquired a non-zero phase (see figure O.2). This is analogous to the Aharonov–Bohm effect, where a particle in the presence of a vector potential ends up with a non-zero phase after a closed loop (Aharonov et al. 1959). This protocol thus provides a way to engineer an artificial gauge field in a lattice, well described by a Harper-Hofstadter Hamiltonian (Harper 1955; Hofstadter 1976).

The previous protocol is intended at the single-particle level and could be verified by working at fillings $\bar{n} \leq 1$. However, artificial magnetism in the presence of interactions is supposed to give rise to new and richer regions in the phase-diagram, where narrow, incompressible quantum Hall phases are supposed to appear on top of the usual superfluid and Mott insulator ones (Sørensen et al. 2005; Umucalılar et al. 2010).

The interest of using a clock transition is the absence of spontaneous emission, which is the main limitation in many of the experiments having implemented these spin-orbit coupling protocols so far. This heating prevents the observation of phenomena beyond

---

[1] For this, we are going to use a lattice at the so-called *anti-magic* wavelength. For the yttebrium clock states, this wavelength corresponds to $\lambda_{\text{am}} \simeq 612\,\text{nm}$ (see figure 3.8 in chapter 3). The protocol proposed by Gerbier et al. (2010) also relies on the use of a *superlattice*, necessary to create a uniform flux along the optical lattice. We actually generate the light at $\lambda_{\text{am}}$ by frequency doubling a source at $\lambda_{\text{sl}} = 1024\,\text{nm}$, and thus, both the anti-magic and the super-lattice are issued from the same source. Moreover, due to the high powers needed, we have implemented a doubly-resonant cavity in which these lattices will be generated, achieving the needed depths thanks to the cavity build-up (Scholl 2014).

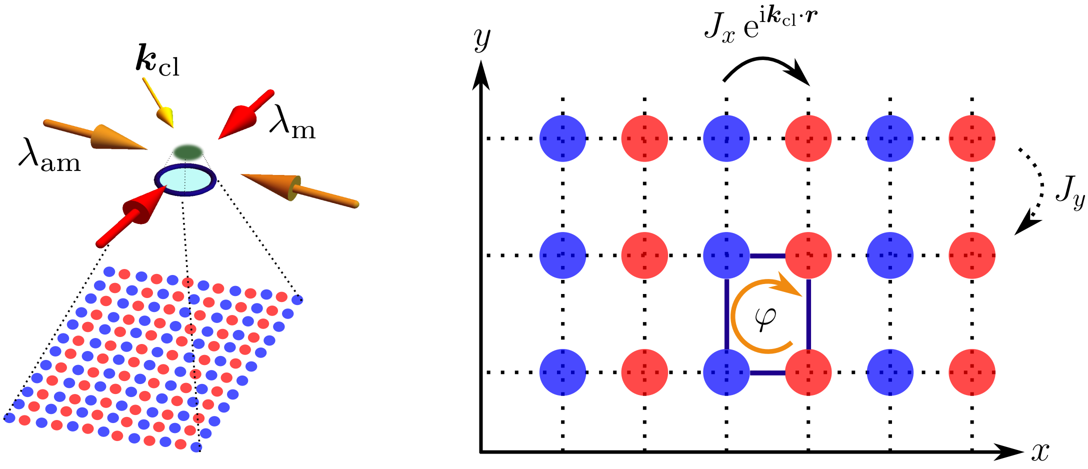

**Figure O.2** – Schematics of the protocol proposed in (Gerbier et al. 2010) for the simulation of artificial gauge fields. The lattice in the $y$-direction is at the magic wavelength and is state-dependent in the $x-$direction. Hopping in the state-dependent direction entails the absorption of a photon, which imprints a phase on the atomic state. Upon a closed loop, the atomic state has picked up a non-zero phase $\varphi$.

mean-field, needing much longer thermalisation scales [see e.g. Lin et al. (2009)]. In a similar fashion, inelastic two-body losses in the excited metastable state are prone to be problematic in such a situation, strongly limitting the signal-to-noise ratio and introducing entropy in the system, thus potentially preventing the observation of these (Baur et al. 2010). Hence, mechanisms such as the Zeno suppression observed in chapter 4 and the one described in the previous paragraphs [see equation (O.1)] could prove useful in the investigation of these strongly correlated phases with alkaline-earth like atoms, suffering from strong inelastic losses in the metastable state.

## III. Switching to fermions

With our experimental setup we can easily address the fermionic isotopes with minor modifications of our laser system. A first advantage of fermions is Pauli exclusion's principle: Two-fermions in the same state cannot interact via $s$-wave scattering. This implies that a polarized sample of fermions in the metastable state will not suffer from inelastic two-body losses. Then, this should allow us to test the protocol previously described to simulate magnetic fields (Gerbier et al. 2010) at the single-particle level, without the limitations inherent to inelastic losses that bosons have.

Another interest of fermions is their large nuclear spin (e.g. $^{173}$Yb has $I = 5/2$). The nuclear spin is decoupled from the electronic angular momentum degrees of freedom, which leads to two-orbital interactions independent of the internal state, obeying the so-called SU$(N = 2I + 1)$ symmetry. These systems are well suited for the simulation of quantum magnetism and impurity Hamiltonians (Gorshkov et al. 2010).

The fermionic isotopes also feature a narrow *orbital* Feshbach resonance among the clock states, allowing to prepare long-lived strongly interacting gases (Zhang et al. 2015; Pagano et al. 2015; Höfer et al. 2015). In an optical lattice, these orbital resonances can be used to induce periodically modulated interactions which, combined with laser-assisted tunneling can lead to an effect known as *density-dependent* light-assisted tunneling (Edmonds et al. 2013; Greschner et al. 2014; Greschner et al. 2015). In a more general perspective, this mechanism has been shown to be key in the simulation of the so-called *dynamical gauge fields*, of wide interest in condensed matter and particle physics (Levin et al. 2005; Kogut 1983).

# Supplementary materials

# APPENDIX A

# Correlations in a gas released from an optical lattice

## A.1 Expansion of a gas released from an optical lattice

### The role of interactions

In the case of a BEC in a dipole trap, interactions are usually on the order of $\mu/h$ (typically a few kHz) and are large compared to the trapping frequencies $\omega$ (usually a few hundred Hz). In this case, interactions notably modify the expansion of the gas once it is released from the trap (Castin et al. 1996). However, in an optical lattice, on-site interactions, on the order of a kHz, need to be compared to the lattice frequencies at the bottom of each well $\omega_{\mathrm{lat}} \propto (V_0 E_{\mathrm{r}})^{1/2}$ which reach values above 10 kHz already at depths corresponding to a few recoil energies. The trapping frequencies dictate the speed at which the wave functions at each site expand $v_{\mathrm{exp}} = (2\hbar\omega_{\mathrm{lat}}/M)^{1/2}$. We then see that wave functions from different sites will start overlapping at a time $t_{\mathrm{ov}} \simeq [\hbar/(E_{\mathrm{r}}\omega_{\mathrm{lat}})]^{1/2}$. At this point, the density of the gas will have been reduced by a factor $(\omega_{\mathrm{lat}} t_{\mathrm{ov}})^3 \gg 1$, and interactions can be safely neglected (Gerbier et al. 2008). Therefore, we consider a purely ballistic expansion in the following discussion.

### Density distribution in TOF

Let us start by considering the field operator of a particle prior to its release from an optical lattice with $L$ sites, which is given by:

$$\hat{\Psi}(\boldsymbol{r}) = \sum_{i=1}^{L} w(\boldsymbol{r} - \boldsymbol{r}_i)\hat{a}_i, \tag{A.1}$$

with $\hat{a}_i$ the operator destroying a particle at a site $i$. In the Schrödinger picture, to evaluate the evolution of the field operator during TOF, $\hat{\Psi}(\boldsymbol{r}, t)$, we first need to calculate the evolution of the Wannier functions $w(\boldsymbol{r} - \boldsymbol{r}_i, t)$. For this, let's write each Wannier function in the momentum basis:

$$w(\boldsymbol{r} - \boldsymbol{r}_i) = \frac{1}{(2\pi)^{3/2}} \int \tilde{w}(\boldsymbol{k}) \mathrm{e}^{\mathrm{i}\boldsymbol{k}\cdot(\boldsymbol{r}-\boldsymbol{r}_i)}\, \mathrm{d}^3 k. \tag{A.2}$$

At a time $t$, the wave function $w(\boldsymbol{r}-\boldsymbol{r}_i,t)$ has evolved under a free-particle Hamiltonian and reads:

$$w(\boldsymbol{r}-\boldsymbol{r}_i,t) = \frac{1}{(2\pi)^{3/2}}\int \tilde{w}(\boldsymbol{k})\mathrm{e}^{\mathrm{i}\left[\boldsymbol{k}\cdot(\boldsymbol{r}-\boldsymbol{r}_i)-\hbar\boldsymbol{k}^2 t/(2M)\right]}\,\mathrm{d}^3k \tag{A.3}$$

$$\simeq \left(\frac{M}{\hbar t}\right)^{3/2}\tilde{w}\left(\boldsymbol{k}=\frac{M(\boldsymbol{r}-\boldsymbol{r}_i)}{\hbar t}\right)\mathrm{e}^{\mathrm{i}M(\boldsymbol{r}-\boldsymbol{r}_i)^2/(2\hbar t)}, \tag{A.4}$$

where we have considered times long enough $\omega_{\mathrm{lat}}t \gg 1$ to perform a stationary phase approximation. The density distribution after TOF is then $\mathcal{N}(\boldsymbol{r},t) = \langle\hat{n}(\boldsymbol{r},t)\rangle = \langle\hat{\Psi}^\dagger(\boldsymbol{r},t)\hat{\Psi}(\boldsymbol{r},t)\rangle$ and reads (Gerbier et al. 2008):

$$\mathcal{N}(\boldsymbol{r},t) = \left(\frac{M}{\hbar t}\right)^3\left|\tilde{w}\left(\frac{M\boldsymbol{r}}{\hbar t}\right)\right|^2\sum_{i,j=1}^{L}\mathrm{e}^{\mathrm{i}M[(\boldsymbol{r}-\boldsymbol{r}_j)^2-(\boldsymbol{r}-\boldsymbol{r}_i)^2]/(2\hbar t)}\langle\hat{a}_i^\dagger\hat{a}_j\rangle, \tag{A.5}$$

where we have used that $\tilde{w}(\boldsymbol{r})$ is a smooth function and therefore $\tilde{w}(\boldsymbol{r}-\boldsymbol{r}_i)\simeq\tilde{w}(\boldsymbol{r}-\boldsymbol{r}_j)\equiv\tilde{w}(\boldsymbol{r})$. We can write the density distribution as the product of two factors $\mathcal{N}(\boldsymbol{r},t)=\mathcal{W}(\boldsymbol{r},t)\mathcal{S}(\boldsymbol{r},t)$. The first one is a smooth envelope function:

$$\mathcal{W}(\boldsymbol{r},t) = \left(\frac{M}{\hbar t}\right)^3\left|\tilde{w}\left(\frac{M\boldsymbol{r}}{\hbar t}\right)\right|^2, \tag{A.6}$$

and the second one is the structure factor:

$$\mathcal{S}(\boldsymbol{r},t) = \sum_{i,j=1}^{L}\mathrm{e}^{\mathrm{i}M[2\boldsymbol{r}\cdot(\boldsymbol{r}_i-\boldsymbol{r}_j)-(\boldsymbol{r}_j^2-\boldsymbol{r}_i^2)]/(2\hbar t)}g(i,j), \tag{A.7}$$

where we have defined the first-order correlation function (Naraschewski et al. 1999) as $g(i,j)=\langle\hat{a}_i^\dagger\hat{a}_j\rangle$ . This function gives an idea of the extension of phase coherence in the system, and allows one to define a coherence length $\ell_{\mathrm{c}}$, after which phase coherence vanishes. For example, in the superfluid regime in the limit $J\gg U$, phase coherence extends over the whole lattice, and $\ell_{\mathrm{c}}\simeq R$, with $R$ the size of the system. However, in the Mott insulating regime, $g(i,j)$ is limited to a single or a few sites and $\ell_{\mathrm{c}}\simeq d$. With this in mind, we can evaluate the importance of the quadratic term $\propto \boldsymbol{r}_j^2-\boldsymbol{r}_i^2$ in the phase of the structure factor. Considering sites distant of $\ell_{\mathrm{c}}$, this term takes different values depending if the sites are close to the center of the cloud or on the edges:

$$\frac{M}{2\hbar t}(\boldsymbol{r}_j^2-\boldsymbol{r}_i^2)\simeq\frac{M\ell_{\mathrm{c}}^2}{2\hbar t}\quad\text{for}\quad \boldsymbol{r}_i,\boldsymbol{r}_j\ll R, \tag{A.8}$$

$$\frac{M}{2\hbar t}(\boldsymbol{r}_j^2-\boldsymbol{r}_i^2)\simeq\frac{M\ell_{\mathrm{c}}R}{\hbar t}\quad\text{for}\quad \boldsymbol{r}_i,\boldsymbol{r}_j\simeq R \tag{A.9}$$

We then see that, in the most restrictive case, this quadratic term will be negligible for times:

$$t_{\mathrm{FF}}\gg\frac{M\ell_{\mathrm{c}}R}{\hbar} \tag{A.10}$$

In the experimental conditions described in chapter 2 this time corresponds to $t_{\mathrm{FF}}\simeq 10\,\mathrm{ms}$ in the Mott regime and to $t_{\mathrm{FF}}\simeq 300\,\mathrm{ms}$ in the superfluid regime. For times $t\geq t_{\mathrm{FF}}$, and in analogy to the Fraunhofer approximation in optical diffraction, the quadratic term in the phase can be neglected and the structure factor in TOF is directly linked to the *in situ* structure factor:

$$S(\boldsymbol{k}) = \sum_{i,j=1}^{L} \mathrm{e}^{\mathrm{i}\boldsymbol{k}\cdot(\boldsymbol{r}_i-\boldsymbol{r}_j)} g(i,j), \tag{A.11}$$

just by making the substitution $\boldsymbol{k} = M\boldsymbol{r}/(\hbar t)$.

## A.2 Density correlations in a Mott insulator

Here, we expose the concepts behind the experimental results presented in section 2.2.5 and used to derive equation (2.27). In these experiments, we looked for density correlations in time of flight. For this, we need to evaluate the following correlation function (Fölling et al. 2005):

$$\begin{aligned}\langle \hat{n}(\boldsymbol{k})\hat{n}(\boldsymbol{k}')\rangle = \mathcal{W}(\boldsymbol{k})\mathcal{W}(\boldsymbol{k}')\times \\ \sum_{ijkl} \mathrm{e}^{\mathrm{i}[\boldsymbol{k}\cdot(\boldsymbol{r}_i-\boldsymbol{r}_j)-M(\boldsymbol{r}_j^2-\boldsymbol{r}_i^2)/(2\hbar t)]}\mathrm{e}^{\mathrm{i}[\boldsymbol{k}'\cdot(\boldsymbol{r}_k-\boldsymbol{r}_l)-M(\boldsymbol{r}_l^2-\boldsymbol{r}_k^2)/(2\hbar t)]}\langle \hat{a}_i^\dagger \hat{a}_j \hat{a}_k^\dagger \hat{a}_l\rangle,\end{aligned} \tag{A.12}$$

where we have used $\boldsymbol{k} = M\boldsymbol{r}/(\hbar t)$. The expectation value in the sum can be rewritten as the sum of two terms: First, an autocorrelation contribution, $\langle \hat{a}_i^\dagger \hat{a}_l\rangle\delta_{kj}$, that leads to a strong peak at $\boldsymbol{k} = \boldsymbol{k}'$ (i.e. $\boldsymbol{r} = \boldsymbol{r}'$ in TOF) and we omit it in the following discussion. The second term is a normal ordered second-order correlation function $\langle \hat{a}_i^\dagger \hat{a}_k^\dagger \hat{a}_j \hat{a}_l\rangle$ and, in a Mott insulator state with $n_0$ atoms per site, where $\langle \hat{a}_i^\dagger \hat{a}_j\rangle = n_0\delta_{ij}$, it can be rewritten as:

$$\langle \hat{a}_i^\dagger \hat{a}_k^\dagger \hat{a}_j \hat{a}_l\rangle = n_0^2\delta_{ij}\delta_{kl} + n_0^2\delta_{il}\delta_{jk} + n_0(n_0-1)\delta_{ik}\delta_{ij}\delta_{il}. \tag{A.13}$$

We then have:

$$\langle n(\boldsymbol{k})n(\boldsymbol{k}')\rangle = \mathcal{W}(\boldsymbol{k})\mathcal{W}(\boldsymbol{k}')\left[n_0^2L^2 + n_0^2\sum_{i,j=1}^{L}\mathrm{e}^{\mathrm{i}(\boldsymbol{k}-\boldsymbol{k}')\cdot(\boldsymbol{r}_i-\boldsymbol{r}_j)} + Ln_0(n_0-1)\right]. \tag{A.14}$$

An interesting feature is that the terms in $\boldsymbol{r}_\alpha^2 - \boldsymbol{r}_\beta^2$ have canceled out exactly, and therefore, no far-field approximation is needed. The last term in the previous expression vanishes for $n_0 = 1$ and acts as a small offset otherwise, and therefore we neglect it in the following. Finally, in order to get rid of the terms already present in the average density profile $\mathcal{N}(\boldsymbol{k}) = n_0L\mathcal{W}(\boldsymbol{k})$ [see equation (2.21)] we can normalize and obtain the reduced second order correlation function:

$$g_2(\boldsymbol{k},\boldsymbol{k}') = \frac{\langle \hat{n}(\boldsymbol{k})\hat{n}(\boldsymbol{k}')\rangle}{\mathcal{N}(\boldsymbol{k})\mathcal{N}(\boldsymbol{k}')} = 1 + \frac{1}{L^2}\sum \mathrm{e}^{\mathrm{i}(\boldsymbol{k}-\boldsymbol{k}')\cdot(\boldsymbol{r}_i-\boldsymbol{r}_j)}, \tag{A.15}$$

or, equivalently:

$$g_2(\boldsymbol{r},\boldsymbol{r}') = 1 + \frac{1}{L^2}\sum \mathrm{e}^{\mathrm{i}M(\boldsymbol{r}-\boldsymbol{r}')\cdot(\boldsymbol{r}_i-\boldsymbol{r}_j)/(\hbar t)}. \tag{A.16}$$

# APPENDIX B

# Inelastic two-body losses equations

## B.1 Correlation functions

Two-body processes are related to the probability of finding two particles at the same position $\boldsymbol{r}$. In order to derive an equation for the loss rate, it is useful to define first the one-body and two-body correlation functions (Naraschewski et al. 1999):

$$G_1(\boldsymbol{r},\boldsymbol{r}') = \langle \hat{\Psi}^\dagger(\boldsymbol{r}')\hat{\Psi}(\boldsymbol{r})\rangle, \tag{B.1}$$

$$G_2(\boldsymbol{r},\boldsymbol{r}') = \langle \hat{\Psi}^\dagger(\boldsymbol{r})\hat{\Psi}^\dagger(\boldsymbol{r}')\hat{\Psi}(\boldsymbol{r})\hat{\Psi}(\boldsymbol{r}')\rangle. \tag{B.2}$$

The one-body correlation function reduces to the density at a given point when evaluated at $\boldsymbol{r} = \boldsymbol{r}'$, i.e. $G_1(\boldsymbol{r},\boldsymbol{r}) = n(\boldsymbol{r})$. The second order correlation function is related to the probability to find one particle at $\boldsymbol{r}$ and another one at $\boldsymbol{r}'$. Here, we will be concerned of two particles meeting at a same point, i.e., we want to evaluate the joint detection probability, which can be written in terms of the normalized second order correlation function as:

$$g_2(\boldsymbol{r}) = \frac{G_2(\boldsymbol{r},\boldsymbol{r})}{n(\boldsymbol{r})^2}. \tag{B.3}$$

## B.2 Equation for the losses

Let us now consider the following Hamiltonian (Dürr et al. 2009):

$$\hat{H} = \int \hat{\Psi}^\dagger(\boldsymbol{r})\hat{H}_{\rm sp}(\boldsymbol{r})\hat{\Psi}(\boldsymbol{r})\,{\rm d}^3r + \frac{{\rm Re}(g)}{2}\int \hat{\Psi}^\dagger(\boldsymbol{r})^2\hat{\Psi}(\boldsymbol{r})^2\,{\rm d}^3r, \tag{B.4}$$

where $\hat{H}_{\rm sp} = -\hbar^2\boldsymbol{\nabla}^2/(2m) + V_{\rm tr}(\boldsymbol{r})$ is the single particle Hamiltonian and $g = 4\pi\hbar^2 a/m$ the interaction strength with $a$ the complex scattering length. Let us also consider the dissipation operator responsible for the two-body losses:

$$\mathcal{L}[\hat{\rho}] = -{\rm Im}(g)\int \left[\hat{C}(\boldsymbol{r})\hat{\rho}\,\hat{C}^\dagger(\boldsymbol{r}) - \frac{1}{2}\hat{C}^\dagger(\boldsymbol{r})\hat{C}(\boldsymbol{r})\hat{\rho} - \frac{1}{2}\hat{\rho}\,\hat{C}^\dagger(\boldsymbol{r})\hat{C}(\boldsymbol{r})\right]\,{\rm d}^3r, \tag{B.5}$$

with $\hat{C}(\boldsymbol{r}) = \hat{\Psi}^2(\boldsymbol{r})$.

The evolution of the system is then given by a Lindblad master equation for the density matrix $\hat{\rho}$:

$$\frac{\partial \hat{\rho}}{\partial t} = \frac{1}{\mathrm{i}\hbar}[\hat{H}, \hat{\rho}] + \frac{1}{\hbar}\mathcal{L}[\hat{\rho}]. \tag{B.6}$$

With this, we can now obtain the equation of motion for the density $n(\boldsymbol{r}) = \langle \hat{\Psi}^{+}(\boldsymbol{r})\hat{\Psi}(\boldsymbol{r})\rangle$:

$$\frac{\partial n(\boldsymbol{r},t)}{\partial t} = \frac{1}{\mathrm{i}\hbar}\mathrm{tr}\left(n(\boldsymbol{r},t)[\hat{H},\hat{\rho}]\right) + \frac{1}{\hbar}\mathrm{tr}\left(n(\boldsymbol{r},t)\mathcal{L}[\hat{\rho}]\right), \tag{B.7}$$

where $\mathrm{tr}(\cdot)$ denotes the trace. The first term conserves the total particle number. However, for the second term we have:

$$\frac{\partial n(\boldsymbol{r},t)}{\partial t} = \frac{2}{\hbar}\mathrm{Im}(g)G_2(\boldsymbol{r},\boldsymbol{r},t) = -\beta G_2(\boldsymbol{r},\boldsymbol{r},t), \tag{B.8}$$

with $\beta = -2\mathrm{Im}(g)/\hbar$. The previous expression can be rewritten as:

$$\frac{\partial n(\boldsymbol{r},t)}{\partial t} = -\beta n(\boldsymbol{r},t)^2 g_2(\boldsymbol{r},t). \tag{B.9}$$

### B.2.1 Loss equation for a BEC

For a BEC we can perform a mean-field approximation $\langle \hat{\Psi}(\boldsymbol{r})\rangle = \varphi_0(\boldsymbol{r})$. With this, we have $G_2(\boldsymbol{r}) = n(\boldsymbol{r})^2$ and thus $g_2(\boldsymbol{r}) = 1$; therefore:

$$\frac{\partial n(\boldsymbol{r},t)}{\partial t} = -\beta n(\boldsymbol{r},t)^2. \tag{B.10}$$

By integrating over the spatial coordinates, one obtains the evolution for the total atom number.

### B.2.2 Loss equation for a deep optical lattice

In an optical lattice, we can develop the field operator in the Wannier basis:

$$\hat{\Psi}(\boldsymbol{r}) = \sum_{n,k} w_n(\boldsymbol{r}-\boldsymbol{r}_k)\hat{a}_{n,k}. \tag{B.11}$$

Restricting ourselves to one single band, we can drop the $n$-index. Moreover, if we consider deep lattices, the overlap between Wannier functions is negligible and we can perform the following approximations:

$$n(\boldsymbol{r}) = \langle \hat{\Psi}^{\dagger}(\boldsymbol{r})\hat{\Psi}(\boldsymbol{r})\rangle = \sum_{i,j}\langle \hat{a}_i^{\dagger}\hat{a}_j\rangle \int w(\boldsymbol{r}-\boldsymbol{r}_i)^* w(\boldsymbol{r}-\boldsymbol{r}_j)\,\mathrm{d}^3 r \simeq \sum_i \langle \hat{n}_i\rangle, \tag{B.12}$$

$$G_2(\boldsymbol{r},\boldsymbol{r}) \simeq \sum_i \langle \hat{a}_i^{\dagger}\hat{a}_i^{\dagger}\hat{a}_i\hat{a}_i\rangle \int |w(\boldsymbol{r}-\boldsymbol{r}_i)|^4\,\mathrm{d}^3 r = \mathcal{W}\sum_i \langle \hat{n}_i(\hat{n}_i-1)\rangle, \tag{B.13}$$

where we have put $\mathcal{W} = \int |w(\boldsymbol{r})|^4\,\mathrm{d}^3 r$. We see that, by doing this, the pair correlation function $g_2 = \langle \hat{n}_i(\hat{n}_i - 1)\rangle / \langle \hat{n}_i\rangle^2$ becomes independent of the lattice site. If we now put $\gamma = \beta\mathcal{W}$ we can write for each lattice site:

$$\frac{\mathrm{d}\langle \hat{n}_i\rangle}{\mathrm{d}t} = -\gamma\langle \hat{n}_i(\hat{n}_i-1)\rangle. \tag{B.14}$$

If we consider a Mott insulator in the atomic limit with an initial filling $\bar{n} = 2$, we can write the initial state as $\hat{\rho} = |2\rangle\langle 2|$, which connects through losses to $\hat{\rho}(t) = p_0(t)|0\rangle\langle 0| + p_2(t)|2\rangle\langle 2|$, with $p_0(0) = 0$ and $p_2(0) = 1$. Thus, the evolution of $p_2(t)$ is found by projecting equation (B.14) onto $|2\rangle$. With this, we have $\langle \hat{n}_i \rangle = 2p_2$ and $\langle \hat{n}_i(\hat{n}_i - 1)\rangle = 2p_2$, which leads to $\dot{p}_2 = -\gamma p_2$ or, summing through all the lattice sites:

$$\frac{\mathrm{d}N_2(t)}{\mathrm{d}t} = -\gamma N_2(t). \tag{B.15}$$

# APPENDIX C

# Evolution of a discrete state coupled to a continuum

## C.1 Optical Bloch equations

In chapter 4 we have dealt with a situation in which atomic pairs in the ground state could be coupled to a state undergoing strong two-body losses, and thus, the coupling slowly empties the ground state in an irreversible manner. A similar effect has been observed for very weak coupling strengths in chapter 5, where atoms in the ground state are coupled to a state which was broadened due to the inhomogeneities induced by the trapping.

The problem of a discrete state $|a\rangle$, coupled to another discrete excited level $|b\rangle$ which is itself coupled to a continuum, for instance, the vacuum state $|\mathrm{vac}\rangle$, is a well-known problem in quantum optics (Cohen-Tannoudji et al. 1992) [see figure C.1(a)]. The evolution of the density matrix of such a system can be written as follows:

$$\dot{\rho}_{\mathrm{vac}} = \Gamma \rho_{bb}, \tag{C.1}$$

$$\dot{\rho}_{aa} = \mathrm{i}\frac{\Omega}{2}(\rho_{ab} - \rho_{ba}), \tag{C.2}$$

$$\dot{\rho}_{bb} = \mathrm{i}\frac{\Omega}{2}(\rho_{ba} - \rho_{ab}) - \Gamma \rho_{bb}, \tag{C.3}$$

$$\dot{\rho}_{ba} = -(\mathrm{i}\delta + \Gamma)(\rho_{ba} - \rho_{ab}) + \mathrm{i}\frac{\Omega}{2}(\rho_{bb} - \rho_{aa}) = \dot{\rho}_{ab}^{*}. \tag{C.4}$$

Here, $\Omega$ is the strength of the coupling between the discrete and state $|b\rangle$, $\delta$ is the detuning and $\Gamma$ is the decay rate from state $|b\rangle$ towards $|\mathrm{vac}\rangle$.

## C.2 Effective Hamiltonian

If we are only interested in the population of the ground state $|a\rangle$, this situation can be mapped into an effective two-level system [see figure C.1(b)] where the interaction couples the discrete state $|a\rangle$ into a continuum of states $|b_k\rangle$ of width $\Gamma$. We can thus describe the processes studied in chapters 4 and 5 through the following non-Hermitian

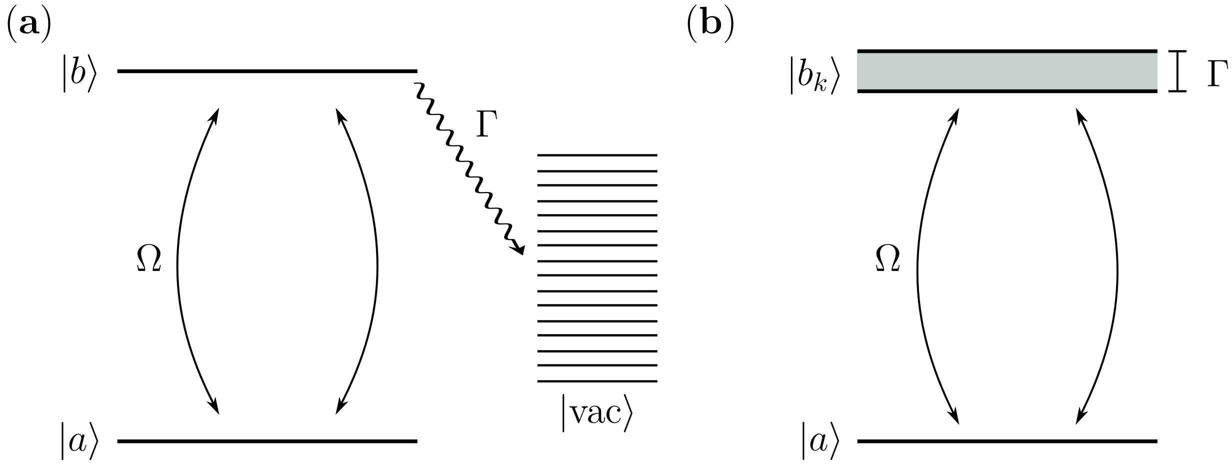

**Figure C.1** – **(a):** Two discrete states $|a\rangle$ and $|b\rangle$ are coupled with a strength given by $\Omega$. The excited state is itself coupled into a continuum of modes $|\mathrm{vac}\rangle$ at a rate given by $\Gamma$. **(b):** Effective two level system where a discrete ground state $|a\rangle$ is coupled into a continuum of width $\Gamma$ with a strength given by $\Omega$.

Hamiltonian (Cohen-Tannoudji et al. 1992):

$$\hat{H}_{\text{eff}} = \hbar \begin{pmatrix} 0 & \Omega/2 \\ \Omega/2 & -\delta - \mathrm{i}\Gamma/2 \end{pmatrix}, \tag{C.5}$$

plus a stochastic quantum jump term that we ignore in the following. Here, $\Gamma$ represents now the effective *width* of the continuum, which is given by the two-body inelastic loss-rate in the case of atom pairs, and by the effective broadening $\Delta$ in the case of the driven bulk BEC.

We can now compute the eigenvalues of this effective Hamiltonian:

$$\lambda_\pm = -\frac{\delta}{2} - \frac{\mathrm{i}\Gamma}{4} \pm \frac{1}{2}\sqrt{\Omega^2 + \delta^2 - \frac{\Gamma^2}{4} + \mathrm{i}\Gamma\delta} \tag{C.6}$$

Let us now put $\delta = 0$ and evaluate the following two limits:

- The strong coupling regime, with $\Omega \gg \Gamma/2$: In this situation the eigenvalues read $\lambda_\pm = -\mathrm{i}\Gamma/4 \pm \Omega/2$, which leads to Rabi oscillations between $|a\rangle$ and $|b\rangle$ at a rate $\Omega$ with an exponentially decaying probability at a rate $\Gamma/2$ of being found in the ground state:

$$P_g(t) = \mathrm{e}^{-\Gamma t/2} \cos^2\left(\frac{\Omega t}{2}\right). \tag{C.7}$$

- The weak coupling regime, with $\Omega \ll \Gamma/2$: In this case, both eigenvalues are complex. In particular, the one with the smaller imaginary part reads $\lambda_+ = \mathrm{i}\Omega^2/(2\Gamma)$ and is purely imaginary, leading to an exponential decay of the population in the ground state at a rate $\gamma_{\text{eff}} = \Omega^2/(2\Gamma)$, as would be predicted by Fermi's golden rule for a discrete state coupled to a continuum with a density of states $1/\Gamma$, with $\Gamma$ the width of the continuum:

$$P_g(t) = \exp\left(-\frac{\Omega^2}{2\Gamma}t\right), \tag{C.8}$$

which is also analogous to the Wigner-Weisskopf decay.

Thus, one expects a crossover from an exponentially damped oscillation, to a pure decay at a rate $\Omega^2/(2\Gamma)$. We show this in figure C.2, where we compare the prediction of the OBEs to the approximations in equations (C.7) and (C.8) of the non-Hermitian effective Hamiltonian $\hat{H}_{\text{eff}}$

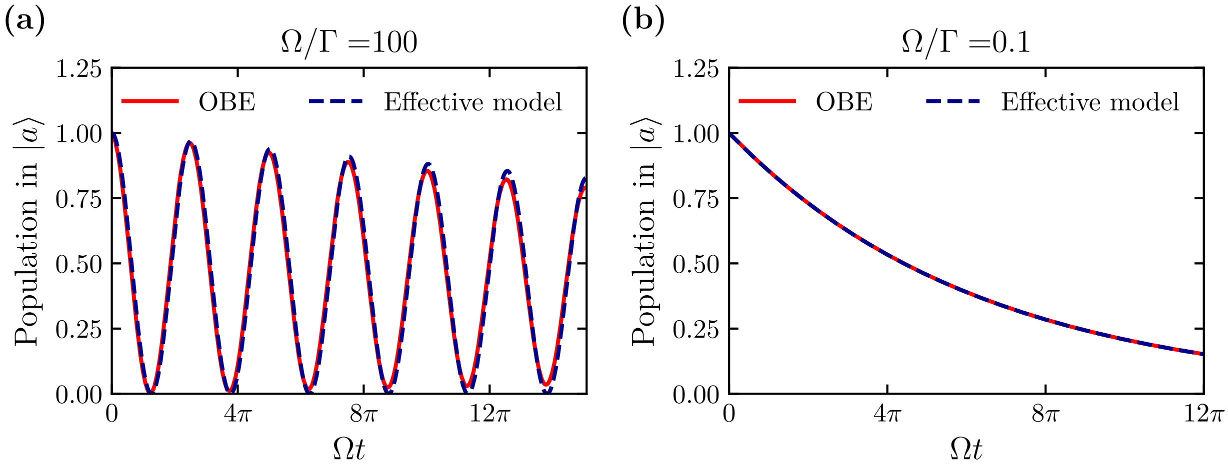

**Figure C.2** – Evolution of the population in the ground state for the system described in the main text. We show the prediction using the optical Bloch equations (red lines) or the decay predicted by equations (C.7) and (C.8) (dashed blue lines), for the strong coupling regime **(a)**, where damped oscillations appear, and the and weak coupling **(b)** regime, where an irreversible decay analogous to the Wigner-Weisskopf decay appears.

# APPENDIX D

# Derivation of the momentum relaxation collision rate

## D.1 Framework

In this section we describe the effect of momentum relaxation in a homogeneous BEC in the form of diffusive collisions. We denote the state of the BEC as $|m, \boldsymbol{k}\rangle$, with $m = a, b$ describing the internal ground state and excited state, respectively, and $\hbar\boldsymbol{k}$ the momentum.

Due to this relaxation, the BEC, considered as a small system $\mathcal{S}$ occupying the modes $\{|a, \boldsymbol{k} = \boldsymbol{0}\rangle\}$ and $\{|b, \boldsymbol{k} = \boldsymbol{k}_\mathrm{L}\rangle\}$, is coupled to a big reservoir $\mathcal{R}$ of modes $\{|a, \boldsymbol{q}\rangle \otimes |b, \boldsymbol{k}_\mathrm{L} - \boldsymbol{q}\rangle\}$, initially in the vacuum state $|\mathrm{vac}\rangle_\mathcal{R}$. To simplify, we assume a homogeneous system of volume $V = L^3$.

In a frame rotating at the laser frequency and under the rotating wave approximation, the total Hamiltonian taking into account these collisions can be described as:

$$\hat{H} = \hat{H}_0 + \hat{V}_\mathrm{AL} + \hat{H}_\mathrm{coll}. \tag{D.1}$$

The first terms are the equivalent of equations (5.10), and (5.12) for a uniform system:

$$\hat{H}_0 = \sum_{\boldsymbol{q}} \varepsilon_{\boldsymbol{q}} \hat{a}^\dagger_{\boldsymbol{q}} \hat{a}_{\boldsymbol{q}} + (\varepsilon_{\boldsymbol{q}} - \hbar\delta_\mathrm{L}) \hat{b}^\dagger_{\boldsymbol{q}} \hat{b}_{\boldsymbol{q}}, \tag{D.2}$$

$$\hat{V}_\mathrm{AL} \simeq \sum_{\boldsymbol{q}} \frac{\hbar\Omega_\mathrm{L}}{2} \hat{b}^\dagger_{\boldsymbol{k}_\mathrm{L}-\boldsymbol{q}} \hat{a}_{\boldsymbol{q}} + \mathrm{h.c.}. \tag{D.3}$$

Here, $\varepsilon_{\boldsymbol{q}} = \hbar^2\boldsymbol{q}^2/(2M)$ and $\hat{a}_{\boldsymbol{q}}$ ($\hat{b}_{\boldsymbol{q}}$) anihilates an atom in the ground (excited) state with momentum $\boldsymbol{q}$. The Hamiltonian describing the diffusive collisions reads:

$$\hat{H}_\mathrm{coll} \simeq \frac{g_{ab}}{V} \sum_{\boldsymbol{q}} \hat{a}^\dagger_{\boldsymbol{q}} \hat{b}^\dagger_{\boldsymbol{k}_\mathrm{L}-\boldsymbol{q}} \hat{a}_{\boldsymbol{0}} \hat{b}_{\boldsymbol{k}_\mathrm{L}} + \mathrm{h.c.}, \tag{D.4}$$

and describes the processes linking the BEC to the reservoir. Before trying to derive a master equation for $\mathcal{S}$, it is convenient to write $\hat{H}_\mathrm{coll}$ in the interaction point of view with respect to $\hat{H}_0$:

$$\hat{H}_\mathrm{coll} = \frac{g_{ab}}{V} \sum_{\boldsymbol{q}} \hat{D}^\dagger_{\boldsymbol{q}} \hat{S}\, \mathrm{e}^{\mathrm{i}\alpha_{\boldsymbol{q}} t} + \mathrm{h.c.}, \tag{D.5}$$

where we have defined two new operators: $\hat{D}^{\dagger}_{\boldsymbol{q}} = \hat{a}^{\dagger}_{\boldsymbol{q}}\hat{b}^{\dagger}_{\boldsymbol{k}_{\mathrm{L}}-\boldsymbol{k}}$ and $\hat{S} = \hat{a}_{\boldsymbol{0}}\hat{b}_{\boldsymbol{k}_{\mathrm{L}}}$ and we have put $\alpha_{\boldsymbol{q}} = \hbar q(q - k_{\mathrm{L}}\cos\theta)/M$, where $\theta$ is the angle between the laser wave vector $\boldsymbol{k}_{\mathrm{L}}$ and the momentum of the scattered particle $\boldsymbol{q}$.

## D.2 Master equation for the BEC and collisional rate

We assume that the whole system can be described by a density matrix $\hat{\rho}$, which can be factorized as $\hat{\rho} = \hat{\rho}_{\mathcal{S}} \otimes \hat{\rho}_{\mathcal{R}}$ with $\hat{\rho}(t=0) = \hat{\rho}_{\mathcal{S}} \otimes |\mathrm{vac}\rangle_{\mathcal{R}}\langle\mathrm{vac}|$. The evolution of the density matrix under the action of $\hat{H}_{\mathrm{coll}}$ is given by (Cohen-Tannoudji et al. 1992):

$$\frac{\mathrm{d}}{\mathrm{d}t}\hat{\rho}(t) = -\frac{1}{\hbar^2}\int_0^t \left[\hat{H}_{\mathrm{coll}}(t), [\hat{H}_{\mathrm{coll}}(t'), \hat{\rho}(t')]\right] \mathrm{d}t'. \tag{D.6}$$

However, we are not interested in the dynamics of the whole system, but only in the effect that relaxation has on the BEC. With this in mind, we can trace over the reservoir and derive an equation of motion for the density matrix of the BEC alone:

$$\frac{\mathrm{d}}{\mathrm{d}t}\hat{\rho}_{\mathcal{S}}(t) = -\frac{1}{\hbar^2}\int_0^t \mathrm{tr}_{\mathcal{R}}\left[\hat{H}_{\mathrm{coll}}(t), [\hat{H}_{\mathrm{coll}}(t'), \hat{\rho}(t')]\right] \mathrm{d}t'. \tag{D.7}$$

After some algebra and the usual assumption of *short-memory* of the reservoir (Cohen-Tannoudji et al. 1992), the only non-vanishing terms lead to the following coarse-grained master equation:

$$\frac{\mathrm{d}}{\mathrm{d}t}\hat{\rho}_{\mathcal{S}}(t) \simeq C(\omega)\left[2\hat{S}\,\hat{\rho}_{\mathcal{S}}(t)\hat{S}^{\dagger} - \hat{S}^{\dagger}\hat{S}\,\hat{\rho}_{\mathcal{S}}(t) - \hat{\rho}_{\mathcal{S}}(t)\hat{S}^{\dagger}\hat{S}\right] \tag{D.8}$$

Here, we have defined

$$C(\omega) = \frac{1}{\hbar^2}\frac{g_{ab}^2}{V^2}\int\sum_{\boldsymbol{q}} \mathrm{e}^{-\mathrm{i}\alpha_{\boldsymbol{q}}\tau}\,\mathrm{d}\tau = \frac{\Gamma}{2} - \mathrm{i}\Delta, \tag{D.9}$$

where we have introduced $\Delta$, the collisional shift due to the reservoir and $\Gamma$, the collisional relaxation rate[2]

$$\Delta = \frac{1}{\hbar^2}\frac{g_{ab}^2}{V^2}\sum_{\boldsymbol{q}}\mathrm{p.v.}\left(\frac{1}{\alpha_{\boldsymbol{q}}}\right) \quad \text{and} \quad \Gamma = \frac{2\pi}{\hbar^2}\frac{g_{ab}^2}{V^2}\sum_{\boldsymbol{q}}\delta(\alpha_{\boldsymbol{q}}), \tag{D.10}$$

where p.v. stands for the Cauchy principal value. The relaxation rate can be computed by taking the continuum limit $\sum_{\boldsymbol{q}} \to V/(2\pi)^3\int \mathrm{d}^3q$ and reads:

$$\Gamma = \frac{\sigma_{ab}v_{\mathrm{r}}}{V}, \tag{D.11}$$

where $\sigma_{ab} = 4\pi a_{ab}^2$ is the inter-species scattering cross section, with $a_{ab}$ the inter-species scattering length and with $v_{\mathrm{r}} = \hbar k_{\mathrm{L}}/M$ the recoil velocity.

Introducing this into equation (D.8), we have that the diffusive collisions lead to a master equation that can be written in the Lindblad form:

$$\frac{\mathrm{d}}{\mathrm{d}t}\hat{\rho}_{\mathcal{S}}(t) = -\frac{1}{\mathrm{i}\hbar}\left[\hbar\Delta\hat{S}^{\dagger}\hat{S}\,, \hat{\rho}_{\mathcal{S}}(t)\right] + \Gamma\left[\hat{S}\,\hat{\rho}_{\mathcal{S}}(t)\hat{S}^{\dagger} - \frac{1}{2}\hat{S}^{\dagger}\hat{S}\,\hat{\rho}_{\mathcal{S}}(t) - \frac{1}{2}\hat{\rho}_{\mathcal{S}}(t)\hat{S}^{\dagger}\hat{S}\right], \tag{D.12}$$

where the collisional shift can be subsequently absorbed in the definition of the detuning when considering the contributions of $\hat{H}_{\mathrm{sp}}$ and $\hat{V}_{\mathrm{AL}}$ in the total evolution.

---

[2] We use the identity $\int_0^{\infty}\exp(\mathrm{i}\omega t)\,\mathrm{d}t = \mathrm{i}\,\mathrm{p.v.}(1/\omega) + \pi\delta(\omega)$.

## D.3 Collisional contribution to the optical Bloch equations

We are now interested in the contribution that diffusive collisions have in the evolution of the expectation values of the coherences $\langle \hat{b}^{\dagger}_{\boldsymbol{k}_\mathrm{L}} \hat{a}_{\boldsymbol{0}} \rangle$. The coherences obey the following exact equations of motion:

$$\frac{\mathrm{d}}{\mathrm{d}t} \langle \hat{b}^{\dagger}_{\boldsymbol{k}_\mathrm{L}} \hat{a}_{\boldsymbol{0}} \rangle (t) = -\frac{\Gamma}{2} \langle \hat{b}^{\dagger}_{\boldsymbol{k}_\mathrm{L}} \hat{a}_{\boldsymbol{0}} \hat{N}_b(\boldsymbol{k}_\mathrm{L}) + \hat{N}_a(\boldsymbol{0}) \hat{b}^{\dagger}_{\boldsymbol{k}_\mathrm{L}} \hat{a}_{\boldsymbol{0}} \rangle (t), \tag{D.13}$$

where we have put $\hat{N}_a(\boldsymbol{0}) = \hat{a}^{\dagger}_{\boldsymbol{0}} \hat{a}_{\boldsymbol{0}}$ and $\hat{N}_b(\boldsymbol{k}_\mathrm{L}) = \hat{b}^{\dagger}_{\boldsymbol{k}_\mathrm{L}} \hat{b}_{\boldsymbol{k}_\mathrm{L}}$. To add this term into the lossy GP model presented in section 5.3.2, we can now perform a mean-field approximation and put $\langle \hat{N}_i \hat{b}^{\dagger}_{\boldsymbol{k}_\mathrm{L}} \hat{a}_{\boldsymbol{0}} \rangle \simeq \langle \hat{N}_i \rangle \langle \hat{b}^{\dagger}_{\boldsymbol{k}_\mathrm{L}} \hat{a}_{\boldsymbol{0}} \rangle$, leading to:

$$\frac{\mathrm{d}}{\mathrm{d}t} \langle \hat{b}^{\dagger}_{\boldsymbol{k}_\mathrm{L}} \hat{a}_{\boldsymbol{0}} \rangle (t) = -\sigma_{ab} v_\mathrm{r} \left( \frac{n_a + n_b}{2} \right) \langle \hat{b}^{\dagger}_{\boldsymbol{k}_\mathrm{L}} \hat{a}_{\boldsymbol{0}} \rangle (t), \tag{D.14}$$

where $n_i = N_i/V$ for a uniform system. Therefore, the momentum relaxation through diffusive collisions can be accounted for by introducing a damping term $\propto \sigma_{ab} v_\mathrm{r} n$ into the mean-field equations (5.17) and (5.18).

# APPENDIX E

# Adiabatic approximations

In this appendix, we discuss the criterion that needs to be satisfied to perform an adiabatic evolution both for an Hermitian and a non-Hermitian Hamiltonian.

## E.1 Hermitian Hamiltonians

Let us consider a system described by a parameter-dependent Hamiltonian $\hat{H}(\xi)$, depending on the variable $\xi(t)$. In its diagonal form, the Hamiltonian reads:

$$\hat{H}(\xi)|\psi_n(\xi)\rangle = E_n(\xi)|\psi_n(\xi)\rangle. \tag{E.1}$$

Let us now consider a given state $|\Phi\rangle$. We can express this state into the eigenbasis defined by $\hat{H}(\xi)$:

$$|\Phi(t)\rangle = \sum_n c_n(t)|\psi_n[\xi(t)]\rangle, \tag{E.2}$$

The dynamics of such a state can be cast in terms of the evolution of the amplitudes $c_n(t)$ by projecting the previous equation onto an eigenstate $|\psi_j\rangle$:

$$\mathrm{i}\hbar\dot{c}_n(t) = E_n(t)c_n(t) - \mathrm{i}\hbar\dot{\xi}\sum_j \langle\psi_n|\partial_\xi\psi_j\rangle c_j(t), \tag{E.3}$$

where we have put:

$$\dot{\xi} = \frac{\mathrm{d}\xi(t)}{\mathrm{d}t} \qquad \text{and} \qquad |\partial_\xi\psi_j\rangle = \frac{\mathrm{d}}{\mathrm{d}\xi}|\psi_j\rangle. \tag{E.4}$$

Let us now write:

$$\bar{c}_n(t) = \exp\left[\frac{\mathrm{i}}{\hbar}\int_0^t E_n(t')\,\mathrm{d}t'\right] c_n(t). \tag{E.5}$$

With this, the evolution of the $\bar{c}_n(t)$ coefficients reads:

$$\dot{\bar{c}}_n(t) = \mathrm{i}\sum_j \exp\left[\mathrm{i}\int_0^t \omega_{nj}(t')\,\mathrm{d}t'\right]\alpha_{nj}(t)\bar{c}_j(t), \tag{E.6}$$

where we have defined the Bohr frequency $\omega_{nj} = (E_n - E_j)/\hbar$ and

$$\alpha_{nj}(t) = \mathrm{i}\dot{\xi}\langle\psi_n(\xi)|\partial_\xi\psi_j(\xi)\rangle. \tag{E.7}$$

We now write equation (E.6) by separating the terms $n = j$ from $n \neq j$:

$$\dot{\bar{c}}_n(t) = -\mathrm{i}\varphi_n(t)\bar{c}_n(t) + \mathrm{i}\sum_{j\neq n} \exp\left[\mathrm{i}\int_0^t \omega_{nj}(t')\,\mathrm{d}t'\right]\alpha_{nj}(t)\bar{c}_j(t), \tag{E.8}$$

where we have defined the term:

$$\varphi_n(t) = -\mathrm{i}\dot{\xi}\langle\psi_n|\partial_\xi\psi_n\rangle \in \mathbb{R}, \tag{E.9}$$

leading to the so-called *Berry phase* (Berry 1984). For the second term in equation (E.8) we note first that, since $\langle\psi_n|\psi_j\rangle = \delta_{nj}$ one has $\partial_t\langle\psi_n|\psi_j\rangle = 0$, i.e. $\langle\dot{\psi}_n|\psi_j\rangle = -\langle\psi_n|\dot{\psi}_j\rangle$ and we can write the following:

$$\frac{\mathrm{d}}{\mathrm{d}t}\langle\psi_n|\hat{H}(t)|\psi_j\rangle = \langle\dot{\psi}_n|\hat{H}(t)|\psi_j\rangle + \langle\psi_n|\partial_t\hat{H}(t)|\psi_j\rangle + \langle\dot{\psi}_n|\hat{H}(t)|\psi_j\rangle \tag{E.10}$$

$$= [E_n(t) - E_j(t)]\langle\psi_n|\dot{\psi}_j\rangle + \langle\psi_n|\partial_t\hat{H}(t)|\psi_j\rangle \tag{E.11}$$

$$= 0, \tag{E.12}$$

which allows us to write:

$$\mathrm{i}\alpha_{nj}(t) = \langle\psi_n|\dot{\psi}_j\rangle = \frac{\langle\psi_n|\partial_t\hat{H}(t)|\psi_j\rangle}{E_j(t) - E_n(t)}. \tag{E.13}$$

And the evolution reads:

$$\dot{\bar{c}}_n(t) = -\mathrm{i}\varphi_n(t)\bar{c}_n(t) - \sum_{j\neq n} \exp\left[\mathrm{i}\int_0^t \omega_{nj}(t')\,\mathrm{d}t'\right]\frac{\langle\psi_n|\partial_t\hat{H}(t)|\psi_j\rangle}{E_j(t) - E_n(t)}\bar{c}_j(t). \tag{E.14}$$

At first order time-dependent perturbation theory, a given state prepared initially in an eigenstate $|\Phi(0)\rangle = |\psi_m(0)\rangle$ remains in this instantaneous eigenstate $|\Phi(t)\rangle = |\Psi_m(t)\rangle$ provided (Messiah 1999):

$$\frac{\hbar|\langle\psi_n|\partial_t\hat{H}(t)|\psi_j\rangle|}{|E_j(t) - E_n(t)|^2} \ll 1 \quad \forall t, \tag{E.15}$$

i.e., the rate of change of the Hamiltonian needs to be small compared to the Bohr frequencies of the system, which is known as the adiabatic approximation. In particular, if a level-crossing occurs, adiabaticity cannot be fulfilled.

## E.2 Non-Hermitian Hamiltonians

Let us now consider a situation in which $\hat{H}(t) \neq \hat{H}^\dagger(t)$. In this case, to express the Hamiltonian in its diagonal form, we need both its left and right eigenvectors (Moiseyev 2011) (a *biorthogonal* basis):

$$\hat{H} = \sum_k \hbar\lambda_k|\psi_k^{\mathrm{R}}\rangle\langle\psi_k^{\mathrm{L}}|, \tag{E.16}$$

Here, the eigenvalues are complex $\hbar\lambda_k = \hbar(\omega_k - \mathrm{i}\gamma_k/2)$. And:

$$\hat{H}|\psi_k^{\mathrm{R}}\rangle = \hbar\lambda_k|\psi_k^{\mathrm{R}}\rangle,$$

$$\langle\psi_k^{\mathrm{L}}|\hat{H} = \hbar\lambda_k\langle\psi_k^{\mathrm{L}}| \qquad \Rightarrow \qquad \hat{H}^\dagger|\psi_k^{\mathrm{L}}\rangle = \hbar\lambda_k^*|\psi_k^{\mathrm{L}}\rangle.$$

with the *normalization* condition $\langle\psi_m^{\mathrm{L}}|\psi_n^{\mathrm{R}}\rangle = \delta_{mn}$. A given state of the system can be expressed in term of the left and right eigenstates as:

$$|\Phi(t)\rangle = \sum_k c_k(t)|\psi_k^{\mathrm{R}}(t)\rangle = \sum_k \langle\psi_k^{\mathrm{L}}|\Phi(t)\rangle|\psi_k^{\mathrm{R}}(t)\rangle. \tag{E.17}$$

Keeping this in mind, we can derive the equivalent of the evolution equation (E.14) for a non-Hermitian Hamiltonian depending on a parameter $\xi(t)$:

$$\dot{\bar{c}}_n(t) = -\langle\psi_n^{\mathrm{L}}|\partial_t\psi_n^{\mathrm{R}}\rangle\bar{c}_n(t) - \sum_{j\neq n}\exp\left[\mathrm{i}\int_0^t [\lambda_n(t') - \lambda_j(t')]\,\mathrm{d}t'\right]\frac{\langle\psi_n^{\mathrm{L}}|\partial_t\hat{H}(t)|\psi_j^{\mathrm{R}}\rangle}{\hbar[\lambda_j(t) - \lambda_n(t)]}\bar{c}_j(t). \tag{E.18}$$

The adiabaticity condition in the non-Hermitian case can be stated as (Nenciu et al. 1992; Ibáñez et al. 2014):

$$\frac{|\langle\psi_n^{\mathrm{L}}|\partial_t\hat{H}(t)|\psi_j^{\mathrm{R}}\rangle|}{\hbar|\lambda_j(t) - \lambda_n(t)|^2}\exp\left[-\int_0^t \mathrm{Im}[\lambda_n(t') - \lambda_j(t')]\,\mathrm{d}t'\right] \ll 1 \quad \forall t. \tag{E.19}$$

This is known as the *quasi-adiabatic* condition. Here, there will be a global loss of population due to the non-zero imaginary parts, but the composition of a given eigenstate will reimain the same, renormalized to the instantaneous total population.

There are several special situations arising in the non-Hermitian case that are worth commenting. First, near the so-called exceptional points, where both the real part and imaginary part of two eigenvalues become equal [see section 4.2.2 and Heiss (2012)]. Here, adiabaticity can never be fulfilled since the denominator vanishes and there is inevitably strong mixing between the two crossing states (as in a regular level crossing in an Hermitian Hamiltonian). Second, the $\lambda_k$ are complex magnitudes, and thus, the exponential term in equation (E.19) contains exponentially growing or decaying terms. For the least dissipative eigenstate, so that $\mathrm{Im}[\lambda_n - \lambda_j] < 0\,\forall j$, all terms are decaying: adiabaticity can then be fulfilled (but note that it is not guaranteed by the decay alone). For the other states, at least one term in the sum grows exponentially. Thus in the former case, dissipation actually helps to enforce adiabaticity while in the latter makes it more difficult to achieve.

# APPENDIX F

## Complementary information for chapter 6

## F.1 Calibration of the spontaneous emission rate (∗∗)

The on-resonance Rabi frequency $\Omega_{\mathrm{L}}$ characterizing the strength of laser excitation is proportional to the square root of the laser power, $\Omega_{\mathrm{L}} = a\sqrt{P_{\mathrm{L}}}$. The coefficient $a = \Gamma_0/(w_{\mathrm{L}}\sqrt{\pi I_{\mathrm{sat}}})$ is given by the laser waist ($1/\mathrm{e}^2$ radius) $w_{\mathrm{L}}$, the saturation intensity $I_{\mathrm{sat}} \simeq 0.14\,\mathrm{mW/cm^2}$ and $\Gamma_0$. We set $\Omega_{\mathrm{L}}$ to weakly saturate the optical transition such that the excited state population is small. The rate of spontaneous emission for a single atom in free space is well approximated by $\gamma_{\mathrm{sp}} \simeq s\Gamma_0/2 = 520\,\mathrm{s}^{-1}$.

We observe Rabi oscillations on the intercombination transition induced by the dissipation laser, and use the measured oscillation frequency to calibrate the coefficient $a$. More precisely, we shine the dissipation laser on a BEC. For experimental convenience, we fix the pulse duration $T$ and vary the laser power $P_{\mathrm{L}}$. We record absorption images after a time of flight long compared to $\Gamma_0^{-1}$, so that all excited atoms have decayed back to the ground state when the image is taken. The width of the measured momentum distribution reflects the internal state of the atoms before decay due to the recoil of excited atoms when a photon is spontaneously emitted. As shown in figure F.1(a), the momentum width displays oscillations, and can be taken as a proxy of the population transferred to the excited state. We infer the oscillation period $aT$ from such curves taken at resonance ($\delta_{\mathrm{L}} = 0$) by fitting a sinusoidal function to the data, and obtained $a \simeq 2\pi \times 2.88\,\mathrm{MHz/mW^{1/2}}$. We independently calibrated the waist of the excitation laser using Gaussian optics propagation and found $w_{\mathrm{L}} \simeq 1\,\mathrm{mm}$, leading to $a \simeq 2\pi \times 2.76\,\mathrm{MHz/mW^{1/2}}$, in excellent agreement with the measured value.

## F.2 Two atoms and two wells (∗∗)

We illustrate the influence of interactions on the dissipative model in the simplest case with two atoms and two lattice sites. The bosonic Hilbert space is spanned by only three states, that can be taken to be $\{|S\rangle, |I\rangle, |A\rangle\}$, with the two symmetric and antisymmetric combinations $|S/A\rangle = (|2,0\rangle \pm |0,2\rangle)/\sqrt{2}$ and $|I\rangle = |1,1\rangle$, with $|n,m\rangle$ a Fock state with $n$ atoms in the left (L) well and $m$ in the right (R) one. In this basis,

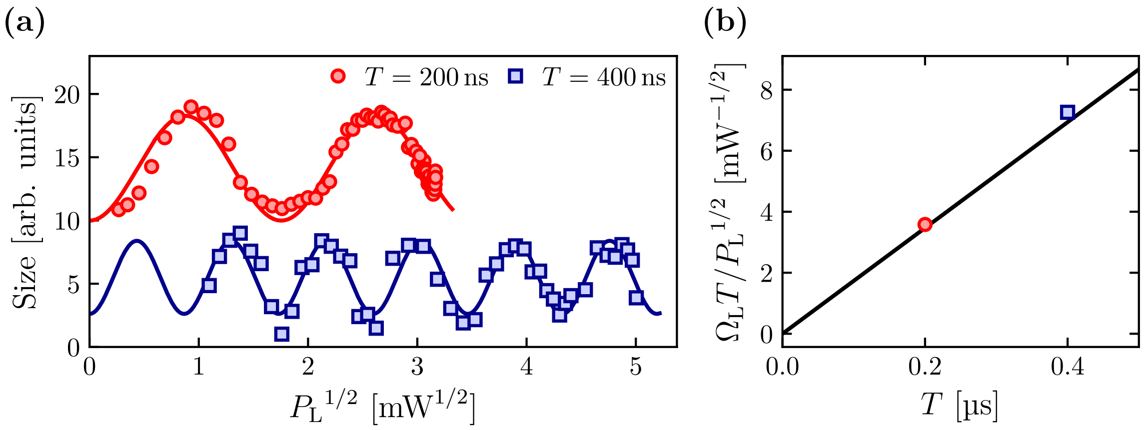

**Figure F.1** – Calibration of Rabi frequency. **(a):** Rabi oscillations on the ${}^1\mathrm{S}_0 - {}^3\mathrm{P}_1$ transition with chosen pulse time $T$ and varying laser power $P_\mathrm{L}$. The cloud size is normalized arbitrarily and curves are vertically shifted for clarity. **(b):** Inferred (data points) and calculated (solid line) oscillation period $aT = \Omega_\mathrm{L} T/\sqrt{P_\mathrm{L}}$. Adapted from Bouganne et al. (2019).

the Bose-Hubbard Hamiltonian reads

$$\hat{H} = U\left(|S\rangle\langle S| + |A\rangle\langle A|\right) - 2J\left(|I\rangle\langle S| + |S\rangle\langle I|\right). \tag{F.1}$$

We now consider the dissipative evolution described by equation (6.12). The dynamics can be analyzed conveniently using the formalism of quantum Monte-Carlo trajectories (Haroche et al. 2013; Daley 2014) [see the discussion in section 4.2.1]. To this end we rewrite the master equation as

$$\begin{aligned}\frac{\mathrm{d}}{\mathrm{d}t}\hat{\rho} &= \frac{1}{\mathrm{i}\hbar}\big[\hat{H},\hat{\rho}\big] + \frac{\gamma_\mathrm{sp}}{2}\Big(\hat{\Delta}\hat{\rho}\hat{\Delta} - \frac{1}{2}\hat{\Delta}^2\hat{\rho} - \frac{1}{2}\hat{\rho}\hat{\Delta}^2\Big), && \text{(F.2)}\\ &= \frac{1}{\mathrm{i}\hbar}\big(\hat{H}_\mathrm{eff}\hat{\rho} - \hat{\rho}\hat{H}_\mathrm{eff}^\dagger\big) + \mathcal{J}\big[\hat{\rho}\big], && \text{(F.3)}\end{aligned}$$

with the number difference operator $\hat{\Delta} = \hat{n}_\mathrm{L} - \hat{n}_\mathrm{R}$. We introduced an effective Hamiltonian

$$\hat{H}_\mathrm{eff} = \hat{H} - \frac{\mathrm{i}\hbar\gamma_\mathrm{sp}}{4}\hat{\Delta}^2, \tag{F.4}$$

and a jump operator

$$\mathcal{J}\big[\hat{\rho}\big] = \frac{\gamma_\mathrm{sp}}{2}\hat{\Delta}\hat{\rho}\hat{\Delta}. \tag{F.5}$$

In the Monte-Carlo picture, the dissipative evolution in an infinitesimal time interval $[t, t+\delta t]$ is stochastic. The system either stays in the state $|\Psi(t)\rangle$ evolved under the effective Hamiltonian, or undergoes a quantum jump to the (unnormalized) state $\hat{\Delta}|\Psi(t)\rangle$ with probability $\delta p = \gamma_\mathrm{sp}\delta t\langle\Psi(t)|\hat{\Delta}^2|\Psi(t)\rangle/2$.

In the limit $J \to 0$, quantum jumps change the symmetric to the antisymmetric state and reciprocally (thereby randomizing the relative phase), but do not occur for the Fock state $|I\rangle$. When $J \neq 0$, the antisymmetric state $|A\rangle$ remains an eigenstate of $\hat{H}_\mathrm{eff}$ with eigenvalue $U - \mathrm{i}\hbar\gamma_\mathrm{sp}$. The other two eigenstates are superpositions $|\pm\rangle = a_\pm|I\rangle + b_\pm|S\rangle$ of $|I\rangle$ and $|S\rangle$ with eigenvalues

$$E_\pm = \frac{U - \mathrm{i}\hbar\gamma_\mathrm{sp}}{2} \pm \frac{1}{2}\sqrt{U^2 - (\hbar\gamma_\mathrm{sp})^2 + 16J^2 - 2\mathrm{i}U\hbar\gamma_\mathrm{sp}}. \tag{F.6}$$

In the limit $U \to +\infty$, the eigenvalues become

$$E_+ \simeq U - \mathrm{i}\hbar\gamma_{\mathrm{sp}} + \frac{4J^2}{U}, \qquad E_- \simeq -\frac{4J^2}{U} - \mathrm{i}\frac{4J^2\hbar\gamma_{\mathrm{sp}}}{U^2}, \tag{F.7}$$

where we restricted the expansions of the real and imaginary parts to leading orders in $J, \gamma_{\mathrm{sp}}$. We thus find that the lowest energy state $|-\rangle$ ($|G'\rangle$ in section 6.1.4) relaxes with a rate $\sim \gamma_{\mathrm{sp}}(2J/U)^2$, much slower than $\gamma_{\mathrm{sp}}$ due to the strong on-site interaction. In contrast, the two other states $|A\rangle$ and $|+\rangle$ relax with a rate $\sim \gamma_{\mathrm{sp}}$.

# F.3 Analysis of the momentum distributions (∗∗)

The main observable in our experiments is the measured atomic distribution after a time-of-flight expansion of $t_{\mathrm{tof}} = 20\,\mathrm{ms}$. In this section, we give the relevant details of the direct analysis (figures 6.1 and 6.2) and of the fitting model (figures 6.3 and 6.4).

## F.3.1 Direct analysis

**Peak amplitude** In figures 6.1 and 6.2, we show the time evolution of the central $\boldsymbol{k} = \boldsymbol{0}$ peak amplitude of the measured momentum distributions for varying lattice depths $V_\perp$. Generally, the evolution of the peak amplitude shows a dramatic change between a fast decay for early times and an algebraic decay for longer times. For each $V_\perp$, we perform a fit using the phenomenological function presented in section 6.1.2:

$$n_{\mathrm{peak}} = \frac{A}{(1 + \gamma_{\mathrm{i}} t/\kappa)^\kappa}, \tag{F.8}$$

which interpolates between the two behaviors. We show the best-fit parameters in figure F.2. The starting time of the algebraic regime is related to the disappearance of long-ranged spatial coherence and narrow peaks in the momentum distribution, as discussed further in section F.3.2.

**Momentum width** In figure 6.1, we show the time evolution of the root-mean-square (RMS) size of the momentum distribution

$$\Delta k_t = \int_{\mathrm{BZ}_1} k_x^2 \mathcal{N}(\boldsymbol{k}, t)\,\mathrm{d}^2 k, \tag{F.9}$$

where the integration is restricted to the first Brillouin zone $\mathrm{BZ}_1$. This restriction is set in order to focus on the fundamental band dynamics, as well as including only the central Bragg peak. The observed saturation at long times is consistent with a uniform $\mathrm{BZ}_1$ of width $2k_{\mathrm{latt}}$ and RMS size $k_{\mathrm{latt}}/\sqrt{3} \simeq 0.29 \times 2k_{\mathrm{latt}}$. Generalizing equation (6.3), we use the following form to fit the growth of momentum width $\Delta k = \sqrt{\Delta k_t^2 - \Delta k_{t=0}^2}$:

$$\Delta k = \sqrt{(\Delta k_\infty^2 - \Delta k_{t=0}^2)[1 - \mathrm{e}^{-(\gamma_{\mathrm{f}} t)^{2\sigma}}]}. \tag{F.10}$$

Here $\Delta k_\infty$ is the asymptotic size for long times, $\sigma$ the exponent characterizing the short-time power-law expansion and $\gamma_{\mathrm{f}}$ a rate related to the amplitude of the power-law. We show the best-fit parameters in figure F.3. At short times, equation (F.10) reduces to $\propto t^\sigma$, and the case of normal diffusion is $\sigma = 1/2$. In figure 6.1(d) , we only show the

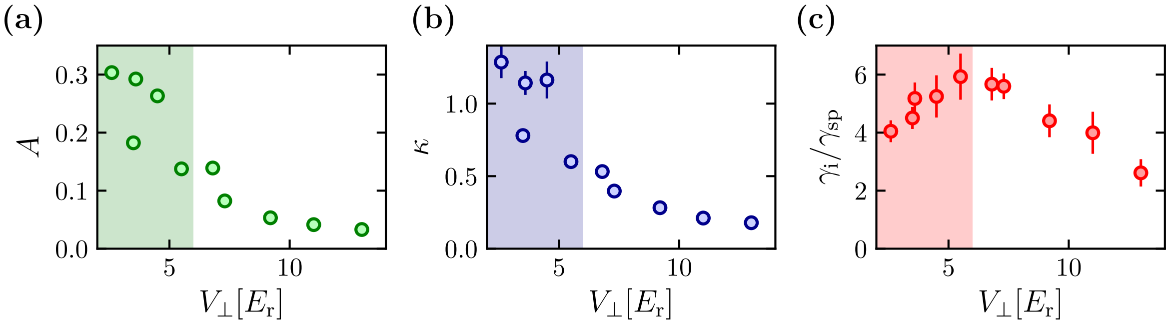

**Figure F.2** – Best-fit parameters on $\mathcal{N}(\boldsymbol{k}=\boldsymbol{0},t)$. **(a)-(c):** Best-fit parameters using equation (F.8) versus horizontal lattice depth. $A$ is the initial central peak amplitude in the momentum distribution, $\kappa$ is the exponent characterizing its long-time algebraic decay and $\gamma_\mathrm{i}$ is its initial decay rate. Error bars are 1-sigma confidence intervals derived from a $\chi^2$ fitting procedure. The shaded areas show the region where the Bose-Hubbard model is not a valid description. Adapted from Bouganne et al. (2019).

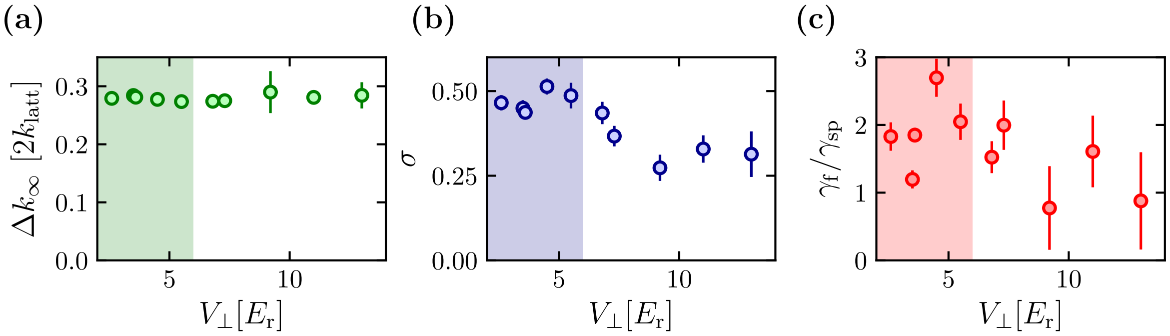

**Figure F.3** – Best-fit parameters on $\Delta k$. **(a)-(c):** Best-fit parameters using equation (F.10) versus horizontal lattice depth. $\Delta k_\infty$ is the final root-mean-square size, $\sigma$ is the exponent characterizing its short-time algebraic growth and $\gamma_\mathrm{f}$ is its rate. Error bars are 1-sigma confidence intervals derived from a $\chi^2$ fitting procedure. The shaded areas show the region where the Bose-Hubbard model is not a valid description. Adapted from Bouganne et al. (2019).

short-time $t^\sigma$ behavior inferred from such a fit. Note that the algebraic behavior of $\Delta k$ is similar to the algebraic behavior of $C_\mathrm{nn}$ [figure 6.1(d) and 6.4]. However, inter-band transitions and the initial structure factor of the gas makes this link non-trivial. In other words, there is no simple connection between the phenomenological equation F.10 and equation F.13.

### F.3.2 Extraction of coherence from the momentum profiles

#### Band structure and notations

We consider a lattice with negligible tunneling along the vertical $z$ direction. We denote by $\boldsymbol{r}_i=(x_i,y_i)$ a lattice site position, by $w(\boldsymbol{r}-\boldsymbol{r}_i)$ the Wannier function in the fundamental Bloch band centered at $\boldsymbol{r}_i$, by $\hat{a}_i$ the corresponding annihilation operator, and by $\hat{n}_i=\hat{a}_i^\dagger\hat{a}_i$ the number operator counting the occupation of site $i$.

In a cubic lattice, energy bands are labeled by a triplet of band indices $\{\boldsymbol{\nu}=(\nu_x,\nu_y,\nu_z)\}$.

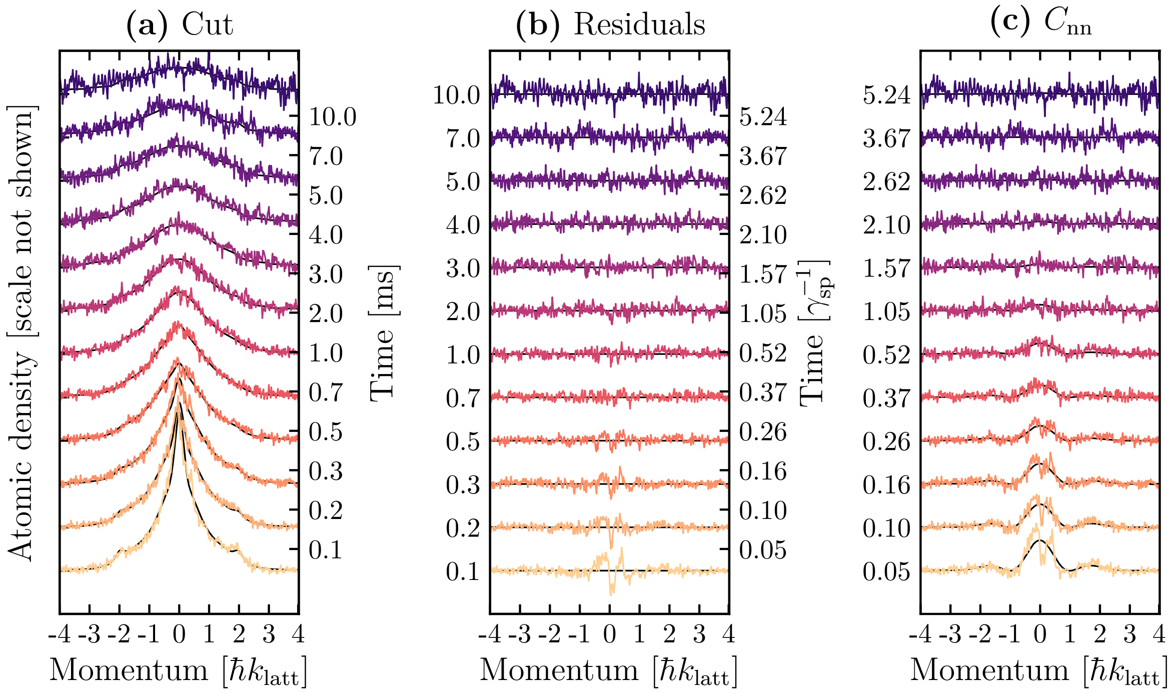

**Figure F.4** – Fitting the momentum profiles. **(a):** Momentum profiles $\mathcal{N}(k_x, k_y = 0)$ along the $x$ axis of the optical lattice for several dissipation times increasing from bottom to top. The profiles correspond to times in the algebraic regime $t \geq \kappa/\gamma_{\mathrm{i}}$, and in-plane lattice depth $V_\perp = 7.3\,E_{\mathrm{r}}$. The solid lines show a fit to the model in equation (F.14). **(b):** Residuals of the fit. **(c):** $C_{\mathrm{nn}}$ contribution in the fits, where we show the residual modulation provided by the part involving $C_{\mathrm{nn}}$. The profiles are averages over 3 realizations of the experiment. Adapted from Bouganne et al. (2019).

Whenever it is relevant, we use similar notations as for the fundamental band: For instance, Wannier functions in the band $\boldsymbol{\nu}$ are noted $w_{\boldsymbol{\nu}}$ and the annihilation operators $\hat{a}_{\boldsymbol{\nu},i}$. If only the fundamental band is relevant, we omit the band index to alleviate the notations. We gather all degenerate bands into *energy levels* indexed by an integer $\nu$. We neglect excited bands with $\nu_z \neq 0$ and group the first relevant bands according to $\nu = 0 \equiv \{\boldsymbol{\nu} = (0,0,0)\}$, $\nu = 1 \equiv \{\boldsymbol{\nu} = (1,0,0), (0,1,0)\}$, $\nu = 2 \equiv \{\boldsymbol{\nu} = (1,1,0), (2,0,0), (0,2,0)\}$, etc. Note that we assume a perfect symmetry between the two horizontal lattice arms, which is verified in the experiment up to about 5 %.

### Momentum distribution and time of flight

Under the assumption that interactions and finite time-of-flight effects can be neglected (Pedri et al. 2001; Gerbier et al. 2008) [see appendix A], the time-of-flight distribution mirrors the initial momentum distribution $\mathcal{N}(\boldsymbol{k})$ evaluated for $\boldsymbol{k} = M\boldsymbol{r}/(\hbar t_{\mathrm{tof}})$, with $\boldsymbol{r}$ the observation point. Using the basis of Wannier functions $w_{\boldsymbol{\nu}}(\boldsymbol{r} - \boldsymbol{r}_i)$, the normalized momentum distribution is given without further approximation by

$$\mathcal{N}(\boldsymbol{k}) = \sum_{\text{bands}\,\boldsymbol{\nu}} \mathcal{S}_{\boldsymbol{\nu}}(\boldsymbol{k}) \mathcal{W}_{\boldsymbol{\nu}}(\boldsymbol{k}). \tag{F.11}$$

Here, $\mathcal{W}_{\boldsymbol{\nu}}(\boldsymbol{k}) = |\widetilde{w}_{\boldsymbol{\nu}}(\boldsymbol{k})|^2$ is a smooth envelope function with $\widetilde{w}_{\boldsymbol{\nu}}$ the Fourier transform of $w_{\boldsymbol{\nu}}$, and $\mathcal{S}_{\boldsymbol{\nu}}$ is a normalized structure factor for band $\boldsymbol{\nu}$,

$$\mathcal{S}_{\boldsymbol{\nu}}(\boldsymbol{k}) = \frac{1}{N} \sum_{i,j} \mathrm{e}^{\mathrm{i}\boldsymbol{k}\cdot(\boldsymbol{r}_i - \boldsymbol{r}_j)} \langle \hat{a}^\dagger_{\boldsymbol{\nu},i} \hat{a}_{\boldsymbol{\nu},j} \rangle, \tag{F.12}$$

i.e. a discrete Fourier transform of the correlation function $\langle \hat{a}^\dagger_{\boldsymbol{\nu},i} \hat{a}_{\boldsymbol{\nu},j} \rangle$.

## Fitting model

The parametrization of the momentum distribution in equation (F.11) is very general, but also too complicated to be of practical use. We truncate the sum in equation (F.11) to make a fit to the experimental data tractable, and argue why this truncation is justified in the algebraic regime which is the focus of the article.

**Systems with short-range coherence** We first consider a system characterized by short-range coherence. The spatial correlation functions $\langle \hat{a}^\dagger_{\boldsymbol{\nu},i} \hat{a}_{\boldsymbol{\nu},j} \rangle$ fall off quickly with the separation $\boldsymbol{R} = \boldsymbol{r}_i - \boldsymbol{r}_j$, in such a way that the physical properties are well captured by the first two dominant terms with $\boldsymbol{R} = \boldsymbol{0}$ and $\boldsymbol{R} = \pm \boldsymbol{e}_{x/y}$, where $\boldsymbol{e}_{x/y}$ are the basis vector of the square lattice corresponding to nearest-neighbors. This regime corresponds in particular to the algebraic stage of the decay of spatial coherences that we report in section 6.1, and corresponds to a structure factor in the fundamental band

$$\mathcal{S}_0(\boldsymbol{k}) \simeq P_0 + \sum_{\boldsymbol{R}=\pm\boldsymbol{e}_{x/y}} C_{\mathrm{nn}} \cos(\boldsymbol{k}\cdot\boldsymbol{R}) \,. \tag{F.13}$$

Although atoms initially populate only the fundamental band, we expect that inter-band transitions gradually populate the lowest excited bands. Since this inter-band transfer is driven by incoherent spontaneous processes, it is reasonable to neglect coherence in these excited bands, corresponding to structure factors in the excited bands $\mathcal{S}_{\nu\neq 0}(\boldsymbol{k}) = P_{\boldsymbol{\nu}}$. Here $P_{\boldsymbol{\nu}} = 1/N \sum_i \langle \hat{a}^\dagger_{\boldsymbol{\nu},i} \hat{a}_{\boldsymbol{\nu},i} \rangle$ is the normalized population of the band $\boldsymbol{\nu}$.

These assumptions result in the following model for the momentum distribution of a system with short-range coherence,

$$\mathcal{N}(\boldsymbol{k}) \simeq \mathcal{S}_0(\boldsymbol{k}) \mathcal{W}_{\boldsymbol{0}}(\boldsymbol{k}) + \sum_{\nu=1,\cdots,3} P_{\boldsymbol{\nu}} \mathcal{W}_{\boldsymbol{\nu}}(\boldsymbol{k}), \tag{F.14}$$

where the free parameters are the populations $P_{\boldsymbol{\nu}}$ and the nearest-neighbor coherence $C_{\mathrm{nn}}$ in the fundamental band. The Wannier envelopes are calculated from the band structure (Bloch et al. 2008) using the experimentally determined lattice depths.

**Non-zero condensed fraction** The preceding discussion assumes explicitly that there is no condensate with long-range phase coherence. Initially, a condensate is generally present (except for lattice depths high enough that the whole system is in the Mott insulator regime). In a broken-symmetry approach (Pitaevskii et al. 2003), the presence of a condensate translates in a non-vanishing expectation value of the bosonic field $\alpha_{\boldsymbol{r}_i} = \langle \hat{a}_{\boldsymbol{\nu}=\boldsymbol{0},i} \rangle \neq 0$ [see section 1.1.3]. We account for a non-zero condensed fraction by assuming that the structure factor of the fundamental band can be written as the sum of a *coherent* component and of a short-ranged one,

$$\mathcal{S}_0'(\boldsymbol{k}) = \mathcal{S}_{0,\mathrm{BEC}}(\boldsymbol{k}) + \mathcal{S}_0(\boldsymbol{k}). \tag{F.15}$$

The coherent component $\mathcal{S}_{0,\mathrm{BEC}}(\boldsymbol{k})$ describes the condensate as in the standard Gross-Pitaevskii theory (Pedri et al. 2001). For simplicity, we model it as the sum of Gaussian functions at the main reciprocal lattice vectors

$$\mathcal{S}_{0,\mathrm{BEC}}(\boldsymbol{k}) = A_0 G_{\mathrm{BEC}}(\boldsymbol{k}) + A_1 \sum_{\boldsymbol{K}=\pm 2k_{\mathrm{latt}}\boldsymbol{e}_{x/y}} G_{\mathrm{BEC}}(\boldsymbol{k}-\boldsymbol{K}). \tag{F.16}$$

The first term corresponds to the central Bragg spot centered in the first Brillouin zone (BZ), of amplitude $A_0$, and the other terms to the lateral spots centered in all copies of the second BZ, of amplitude $A_1$. The function $G_{\mathrm{BEC}}(\boldsymbol{k})$ is a normalized Gaussian function of fixed width. We calculate the width accounting for near field effects (Gerbier et al. 2008). Using the expressions given in (Gerbier et al. 2008) and assuming a Thomas-Fermi profile, we obtain a near-Gaussian distribution of root-mean-square width $\sigma_{\mathrm{BEC}} \simeq 0.13 \times k_{\mathrm{latt}}$ for the expansion time of 20 ms used in our experiments. The short-ranged component $\mathcal{S}_0(\boldsymbol{k})$ is treated as discussed before in equation (F.13).

**Fit results** We fit equation (F.14) in combination with equation (F.15) to the measured momentum profiles. The free parameters are the amplitudes of the condensate peaks $A_0, A_1$ in equation (F.16), the populations $P_{\boldsymbol{\nu}}$ and the nearest-neighbor coherence $C_{\mathrm{nn}}$ in equation (F.14). We minimize the reduced

$$\chi^2 = \frac{1}{N_{\mathrm{dof}}} \int \frac{[n_{\mathrm{obs}}(\boldsymbol{k}) - n_{\mathrm{fit}}(\boldsymbol{k})]^2}{\sigma_{\mathrm{obs}}^2} \, \mathrm{d}^2 k, \tag{F.17}$$

with $n_{\mathrm{obs}}$ the observed distribution, $n_{\mathrm{fit}}$ the fitting model in equation (F.15), $\sigma_{\mathrm{obs}}$ the typical noise on the images and $N_{\mathrm{dof}}$ the number of degrees of freedom, i.e. the number of data points minus the number of fit parameters.

Figure F.4 shows cuts through the 2D profiles along one lattice axis for $V_\perp = 7.3\,E_{\mathrm{r}}$, together with the fits (solid lines), residuals of the fits and $C_{\mathrm{nn}}$ contribution in the fits. The duration of the dissipation laser pulse increases from bottom to top. We find a good agreement between the observed profiles and the data. The residuals are comparable or lower than the imaging noise (corresponding to optical densities $\sim 0.02$ and dominated by photonic shot noise and residual imperfections of the fringe reduction algorithm). The reduced $\chi^2$ is roughly equal to 1 for all dissipation times. The $C_{\mathrm{nn}}$ contribution in the fits corresponds to the quantity $[\mathcal{S}_0(\boldsymbol{k}) - P_0]\mathcal{W}_{\boldsymbol{0}}(\boldsymbol{k})$. We tried to include second nearest-neighbor coherences in the fundamental band, or coherences in the excited bands. We found that it does not improve the quality of the fits. We also attempted to force coherence in the first excited band instead of the ground band, and systematically found a markedly higher $\chi^2$ value.

Because of a finite noise in the images (coming mostly from photon shot noise), the resolution in the determination of $C_{\mathrm{nn}}$ is also finite, and we estimate it around 0.01 to 0.02. Such a limitation explains the apparent long-times saturation of the signal for the highest lattice depths $V_\perp \geq 9\,E_{\mathrm{r}}$.

### Evolution of condensed fraction

At the start of the algebraic regime for $t \gtrsim \kappa/\gamma_{\rm i}$, the condensed fraction is almost zero, and its contribution vanishes quickly. We are interested here in how it decays for earlier times. We first note from figure F.2(c) that the initial decay rate $\gamma_{\rm i}$ is substantially higher than $\gamma_{\rm sp}$. Second, as shown in figure F.5(a), with the example value of $V_\perp \simeq 7.3\,E_{\rm r}$, the diffraction peaks in the momentum distribution decay exponentially. We fit a decay rate $\gamma_{\rm BEC}$ from such a decay and compare it to the initial decay rate $\gamma_{\rm i}$ determined from the phenomenological analysis in equation (F.8) and shown in figure F.5(b). The two analyses give decay rates in very good agreement. This suggests that our interpretation that the initial decay of the coherence is dominated by the loss of long-ranged coherence, captured by a condensed fraction in the cloud, is correct. The results are only shown for $V_\perp \leq 8\,E_{\rm r}$, for which the initial state is a superfluid. Above this limit the initial condensed fraction is small and barely discernible from noise. This arises from the vicinity of the Mott transition where strong interactions deplete the condensate.

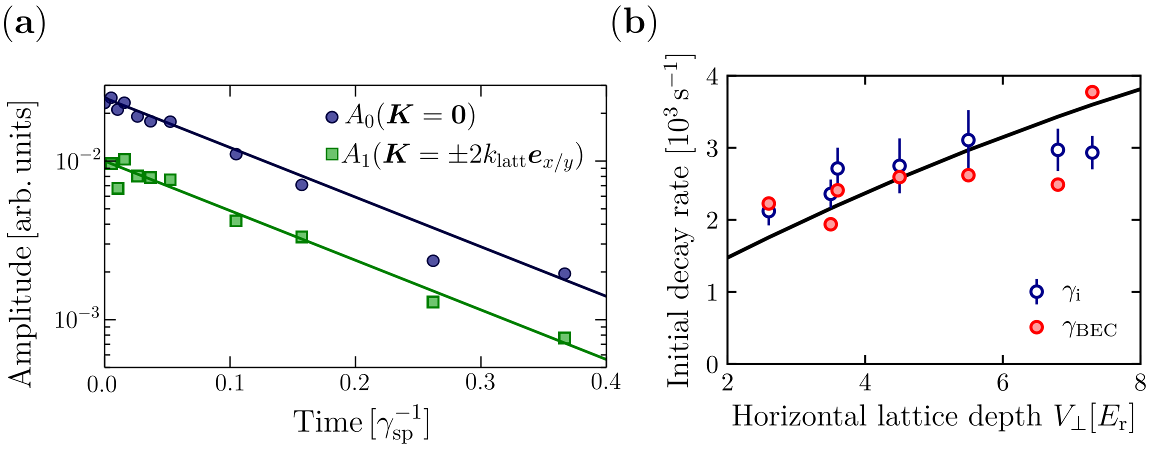

**Figure F.5** – Initial coherence decay rates. **(a):** Decay of the fitted condensed fraction peak amplitudes $A_0$ and $A_1$ [see equation (F.16)]. The in-plane lattice depth is $V_\perp \simeq 7.3\,E_{\rm r}$. The solid lines are exponential fits of $A_0$ and $A_1$ with an identical rate $\gamma_{\rm BEC} \simeq 7.1\,\gamma_{\rm sp}$. **(b):** Comparison between both determinations of the initial decay rates: $\gamma_{\rm i}$ extracted from equation (F.8) and $\gamma_{\rm BEC}$ extracted from fits as shown in **(a)**. For comparison, we also show the quantity $0.85\,U/\hbar$ as a solid line. Adapted from Bouganne et al. (2019).

Interestingly, we observe that the trend is similar to the evolution of the interaction strength [solid black line in figure F.5(b)], which indicates a probable role played by the interactions in the initial decay of the coherence. A similar enhancement of the decay rate compared to non-interacting systems was also observed in the numerical calculations presented in Pichler et al. (2010).

## F.4 Scaling behavior in the loss dynamics (∗∗)

We fit the atom number decay using an ad hoc function that reproduces well the observed behavior,

$$N = \frac{N_0}{1 + (\gamma_{\rm 2B} t)^\beta}. \tag{F.18}$$

We show the best-fit parameters in figure F.6 (black circles). The fitted exponent $\beta$ approaches a constant value $\sim 1/2$ [figure F.6(a)] for lattice depths $V_\perp \gtrsim 5\,E_\mathrm{r}$.

In figure F.6(b), we show that the ratio $\hbar\gamma_{2\mathrm{B}}/U$ between the fitted two-body loss rate and the on-site interaction energy $U$ saturates to a constant value $\simeq 0.1$ for lattice depths above $5\,E_\mathrm{r}$. In the Bose-Hubbard regime, the atom number decay is governed by a strictly local rate equation of the form

$$\frac{\mathrm{d}\bar{n}_i}{\mathrm{d}t} = -\gamma_{2\mathrm{B}}\langle \hat{n}_i(\hat{n}_i - 1)\rangle, \tag{F.19}$$

with $\bar{n}_i = \langle \hat{n}_i \rangle$ the mean density and

$$\gamma_{2\mathrm{B}} = K_2 \int |w(\boldsymbol{r})|^4\,\mathrm{d}^3r = \frac{MK_2}{4\pi\hbar^2 a}U. \tag{F.20}$$

Here $K_2$ is a two-body inelastic rate constant, and we emphasized that the ratio $\hbar\gamma_{2\mathrm{B}}/U$ is independent of the horizontal lattice depth $V_\perp$. This matches our observations for $V_\perp \geq 5\,E_\mathrm{r}$, where the Bose-Hubbard description is justified. For lower lattice depths, the assumption of strictly local losses underlying the Bose-Hubbard description starts to break down: Additional terms not included in equation (F.19) (for instance, involving nearest-neighbor density correlations $\propto \langle \hat{n}_i\hat{n}_j\rangle$, or density-induced tunneling $\propto \langle \hat{a}_i^\dagger \hat{n}_i \hat{a}_j\rangle$) start playing a role in the decay. These additional processes are effectively taken into account in the fitted loss rates. This explains the apparent increase of $\gamma_{2\mathrm{B}}$ for $V_\perp \leq 5\,E_\mathrm{r}$, which should rather be taken as an artifact of the Bose-Hubbard description for low lattice depths.

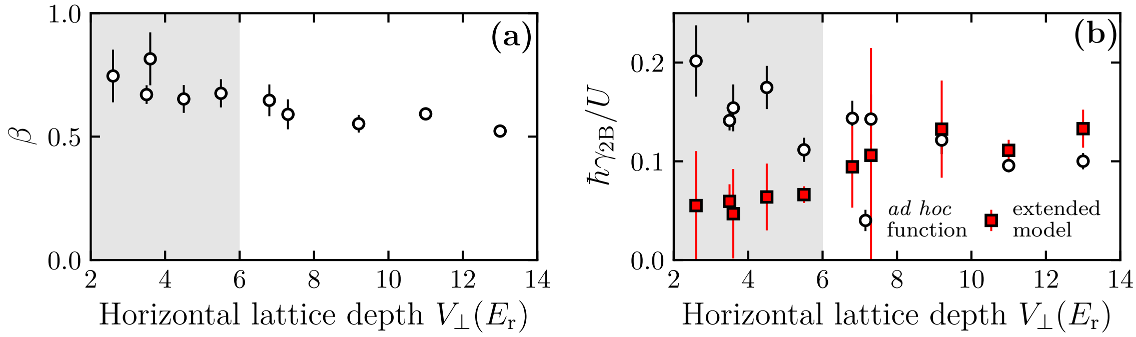

**Figure F.6** – Analysis of atom losses. **(a):** Fitted exponent for the atom number time evolution using equation (F.18) versus horizontal lattice depth. The exponent converges to $\beta = 1/2$ for horizontal lattice depths $V_\perp \gtrsim 6\,E_\mathrm{r}$. **(b):** Two-body loss rate determined using the ad hoc function in equation F.18 (empty circles) or our extended model presented in section 6.4 (filled squares) versus horizontal lattice depth. The shaded areas shows the region where the Bose-Hubbard model is not a valid description. Error bars are 1-sigma confidence intervals derived from a $\chi^2$ fitting procedure. Adapted from Bouganne et al. (2019).

We present in section 6.4 an extended model including inhomogeneities and losses. Using $\gamma_{2\mathrm{B}}$ as a free parameter in this extended model provides an independent determination [squares in figure F.6(b)]. Both sets of fitted values based either on the empirical equation (F.18) or on the extended model are consistent with each other in the Bose-Hubbard regime.

### Interpretation of the loss dynamics

Let us focus on the regime where the Bose-Hubbard description holds, and also assume that the two-body correlation function entering equation (F.19) is of the form $\langle \hat{n}_i(\hat{n}_i - 1)\rangle = \bar{n}_i^2 h(t)$, where $h$ depends on time but not on the density $\bar{n}$. Integration of equation (F.19) is straightforward for a uniform system, giving the decay law

$$\bar{n}_i(t) = \frac{\bar{n}_{i,0}}{1 + \gamma_{2\mathrm{B}}\bar{n}_{i,0}H(t)}, \tag{F.21}$$

with $H(t) = \int_0^t h(t')\,\mathrm{d}t'$ a primitive of $h$.

We now consider a two-dimensional system in a harmonic trap, as in our experiment, where the local density approximation applies. The initial density then obeys a law of the form $\bar{n}_{i,0} = n_0(x_i)$ with a reduced variable $x_i = (\mu - M\Omega_\perp^2 d^2 \boldsymbol{r}_i^2/2)/U$. Here $\mu$ is the chemical potential, $\Omega_\perp$ the trap frequency and $\boldsymbol{r}_i$ the position of site $i$ in units of $d$. Taking a continuum limit, the atom number $N(t) = \sum_i \bar{n}_i$ obeys

$$N(t) = \frac{2\pi U}{M\Omega_\perp^2 d^2}\int_0^{x_0} \frac{n_0(x)}{1 + \gamma_{2\mathrm{B}} n_0(x) H(t)}\,\mathrm{d}x, \tag{F.22}$$

with $x_0 = \mu/U$. When $t \to \infty$, we find that the atom number decays according to the asymptotic law

$$N(t) \to 2\pi \frac{U}{\gamma_{2\mathrm{B}}}\frac{x_0}{M\Omega_\perp^2 d^2}\frac{1}{H(t)}. \tag{F.23}$$

The asymptotic decay depends weakly on the lattice depth: $U/\gamma_{2\mathrm{B}}$ depends only on atomic properties (see previous paragraph), and $x_0/M\Omega_\perp^2 d^2 \simeq 2000/E_\mathrm{r}$ typically varies very little with the lattice depth.

We discuss in section 6.1 that we observe a decay law empirically captured by equation (F.18). From the previous discussion, we infer that this decay law would correspond to a two-body correlation function $\langle \hat{n}_i(\hat{n}_i - 1)\rangle \propto 1/\sqrt{t}$. Asymptotically, the two-body correlation function $\langle \hat{n}_i(\hat{n}_i - 1)\rangle$ vanishes. A system of hardcore bosons where only empty or singly-occupied sites are allowed is an asymptotic state compatible with this behavior: Since $\bar{n}_i = p_1 = 1 - p_0$ and $\langle \hat{n}_i^2\rangle = p_1$ for hardcore bosons, one necessarily has $\langle \hat{n}_i(\hat{n}_i - 1)\rangle = 0$. A possible interpretation is thus that the system is driven to such a hardcore bosons state by inelastic losses. This scenario is reminiscent of an experiment performed on molecules in a one-dimensional optical lattice (Syassen et al. 2008).

# Bibliography

Aharonov, Y. and D. Bohm (1959). *Significance of electromagnetic potentials in the quantum theory*. Physical Review **115**.3, 485–491 (cited on page 160).

Aidelsburger, M. (2018). *Artificial gauge fields and topology with ultracold atoms in optical lattices*. Journal of Physics B: Atomic, Molecular and Optical Physics **51**.**19**, 193001 (cited on page 3).

Altman, E., A. Polkovnikov, E. Demler, B. I. Halperin, and M. D. Lukin (2005). *Superfluid-insulator transition in a moving system of interacting bosons*. Physical Review Letters **95**.**2**, 020402 (cited on page 25).

Altman, E., W. Hofstetter, E. Demler, and M. D. Lukin (2003). *Phase diagram of two-component bosons on an optical lattice*. New Journal of Physics **5**, 113–113 (cited on page 159).

Altman, E., E. Demler, and M. D. Lukin (2004). *Probing many-body states of ultracold atoms via noise correlations*. Physical Review A **70**.**1**, 013603 (cited on page 59).

Anderson, M. H., J. R. Ensher, M. R. Matthews, C. E. Wieman, and E. A. Cornell (1995). *Observation of Bose-Einstein condensation in a dilute atomic vapor*. Science **269**.**5221**, 198–201 (cited on page 2).

Anderson, P. W. (1997). *Basic notions of condensed matter physics*. Advanced Books Classics. Westview Press (cited on page 15).

Andrews, M. R., C. G. Townsend, H.-J. Miesner, D. S. Durfee, D. M. Kurn, and W. Ketterle (1997). *Observation of interference between two Bose condensates*. Science **275**.**5300**, 637–641 (cited on page 2).

Ashcroft, N. and N. Mermin (1976). *Solid state physics*. HRW international editions. Holt, Rinehart and Winston (cited on pages 17, 18, 20, 31, 57, 78).

Band, Y. B., B. Malomed, and M. Trippenbach (2002). *Adiabaticity in nonlinear quantum dynamics: Bose-Einstein condensate in a time-varying box*. Physical Review A **65**.**3**, 033607 (cited on page 53).

Barber, Z. W., C. W. Hoyt, C. W. Oates, L. Hollberg, A. V. Taichenachev, and V. I. Yudin (2006). *Direct excitation of the forbidden clock transition in neutral 174-Yb atoms confined to an optical lattice*. Physical Review Letters **96**.**8**, 083002 (cited on pages 74, 76).

Barber, Z. W., J. E. Stalnaker, N. D. Lemke, N. Poli, C. W. Oates, T. M. Fortier, S. A. Diddams, L. Hollberg, C. W. Hoyt, A. V. Taichenachev, and V. I. Yudin (2008).

*Optical lattice induced light shifts in an Yb atomic clock.* Physical Review Letters **100.10**, 103002 (cited on pages 76, 80).

Barber, Z. (2007). *Ytterbium optical lattice clock.* PhD Thesis. University of Colorado at Boulder (cited on page 38).

Barontini, G., R. Labouvie, F. Stubenrauch, A. Vogler, V. Guarrera, and H. Ott (2013). *Controlling the dynamics of an open many-body quantum system with localized dissipation.* Physical Review Letters **110.3**, 035302 (cited on pages 4, 92).

Basov, D. N. and T. Timusk (2005). *Electrodynamics of high-Tc superconductors.* Reviews of Modern Physics **77.2**, 721–779 (cited on page 1).

Baur, S. K. and E. J. Mueller (2010). *Two-body recombination in a quantum-mechanical lattice gas: Entropy generation and probing of short-range magnetic correlations.* Physical Review A **82.2**, 023626 (cited on pages 114, 161).

Bednorz, J. G. and K. A. Müller (1986). *Possible high-Tc superconductivity in the Ba-La-Cu-O system.* Zeitschrift für Physik B Condensed Matter **64.2**, 189–193 (cited on page 1).

Beige, A., D. Braun, B. Tregenna, and P. L. Knight (2000). *Quantum computing using dissipation to remain in a decoherence-free subspace.* Physical Review Letters **85.8**, 1762–1765 (cited on page 91).

Berry, M. V. (1984). *Quantal phase factors accompanying adiabatic changes.* Proceedings of the Royal Society of London. A. Mathematical and Physical Sciences (cited on page 182).

Bethe, H. A. and E. E. Salpeter (1957). *Quantum mechanics of one- and two-electron atoms.* Berlin Heidelberg: Springer-Verlag (cited on page 36).

Bishof, M., M. J. Martin, M. D. Swallows, C. Benko, Y. Lin, G. Quéméner, A. M. Rey, and J. Ye (2011). *Inelastic collisions and density-dependent excitation suppression in a 87-Sr optical lattice clock.* Physical Review A **84.5**, 052716 (cited on page 100).

Blakie, P. B. and J. V. Porto (2004). *Adiabatic loading of bosons into optical lattices.* Physical Review A **69.1**, 013603 (cited on page 28).

Bloch, I., T. W. Hänsch, and T. Esslinger (2000). *Measurement of the spatial coherence of a trapped Bose gas at the phase transition.* Nature **403.6766**, 166 (cited on page 2).

Bloch, I., J. Dalibard, and W. Zwerger (2008). *Many-body physics with ultracold gases.* Reviews of Modern Physics **80.3**, 885–964 (cited on pages 2, 20, 35, 50, 56, 141, 149, 190).

Boninsegni, M. and N. V. Prokof'ev (2012). *Colloquium: Supersolids: What and where are they?* Reviews of Modern Physics **84.2**, 759–776 (cited on page 2).

Borkowski, M., A. A. Buchachenko, R. Ciuryło, P. S. Julienne, H. Yamada, Y. Kikuchi, K. Takahashi, Y. Takasu, and Y. Takahashi (2017). *Beyond-Born-Oppenheimer effects in sub-kHz-precision photoassociation spectroscopy of ytterbium atoms.* Physical Review A **96.6**, 063405 (cited on page 47).

Bosch Aguilera, M., R. Bouganne, A. Dareau, M. Scholl, Q. Beaufils, J. Beugnon, and F. Gerbier (2018). *Non-linear relaxation of interacting bosons coherently driven on a narrow optical transition.* EPL (Europhysics Letters) **123.4**, 40004 (cited on pages 118, 128, 130, 132, 136).

Bouganne, R., M. Bosch Aguilera, A. Dareau, E. Soave, J. Beugnon, and F. Gerbier (2017). *Clock spectroscopy of interacting bosons in deep optical lattices*. New Journal of Physics **19.11**, 113006 (cited on pages 60, 91, 93, 95–97, 99, 101, 124, 141, 155).

Bouganne, R. (2018). *Probing ultracold ytterbium in optical lattices with resonant light: from coherent control to dissipative dynamics*. PhD Thesis. Sorbonne Université, Université Pierre et Marie Curie, Paris 6 (cited on pages 40, 48, 71, 140).

Bouganne, R., M. Bosch Aguilera, A. Ghermaoui, J. Beugnon, and F. Gerbier (2019). *Anomalous momentum diffusion in a dissipative many-body system*. arXiv:1905.04808 [cond-mat] (cited on pages 140, 142, 144–146, 154, 186, 188, 189, 192, 193).

Bowers, C. J., D. Budker, E. D. Commins, D. DeMille, S. J. Freedman, A.-T. Nguyen, S.-Q. Shang, and M. Zolotorev (1996). *Experimental investigation of excited-state lifetimes in atomic ytterbium*. Physical Review A **53.5**, 3103–3109 (cited on page 72).

Bradley, C. C., C. A. Sackett, J. J. Tollett, and R. G. Hulet (1995). *Evidence of Bose-Einstein condensation in an atomic gas with attractive interactions*. Physical Review Letters **75.9**, 1687–1690 (cited on page 2).

Breuer, H. P. and F. Petruccione (2007). *The theory of open quantum systems*. Oxford University Press (cited on pages 4, 102).

Bromley, S. L., B. Zhu, M. Bishof, X. Zhang, T. Bothwell, J. Schachenmayer, T. L. Nicholson, R. Kaiser, S. F. Yelin, M. D. Lukin, A. M. Rey, and J. Ye (2016). *Collective atomic scattering and motional effects in a dense coherent medium*. Nature Communications **7**, 11039 (cited on page 3).

Bromley, S. L., S. Kolkowitz, T. Bothwell, D. Kedar, A. Safavi-Naini, M. L. Wall, C. Salomon, A. M. Rey, and J. Ye (2018). *Dynamics of interacting fermions under spin–orbit coupling in an optical lattice clock*. Nature Physics **14.4**, 399 (cited on page 3).

Brown, R. H. and R. Q. Twiss (1956). *A test of a new type of stellar interferometer on sirius*. Nature **178.4541**, 1046 (cited on page 60).

Böttcher, F., J.-N. Schmidt, M. Wenzel, J. Hertkorn, M. Guo, T. Langen, and T. Pfau (2019). *Transient supersolid properties in an array of dipolar quantum droplets*. Physical Review X **9.1**, 011051 (cited on page 2).

Cabrera, C. R., L. Tanzi, J. Sanz, B. Naylor, P. Thomas, P. Cheiney, and L. Tarruell (2018). *Quantum liquid droplets in a mixture of Bose-Einstein condensates*. Science **359.6373**, 301–304 (cited on page 2).

Cai, Z. and T. Barthel (2013). *Algebraic versus exponential decoherence in dissipative many-particle systems*. Physical Review Letters **111.15**, 150403 (cited on page 140).

Cao, C., E. Elliott, J. Joseph, H. Wu, J. Petricka, T. Schäfer, and J. E. Thomas (2011). *Universal quantum viscosity in a unitary Fermi gas*. Science **331.6013**, 58–61 (cited on page 2).

Capogrosso-Sansone, B., Ş. G. Söyler, N. Prokof'ev, and B. Svistunov (2008). *Monte Carlo study of the two-dimensional Bose-Hubbard model*. Physical Review A **77.1**, 015602 (cited on page 25).

Cappellini, G., M. Mancini, G. Pagano, P. Lombardi, L. Livi, M. Siciliani de Cumis, P. Cancio, M. Pizzocaro, D. Calonico, F. Levi, C. Sias, J. Catani, M. Inguscio, and L.

Fallani (2014). *Direct observation of coherent interorbital spin-exchange dynamics.* Physical Review Letters **113.12**, 120402 (cited on page 100).

Carmichael, H. (1993). *An open systems approach to quantum optics.* Vol. 18. Lecture Notes in Physics Monographs. Berlin, Heidelberg: Springer Berlin Heidelberg (cited on page 104).

Castin, Y. and R. Dum (1996). *Bose-Einstein condensates in time dependent traps.* Physical Review Letters **77.27**, 5315–5319 (cited on pages 13, 165).

Cataliotti, F. S., S. Burger, C. Fort, P. Maddaloni, F. Minardi, A. Trombettoni, A. Smerzi, and M. Inguscio (2001). *Josephson junction arrays with Bose-Einstein condensates.* Science **293.5531**, 843–846 (cited on page 29).

Cayla, H., C. Carcy, Q. Bouton, R. Chang, G. Carleo, M. Mancini, and D. Clément (2018). *Single-atom-resolved probing of lattice gases in momentum space.* Physical Review A **97.6**, 061609 (cited on page 58).

Cazalilla, M. A., A. F. Ho, and M. Ueda (2009). *Ultracold gases of ytterbium: ferromagnetism and Mott states in an SU(6) Fermi system.* New Journal of Physics **11.10**, 103033 (cited on page 3).

Cazalilla, M. A. and A. M. Rey (2014). *Ultracold Fermi gases with emergent SU(N) symmetry.* Reports on Progress in Physics **77.12**, 124401 (cited on pages 3, 67).

Chen, W., Ş. Kaya Özdemir, G. Zhao, J. Wiersig, and L. Yang (2017). *Exceptional points enhance sensing in an optical microcavity.* Nature **548.7666**, 192–196 (cited on page 109).

Chevy, F., V. Bretin, P. Rosenbusch, K. W. Madison, and J. Dalibard (2002). *Transverse breathing mode of an elongated Bose-Einstein condensate.* Physical Review Letters **88.25**, 250402 (cited on page 16).

Cho, J. W., H.-g. Lee, S. Lee, J. Ahn, W.-K. Lee, D.-H. Yu, S. K. Lee, and C. Y. Park (2012). *Optical repumping of triplet-P states enhances magneto-optical trapping of ytterbium atoms.* Physical Review A **85.3**, 035401 (cited on page 38).

Chou, C. W., D. B. Hume, T. Rosenband, and D. J. Wineland (2010). *Optical clocks and relativity.* Science **329.5999**, 1630–1633 (cited on page 67).

Chu, S. (1998). *Nobel lecture: The manipulation of neutral particles.* Reviews of Modern Physics **70.3**, 685–706 (cited on page 2).

Cirac, J. I. and P. Zoller (2012). *Goals and opportunities in quantum simulation.* Nature Physics **8**, 264–266 (cited on page 2).

Clément, D., N. Fabbri, L. Fallani, C. Fort, and M. Inguscio (2009). *Exploring correlated 1D Bose gases from the superfluid to the Mott-insulator state by inelastic light scattering.* Physical Review Letters **102.15**, 155301 (cited on page 119).

Cohen-Tannoudji, C., J. Dupont-Roc, and G. Grynberg (1992). *Atom-photon interactions: basic processes and applications.* Wiley-Interscience publication. J. Wiley (cited on pages 75, 110, 111, 125, 131, 133, 148, 150, 173, 174, 178).

Cohen-Tannoudji, C. N. (1998). *Nobel lecture: Manipulating atoms with photons.* Reviews of Modern Physics **70.3**, 707–719 (cited on page 2).

Cook, R. J. (1988). *What are Quantum Jumps?* Physica Scripta **T21**, 49–51 (cited on page 104).

Daley, A. J., J. Ye, and P. Zoller (2011). *State-dependent lattices for quantum computing with alkaline-earth-metal atoms.* The European Physical Journal D **65**.**1**, 207–217 (cited on page 3).

Daley, A. J. (2011). *Quantum computing and quantum simulation with group-II atoms.* Quantum Information Processing **10**.**6**, 865 (cited on pages 3, 67).

Daley, A. J. (2014). *Quantum trajectories and open many-body quantum systems.* Advances in Physics **63**.**2**, 77–149 (cited on pages 146, 186).

Dalfovo, F., S. Giorgini, L. P. Pitaevskii, and S. Stringari (1999). *Theory of Bose-Einstein condensation in trapped gases.* Reviews of Modern Physics **71**.**3**, 463–512 (cited on pages 2, 10, 13–16).

Dalibard, J. and C. Cohen-Tannoudji (1985). *Atomic motion in laser light: Connection between semiclassical and quantum descriptions.* Journal of Physics B: Atomic and Molecular Physics **18**.**8**, 1661–1683 (cited on page 148).

Dalibard, J., Y. Castin, and K. Mølmer (1992). *Wave-function approach to dissipative processes in quantum optics.* Physical Review Letters **68**.**5**, 580–583 (cited on pages 104, 105).

Dalibard, J., F. Gerbier, G. Juzeliūnas, and P. Öhberg (2011). *Colloquium: Artificial gauge potentials for neutral atoms.* Reviews of Modern Physics **83**.**4**, 1523–1543 (cited on page 3).

Dareau, A., M. Scholl, Q. Beaufils, D. Döring, J. Beugnon, and F. Gerbier (2015). *Doppler spectroscopy of an ytterbium Bose-Einstein condensate on the clock transition.* Physical Review A **91**.**2**, 023626 (cited on page 69).

Dareau, A. (2015). *Manipulation cohérente d'un condensat de Bose-Einstein d'ytterbium sur la transition "d'horloge" : de la spectroscopie au magnétisme artificiel.* PhD Thesis. École Normale Superieure (cited on pages 38, 40–42, 46, 68–70).

Davis, K. B., M.-O. Mewes, M. A. Joffe, M. R. Andrews, and W. Ketterle (1995). *Evaporative cooling of sodium atoms.* Physical Review Letters **74**.**26**, 5202–5205 (cited on page 2).

DeMarco, B. and D. S. Jin (1999). *Onset of Fermi degeneracy in a trapped atomic gas.* Science **285**.**5434**, 1703–1706 (cited on page 2).

Denschlag, J. H., J. E. Simsarian, H. Häffner, C. McKenzie, A. Browaeys, D. Cho, K. Helmerson, S. L. Rolston, and W. D. Phillips (2002). *A Bose-Einstein condensate in an optical lattice.* Journal of Physics B: Atomic, Molecular and Optical Physics **35**.**14**, 3095 (cited on pages 50, 141).

Domenico, G. D., S. Schilt, and P. Thomann (2010). *Simple approach to the relation between laser frequency noise and laser line shape.* Applied Optics **49**.**25**, 4801–4807 (cited on page 89).

Doppler, J., A. A. Mailybaev, J. Böhm, U. Kuhl, A. Girschik, F. Libisch, T. J. Milburn, P. Rabl, N. Moiseyev, and S. Rotter (2016). *Dynamically encircling an exceptional point for asymmetric mode switching.* Nature **537**.**7618**, 76–79 (cited on page 109).

Drever, R. W. P., J. L. Hall, F. V. Kowalski, J. Hough, G. M. Ford, A. J. Munley, and H. Ward (1983). *Laser phase and frequency stabilization using an optical resonator.* Applied Physics B **31**.**2**, 97–105 (cited on page 71).

Dum, R., P. Zoller, and H. Ritsch (1992). *Monte Carlo simulation of the atomic master equation for spontaneous emission*. Physical Review A **45**.**7**, 4879–4887 (cited on page 104).

Dürr, S., J. J. García-Ripoll, N. Syassen, D. M. Bauer, M. Lettner, J. I. Cirac, and G. Rempe (2009). *Lieb-Liniger model of a dissipation-induced Tonks-Girardeau gas*. Physical Review A **79**.**2**, 023614 (cited on page 169).

Edmonds, M. J., M. Valiente, G. Juzeliūnas, L. Santos, and P. Öhberg (2013). *Simulating an interacting gauge theory with ultracold Bose gases*. Physical Review Letters **110**.**8**, 085301 (cited on page 162).

Ellinger, K., J. Cooper, and P. Zoller (1994). *Light-pressure force in N-atom systems*. Physical Review A **49**.**5**, 3909–3933 (cited on page 148).

Ernst, P. T., S. Götze, J. S. Krauser, K. Pyka, D.-S. Lühmann, D. Pfannkuche, and K. Sengstock (2010). *Probing superfluids in optical lattices by momentum-resolved Bragg spectroscopy*. Nature Physics **6**.**1**, 56–61 (cited on page 119).

Facchi, P. and S. Pascazio (2008). *Quantum Zeno dynamics: Mathematical and physical aspects*. Journal of Physics A: Mathematical and Theoretical **41**.**49**, 493001 (cited on page 91).

Feng, L., Y.-L. Xu, W. S. Fegadolli, M.-H. Lu, J. E. B. Oliveira, V. R. Almeida, Y.-F. Chen, and A. Scherer (2013). *Experimental demonstration of a unidirectional reflectionless parity-time metamaterial at optical frequencies*. Nature Materials **12**.**2**, 108–113 (cited on page 109).

Ferrier-Barbut, I., H. Kadau, M. Schmitt, M. Wenzel, and T. Pfau (2016). *Observation of quantum droplets in a strongly dipolar Bose gas*. Physical Review Letters **116**.**21**, 215301 (cited on page 2).

Feynman, R. P. (1955). “Application of quantum mechanics to liquid helium”. *Progress in Low Temperature Physics*. Vol. 1. Elsevier, pp. 17–53 (cited on page 118).

Feynman, R. P. (1982). *Simulating physics with computers*. International Journal of Theoretical Physics **21**.**6**, 467–488 (cited on page 1).

Fisher, M. P. A., P. B. Weichman, G. Grinstein, and D. S. Fisher (1989). *Boson localization and the superfluid-insulator transition*. Physical Review B **40**.**1**, 546–570 (cited on page 22).

Foss-Feig, M., M. Hermele, and A. M. Rey (2010). *Probing the Kondo lattice model with alkaline-earth-metal atoms*. Physical Review A **81**.**5**, 051603 (cited on page 67).

Foss-Feig, M., A. J. Daley, J. K. Thompson, and A. M. Rey (2012). *Steady-state many-body entanglement of hot reactive fermions*. Physical Review Letters **109**.**23**, 230501 (cited on page 92).

Franchi, L., L. F. Livi, G. Cappellini, G. Binella, M. Inguscio, J. Catani, and L. Fallani (2017). *State-dependent interactions in ultracold 174Yb probed by optical clock spectroscopy*. New Journal of Physics **19**.**10**, 103037 (cited on pages 91, 100, 101, 124).

Fried, D. G., T. C. Killian, L. Willmann, D. Landhuis, S. C. Moss, D. Kleppner, and T. J. Greytak (1998). *Bose-Einstein condensation of atomic hydrogen*. Physical Review Letters **81**.**18**, 3811–3814 (cited on pages 120, 136).

Fölling, S., F. Gerbier, A. Widera, O. Mandel, T. Gericke, and I. Bloch (2005). *Spatial quantum noise interferometry in expanding ultracold atom clouds.* Nature **434.7032**, 481–484 (cited on pages 59–61, 167).

Fölling, S., A. Widera, T. Müller, F. Gerbier, and I. Bloch (2006). *Formation of spatial shell structure in the superfluid to Mott insulator transition.* Physical Review Letters **97.6**, 060403 (cited on page 27).

García-Ripoll, J. J., S. Dürr, N. Syassen, D. M. Bauer, M. Lettner, G. Rempe, and J. I. Cirac (2009). *Dissipation-induced hard-core boson gas in an optical lattice.* New Journal of Physics **11.1**, 013053 (cited on pages 4, 92, 158, 159).

Gardiner, C. W. and A. S. Bradley (2001). *Analysis of g2 for the cold collision frequency shift in the hydrogen condensate experiments.* Journal of Physics B: Atomic, Molecular and Optical Physics **34.23**, 4663 (cited on page 135).

Gaunt, A. L., T. F. Schmidutz, I. Gotlibovych, R. P. Smith, and Z. Hadzibabic (2013). *Bose-Einstein condensation of atoms in a uniform potential.* Physical Review Letters **110.20**, 200406 (cited on page 137).

Georgescu, I., S. Ashhab, and F. Nori (2014). *Quantum simulation.* Reviews of Modern Physics **86.1**, 153–185 (cited on page 1).

Gerbier, F., S. Trotzky, S. Fölling, U. Schnorrberger, J. D. Thompson, A. Widera, I. Bloch, L. Pollet, M. Troyer, B. Capogrosso-Sansone, N. V. Prokof'ev, and B. V. Svistunov (2008). *Expansion of a quantum gas released from an optical lattice.* Physical Review Letters **101.15**, 155303 (cited on pages 56, 58, 165, 166, 189, 191).

Gerbier, F., A. Widera, S. Fölling, O. Mandel, T. Gericke, and I. Bloch (2005). *Phase coherence of an atomic Mott insulator.* Physical Review Letters **95.5**, 050404 (cited on page 57).

Gerbier, F. and J. Dalibard (2010). *Gauge fields for ultracold atoms in optical superlattices.* New Journal of Physics **12.3**, 033007 (cited on pages 3, 67, 160, 161).

Gericke, T., F. Gerbier, A. Widera, S. Fölling, O. Mandel, and I. Bloch (2007). *Adiabatic loading of a Bose–Einstein condensate in a 3D optical lattice.* Journal of Modern Optics **54.5**, 735–743 (cited on pages 32, 53).

Giorgini, S., L. P. Pitaevskii, and S. Stringari (2008). *Theory of ultracold atomic Fermi gases.* Reviews of Modern Physics **80.4**, 1215–1274 (cited on page 2).

Girardeau, M. (1960). *Relationship between systems of impenetrable bosons and fermions in one dimension.* Journal of Mathematical Physics **1.6**, 516–523 (cited on pages 92, 158).

Goldman, N., G. Juzeliūnas, P. Öhberg, and I. B. Spielman (2014). *Light-induced gauge fields for ultracold atoms.* Reports on Progress in Physics **77.12**, 126401 (cited on pages 3, 121, 137).

Goldman, V. V., I. F. Silvera, and A. J. Leggett (1981). *Atomic hydrogen in an inhomogeneous magnetic field: Density profile and Bose-Einstein condensation.* Physical Review B **24.5**, 2870–2873 (cited on page 126).

Gorshkov, A. V., A. M. Rey, A. J. Daley, M. M. Boyd, J. Ye, P. Zoller, and M. D. Lukin (2009). *Alkaline-earth-metal atoms as few-qubit quantum registers.* Physical Review Letters **102.11**, 110503 (cited on page 67).

Gorshkov, A. V., M. Hermele, V. Gurarie, C. Xu, P. S. Julienne, J. Ye, P. Zoller, E. Demler, M. D. Lukin, and A. M. Rey (2010). *Two-orbital SU(N) magnetism with ultracold alkaline-earth atoms.* Nature Physics **6**.**4**, 289–295 (cited on pages 3, 67, 161).

Gotlibovych, I., T. F. Schmidutz, A. L. Gaunt, N. Navon, R. P. Smith, and Z. Hadzibabic (2014). *Observing properties of an interacting homogeneous Bose-Einstein condensate: Heisenberg-limited momentum spread, interaction energy, and free expansion dynamics.* Physical Review A **89**.**6**, 061604 (cited on page 119).

Graham, P. W., J. M. Hogan, M. A. Kasevich, and S. Rajendran (2013). *New method for gravitational wave detection with atomic sensors.* Physical Review Letters **110**.**17**, 171102 (cited on page 67).

Greiner, M. (2003). *Ultracold quantum gases in three-dimensional optical lattice potentials.* PhD Thesis. Ludwig-Maximilians-Universität München (cited on pages 28, 29).

Greiner, M., O. Mandel, T. W. Hänsch, and I. Bloch (2002a). *Collapse and revival of the matter wave field of a Bose–Einstein condensate.* Nature **419**.**6902**, 51 (cited on pages 58, 59).

Greiner, M., O. Mandel, T. Esslinger, T. W. Hänsch, and I. Bloch (2002b). *Quantum phase transition from a superfluid to a Mott insulator in a gas of ultracold atoms.* Nature **415**.**6867**, 39–44 (cited on pages 2, 25, 56).

Greschner, S., G. Sun, D. Poletti, and L. Santos (2014). *Density-dependent synthetic gauge fields using periodically modulated interactions.* Physical Review Letters **113**.**21**, 215303 (cited on page 162).

Greschner, S., D. Huerga, G. Sun, D. Poletti, and L. Santos (2015). *Density-dependent synthetic magnetism for ultracold atoms in optical lattices.* Physical Review B **92**.**11**, 115120 (cited on page 162).

Grimm, R., M. Weidemüller, and Y. B. Ovchinnikov (2000). *Optical dipole traps for neutral atoms.* Advances In Atomic, Molecular, and Optical Physics **42**, 95 –170 (cited on pages 42, 49, 54, 80).

Gupta, S., Z. Hadzibabic, M. W. Zwierlein, C. A. Stan, K. Dieckmann, C. H. Schunck, E. G.M. v. Kempen, B. J. Verhaar, and W. Ketterle (2003). *Radio-frequency spectroscopy of ultracold fermions.* Science **300**.**5626**, 1723–1726 (cited on page 120).

Görlitz, A., T. L. Gustavson, A. E. Leanhardt, R. Löw, A. P. Chikkatur, S. Gupta, S. Inouye, D. E. Pritchard, and W. Ketterle (2003). *Sodium Bose-Einstein condensates in the F=2 state in a large-volume optical trap.* Physical Review Letters **90**.**9**, 090401 (cited on page 120).

Hahn, E. L. (1950). *Spin Echoes.* Physical Review **80**.**4**, 580–594 (cited on page 87).

Harber, D. M., H. J. Lewandowski, J. M. McGuirk, and E. A. Cornell (2002). *Effect of cold collisions on spin coherence and resonance shifts in a magnetically trapped ultracold gas.* Physical Review A **66**.**5**, 053616 (cited on page 120).

Haroche, S. and J.-M. Raimond (2013). *Exploring the quantum: atoms, cavities, and photons.* OCLC: 894721442. Oxford: Oxford University Press (cited on pages 102, 123, 148, 186).

Harper, P. G. (1955). *Single band motion of conduction electrons in a uniform magnetic field.* Proceedings of the Physical Society. Section A **68.10**, 874–878 (cited on page 160).

Heiss, W. D. (2012). *The physics of exceptional points.* Journal of Physics A: Mathematical and Theoretical **45.44**, 444016 (cited on pages 107, 108, 183).

Henriet, L., J. S. Douglas, D. E. Chang, and A. Albrecht (2019). *Critical open-system dynamics in a one-dimensional optical-lattice clock.* Physical Review A **99.2**, 023802 (cited on page 140).

Hess, H. F. (1986). *Evaporative cooling of magnetically trapped and compressed spin-polarized hydrogen.* Physical Review B **34.5**, 3476–3479 (cited on page 2).

Hild, S., T. Fukuhara, P. Schauß, J. Zeiher, M. Knap, E. Demler, I. Bloch, and C. Gross (2014). *Far-from-equilibrium spin transport in Heisenberg quantum magnets.* Physical Review Letters **113.14**, 147205 (cited on page 159).

Ho, T.-L. and Q. Zhou (2009). *Squeezing out the entropy of fermions in optical lattices.* Proceedings of the National Academy of Sciences **106.17**, 6916–6920 (cited on page 28).

Hofstadter, D. R. (1976). *Energy levels and wave functions of Bloch electrons in rational and irrational magnetic fields.* Physical Review B **14.6**, 2239–2249 (cited on page 160).

Holland, M., S. Marksteiner, P. Marte, and P. Zoller (1996). *Measurement induced localization from spontaneous decay.* Physical Review Letters **76.20**, 3683–3686 (cited on page 139).

Honda, K., Y. Takahashi, T. Kuwamoto, M. Fujimoto, K. Toyoda, K. Ishikawa, and T. Yabuzaki (1999). *Magneto-optical trapping of Yb atoms and a limit on the branching ratio of the 1P1 state.* Physical Review A **59.2**, R934–R937 (cited on page 37).

Hu, L., N. Poli, L. Salvi, and G. M. Tino (2017). *Atom interferometry with the Sr optical clock transition.* Physical Review Letters **119.26**, 263601 (cited on page 67).

Hänsch, T. W. and A. L. Schawlow (1975). *Cooling of gases by laser radiation.* Optics Communications **13.1**, 68–69 (cited on page 2).

Höfer, M., L. Riegger, F. Scazza, C. Hofrichter, D. Fernandes, M. Parish, J. Levinsen, I. Bloch, and S. Fölling (2015). *Observation of an orbital interaction-induced feshbach resonance in 173-Yb.* Physical Review Letters **115.26**, 265302 (cited on page 161).

Ibáñez, S. and J. G. Muga (2014). *Adiabaticity condition for non-Hermitian Hamiltonians.* Physical Review A **89.3**, 033403 (cited on pages 107, 110, 183).

Itano, W. M., D. J. Heinzen, J. J. Bollinger, and D. J. Wineland (1990). *Quantum Zeno effect.* Physical Review A **41.5**, 2295–2300 (cited on pages 91, 104).

Jaksch, D., C. Bruder, J. I. Cirac, C. W. Gardiner, and P. Zoller (1998). *Cold bosonic atoms in optical lattices.* Physical Review Letters **81.15**, 3108–3111 (cited on pages 2, 21, 22).

Jaksch, D. and P. Zoller (2003). *Creation of effective magnetic fields in optical lattices: the Hofstadter butterfly for cold neutral atoms.* New Journal of Physics **5**, 56–56 (cited on page 3).

Javanainen, J. and J. Ruostekoski (2006). *Symbolic calculation in development of algorithms: split-step methods for the Gross–Pitaevskii equation.* Journal of Physics A: Mathematical and General **39.12**, L179–L184 (cited on page 125).

Jin, D. S., J. R. Ensher, M. R. Matthews, C. E. Wieman, and E. A. Cornell (1996). *Collective excitations of a Bose-Einstein condensate in a dilute gas.* Physical Review Letters **77.3**, 420–423 (cited on page 16).

Kagan, Y., B. V. Svistunov, and G. V. Shlyapnikov (1985). *Effect of Bose condensation on inelastic processes in gases.* Soviet Journal of Experimental and Theoretical Physics Letters **42**, 209 (cited on page 124).

Kajtoch, D., E. Witkowska, and A. Sinatra (2018). *Adiabaticity when raising a uniform three-dimensional optical lattice in a bimodal Bose-Einstein condensate.* Physical Review A **98.2**, 023621 (cited on pages 30, 31).

Kapitza, P. L. and P. a. M. Dirac (1933). *The reflection of electrons from standing light waves.* Mathematical Proceedings of the Cambridge Philosophical Society **29.2**, 297–300 (cited on page 50).

Katori, H. (2011). *Optical lattice clocks and quantum metrology.* Nature Photonics **5.4**, 203–210 (cited on page 3).

Ketterle, W, D. Durfee, and D M. Stamper-Kurn (1999). *Making, probing and understanding Bose-Einstein condensates.* Vol. 140. Proceedings of the International School of Physics "Enrico Fermi" (cited on pages 35, 41, 44, 46).

Killian, T. C. (2000). *1S-2S spectrum of a hydrogen Bose-Einstein condensate.* Physical Review A **61.3**, 033611 (cited on pages 117, 125, 126, 136).

Killian, T. C., D. G. Fried, L. Willmann, D. Landhuis, S. C. Moss, T. J. Greytak, and D. Kleppner (1998). *Cold collision frequency shift of the 1S-2S transition in hydrogen.* Physical Review Letters **81.18**, 3807–3810 (cited on pages 120, 136).

Kitagawa, M., K. Enomoto, K. Kasa, Y. Takahashi, R. Ciuryło, P. Naidon, and P. S. Julienne (2008). *Two-color photoassociation spectroscopy of ytterbium atoms and the precise determinations of s-wave scattering lengths.* Physical Review A **77.1**, 012719 (cited on pages 14, 47, 95, 100, 101).

Kogut, J. B. (1983). *The lattice gauge theory approach to quantum chromodynamics.* Reviews of Modern Physics **55.3**, 775–836 (cited on page 162).

Kohn, W. (1959). *Analytic properties of Bloch waves and Wannier functions.* Physical Review **115.4**, 809–821 (cited on page 19).

Kolkowitz, S., S. L. Bromley, T. Bothwell, M. L. Wall, G. E. Marti, A. P. Koller, X. Zhang, A. M. Rey, and J. Ye (2017). *Spin–orbit-coupled fermions in an optical lattice clock.* Nature **542.7639**, 66–70 (cited on page 3).

Ku, M. J. H., A. T. Sommer, L. W. Cheuk, and M. W. Zwierlein (2012). *Revealing the superfluid lambda transition in the universal thermodynamics of a unitary Fermi gas.* Science **335.6068**, 563–567 (cited on page 2).

Labouvie, R., B. Santra, S. Heun, and H. Ott (2016). *Bistability in a driven-dissipative superfluid.* Physical Review Letters **116.23**, 235302 (cited on page 4).

Landau, L. (1941). *Theory of the superfluidity of helium II.* Physical Review **60.4**, 356–358 (cited on page 118).

Leggett, A. J. (1970). *Can a solid be "superfluid"?* Physical Review Letters **25.22**, 1543–1546 (cited on page 2).

Leggett, A. J. (2001). *Bose-Einstein condensation in the alkali gases: some fundamental concepts.* Reviews of Modern Physics **73.2**, 307–356 (cited on pages 2, 10, 16).

Leggett, A. J. (2006). *Quantum liquids: Bose condensation and Cooper pairing in condensed-matter systems.* Oxford University Press (cited on pages 10, 15).

Leibfried, D., R. Blatt, C. Monroe, and D. Wineland (2003). *Quantum dynamics of single trapped ions.* Reviews of Modern Physics **75.1**, 281–324 (cited on page 79).

Levin, M. and X.-G. Wen (2005). *Colloquium: Photons and electrons as emergent phenomena.* Reviews of Modern Physics **77.3**, 871–879 (cited on page 162).

Lewenstein, M., A. Sanpera, and V. Ahufinger (2012). *Ultracold atoms in optical lattices: simulating quantum many-body systems.* Oxford University Press (cited on page 2).

Lin, Y.-J., R. L. Compton, K. Jiménez-García, J. V. Porto, and I. B. Spielman (2009). *Synthetic magnetic fields for ultracold neutral atoms.* Nature **462.7273**, 628–632 (cited on pages 3, 161).

Lin, Y.-J., K. Jiménez-García, and I. B. Spielman (2011a). *Spin–orbit-coupled Bose Einstein condensates.* Nature **471.7336**, 83–86 (cited on page 122).

Lin, Z., H. Ramezani, T. Eichelkraut, T. Kottos, H. Cao, and D. N. Christodoulides (2011b). *Unidirectional invisibility induced by PT-symmetric periodic structures.* Physical Review Letters **106.21**, 213901 (cited on page 109).

Livi, L., G. Cappellini, M. Diem, L. Franchi, C. Clivati, M. Frittelli, F. Levi, D. Calonico, J. Catani, M. Inguscio, and L. Fallani (2016). *Synthetic dimensions and spin-orbit coupling with an optical clock transition.* Physical Review Letters **117.22**, 220401 (cited on pages 3, 67, 122).

Lopes, R., C. Eigen, A. Barker, K. G. Viebahn, M. Robert-de Saint-Vincent, N. Navon, Z. Hadzibabic, and R. P. Smith (2017). *Quasiparticle energy in a strongly interacting homogeneous Bose-Einstein condensate.* Physical Review Letters **118.21**, 210401 (cited on page 119).

Ludlow, A. D., N. D. Lemke, J. A. Sherman, C. W. Oates, G. Quéméner, J. von Stecher, and A. M. Rey (2011). *Cold-collision-shift cancellation and inelastic scattering in a Yb optical lattice clock.* Physical Review A **84.5**, 052724 (cited on page 100).

Ludlow, A. D., M. M. Boyd, J. Ye, E. Peik, and P. Schmidt (2015). *Optical atomic clocks.* Reviews of Modern Physics **87.2**, 637–701 (cited on pages 3, 67, 79, 80).

Lüschen, H. P., P. Bordia, S. S. Hodgman, M. Schreiber, S. Sarkar, A. J. Daley, M. H. Fischer, E. Altman, I. Bloch, and U. Schneider (2017). *Signatures of many-body localization in a controlled open quantum system.* Physical Review X **7.1**, 011034 (cited on page 4).

Mancini, M., G. Pagano, G. Cappellini, L. Livi, M. Rider, J. Catani, C. Sias, P. Zoller, M. Inguscio, M. Dalmonte, and L. Fallani (2015). *Observation of chiral edge states with neutral fermions in synthetic Hall ribbons.* Science **349.6255**, 1510–1513 (cited on page 122).

Margalit, Y., Z. Zhou, S. Machluf, D. Rohrlich, Y. Japha, and R. Folman (2015). *A self-interfering clock as a "which path" witness.* Science **349.6253**, 1205–1208 (cited on page 67).

Marte, P., R. Dum, R. Taïeb, and P. Zoller (1993). *Resonance fluorescence from quantized one-dimensional molasses.* Physical Review A **47.2**, 1378–1390 (cited on page 149).

Matthews, M. R., B. P. Anderson, P. C. Haljan, D. S. Hall, C. E. Wieman, and E. A. Cornell (1999). *Vortices in a Bose-Einstein condensate.* Physical Review Letters **83.13**, 2498–2501 (cited on page 2).

McGrew, W. F., X. Zhang, H. Leopardi, R. J. Fasano, D. Nicolodi, K. Beloy, J. Yao, J. A. Sherman, S. A. Schäffer, J. Savory, R. C. Brown, S. Römisch, C. W. Oates, T. E. Parker, T. M. Fortier, and A. D. Ludlow (2019). *Towards the optical second: Verifying optical clocks at the SI limit.* Optica **6.4**, 448–454 (cited on page 3).

Messiah, A. (1999). *Quantum mechanics.* Dover books on physics. Dover Publications (cited on pages 12, 28, 182).

Metcalf, H. J., P. v. d. Straten, and P. v. d. Straten (1999). *Laser cooling and trapping.* Graduate Texts in Contemporary Physics. New York: Springer-Verlag (cited on pages 35, 37, 38, 41, 49).

Milburn, T. J., J. Doppler, C. A. Holmes, S. Portolan, S. Rotter, and P. Rabl (2015). *General description of quasi-adiabatic dynamical phenomena near exceptional points.* Physical Review A **92.5**, 052124 (cited on page 109).

Misra, B. and E. C. G. Sudarshan (1977). *The Zeno's paradox in quantum theory.* Journal of Mathematical Physics **18.4**, 756–763 (cited on pages 91, 104).

Moiseyev, N. (2011). *Non-Hermitian quantum mechanics.* Cambridge University Press (cited on pages 106, 182).

Morsch, O. and M. Oberthaler (2006). *Dynamics of Bose-Einstein condensates in optical lattices.* Reviews of Modern Physics **78.1**, 179–215 (cited on pages 28, 50).

Mun, J., P. Medley, G. K. Campbell, L. G. Marcassa, D. E. Pritchard, and W. Ketterle (2007). *Phase diagram for a Bose-Einstein condensate moving in an optical lattice.* Physical Review Letters **99.15**, 150604 (cited on page 25).

Müller, M., S. Diehl, G. Pupillo, and P. Zoller (2012). *Engineered open systems and quantum simulations with atoms and ions.* Advances in Atomic, Molecular, and Optical Physics **61**, 1–80 (cited on page 140).

Nakagawa, M., N. Kawakami, and M. Ueda (2018). *Non-Hermitian Kondo effect in ultracold alkaline-earth atoms.* Physical Review Letters **121.20**, 203001 (cited on page 109).

Naraschewski, M. and R. J. Glauber (1999). *Spatial coherence and density correlations of trapped Bose gases.* Physical Review A **59.6**, 4595–4607 (cited on pages 11, 56, 166, 169).

Nascimbène, S., N. Navon, K. J. Jiang, F. Chevy, and C. Salomon (2010). *Exploring the thermodynamics of a universal Fermi gas.* Nature **463.7284**, 1057–1060 (cited on page 2).

Nenciu, G. and G. Rasche (1992). *On the adiabatic theorem for nonself-adjoint Hamiltonians.* Journal of Physics A: Mathematical and General **25.21**, 5741–5751 (cited on pages 110, 183).

Nogrette, F., D. Heurteau, R. Chang, Q. Bouton, C. I. Westbrook, R. Sellem, and D. Clément (2015). *Characterization of a detector chain using a FPGA-based time-to-digital converter to reconstruct the three-dimensional coordinates of single particles at high flux.* Review of Scientific Instruments **86.11**, 113105 (cited on page 58).

Notermans, R., R. Rengelink, and W. Vassen (2016). *Comparison of spectral linewidths for quantum degenerate bosons and fermions.* Physical Review Letters **117.21**, 213001 (cited on page 120).

Nozières, P. (2004). *Is the roton in superfluid 4He the ghost of a Bragg spot?* Journal of Low Temperature Physics **137.1**, 45–67 (cited on page 2).

Nozières, P. and D. Pines (1999). *Theory of quantum liquids.* Advanced Books Classics. Avalon Publishing (cited on page 118).

Ockeloen, C. F., A. F. Tauschinsky, R. J. C. Spreeuw, and S. Whitlock (2010). *Detection of small atom numbers through image processing.* Physical Review A **82.6**, 061606 (cited on page 48).

Olmos, B., D. Yu, Y. Singh, F. Schreck, K. Bongs, and I. Lesanovsky (2013). *Long-range interacting many-body systems with alkaline-earth-metal atoms.* Physical Review Letters **110.14**, 143602 (cited on page 3).

Ovchinnikov, Y. B., J. H. Müller, M. R. Doery, E. J. D. Vredenbregt, K. Helmerson, S. L. Rolston, and W. D. Phillips (1999). *Diffraction of a released Bose-Einstein condensate by a pulsed standing light wave.* Physical Review Letters **83.2**, 284–287 (cited on page 50).

Pagano, G., M. Mancini, G. Cappellini, L. Livi, C. Sias, J. Catani, M. Inguscio, and L. Fallani (2015). *Strongly interacting gas of two-electron fermions at an orbital feshbach resonance.* Physical Review Letters **115.26**, 265301 (cited on page 161).

Palevsky, H., K. Otnes, and K. E. Larsson (1958). *Excitation of rotons in helium II by cold neutrons.* Physical Review **112.1**, 11–18 (cited on page 118).

Papp, S. B., J. M. Pino, R. J. Wild, S. Ronen, C. E. Wieman, D. S. Jin, and E. A. Cornell (2008). *Bragg spectroscopy of a strongly interacting 85-Rb Bose-Einstein condensate.* Physical Review Letters **101.13**, 135301 (cited on page 119).

Pathria, R. K. and P. D. Beale (2011). *Statistical mechanics.* Academic Press (cited on page 10).

Patil, Y., S. Chakram, and M. Vengalattore (2015). *Measurement-induced localization of an ultracold lattice gas.* Physical Review Letters **115.14**, 140402 (cited on page 4).

Pedri, P., L. Pitaevskii, S. Stringari, C. Fort, S. Burger, F. S. Cataliotti, P. Maddaloni, F. Minardi, and M. Inguscio (2001). *Expansion of a coherent array of Bose-Einstein condensates.* Physical Review Letters **87.22**, 220401 (cited on pages 29, 189, 191).

Penrose, O. and L. Onsager (1956). *Bose-Einstein condensation and liquid helium.* Physical Review **104.3**, 576–584 (cited on pages 10, 24).

Pethick, C. J. and H. Smith (2008). *Bose–Einstein condensation in dilute gases.* Cambridge University Press (cited on pages 10, 12).

Petter, D., G. Natale, R. van Bijnen, A. Patscheider, M. Mark, L. Chomaz, and F. Ferlaino (2019). *Probing the roton excitation spectrum of a stable dipolar Bose gas.* Physical Review Letters **122**.**18**, 183401 (cited on page 119).

Pfau, T., S. Spälter, C. Kurtsiefer, C. R. Ekstrom, and J. Mlynek (1994). *Loss of spatial coherence by a single spontaneous emission.* Physical Review Letters **73**.**9**, 1223–1226 (cited on page 139).

Phillips, W. D. (1998). *Nobel lecture: Laser cooling and trapping of neutral atoms.* Reviews of Modern Physics **70**.**3**, 721–741 (cited on page 2).

Pichler, H., A. J. Daley, and P. Zoller (2010). *Nonequilibrium dynamics of bosonic atoms in optical lattices: Decoherence of many-body states due to spontaneous emission.* Physical Review A **82**.**6**, 063605 (cited on pages 139, 143, 148–150, 192).

Pitaevskii, L. P. and S. Stringari (2003). *Bose-Einstein condensation.* Oxford University Press (cited on pages 10, 11, 16, 124, 190).

Plenio, M. B. and P. L. Knight (1998). *The quantum-jump approach to dissipative dynamics in quantum optics.* Reviews of Modern Physics **70**.**1**, 101–144 (cited on pages 105, 146, 147).

Poletti, D., J.-S. Bernier, A. Georges, and C. Kollath (2012). *Interaction-induced impeding of decoherence and anomalous diffusion.* Physical Review Letters **109**.**4**, 045302 (cited on pages 140, 151, 152).

Poletti, D., P. Barmettler, A. Georges, and C. Kollath (2013). *Emergence of glasslike dynamics for dissipative and strongly interacting bosons.* Physical Review Letters **111**.**19**, 195301 (cited on pages 140, 147, 150–155).

Raman, C., M. Köhl, R. Onofrio, D. S. Durfee, C. E. Kuklewicz, Z. Hadzibabic, and W. Ketterle (1999). *Evidence for a critical velocity in a Bose-Einstein condensed gas.* Physical Review Letters **83**.**13**, 2502–2505 (cited on page 2).

Ramsey, N. (1986). *Molecular beams.* Oxford Classic Texts in the Physical Sciences. Oxford, New York: Oxford University Press (cited on page 86).

Riehle, F. (2015). *Towards a redefinition of the second based on optical atomic clocks.* Comptes Rendus Physique. The measurement of time / La mesure du temps **16**.**5**, 506–515 (cited on page 3).

Rokhsar, D. S. and B. G. Kotliar (1991). *Gutzwiller projection for bosons.* Physical Review B **44**.**18**, 10328–10332 (cited on page 22).

Rooij, R. v., J. S. Borbely, J. Simonet, M. D. Hoogerland, K. S. E. Eikema, R. A. Rozendaal, and W. Vassen (2011). *Frequency metrology in quantum degenerate helium: direct measurement of the 2 3S1 - 2 1S0 transition.* Science **333**.**6039**, 196–198 (cited on page 120).

Savard, T. A., K. M. O'Hara, and J. E. Thomas (1997). *Laser-noise-induced heating in far-off resonance optical traps.* Physical Review A **56**.**2**, R1095–R1098 (cited on page 44).

Scazza, F., C. Hofrichter, M. Höfer, P. C. De Groot, I. Bloch, and S. Fölling (2014). *Observation of two-orbital spin-exchange interactions with ultracold SU(N)-symmetric fermions.* Nature Physics **10**.**10**, 779–784 (cited on pages 67, 100).

Scazza, F. (2015). *Probing SU(N)-symmetric orbital interactions with ytterbium Fermi gases in optical lattices*. PhD Thesis. Ludwig-Maximilians-Universität München (cited on page 36).

Scholl, M. (2014). *Probing an ytterbium Bose-Einstein condensate using an ultranarrow optical line : towards artificial gauge fields in optical lattices*. PhD Thesis. Université Pierre et Marie Curie - Paris 6 (cited on pages 38, 40–42, 45, 46, 160).

Schweikhard, V., I. Coddington, P. Engels, V. P. Mogendorff, and E. A. Cornell (2004). *Rapidly rotating Bose-Einstein condensates in and near the lowest Landau level*. Physical Review Letters **92**.**4**, 040404 (cited on page 3).

Sciolla, B., D. Poletti, and C. Kollath (2015). *Two-time correlations probing the dynamics of dissipative many-body quantum systems: Aging and fast relaxation*. Physical Review Letters **114**.**17**, 170401 (cited on page 148).

Semeghini, G., G. Ferioli, L. Masi, C. Mazzinghi, L. Wolswijk, F. Minardi, M. Modugno, G. Modugno, M. Inguscio, and M. Fattori (2018). *Self-bound quantum droplets of atomic mixtures in free space*. Physical Review Letters **120**.**23**, 235301 (cited on page 2).

Sherson, J. F., C. Weitenberg, M. Endres, M. Cheneau, I. Bloch, and S. Kuhr (2010). *Single-atom-resolved fluorescence imaging of an atomic Mott insulator*. Nature **467**.**7311**, 68–72 (cited on page 27).

Sheshadri, K., H. R. Krishnamurthy, R. Pandit, and T. V. Ramakrishnan (1993). *Superfluid and insulating phases in an interacting-boson model: mean-field theory and the RPA*. EPL (Europhysics Letters) **22**.**4**, 257 (cited on page 22).

Sidorenkov, L. A., M. K. Tey, R. Grimm, Y.-H. Hou, L. Pitaevskii, and S. Stringari (2013). *Second sound and the superfluid fraction in a Fermi gas with resonant interactions*. Nature **498**.**7452**, 78–81 (cited on page 2).

Sponselee, K., L. Freystatzky, B. Abeln, M. Diem, B. Hundt, A. Kochanke, T. Ponath, B. Santra, L. Mathey, K. Sengstock, and C Becker (2019). *Dynamics of ultracold quantum gases in the dissipative Fermi–Hubbard model*. Quantum Science and Technology **4**.**1**, 014002 (cited on page 92).

Stamper-Kurn, D. M., A. P. Chikkatur, A. Görlitz, S. Inouye, S. Gupta, D. E. Pritchard, and W. Ketterle (1999). *Excitation of phonons in a Bose-Einstein condensate by light scattering*. Physical Review Letters **83**.**15**, 2876–2879 (cited on pages 16, 119).

Steinhauer, J., R. Ozeri, N. Katz, and N. Davidson (2002). *Excitation spectrum of a Bose-Einstein condensate*. Physical Review Letters **88**.**12**, 120407 (cited on page 119).

Stenger, J., S. Inouye, A. P. Chikkatur, D. M. Stamper-Kurn, D. E. Pritchard, and W. Ketterle (1999). *Bragg spectroscopy of a Bose-Einstein condensate*. Physical Review Letters **82**.**23**, 4569–4573 (cited on pages 16, 119).

Stern, A. (2008). *Anyons and the quantum Hall effect—A pedagogical review*. Annals of Physics. January Special Issue 2008 **323**.**1**, 204–249 (cited on page 1).

Streed, E. W., J. Mun, M. Boyd, G. K. Campbell, P. Medley, W. Ketterle, and D. E. Pritchard (2006). *Continuous and pulsed quantum Zeno effect*. Physical Review Letters **97**.**26**, 260402 (cited on page 91).

Syassen, N., D. M. Bauer, M. Lettner, T. Volz, D. Dietze, J. J. García-Ripoll, J. I. Cirac, G. Rempe, and S. Dürr (2008). *Strong dissipation inhibits losses and induces correlations in cold molecular gases.* Science **320**.**5881**, 1329–1331 (cited on pages 4, 91, 147, 158, 159, 194).

Sørensen, A. S., E. Demler, and M. D. Lukin (2005). *Fractional quantum Hall states of atoms in optical lattices.* Physical Review Letters **94**.**8**, 086803 (cited on pages 3, 160).

Taichenachev, A. V., V. I. Yudin, C. W. Oates, C. W. Hoyt, Z. W. Barber, and L. Hollberg (2006). *Magnetic field-induced spectroscopy of forbidden optical transitions with application to lattice-based optical atomic clocks.* Physical Review Letters **96**.**8**, 083001 (cited on pages 74, 76).

Takasu, Y., K. Maki, K. Komori, T. Takano, K. Honda, M. Kumakura, T. Yabuzaki, and Y. Takahashi (2003). *Spin-singlet Bose-Einstein condensation of two-electron atoms.* Physical Review Letters **91**.**4**, 040404 (cited on page 3).

Tanzi, L., E. Lucioni, F. Famà, J. Catani, A. Fioretti, C. Gabbanini, R. Bisset, L. Santos, and G. Modugno (2019). *Observation of a dipolar quantum gas with metastable supersolid properties.* Physical Review Letters **122**.**13**, 130405 (cited on page 2).

Tarruell, L. (2014). "Spectroscopic tools for experiments with ultracold fermions in optical lattices". *Quantum gas experiments.* Cold atoms. Imperial College Press, pp. 251–266 (cited on page 120).

Tarruell, L. and L. Sanchez-Palencia (2018). *Quantum simulation of the Hubbard model with ultracold fermions in optical lattices.* Comptes Rendus Physique. Quantum simulation / Simulation quantique **19**.**6**, 365–393 (cited on page 2).

Tomita, T., S. Nakajima, I. Danshita, Y. Takasu, and Y. Takahashi (2017). *Observation of the Mott insulator to superfluid crossover of a driven-dissipative Bose-Hubbard system.* Science Advances **3**.**12**, e1701513 (cited on page 92).

Tonks, L. (1936). *The complete equation of state of one, two and three-dimensional gases of hard elastic spheres.* Physical Review **50**.**10**, 955–963 (cited on pages 92, 158).

Toth, E., A. M. Rey, and P. B. Blakie (2008). *Theory of correlations between ultracold bosons released from an optical lattice.* Physical Review A **78**.**1**, 013627 (cited on page 58).

Traverso, A., R. Chakraborty, Y. N. Martinez de Escobar, P. G. Mickelson, S. B. Nagel, M. Yan, and T. C. Killian (2009). *Inelastic and elastic collision rates for triplet states of ultracold strontium.* Physical Review A **79**.**6**, 060702 (cited on page 100).

Tsui, D. C., H. L. Stormer, and A. C. Gossard (1982). *Two-dimensional magnetotransport in the extreme quantum limit.* Physical Review Letters **48**.**22**, 1559–1562 (cited on page 1).

Törmä, P. (2014). "Spectroscopies - Theory". *Quantum gas experiments.* Cold atoms. Imperial College Press, pp. 199–250 (cited on page 120).

Törmä, P. (2016). *Physics of ultracold Fermi gases revealed by spectroscopies.* Physica Scripta **91**.**4**, 043006 (cited on page 120).

Umucalılar, R. O. and E. J. Mueller (2010). *Fractional quantum Hall states in the vicinity of Mott plateaus.* Physical Review A **81**.**5**, 053628 (cited on pages 3, 160).

Vallet, G., E. Bookjans, U. Eismann, S. Bilicki, R. L. Targat, and J. Lodewyck (2017). *A noise-immune cavity-assisted non-destructive detection for an optical lattice clock in the quantum regime.* New Journal of Physics **19.8**, 083002 (cited on page 63).

Veeravalli, G., E. Kuhnle, P. Dyke, and C. J. Vale (2008). *Bragg spectroscopy of a strongly interacting Fermi gas.* Physical Review Letters **101.25**, 250403 (cited on page 120).

Vogels, J. M., K. Xu, C. Raman, J. R. Abo-Shaeer, and W. Ketterle (2002). *Experimental observation of the Bogoliubov transformation for a Bose-Einstein condensed gas.* Physical Review Letters **88.6**, 060402 (cited on page 119).

Wannier, G. H. (1937). *The structure of electronic excitation levels in insulating crystals.* Physical Review **52.3**, 191–197 (cited on page 18).

Weiner, J., V. S. Bagnato, S. Zilio, and P. S. Julienne (1999). *Experiments and theory in cold and ultracold collisions.* Reviews of Modern Physics **71.1**, 1–85 (cited on page 141).

Wineland, D. J. and W. M. Itano (1979). *Laser cooling of atoms.* Physical Review A **20.4**, 1521–1540 (cited on page 79).

Yamaguchi, A., S. Uetake, S. Kato, H. Ito, and Y. Takahashi (2010). *High-resolution laser spectroscopy of a Bose–Einstein condensate using the ultranarrow magnetic quadrupole transition.* New Journal of Physics **12.10**, 103001 (cited on page 120).

Yamaguchi, A. (2008). *Metastable state of ultracold and quantum degenerate ytterbium atoms: high-resolution spectroscopy and cold collisions.* PhD Thesis. Kyoto University (cited on page 38).

Yan, B., S. A. Moses, B. Gadway, J. P. Covey, K. R. A. Hazzard, A. M. Rey, D. S. Jin, and J. Ye (2013). *Observation of dipolar spin-exchange interactions with lattice-confined polar molecules.* Nature **501.7468**, 521–525 (cited on pages 91, 159).

Yanay, Y. and E. J. Mueller (2014). *Heating from continuous number density measurements in optical lattices.* Physical Review A **90.2**, 023611 (cited on pages 139, 143).

Yarnell, J. L., G. P. Arnold, P. J. Bendt, and E. C. Kerr (1959). *Excitations in liquid helium: neutron scattering measurements.* Physical Review **113.6**, 1379–1386 (cited on page 118).

Yi, W., A. J. Daley, G. Pupillo, and P. Zoller (2008). *State-dependent, addressable subwavelength lattices with cold atoms.* New Journal of Physics **10.7**, 073015 (cited on page 67).

Zambelli, F., L. Pitaevskii, D. M. Stamper-Kurn, and S. Stringari (2000). *Dynamic structure factor and momentum distribution of a trapped Bose gas.* Physical Review A **61.6**, 063608 (cited on pages 16, 118, 119, 126, 127, 136).

Zhang, R., Y. Cheng, H. Zhai, and P. Zhang (2015). *Orbital feshbach resonance in alkali-earth atoms.* Physical Review Letters **115.13**, 135301 (cited on page 161).

Zhu, B., B. Gadway, M. Foss-Feig, J. Schachenmayer, M. Wall, K. Hazzard, B. Yan, S. Moses, J. Covey, D. Jin, J. Ye, M. Holland, and A. Rey (2014). *Suppressing the loss of ultracold molecules via the continuous quantum Zeno effect.* Physical Review Letters **112.7**, 070404 (cited on pages 4, 91, 159).

Zurek, W. H. (2007). *Decoherence and the transition from quantum to classical — revisited*. Progress in Mathematical Physics, 1–31 (cited on page 3).

Zwerger, W. (2003). *Mott–Hubbard transition of cold atoms in optical lattices*. Journal of Optics B: Quantum and Semiclassical Optics **5.2**, S9 (cited on pages 17, 22, 23, 56, 141).

Zwierlein, M. W., Z. Hadzibabic, S. Gupta, and W. Ketterle (2003). *Spectroscopic insensitivity to cold collisions in a two-state mixture of fermions*. Physical Review Letters **91.25**, 250404 (cited on page 120).

Zych, M., F. Costa, I. Pikovski, and Č. Brukner (2011). *Quantum interferometric visibility as a witness of general relativistic proper time*. Nature Communications **2**, 505 (cited on page 67).